

Photophysics of Carbon Nanotubes

by

Georgii G. Samsonidze

Submitted to the

Department of Electrical Engineering and Computer Science

in partial fulfillment of the requirements for the degree of

Doctor of Philosophy in Electrical Engineering and Computer Science

at the

MASSACHUSETTS INSTITUTE OF TECHNOLOGY

February 2007

© Massachusetts Institute of Technology 2007. All rights reserved.

Author

Department of Electrical Engineering and Computer Science


October 31, 2006

Certified by

Mildred S. Dresselhaus

Institute Professor of Electrical Engineering and Physics

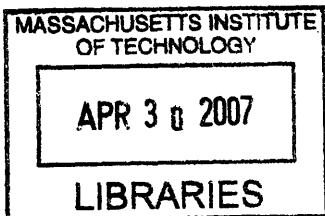
Thesis Supervisor



Accepted by

Arthur C. Smith

Chairman, Department Committee on Graduate Students



ARCHIVES

Photophysics of Carbon Nanotubes

by

Georgii G. Samsonidze

Submitted to the Department of Electrical Engineering and Computer Science
on October 31, 2006, in partial fulfillment of the
requirements for the degree of
Doctor of Philosophy in Electrical Engineering and Computer Science

Abstract

This thesis reviews the recent advances made in optical studies of single-wall carbon nanotubes. Studying the electronic and vibrational properties of carbon nanotubes, we find that carbon nanotubes less than 1 nm in diameter exhibit dramatic changes in their electron and phonon dispersion relations due to the curvature of the nanotube sidewall and the enhanced electron correlation effects associated with one dimensionality. The optical transition energies in small-diameter carbon nanotubes show a strong dependence on their geometrical structure, as was first observed in the photoluminescence experiments. The frequencies of the Raman-active phonon modes also become very sensitive to the geometrical structure of small-diameter carbon nanotubes. In particular, certain phonon modes exhibit anomalous behavior that significantly affects resonance Raman spectra of small-diameter carbon nanotubes. We have developed the extended tight-binding and advanced force-constant models that properly take into account the curvature effects in the small-diameter limit. The many-body corrections are fitted to the photoluminescence and resonance Raman spectroscopy data. The resulting extended tight-binding model with semiempirical many-body corrections shows a good agreement with the experimental results. The electron-photon and electron-phonon transition matrix elements are calculated within the framework of the extended tight-binding model. Finally, the photoluminescence and Raman intensities in the graphene sheet and carbon nanotubes are calculated. The calculated intensities show a reasonable agreement with the experimental results and allow structural characterization of carbon nanotubes by their spectroscopic signatures.

Thesis Supervisor: Mildred S. Dresselhaus

Title: Institute Professor of Electrical Engineering and Physics

Acknowledgments

I am very grateful to Prof. Mildred S. Dresselhaus for guiding me through the years of my graduate school at MIT. I thank Dr. Gene Dresselhaus for his help and advice, and Mrs. Laura Doughty for her help with administrative issues. I would like to thank Prof. Jing Kong for providing me with the computer where most calculations in this thesis were performed. I would like to thank my former and present graduate student colleagues at MIT. I am thankful to Prof. Riichiro Saito who invited me to visit University of Electro-Communications, Tokyo, Japan and Tohoku University, Sendai, Japan, to Dr. A. Gruneis who hosted me in Tokyo and Sendai, and to Dr. Jie Jiang for valuable discussions. I am grateful to Prof. Marcos A. Pimenta and Prof. A. Jorio who invited me to visit University Federal Minas Gerais, Belo Horizonte, Brazil, and for hosting me in Belo Horizonte. I am also grateful to my family for their constant support.

Contents

1	Introduction	17
2	Nanotube structure	21
2.1	Graphene sheet	22
2.2	Chirality and handedness	23
2.3	Translational symmetry	27
2.4	Helical symmetry	30
2.5	Cutting lines	33
2.5.1	Helical-helical representation	37
2.5.2	Angular-helical representation	39
2.5.3	Helical-linear representation	41
2.6	Summary of results	43
3	Electronic properties	47
3.1	Tight-binding framework	48
3.2	Simple tight-binding model	53
3.3	Metallicity	58
3.4	Density of electronic states	64
3.5	Trigonal Warping Effect	70
3.6	Extended tight-binding model	78
3.6.1	Long-range interactions	89
3.6.2	Curvature-induced rehybridization	91
3.6.3	Geometrical structure relaxation	93

3.7	Many-body effects	98
3.8	Summary and future work	101
4	Vibrational properties	103
4.1	Force-constant framework	104
4.2	Basic force-constant model	112
4.2.1	Electron and neutron scattering	115
4.2.2	Resonance Raman scattering	115
4.2.3	Phonon trigonal warping effect	118
4.2.4	X-ray scattering	121
4.3	Advanced force-constant model	123
4.3.1	DFT-LDA calculations	126
4.3.2	ETB calculations	130
4.4	Curvature-adapted force-constant model	135
4.4.1	Zone-folding technique	135
4.4.2	Curvature-adapted model	137
4.4.3	Force constant corrections	141
4.5	Direct calculation of the dynamical matrix	143
4.5.1	Supercell method	144
4.5.2	Linear response method	149
4.6	Phonon frequency softening	152
4.6.1	Peierls instability	152
4.6.2	Kohn anomaly	158
4.7	Summary	162
5	Interaction with light	165
5.1	Electron-photon interaction	166
5.1.1	Dipole selection rules	173
5.2	Electron-phonon interaction	177
5.2.1	Vibrational selection rules	189
5.3	Resonance Raman scattering	191

5.3.1	First-order RRS process in graphene	192
5.3.2	Second-order RRS process in graphene	194
5.3.3	The RRS process in nanotubes	202
5.4	Band gap photoluminescence	206
5.5	Concluding remarks and future directions	208
6	Conclusions	209

List of Figures

2-1	22
2-2	24
2-3	26
2-4	29
2-5	33
2-6	35
2-7	38
2-8	40
2-9	42
3-1	48
3-2	51
3-3	52
3-4	55
3-5	57
3-6	59
3-7	61
3-8	62
3-9	65
3-10	67
3-11	69
3-12	71
3-13	74

3-14 75
3-15 77
3-16 79
3-17 80
3-18 83
3-19 85
3-20 87
3-21 88
3-22 90
3-23 91
3-24 92
3-25 95
3-26 97
3-27 100

4-1 106
4-2 108
4-3 109
4-4 111
4-5 113
4-6 116
4-7 117
4-8 119
4-9 120
4-10 122
4-11 124
4-12 128
4-13 129
4-14 132
4-15 133

4-16	134
4-17	136
4-18	137
4-19	139
4-20	140
4-21	142
4-22	146
4-23	159
4-24	160
5-1	169
5-2	171
5-3	172
5-4	172
5-5	175
5-6	181
5-7	182
5-8	183
5-9	186
5-10	187
5-11	188
5-12	188
5-13	193
5-14	196
5-15	198
5-16	200
5-17	201

List of Tables

2.1	Structural parameters for SWNTs	45
3.1	The ETB transfer and overlap integrals t and s	82
3.2	The ETB short-range repulsive potential v	84
4.1	The character table for the point group D_{6h} at the Γ point	107
4.2	The character table for the point group D_{3h} at the K point	110
4.3	The BFC force constants ϕ fitted to the INS and EELS data	116
4.4	The BFC force constants ϕ fitted to the RRS data	117
4.5	The BFC force constants ϕ fitted to the phonon TWE data	119
4.6	The BFC force constants ϕ fitted to the IXS data	122
4.7	The AFC force constants ϕ calculated from DFT-LDA	127
4.8	The AFC force constants ϕ calculated from ETB	131
5.1	The atomic dipole transition matrix elements d	170
5.2	The off-site atomic deformation potential matrix elements α	184
5.3	The on-site atomic deformation potential matrix elements λ	185

Chapter 1

Introduction

Single-wall carbon nanotubes (SWNTs) are a novel form of sp^2 carbon. While the sp^2 carbon normally takes the form of the flat hexagonal monolayers, SWNTs have a cylindrical shape of variable lengths and diameters on the order of $1\ \mu\text{m}$ and $1\ \text{nm}$, respectively. The large aspect ratio makes the SWNTs almost perfect one-dimensional (1D) wires. Also, SWNTs have a hollow interior, implying that there are no inner atoms but only surface atoms. A virtually infinite surface-to-volume ratio in SWNTs offers extraordinary sensitivity for gas sensor applications. However, SWNTs are not chemically very reactive since they do not have surface dangling bonds. This reduces the noise level for electronic circuit applications, but at the same time lowers the quality of electric contacts. The chemical reactivity can be improved by functionalizing SWNTs with various surfactants and polymers, or by doping SWNTs with boron or nitrogen atoms that introduce the structural defects carrying unpaired electrons.

Because of their unique structure, SWNTs exhibit unusual physical, chemical, electrical, thermal, magnetic, biological, optical, mechanical, and kinetic properties. The SWNTs can be either truly metallic, or small or large gap semiconducting depending entirely on their geometry characterized by diameter, chiral angle, and handedness. Truly metallic SWNTs exhibit ballistic transport at room temperature and theoretically can withstand 1000 times more current density than copper conductors. Both metallic and semiconducting SWNTs are very efficient thermal conductors operating in the ballistic regime. Potentially good field emitters because of their atomically

sharp tips, SWNTs exhibit low optical quantum efficiency because of the dark excitonic states lying lower in energy than the bright states, with the dark states acting as traps at ambient temperatures. The SWNTs are one of the strongest materials ever synthesized because of their strong sp^2 bonds between carbon atoms within the hexagonal monolayers.

The unusual properties of SWNTs suggest many potential applications such as metallic wires, semiconducting devices, and heat sinks in integrated circuits, display devices, gas filters and sensors, mechanical oscillators, composite fibers in polymers and in different forms of structural enforcements. The electrical circuit applications are complicated by the absence of a reliable technique to arrange multiple SWNTs on a Si wafer. In display devices SWNTs might serve as electron emitters rather than field emitters because of the low optical quantum efficiency. Future applications of SWNTs include gas filters and sensors because of the virtually infinite surface-to-volume ratio and the possibility for doping or functionalizing SWNTs with different impurities or molecules. Because of their small dimensions and remarkable strength, SWNTs are proposed as high frequency mechanical oscillators. Strong mechanical properties suggest many different applications such as sports equipment, combat jackets, bridge construction, electric motor brushes, and the space elevator. Finally, SWNTs provide an ideal prototype system in which to study 1D physics.

Different techniques have been developed over the years to synthesize SWNTs in large quantities, including arc discharge, laser ablation, high pressure CO decomposition (HiPCO), chemical vapor deposition (CVD), and pyrolysis in the channels of porous zeolite. These techniques do not provide control over the synthesis process yielding both metallic and semiconducting SWNTs with a wide range of diameters and of all chiral angles and two kinds of handedness. Hence, various post production separation techniques have been introduced, such as precipitation of SWNTs functionalized with octadecylamine, chromatography of DNA wrapped SWNTs, alternating current dielectrophoresis, functionalization with diazonium salts, centrifugation with diluted bromine, and burning off metallic SWNTs by high current in electrical circuits. However, most of these techniques provide a moderate separation of SWNTs by their

metallicity along with the competitive separation by their diameter. The controlled mass production of SWNTs for industrial applications is still an open issue.

Various probes have been employed to characterize SWNT samples including atomic force microscopy (AFM), transmission electron microscopy (TEM), electron diffraction, scanning tunneling microscopy (STM), scanning tunneling spectroscopy (STS), and X-ray diffraction (XRD). Among these characterization methods, different optical spectroscopy techniques such as absorption spectroscopy, infrared (IR) spectroscopy, resonance Raman spectroscopy (RRS), and band gap photoluminescence (PL) serve a vital role as they provide a quick, accurate, contactless, non-destructive probe for electronic and vibrational properties of SWNTs under ambient conditions. While molecular optical spectroscopy shows weak discrete overtones and combination modes and solid state optical spectroscopy gives broad spectral features, the SWNT optical spectroscopy takes the advantages of both yielding a rich and intense quasi-discrete spectrum. In this thesis, we focus our attention on the RRS and PL as the most commonly used optical spectroscopy techniques.

This thesis is organized as follows. In Chapter 2, the SWNT structure is discussed. The concept of cutting lines leading to the zone-folding scheme is developed based on the SWNT symmetry. The basic electronic properties of SWNTs are reviewed in Chapter 3 using the zone-folding technique. In the light of recent advances in the PL and RRS studies of SWNTs, an extended tight-binding model is developed taking into account the curvature of the SWNT sidewall. Comparison of experiment and theory indicates that optical transitions in SWNTs are governed by the excitonic resonances, and are strongly affected by the geometry of SWNTs less than 1 nm in diameter. In Chapter 4, we overview experimental measurements and force-constant models for the phonon dispersion relations in SWNTs. We develop an advanced tight-binding model and we exploit the origin of the experimentally observed frequency softening in the graphene sheet and metallic SWNTs. In Chapter 5, the electron-photon and electron-phonon interactions are investigated within the framework of the extended tight-binding model. The theoretical calculations of the RRS intensities in the graphene sheet show a quantitative agreement with experimental measurements

and clarify the origin of the previously unassigned spectral features. On the other hand, the theoretical calculations of the PL and RRS intensities in SWNTs do not show good agreement with the experimental results. Excitonic wavefunctions must be taken into account for the PL and RRS intensity calculations in SWNTs to achieve better agreement with experiment. Finally, Chapter 6 gives conclusions of this thesis along with suggestions for future research.

Chapter 2

Nanotube structure

A single-wall carbon nanotube (SWNT) can be considered as a strip of a graphene sheet (a single layer of crystalline graphite) rolled into a seamless cylinder. Making an imaginary cut along the axial direction on the cylinder surface, the SWNT can be unrolled into a nanographite ribbon (a strip of a graphene sheet) and mapped onto a graphene sheet. Properties of a graphene sheet are therefore crucial for understanding SWNT physics. In this Chapter, we consider the real and reciprocal space representations of a graphene sheet and, consequently, of SWNTs.

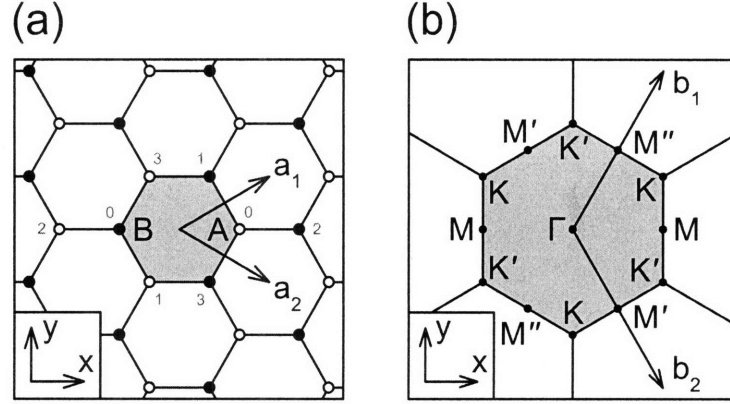


Figure 2-1: (a) A single graphene sheet. The unit cell is shaded in gray. The open and solid dots indicate the A and B sublattices, respectively. The lattice vectors \mathbf{a}_1 and \mathbf{a}_2 are shown by arrows. (b) The reciprocal lattice of a single graphene sheet. The first Brillouin zone is shaded in gray. The dots labeled by Γ , K, K', M, M', and M'' indicate the high-symmetry points. The reciprocal lattice vectors \mathbf{b}_1 and \mathbf{b}_2 are shown by arrows.

2.1 Graphene sheet

A single graphene sheet consists of sp^2 -hybridized carbon atoms packed in a two-dimensional (2D) hexagonal lattice. The Cartesian coordinate system is oriented with respect to the hexagonal lattice in such a way that the armchair (A) direction lies along the x -axis and the zigzag (Z) direction along the y -axis, as shown in Fig. 2-1 (a). The graphene sheet is generated from the unit cell by the lattice vectors \mathbf{a}_1 and \mathbf{a}_2 . The lattice vectors make an angle of 60° :

$$\begin{cases} \mathbf{a}_1 = \frac{\sqrt{3}a}{2} \hat{\mathbf{x}} + \frac{a}{2} \hat{\mathbf{y}}, \\ \mathbf{a}_2 = \frac{\sqrt{3}a}{2} \hat{\mathbf{x}} - \frac{a}{2} \hat{\mathbf{y}}, \end{cases} \quad (2.1)$$

where $a = \sqrt{3}a_{CC} = 0.246 \text{ nm}$ is the lattice constant for the graphene sheet, $a_{CC} = 0.142 \text{ nm}$ is the nearest-neighbor interatomic distance, and $(\hat{\mathbf{x}}, \hat{\mathbf{y}})$ are the unitary basis vectors [129]. The vectors \mathbf{a}_1 and \mathbf{a}_2 given by Eq. (2.1) are shown by arrows in Fig. 2-1 (a). The choice of the unit cell is arbitrary due to the random selection of the center of the coordinate system. Considering that the symmetry of the graphene sheet is

described by the point group D_{6h} , we place the center of the coordinate system at the center of the hexagon through which the high-symmetry rotation axis C_6 goes. Using the lattice vectors \mathbf{a}_1 and \mathbf{a}_2 , we construct the hexagonal unit cell shown in gray in Fig. 2-1 (a). This unit cell contains two carbon atoms from the A and B sublattices shown, respectively, by open and solid dots in Fig. 2-1 (a).

Let us now consider the reciprocal lattice of the graphene sheet. The reciprocal lattice vectors \mathbf{b}_1 and \mathbf{b}_2 are related to the real lattice vectors \mathbf{a}_1 and \mathbf{a}_2 according to the standard definition:

$$\mathbf{a}_i \cdot \mathbf{b}_j = 2\pi\delta_{ij}, \quad (2.2)$$

where δ_{ij} is the Kronecker delta function. Substituting \mathbf{a}_1 and \mathbf{a}_2 from Eq. (2.1) into Eq. (2.2) yields \mathbf{b}_1 and \mathbf{b}_2 making an angle of 120° :

$$\begin{cases} \mathbf{b}_1 = \frac{2\pi}{\sqrt{3}a} \hat{\mathbf{x}} + \frac{2\pi}{a} \hat{\mathbf{y}}, \\ \mathbf{b}_2 = \frac{2\pi}{\sqrt{3}a} \hat{\mathbf{x}} - \frac{2\pi}{a} \hat{\mathbf{y}}. \end{cases} \quad (2.3)$$

The vectors \mathbf{b}_1 and \mathbf{b}_2 given by Eq. (2.3) are shown by arrows in Fig. 2-1 (b). The first Brillouin zone defined by these vectors is shaded in gray in Fig. 2-1 (b). Note that the first Brillouin zone has the same hexagonal shape as the unit cell, but the orientation of the hexagons is different. Namely, the armchair direction in real space (x -axis in Fig. 2-1 (a)) corresponds to the zigzag direction in reciprocal space (x -axis in Fig. 2-1 (b)), and *vice versa*. This orientation is switched to the opposite one if the lattice vectors \mathbf{a}_1 and \mathbf{a}_2 are chosen to make an angle of 120° , implying the reciprocal lattice vectors \mathbf{b}_1 and \mathbf{b}_2 are making an angle of 60° [1].

2.2 Chirality and handedness

When matching a SWNT with the corresponding nanographite ribbon, the SWNT circumference corresponds to the nanographite ribbon width. Plotted on a flat graphene sheet, this circumference/ribbon width is known as the chiral vector \mathbf{C}_h [129]. Pro-

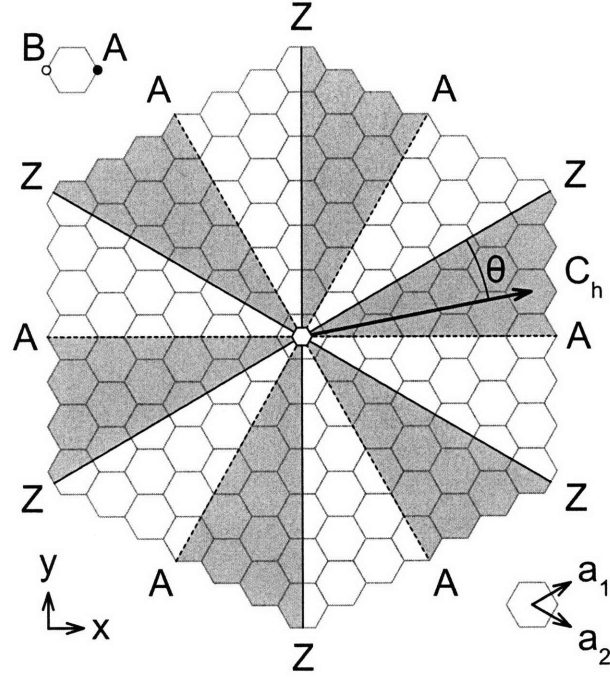


Figure 2-2: The graphene sheet broken into 30° -sectors, in one of which the chiral vector of the SWNT lies. The zigzag and armchair directions are shown by the solid and dashed lines labeled by Z and A, respectively. A small hexagon at the center of the coordinates represents a C_6 symmetry axis. The chiral vector and the chiral angle of a (4, 2) SWNT are shown by the arrow and the arc labeled by C_h and θ , respectively.

ected on the lattice vectors \mathbf{a}_1 and \mathbf{a}_2 , the chiral vector can be written in the form:

$$\mathbf{C}_h = n\mathbf{a}_1 + m\mathbf{a}_2, \quad (2.4)$$

where (n, m) is a pair of indices uniquely determining the geometrical structure of an infinitely long SWNT. For illustrative purposes, the chiral vector of a (4, 2) SWNT is shown in Fig. 2-2. The (4, 2) SWNT is one of the smallest-diameter SWNTs ever synthesized [167].

Switching to polar coordinates, the chiral vector is defined by its length $C_h = \pi d_t$, where d_t is the SWNT diameter, and by its angle θ to the closest of the three zigzag chains in the graphene sheet, known as the chiral angle [129]. Since the symmetry of the graphene sheet is described by the point group D_{6h} , all the unique chiral vectors

are confined to a 30° -sector on the graphene sheet. The total of 12 such sectors are shaded in alternating gray and white in Fig. 2-2, separated by the three zigzag and three armchair directions. The rightmost gray sector in Fig. 2-2 contains the chiral vectors with the structural indices in the range $0 < m < n$ and the chiral angles in the range $0 < \theta < 30^\circ$. The chiral vectors aligned along the upper Z boundary of this sector correspond to the case $m = 0$ and $\theta = 0$, while for the lower A boundary we have $m = n$ and $\theta = 30^\circ$. According to this construction, SWNTs are classified as chiral ($0 < \theta < 30^\circ$) and achiral ($\theta = 0$ and $\theta = 30^\circ$), which in turn are known as zigzag ($\theta = 0$) and armchair ($\theta = 30^\circ$) SWNTs [129]. Choosing another 30° -sector in Fig. 2-2, the range of the structural indices corresponding to chiral, zigzag and armchair SWNTs changes but their chiral angles remain the same. For example, the structural indices varying in the range $0 < n < m$ produce the chiral vectors in the rightmost white sector in Fig. 2-2. In other words, the chiral vector (n, m) in the rightmost gray sector is equivalent to the chiral vector (m, n) in the rightmost white sector, where the condition $0 < m < n$ is maintained in both cases.

The aforementioned chiral vectors (n, m) and (m, n) correspond to the two SWNTs of the same chiral angle θ and diameter d_t but of opposite handedness χ , related to each other by spatial inversion [138]. The two SWNTs of opposite handedness χ can be obtained from the same chiral vector (n, m) by rolling the graphene sheet in the two opposite directions, so that the printed side of Fig. 2-2 becomes either the outer or the inner sidewall of the SWNT [138]. Assuming the chiral vector lies in the rightmost gray sector in Fig. 2-2 and the printed side of Fig. 2-2 is the outer sidewall of the SWNT, two of the three zigzag chains in the graphene sheet form right-handed helices, while the third zigzag chain follows a left-handed helix. At the same time, two of the three armchair chains are left-handed helices, and the third armchair chain is a right-handed helix (see Fig. 2-2). The SWNT handedness χ is thus denoted as zigzag-right/armchair-left (ZR/AL). By switching to the white sectors in Fig. 2-2 or by rolling the graphene sheet in the opposite direction (but not both), we obtain the SWNT of handedness $\chi = \text{ZL/AR}$. The SWNT handedness can also be defined mathematically by a quantity x related to the classification of SWNTs given

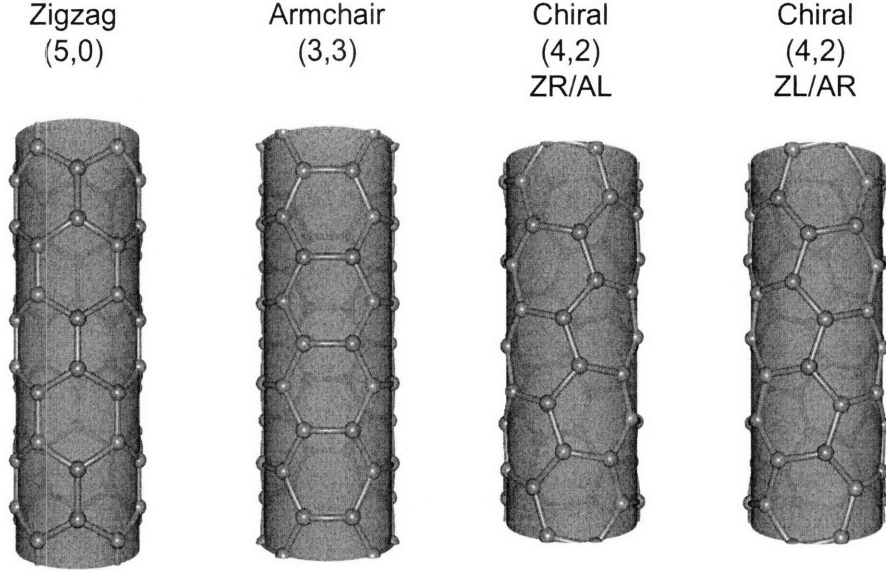


Figure 2-3: The schematic models of zigzag (5,0), armchair (3,3), and chiral (4,2) SWNTs that contain 3, 5, and 1 translational unit cells, respectively. The chiral (4,2) SWNTs of both zigzag-right/armchair-left (ZR/AL) and zigzag-left/armchair-right (ZL/AR) handedness are shown.

in Section 3.3 [136]. Note that achiral SWNTs have no handedness, implying that there are twice as many chiral SWNTs for each pair of the structural (n, m) indices as achiral SWNTs. This aspect must be taken into account when analyzing the (n, m) distribution in a SWNT sample [138]. To visualize the concept of the SWNT handedness, we draw in Fig. 2-3 the schematic models of zigzag (5,0), armchair (3,3), and chiral (4,2) ZR/AL- and ZL/AR-handed SWNTs.

We conclude that the structural indices can be defined in the range $0 \leq m \leq n$ (the rightmost gray sector in Fig. 2-2) and the chiral angle in the range $0 \leq \theta \leq 30^\circ$. Chiral nanotubes ($0 < m < n$ and $0 < \theta < 30^\circ$) are either ZR/AL- or ZL/AR-handed. Achiral SWNTs are either zigzag ($m = 0$ and $\theta = 0$) or armchair ($m = n$ and $\theta = 30^\circ$). Once the range of the structural indices is established, the relations between them and the SWNT diameter d_t and chiral angle θ are easily derived [129]:

$$\begin{cases} d_t = \frac{a}{\pi} \sqrt{n^2 + nm + m^2}, \\ \theta = \arctan \frac{\sqrt{3}m}{2n + m}. \end{cases} \quad (2.5)$$

Alternatively to chiral angle θ , one can consider angle $\phi = \pi/6 - \theta$ between the chiral vector \mathbf{C}_h and the closest of the three armchair chains in the graphene sheet of Fig. 2-2 [169].

2.3 Translational symmetry

The fundamental property of an infinitely long SWNT is its translational periodicity from where the concept of reciprocal space arises. The translational periodicity is described by the translational vector \mathbf{T} along the axial direction of the SWNT. In the unrolled graphene sheet, the translational vector \mathbf{T} is orthogonal to the chiral vector \mathbf{C}_h that spans the circumference of the SWNT. Therefore, \mathbf{T} is proportional to \mathbf{C}_h rotated counterclockwise by 90° . In other words, \mathbf{T} is proportional to the vector product of $\hat{\mathbf{z}}$ and \mathbf{C}_h , where $\hat{\mathbf{z}}$ is the unit vector normal to the graphene sheet. Substituting \mathbf{C}_h from Eq. (2.4) into $\mathbf{T} \propto \hat{\mathbf{z}} \times \mathbf{C}_h$ yields $\mathbf{T} \propto (2m+n)\mathbf{a}_1/\sqrt{3} - (2n+m)\mathbf{a}_2/\sqrt{3}$. Clearly, \mathbf{T} must be further multiplied by $\sqrt{3}$ to extend over an integer number of hexagons in the graphene sheet. We then obtain $\mathbf{T} \propto (2m+n)\mathbf{a}_1 - (2n+m)\mathbf{a}_2$. The two integer numbers $(2m+n)$ and $(2n+m)$ may have a common divisor $d_R > 1$, and in this case \mathbf{T} spans d_R translational unit cells in the axial direction of the SWNT. Dividing \mathbf{T} by d_R yields:

$$\mathbf{T} = t_1\mathbf{a}_1 + t_2\mathbf{a}_2, \quad (2.6)$$

where $t_1 = (2m+n)/d_R$, $t_2 = -(2n+m)/d_R$, $d_R = \text{gcd}(2n+m, 2m+n)$, and the function $\text{gcd}(i, j)$ denotes the greatest common divisor of the two integers i and j [129].

The chiral vector \mathbf{C}_h and the translational vector \mathbf{T} given by Eqs. (2.4) and (2.6) define the translational unit cell of the SWNT. The area of the translational unit cell is given by the absolute value of the vector product of these two vectors, $|\mathbf{C}_h \times \mathbf{T}| = \sqrt{3}a^2(n^2 + nm + m^2)/d_R$. Dividing it by the area of the hexagonal unit cell in the graphene sheet, $|\mathbf{a}_1 \times \mathbf{a}_2| = \sqrt{3}a^2/2$, we obtain the number of hexagons in the trans-

lational unit cell of the SWNT:

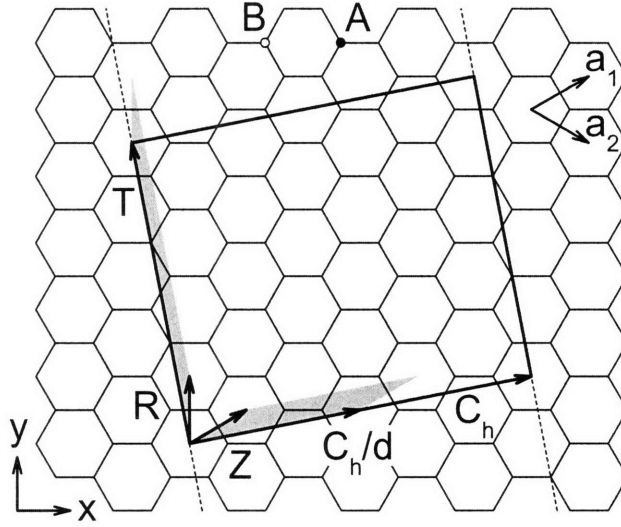


Figure 2-4: The rectangle shows the translational unit cell of the (4, 2) SWNT projected on the graphene sheet. The dashed lines indicate the edges of the nanographite ribbon corresponding to the unrolled SWNT. The arrows show the chiral vector \mathbf{C}_h that spans the circumference of the SWNT, the rotational vector \mathbf{C}_h/d , the translational vector \mathbf{T} , and the screw vectors \mathbf{Z} and \mathbf{R} . The angular-helical ($\mathbf{C}_h/d, \mathbf{Z}$) and the helical-linear (\mathbf{R}, \mathbf{T}) reduced unit cells are shaded in gray.

$$N = \frac{2(n^2 + nm + m^2)}{d_R}. \quad (2.7)$$

For the (4, 2) SWNT, we find $d_R = 2$, $(t_1, t_2) = (4, -5)$, and $N = 28$. The translational unit cell of the (4, 2) SWNT projected onto the graphene sheet is shown by a rectangle in Fig. 2-4, where the chiral vector \mathbf{C}_h is the same as in Fig. 2-2. One can see in Fig. 2-4 that the vector \mathbf{T} connects the two equivalent hexagons in the adjacent translational unit cells. Since $\text{gcd}(t_1, t_2) = 1$ by definition in Eq. (2.6), the vector \mathbf{T} can never connect the two inequivalent hexagons within the same translational unit cell. On the contrary, the structural indices can be arbitrary within the range $0 \leq m \leq n$, so that $d = \text{gcd}(n, m)$ can take any values between 1 and n . Therefore, the chiral vector \mathbf{C}_h connects d inequivalent hexagons in the circumferential direction of the SWNT. The rotational vector in the circumferential direction is thus given by \mathbf{C}_h/d . For the (4, 2) SWNT, we find $d = 2$. Indeed, the chiral vector \mathbf{C}_h of the (4, 2) SWNT connects the two inequivalent hexagons within the same translational

unit cell, as one can see in Fig. 2-4.

The quantity $d = \gcd(n, m)$ defined above for the chiral vector \mathbf{C}_h is related to the quantity $d_R = \gcd(2n + m, 2m + n)$ introduced in Eq. (2.6) for the translational vector \mathbf{T} . Applying Euclid's law [$\gcd(i, j) = \gcd(i - j, j)$ if $j < i$] yields $d = \gcd(n - m, m)$ and $d_R = \gcd(n - m, 3m)$. We then conclude that $d_R = 3d$ if $\text{mod}(n - m, 3d) = 0$ and $d_R = d$ otherwise, where $\text{mod}(i, j)$ is the remainder of the division of i by j [129]. Depending on whether $d_R = d$ or $d_R = 3d$, the length of the translational vector \mathbf{T} differs according to Eq. (2.6). Therefore, the two types of SWNTs for which $d_R = d$ and $d_R = 3d$, respectively, have distinct physical properties, and in particular very different electronic dispersion relations [136].

2.4 Helical symmetry

The vectors \mathbf{C}_h/d and \mathbf{T} define the pure rotational and translational symmetries of the SWNT, respectively. Additionally, the SWNT has the helical symmetry described by the screw vector comprised of both rotational and translational components. Among the $N - 1$ inequivalent vectors connecting the pairs of hexagons within the translational unit cell of the SWNT, $d - 1$ are the pure rotations $i\mathbf{C}_h/d$ ($i = 1, \dots, d - 1$). The remaining $N - d$ are inequivalent screw vectors. In principle, any non-collinear pair of the N roto-translational vectors ($d - 1$ rotational, $N - d$ screw, and 1 translational) generates a unit cell with the number of hexagons anywhere between 1 to N . However, we restrict our consideration to the smallest possible single-hexagon unit cells (thereafter called reduced unit cells) in order to fully utilize the symmetry of the SWNT. This approach provides a direct mapping of the reciprocal space of SWNTs to that of the graphene sheet. Such mapping is the origin of the zone-folding technique, as will be discussed in Section 2.5.

The choice of a reduced unit cell is not unique. An obvious choice is the unit cell of the graphene sheet formed by the lattice vectors \mathbf{a}_1 and \mathbf{a}_2 , as shown in Fig. 2-1 (a). The disadvantage of this approach is that both the \mathbf{a}_1 and \mathbf{a}_2 vectors become

the screw vectors in chiral SWNTs.¹ The helical symmetry mixes the angular μ and linear k momenta associated with the pure rotational and translational symmetry into the two helical momenta [12]. We therefore refer to this unit cell as the helical-helical reduced unit cell [12]. To decouple the angular μ and linear k momenta, we can set the lattice vectors to be \mathbf{C}_h/d and \mathbf{T} , but then the number of hexagons in the unit cell increases to number N/d that exceeds one.² As an intermediate solution, we choose only one of the lattice vectors to be either rotational \mathbf{C}_h/d or translational \mathbf{T} and we pick an appropriate screw vector as the other lattice vector, thus decoupling either the angular μ or linear k momentum without extending the reduced unit cell beyond one hexagon. In the first case, we select the screw vector \mathbf{Z} that has the smallest component in the axial direction of the SWNT,³ as proposed by M. Damnjanović et al. [32]. In the second case, we select the screw vector \mathbf{R} that has the smallest component in the circumferential direction of the SWNT, as defined by R. Saito et al. [129]. The pairs of lattice vectors $(\mathbf{C}_h/d, \mathbf{Z})$ and (\mathbf{R}, \mathbf{T}) define the angular-helical and the helical-linear reduced unit cells, respectively [12]. For the $(4, 2)$ SWNT, the screw vectors satisfying these constraints are given by $\mathbf{Z} = \mathbf{a}_1$ and $\mathbf{R} = \mathbf{a}_1 - \mathbf{a}_2$, as one can see in Fig. 2-2. Note that the reduced unit cells shaded in gray in Fig. 2-2 cover distinct parts of different hexagons. What matters, however, is that the reduced unit cells consist of two carbon atoms, A and B, just like the unit cell of the graphene sheet shown in Fig. 2-1.

In the above we have determined the screw vectors $\mathbf{Z} = \mathbf{a}_1$ and $\mathbf{R} = \mathbf{a}_1 - \mathbf{a}_2$ for the $(4, 2)$ SWNT. For a general (n, m) SWNT, we can write the screw vectors \mathbf{Z} and \mathbf{R} in the form:

$$\begin{cases} \mathbf{Z} = u\mathbf{a}_1 + v\mathbf{a}_2, \\ \mathbf{R} = p\mathbf{a}_1 + q\mathbf{a}_2. \end{cases} \quad (2.8)$$

In order to find the unknown integers (u, v) and (p, q) , we rewrite the aforementioned constraints on the screw vectors \mathbf{Z} and \mathbf{R} in terms of vector algebra. For the screw vector \mathbf{Z} , having the smallest component in the axial direction yields $|\mathbf{C}_h \times \mathbf{Z}| =$

¹For zigzag SWNTs, \mathbf{a}_1 is a pure rotation. For armchair SWNTs, $\mathbf{a}_1 - \mathbf{a}_2$ is a pure translation.

²It is easy to show that $\text{mod}(N, d) = 0$ and therefore the number N/d is an integer.

³Among d such vectors, we choose the one that has the smallest component in the \mathbf{C}_h direction.

$d|\mathbf{a}_2 \times \mathbf{a}_1|$. There are d distinct vectors that satisfy this condition. Among these d vectors, choosing the one with the smallest component in the circumferential direction implies $0 < |\mathbf{Z} \times \mathbf{T}| < N/d|\mathbf{a}_2 \times \mathbf{a}_1|$. Substituting \mathbf{Z} , \mathbf{C}_h , and \mathbf{T} from Eqs. (2.8), (2.4), and (2.6) into these expressions, we obtain [140]:

$$\begin{cases} mu - nv = d, \\ 0 < t_1v - t_2u < N/d. \end{cases} \quad (2.9)$$

For the screw vector \mathbf{R} , having the smallest component in the circumferential direction suggests $|\mathbf{R} \times \mathbf{T}| = |\mathbf{a}_2 \times \mathbf{a}_1|$, while being confined within the translational unit cell implies $0 < |\mathbf{C}_h \times \mathbf{R}| < N|\mathbf{a}_2 \times \mathbf{a}_1|$. Substituting \mathbf{R} , \mathbf{T} , and \mathbf{C}_h from Eqs. (2.8), (2.6), and (2.4) yields [129]:

$$\begin{cases} t_1q - t_2p = 1, \\ 0 < mp - nq < N. \end{cases} \quad (2.10)$$

Eqs. (2.9) and (2.10) uniquely determine the (u, v) and (p, q) components of the screw vectors \mathbf{Z} and \mathbf{R} given by Eq. (2.8). For the (4, 2) SWNT, we find $(u, v) = (1, 0)$ and $(p, q) = (1, -1)$.

The screw vectors \mathbf{Z} and \mathbf{R} defined by Eq. (2.8) are expressed in terms of the graphene unit vectors \mathbf{a}_1 and \mathbf{a}_2 . However, it is more instructive to rewrite them in terms of the SWNT unit vectors \mathbf{C}_h and \mathbf{T} . Reversing Eqs. (2.4) and (2.6) and utilizing Eq. (2.7) gives $N\mathbf{a}_1 = m\mathbf{T} - t_2\mathbf{C}_h$ and $N\mathbf{a}_2 = t_1\mathbf{C}_h - n\mathbf{T}$. Substituting these expressions into Eq. (2.8) and using Eqs. (2.9) and (2.10), we find [129, 140]:

$$\begin{cases} N\mathbf{Z} = W\mathbf{C}_h + d\mathbf{T}, \\ N\mathbf{R} = \mathbf{C}_h + M\mathbf{T}, \end{cases} \quad (2.11)$$

where the new quantities $W = t_1v - t_2u$ and $M = mp - nq$ are defined. For the (4, 2) SWNT, we obtain $W = 5$ and $M = 6$.

The helical symmetry of the SWNT can be understood from Eq. (2.11). The screw vectors \mathbf{Z} and \mathbf{R} applied N times span over all the N inequivalent hexagons in the

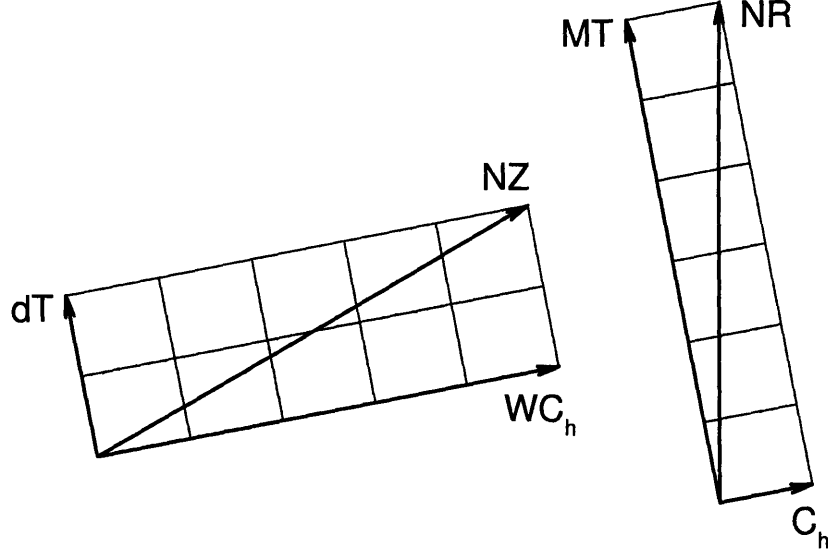


Figure 2-5: The screw vectors $N\mathbf{Z}$ (left panel) and $N\mathbf{R}$ (right panel) applied to the translational unit cell of the (4, 2) SWNT. Both the $N\mathbf{Z}$ and $N\mathbf{R}$ vectors cover all the $N = 28$ inequivalent hexagons in the translational unit cell. While $N\mathbf{Z}$ makes $W = 5$ revolutions around the SWNT axis and spans the $d = 2$ translational unit cells, $N\mathbf{R}$ extends over the $M = 6$ translational unit cells per revolution.

translational unit cell of the SWNT, since the unit cell is reduced to one hexagon. The vector $N\mathbf{Z}$ makes W revolutions around the SWNT circumference and extends over the d translational unit cells. On the other hand, the vector $N\mathbf{R}$ makes one revolution around the SWNT circumference and extends over the M translational unit cells. The numbers W and M therefore play the roles of the rotational and translational components of the screw vectors \mathbf{Z} and \mathbf{R} , respectively. For illustrative purposes, the vectors $N\mathbf{Z}$ and $N\mathbf{R}$ for the (4, 2) SWNT ($d = 2$, $N = 28$, $W = 5$, and $M = 6$) are shown in Fig. 2-5.

2.5 Cutting lines

Let us now consider the reciprocal space of the SWNT. Just like the real lattice of the SWNT is formed by *rolling* the real lattice of the graphene sheet, the reciprocal lattice of the SWNT is obtained by *folding* the reciprocal lattice of the graphene sheet. This is known as the zone-folding technique [129]. It allows one to obtain the

dispersion relations of the SWNT from the corresponding dispersion relations of the graphene sheet. It is equally applicable to electrons, phonons, and other quasiparticle excitations that may occur in SWNTs. In this Section, we develop the zone-folding technique for SWNTs. We first consider the quantum confinement phenomena in SWNTs from the real space and reciprocal space point of views.

The basic condition for the charge carriers in the SWNT to experience quantum confinement is $C_h < l_\phi$, where $C_h = \pi d_t$ is the SWNT circumference length and l_ϕ is the quantum phase coherence length. The diameter d_t of a typical SWNT is about 1 nm, while l_ϕ is estimated to be about 20 nm at room temperature [157], so the above condition holds. Then, the electron plane waves form standing wave patterns in the circumferential direction of the SWNT. The standing waves are characterized by their angular momentum μ that shows how many nodes the wavefunction exhibits along the circumference of the SWNT. The modulation patterns of the standing waves with $\mu = 0, \pm 1, \pm 2, \pm 3$ are shown in Fig. 2-6 (a). The angular momentum μ of a standing wave in the SWNT corresponds to the linear momentum \mathbf{k} of a plane wave in the graphene sheet such that $\mathbf{k} \cdot \mathbf{C}_h = 2\pi\mu$. Thus, the allowed wavevectors in the reciprocal space of the graphene sheet are given by:

$$\mathbf{k} = \frac{2\mu}{d_t} \frac{\mathbf{C}_h}{C_h} + k \frac{\mathbf{T}}{T}, \quad (2.12)$$

where k is the linear momentum along the SWNT axis and $T = |\mathbf{T}|$ is the SWNT translational period. For discrete values of μ , the above expression generates a set of equidistant parallel lines separated by $2/d_t$, where k changes continuously along the lines. These lines are known as the cutting lines. The cutting lines for the (4, 2) SWNT are shown by the solid lines in Fig. 2-6 (b).

A formal approach to the reciprocal space of the SWNT requires construction of the reciprocal lattice vectors \mathbf{K}_1 and \mathbf{K}_2 . In Section 2.1 devoted to the graphene sheet, we derived the reciprocal lattice vectors \mathbf{b}_1 and \mathbf{b}_2 of Eq. (2.3) from the lattice vectors \mathbf{a}_1 and \mathbf{a}_2 of Eq. (2.1) using the standard definition of Eq. (2.2). For SWNTs, the chiral \mathbf{C}_h and translational \mathbf{T} vectors play the role of \mathbf{a}_1 and \mathbf{a}_2 in Eq. (2.2),

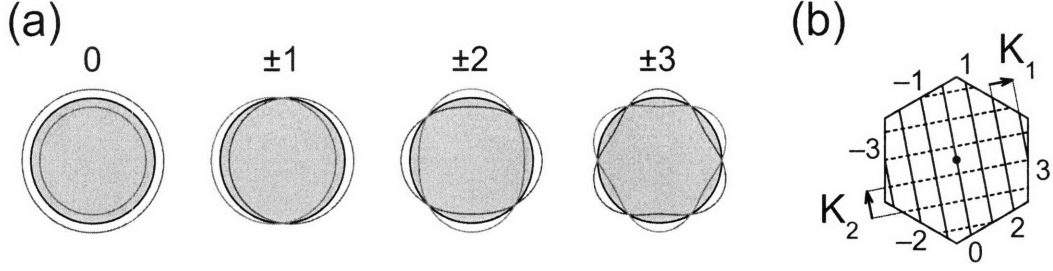


Figure 2-6: (a) Standing waves in the circumferential direction of the SWNT with angular momenta $\mu = 0, \pm 1, \pm 2, \pm 3$. The SWNT cross-section is shaded in gray. The red and green curves represent the standing wave modulation patterns with respect to the SWNT sidewall (the gray disc circumference) shifted by a half-period with respect to each other. (b) The first Brillouin zone of the graphene sheet. The solid lines, known as the cutting lines, represent the quantized states with angular momenta $\mu = 0, \pm 1, \pm 2, \pm 3$ for the $(4, 2)$ SWNT. The linear momentum k varies along the solid lines. The dashed lines break the solid lines into equivalent segments, indicating the periodicity of the linear momentum k due to the translational symmetry of the SWNT. The arrows show the reciprocal lattice vectors \mathbf{K}_1 and \mathbf{K}_2 . The black dot denotes the Γ point.

while \mathbf{K}_1 and \mathbf{K}_2 stand for \mathbf{b}_1 and \mathbf{b}_2 . Since the vectors \mathbf{C}_h and \mathbf{T} are orthogonal, we conclude from Eq. (2.2) that $\mathbf{K}_1 = 2\pi\mathbf{C}_h/C_h^2$ and $\mathbf{K}_2 = 2\pi\mathbf{T}/T^2$. Substituting \mathbf{C}_h and \mathbf{T} from Eqs. (2.4) and (2.6) into these expressions yields \mathbf{K}_1 and \mathbf{K}_2 in terms of \mathbf{a}_1 and \mathbf{a}_2 . By comparing Eqs. (2.1) and (2.3), we express \mathbf{a}_1 and \mathbf{a}_2 as functions of \mathbf{b}_1 and \mathbf{b}_2 in the form $4\pi\mathbf{a}_1 = a^2(2\mathbf{b}_1 + \mathbf{b}_2)$ and $4\pi\mathbf{a}_2 = a^2(2\mathbf{b}_2 + \mathbf{b}_1)$. We then rewrite \mathbf{K}_1 and \mathbf{K}_2 in terms of \mathbf{b}_1 and \mathbf{b}_2 [129]:

$$\begin{cases} \mathbf{K}_1 = \frac{t_1\mathbf{b}_2 - t_2\mathbf{b}_1}{N}, \\ \mathbf{K}_2 = \frac{m\mathbf{b}_1 - n\mathbf{b}_2}{N}. \end{cases} \quad (2.13)$$

The vector \mathbf{K}_1 defines the separation between the adjacent cutting lines. Its magnitude $K_1 = 2\pi/C_h = 2/d_t$ is related to the formation of the standing waves in the circumferential direction of the SWNT, as discussed above. The standing waves, and therefore the cutting lines, are associated with discrete values of the angular momentum μ . The vector \mathbf{K}_2 defines the length of the cutting lines. Its magnitude $K_2 = 2\pi/T$ determines the periodicity of the linear momentum k that continuously

changes along the cutting lines. The periodicity of k originates from the translational symmetry of the SWNT described by the vector \mathbf{T} . The length of the cutting lines for the (4, 2) SWNT is indicated by the dashed lines in Fig. 2-6 (b). In terms of the vectors \mathbf{K}_1 and \mathbf{K}_2 , the momentum quantization condition expressed by Eq. (2.12) takes the following form:

$$\mathbf{k} = \mu \mathbf{K}_1 + k \frac{\mathbf{K}_2}{K_2}, \quad (2.14)$$

Considering that there are N hexagons in the translational unit cell of the SWNT, we conclude that the first Brillouin zone of the SWNT consists of N cutting lines. These cutting lines must be arranged into a rectangle with the sides parallel to the \mathbf{K}_1 and \mathbf{K}_2 vectors. Only then can the first Brillouin zone be folded into a one-dimensional (1D) reciprocal space of the SWNT. The dimensions of the rectangular Brillouin zone are determined by the choice of the reduced unit cell. The reduced unit cell generates the reciprocal lattice vectors \mathbf{Q}_1 and \mathbf{Q}_2 that arrange the N cutting lines into the first Brillouin zone of a rectangular shape. Below we construct the first Brillouin zones for the angular-helical and helical-linear reduced unit cells defined in Section 2.4. We show that these Brillouin zones have rectangular shapes of different dimensions, so that the angular μ and linear k momenta vary in different ranges [140]. Furthermore, either the linear k or angular μ momentum become a projection of the helical momentum and therefore it is not conserved at the Brillouin zone boundaries [12]. The resulting momentum discontinuities must be taken into account for Umklapp scattering processes. Any angular or linear momentum transfer beyond the first Brillouin zone is translated back into the first Brillouin zone, correcting for the momentum discontinuities at the Brillouin zone boundaries. The selection rules that govern the scattering processes in SWNTs thus depend on the choice of the reduced unit cell. However, none of the symmetry-related properties of SWNTs are affected by the changes to the selection rules. The choice of the reduced unit cell is a matter of convenience, whether one is more interested in the angular μ or linear k momentum conservation for an analysis of the scattering processes in SWNTs [140].

2.5.1 Helical-helical representation

Before considering the angular-helical and helical-linear reduced unit cells, let us discuss the simplest case of the helical-helical reduced unit cell. As defined in Section 2.4, the helical-helical reduced unit cell is formed by the lattice vectors \mathbf{a}_1 and \mathbf{a}_2 . The reciprocal lattice vectors \mathbf{Q}_1 and \mathbf{Q}_2 are therefore given by $\mathbf{Q}_1 = \mathbf{b}_1$ and $\mathbf{Q}_2 = \mathbf{b}_2$, according to the definition in Eq. (2.2). By reverting to Eq. (2.13), we express the vectors \mathbf{b}_1 and \mathbf{b}_2 , and therefore \mathbf{Q}_1 and \mathbf{Q}_2 , in terms of \mathbf{K}_1 and \mathbf{K}_2 :

$$\begin{cases} \mathbf{Q}_1 = n\mathbf{K}_1 + t_1\mathbf{K}_2, \\ \mathbf{Q}_2 = m\mathbf{K}_1 + t_2\mathbf{K}_2. \end{cases} \quad (2.15)$$

The reciprocal lattice vectors \mathbf{Q}_1 and \mathbf{Q}_2 given by Eq. (2.15) are misaligned with respect to the \mathbf{K}_1 and \mathbf{K}_2 vectors.⁴ Therefore, the N cutting lines cannot be arranged into the rectangular Brillouin zone. Let us consider the first Brillouin zone for the (4, 2) SWNT as an example. Figure 2-7 shows the cutting lines for the (4, 2) SWNT in the reciprocal space of the graphene sheet, similar to Fig. 2-6 (b). The first Brillouin zone defined by the vectors $\mathbf{Q}_1 = \mathbf{b}_1$ and $\mathbf{Q}_2 = \mathbf{b}_2$ is shaded in dark gray in Fig. 2-7, while the adjacent Brillouin zones are shown as light gray. Since the first Brillouin zone is not rectangular, it contains cutting lines of different lengths, as one can see in Fig. 2-7. Because of their different lengths, the cutting lines cannot be folded into a 1D reciprocal space of the SWNT. Hence, the zone-folding technique is not applicable to the helical-helical representation of the cutting lines.

The absence of the rectangular Brillouin zone implies the breaking of momentum conservation across the Brillouin zone boundary. Let us consider the cutting line passing through the Γ point of the first Brillouin zone (the dot in the dark gray hexagon in Fig. 2-7). This cutting line carries angular momentum $\mu = 0$ within the first Brillouin zone (the dark gray hexagon in Fig. 2-7). Crossing the boundaries to the adjacent Brillouin zones (the upper and lower light gray hexagons in Fig. 2-7), this cutting line changes its angular momentum to either $\mu = +2$ (the upper hexagon)

⁴According to the definition in Eq. (2.6), t_1 and t_2 are never equal to zero. For zigzag SWNTs, $m = 0$ and therefore \mathbf{Q}_2 is parallel to \mathbf{K}_1 .

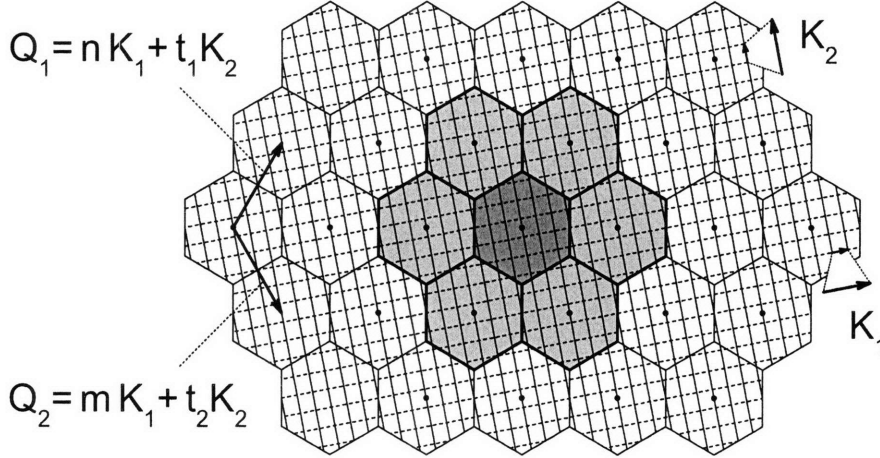


Figure 2-7: The reciprocal space of the graphene sheet. The solid lines represent the cutting lines for the (4, 2) SWNT. The dashed lines indicate the length of the cutting lines. The first Brillouin zone of the helical-helical reduced unit cell formed by the vectors $(\mathbf{a}_1, \mathbf{a}_2)$ is shaded in dark gray. The adjacent Brillouin zones are shaded in light gray. The arrows show the reciprocal lattice vectors $\mathbf{Q}_1 = n\mathbf{K}_1 + t_1\mathbf{K}_2$ and $\mathbf{Q}_2 = m\mathbf{K}_1 + t_2\mathbf{K}_2$ and the cutting line vectors \mathbf{K}_1 and \mathbf{K}_2 . The dots show the Γ points.

or $\mu = -2$ (the lower hexagon). According to Eq. (2.15), the angular momentum μ changes by $\pm m$ at the Brillouin zone boundaries. In a similar fashion, we can trace the change of linear momentum k along the dashed lines in Fig. 2-7. The Γ point of the first Brillouin zone (the dot in the dark gray hexagon in Fig. 2-7) corresponds to the linear momentum $k = 0$. Crossing over the 6 cutting lines brings us to the adjacent Brillouin zones (the right and left light gray hexagons in Fig. 2-7). The linear momentum changes to either $k = +2\pi/T$ (the right hexagon) or $k = -2\pi/T$ (the left hexagon). According to Eq. (2.15), the linear momentum k changes by $\pm(t_1 + t_2)2\pi/T$ at the Brillouin zone boundaries. Thus, both the angular μ and linear k momenta exhibit discontinuities at the Brillouin zone boundaries [140].

The conservation of the angular μ and linear k momenta is associated with rotational and translational symmetries of the SWNT, respectively. The helical-helical reduced unit cell is formed by the screw vectors \mathbf{a}_1 and \mathbf{a}_2 that mix rotational and translational symmetries of the SWNT. The screw vectors \mathbf{a}_1 and \mathbf{a}_2 give rise to the helical momenta, whose angular μ and linear k projections exhibit discontinuities at

the Brillouin zone boundaries. Accordingly, the reduced unit cell formed by the screw vectors \mathbf{a}_1 and \mathbf{a}_2 is called the helical-helical reduced unit cell [12].

2.5.2 Angular-helical representation

The angular-helical reduced unit cell is formed by the lattice vectors \mathbf{C}_h/d and \mathbf{Z} , as defined in Section 2.4 above. The reciprocal lattice vectors \mathbf{Q}_1 and \mathbf{Q}_2 can be derived from the standard definition in Eq. (2.2). The orthogonality conditions $\mathbf{Q}_1 \cdot \mathbf{Z} = 0$ and $\mathbf{Q}_2 \cdot \mathbf{C}_h/d = 0$ suggest that $\mathbf{Q}_1 \propto \hat{\mathbf{z}} \times \mathbf{Z}$ and $\mathbf{Q}_2 \propto \mathbf{T}$. Substituting \mathbf{Z} from Eq. (2.8) and using Eq. (2.1) yields $\mathbf{Q}_1 \propto (2v + u) \mathbf{a}_1 - (2u + v) \mathbf{a}_2$. The normalization conditions require that $\mathbf{Q}_1 \cdot \mathbf{C}_h/d = 2\pi$ and $\mathbf{Q}_2 \cdot \mathbf{Z} = 2\pi$. Substituting \mathbf{C}_h and \mathbf{Z} of Eqs. (2.4) and (2.8) we obtain $\mathbf{Q}_1 = 4\pi [(2u + v) \mathbf{a}_2 - (2v + u) \mathbf{a}_1] / (3a^2)$ and $\mathbf{Q}_2 = 4\pi [(2m + n) \mathbf{a}_1 - (2n + m) \mathbf{a}_2] / (3da^2)$ with the help of Eqs. (2.9) and (2.6). These expressions give \mathbf{Q}_1 and \mathbf{Q}_2 in terms of \mathbf{a}_1 and \mathbf{a}_2 . By comparing Eqs. (2.1) and (2.3), we can write \mathbf{a}_1 and \mathbf{a}_2 as functions of \mathbf{b}_1 and \mathbf{b}_2 in the form $4\pi \mathbf{a}_1 = a^2 (2\mathbf{b}_1 + \mathbf{b}_2)$ and $4\pi \mathbf{a}_2 = a^2 (2\mathbf{b}_2 + \mathbf{b}_1)$. We then express \mathbf{b}_1 and \mathbf{b}_2 in terms of \mathbf{K}_1 and \mathbf{K}_2 as follows, $\mathbf{b}_1 = n\mathbf{K}_1 + t_1\mathbf{K}_2$ and $\mathbf{b}_2 = m\mathbf{K}_1 + t_2\mathbf{K}_2$, according to Eq. (2.15). Finally, we obtain \mathbf{Q}_1 and \mathbf{Q}_2 as functions of \mathbf{K}_1 and \mathbf{K}_2 using Eqs. (2.6), (2.7), (2.9), and (2.11) [140]:

$$\begin{cases} \mathbf{Q}_1 = d\mathbf{K}_1 - W\mathbf{K}_2, \\ \mathbf{Q}_2 = \frac{N}{d}\mathbf{K}_2. \end{cases} \quad (2.16)$$

For the (4, 2) SWNT ($d = 2$, $W = 5$, and $N = 28$), the reciprocal lattice vectors \mathbf{Q}_1 and \mathbf{Q}_2 of Eq. (2.16) are shown by arrows in Fig. 2-8. Note that the vector \mathbf{Q}_2 is parallel to the cutting lines. The rectangular Brillouin zone can thus be constructed from the N cutting lines, even though the vector \mathbf{Q}_1 is misaligned with respect to the \mathbf{K}_1 and \mathbf{K}_2 directions. For the (4, 2) SWNT, the rectangular Brillouin zone contains 2 cutting lines of length $14K_2$, as shown in dark gray in Fig. 2-8. For a general (n, m) SWNT, the borders of the rectangular Brillouin zone are given by the vectors $d\mathbf{K}_1$ and $N/d\mathbf{K}_2$, which follows from Eq. (2.16). The rectangular Brillouin zone thus consists of the d cutting lines of length $NK_2/d = 2\pi N / (dT)$. The zone-folding technique

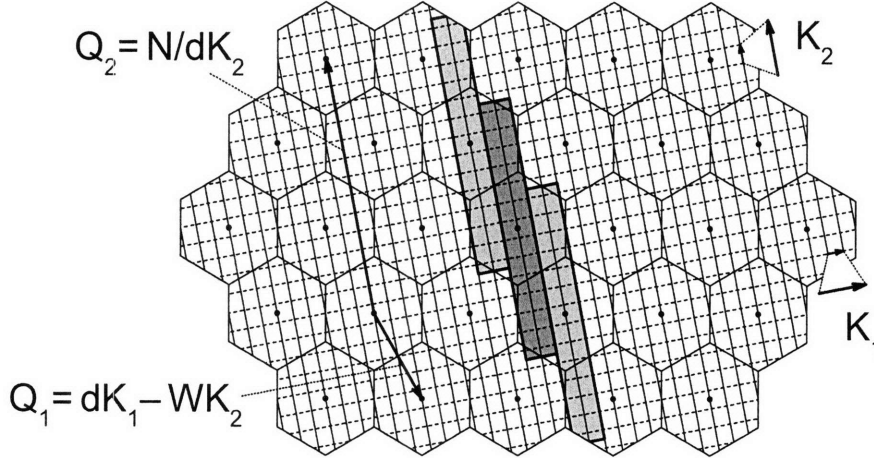


Figure 2-8: The reciprocal space of the graphene sheet. The solid lines represent the cutting lines for the (4, 2) SWNT. The dashed lines indicate the length of the cutting lines. The first Brillouin zone of the angular-helical reduced unit cell formed by the vectors $(\mathbf{C}_h/d, \mathbf{Z})$ is shaded in dark gray. The adjacent Brillouin zones are shaded in light gray. The arrows show the reciprocal lattice vectors $\mathbf{Q}_1 = d\mathbf{K}_1 - W\mathbf{K}_2$ and $\mathbf{Q}_2 = N/d\mathbf{K}_2$ and the cutting line vectors \mathbf{K}_1 and \mathbf{K}_2 . The dots show the Γ points.

projects the d cutting lines into the 1D Brillouin zone of length NK_2/d .

Fig. 2-8 shows the rectangular Brillouin zone (in dark gray) and the two adjacent Brillouin zones shifted by the vectors $\pm\mathbf{Q}_1$ (in light gray) for the (4, 2) SWNT. We can consider the momentum conservation across the Brillouin zone boundary using Fig. 2-8, similar to the preceding discussion in Section 2.5.1. Moving along the cutting lines, the angular momentum μ is conserved when crossing the Brillouin zone boundaries. In contrast, the linear momentum k changes by $\pm WK_2 = \pm 5K_2$ when crossing the zone boundaries perpendicular to the cutting lines (from the dark gray to one of the light gray rectangles in Fig. 2-8). Thus, k represents the linear projection of the *helical momentum*, and the reduced unit cell formed by the lattice vectors \mathbf{C}_h/d and \mathbf{Z} is called the *angular-helical reduced unit cell* [12].

The shape of the rectangular Brillouin zone and the linear momentum nonconservation at its boundaries can be understood from the shape of the angular-helical reduced unit cell. The latter is formed by the vectors \mathbf{C}_h/d and \mathbf{Z} . The vector \mathbf{C}_h/d is a pure rotation, thus \mathbf{Q}_2 of Eq. (2.16) has no \mathbf{K}_1 component, and the angular mo-

momentum μ is conserved across the Brillouin zone boundary. The vector \mathbf{C}_h/d spans $1/d$ -th of the SWNT circumference, so the d distinct values of the angular momentum μ appear, and the rectangular Brillouin zone consists of the d cutting lines. The screw vector \mathbf{Z} plays the role of the translational vector, therefore the linear projection k of the helical momentum exhibits discontinuities at the Brillouin zone boundaries. The translational component of the screw vector \mathbf{Z} is given by dT/N , according to Eq. (2.11), so the size of the rectangular Brillouin zone in the cutting line direction is equal to $NK_2/d = 2\pi N/(dT)$. The rotational and translational components of the screw vector \mathbf{Z} are proportional to W and d , respectively, and thus the linear projection k exhibits discontinuities of magnitude WK_2 when crossing over the d cutting lines in the direction perpendicular to them [140]. The linear projection k nonconservation can be demonstrated within the formalism of the line groups [12].

2.5.3 Helical-linear representation

The helical-linear reduced unit cell is formed by the lattice vectors \mathbf{R} and \mathbf{T} , as defined in Section 2.4. The reciprocal lattice vectors \mathbf{Q}_1 and \mathbf{Q}_2 can be derived from the definition in Eq. (2.2). The orthogonality conditions $\mathbf{Q}_1 \cdot \mathbf{T} = 0$ and $\mathbf{Q}_2 \cdot \mathbf{R} = 0$ suggest that $\mathbf{Q}_1 \propto \mathbf{C}_h$ and $\mathbf{Q}_2 \propto \hat{\mathbf{z}} \times \mathbf{R}$. Substituting \mathbf{R} from Eq. (2.8) and using Eq. (2.1) yields $\mathbf{Q}_2 \propto (2q + p) \mathbf{a}_1 - (2p + q) \mathbf{a}_2$. The normalization conditions require that $\mathbf{Q}_1 \cdot \mathbf{R} = 2\pi$ and $\mathbf{Q}_2 \cdot \mathbf{T} = 2\pi$. Substituting \mathbf{R} and \mathbf{T} of Eqs. (2.8) and (2.6) we obtain $\mathbf{Q}_1 = 4\pi [n\mathbf{a}_1 + m\mathbf{a}_2] / (d_R a^2)$ and $\mathbf{Q}_2 = 4\pi [(2q + p) \mathbf{a}_1 - (2p + q) \mathbf{a}_2] / (3a^2)$ with the help of Eqs. (2.4), (2.6), and (2.10). These expressions give \mathbf{Q}_1 and \mathbf{Q}_2 in terms of \mathbf{a}_1 and \mathbf{a}_2 . By comparing Eqs. (2.1) and (2.3), we can write \mathbf{a}_1 and \mathbf{a}_2 as functions of \mathbf{b}_1 and \mathbf{b}_2 in the form $4\pi\mathbf{a}_1 = a^2(2\mathbf{b}_1 + \mathbf{b}_2)$ and $4\pi\mathbf{a}_2 = a^2(2\mathbf{b}_2 + \mathbf{b}_1)$. We then express \mathbf{b}_1 and \mathbf{b}_2 in terms of \mathbf{K}_1 and \mathbf{K}_2 as follows, $\mathbf{b}_1 = n\mathbf{K}_1 + t_1\mathbf{K}_2$ and $\mathbf{b}_2 = m\mathbf{K}_1 + t_2\mathbf{K}_2$, according to Eq. (2.15). Finally, we obtain \mathbf{Q}_1 and \mathbf{Q}_2 as functions of \mathbf{K}_1 and \mathbf{K}_2 using Eqs. (2.6), (2.7), (2.10), and (2.11) [140]:

$$\begin{cases} \mathbf{Q}_1 = N\mathbf{K}_1, \\ \mathbf{Q}_2 = -M\mathbf{K}_1 + \mathbf{K}_2. \end{cases} \quad (2.17)$$

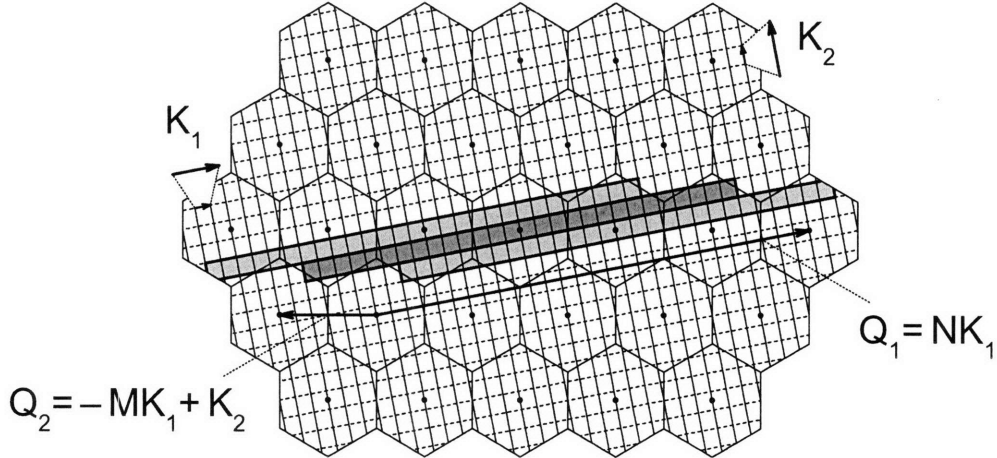


Figure 2-9: The reciprocal space of the graphene sheet. The solid lines represent the cutting lines for the (4, 2) SWNT. The dashed lines indicate the length of the cutting lines. The first Brillouin zone of the helical-linear reduced unit cell formed by the vectors (\mathbf{R}, \mathbf{T}) is shaded in dark gray. The adjacent Brillouin zones are shaded in light gray. The arrows show the reciprocal lattice vectors $\mathbf{Q}_1 = N\mathbf{K}_1$ and $\mathbf{Q}_2 = -M\mathbf{K}_1 + \mathbf{K}_2$ and the cutting line vectors \mathbf{K}_1 and \mathbf{K}_2 . The dots show the Γ points.

For the (4, 2) SWNT ($N = 28$ and $M = 6$), the reciprocal lattice vectors \mathbf{Q}_1 and \mathbf{Q}_2 of Eq. (2.17) are shown by arrows in Fig. 2-9. Note that the vector \mathbf{Q}_1 is perpendicular to the cutting lines. The rectangular Brillouin zone can thus be constructed from the N cutting lines, even though the vector \mathbf{Q}_2 is misaligned with respect to the \mathbf{K}_1 and \mathbf{K}_2 directions. For the (4, 2) SWNT, the rectangular Brillouin zone contains 28 cutting lines of length K_2 , as shown in dark gray in Fig. 2-9. For a general (n, m) SWNT, the borders of the rectangular Brillouin zone are given by the vectors $N\mathbf{K}_1$ and \mathbf{K}_2 , which follows from Eq. (2.17). The rectangular Brillouin zone thus consists of the N cutting lines of length $K_2 = 2\pi/T$. The zone-folding technique projects the N cutting lines into the 1D Brillouin zone of length K_2 .

Fig. 2-9 shows the rectangular Brillouin zone (in dark gray) and the two adjacent Brillouin zones shifted by the vectors $\pm\mathbf{Q}_2$ (in light gray) for the (4, 2) SWNT. We can consider the momentum conservation across the Brillouin zone boundary using Fig. 2-9, similar to the preceding discussions in Sections 2.5.1 and 2.5.2. Moving along the cutting lines, the angular momentum μ changes by $\pm M = \pm 6$ when crossing the

Brillouin zone boundaries (from the dark gray to one of the light gray rectangles in Fig. 2-9). In contrast, the linear momentum k is conserved when crossing the zone boundaries perpendicular to the cutting lines. Thus, μ represents the angular projection of the *helical momentum*, and the reduced unit cell formed by the lattice vectors \mathbf{R} and \mathbf{T} is called the *helical-linear reduced unit cell* [12].

The shape of the rectangular Brillouin zone and the angular momentum nonconservation at its boundaries can be understood from the shape of the helical-linear reduced unit cell. The latter is formed by the vectors \mathbf{R} and \mathbf{T} . The screw vector \mathbf{R} plays the role of the rotational vector, therefore the angular projection μ of the helical momentum exhibits discontinuities at the Brillouin zone boundaries. The vector \mathbf{R} spans $1/N$ -th of the SWNT circumference, according to Eq. (2.11), so the N distinct values of the angular projection μ appear, and the rectangular Brillouin zone consists of the N cutting lines. The vector \mathbf{T} is a pure translation, thus \mathbf{Q}_1 of Eq. (2.17) has no \mathbf{K}_2 component, and the linear momentum k is conserved across the Brillouin zone boundary. The length of the vector \mathbf{T} determines the size of the rectangular Brillouin zone in the direction of the cutting lines $K_2 = 2\pi/T$. The rotational and translational components of the screw vector \mathbf{R} are proportional to 1 and M , respectively, and thus the angular projection μ exhibits discontinuities of magnitude M per cutting line length when crossing the rectangular Brillouin zone along the cutting line direction [140]. The angular projection μ nonconservation can be demonstrated within the formalism of the group of the wavevector [12].

2.6 Summary of results

In this Chapter, we considered the SWNT structure in real and reciprocal space. We reviewed the rotational, translational, and helical symmetries of the SWNT in real space. We developed the helical-helical, angular-helical, and helical-linear representations of the cutting lines in reciprocal space. The angular-helical representation is associated with pure rotations and is commonly used with the formalism of the line groups [12]. The helical-linear representation, also known as the extended represen-

tation of the cutting lines [140], is associated with pure translations and is commonly used with the formalism of the group of the wavevector [12]. In the angular-helical and helical-linear representations, the linear k and angular μ momenta, respectively, become projections of the helical momentum and therefore are not conserved at the Brillouin zone boundaries. The momentum nonconservation must be treated as follows. Any angular or linear momentum transfer beyond the first Brillouin zone is translated back into the first Brillouin zone, correcting for the momentum discontinuities at the Brillouin zone boundaries. We thus obtain different selection rules within the angular-helical and helical-linear representations. However, none of the symmetry-related properties of SWNTs are affected by this difference. The choice of the representation is arbitrary, and it depends on whether we are interested in the angular μ or linear k momentum conservation for an analysis of the scattering processes in SWNTs. Because of the helical symmetry of SWNTs, there is no representation that would conserve both μ and k and allow application of the zone-folding technique. The structural parameters of the SWNT introduced in this Chapter are summarized in Table 2.1.

Table 2.1: Structural parameters for single-wall carbon nanotubes

Graphene sheet				
symbol	name	formula	value	
a_{CC}	interatomic distance	—	0.142 nm	
a	lattice constant	$a = \sqrt{3}a_{CC}$	0.246 nm	
\mathbf{a}_1	lattice vector	$\mathbf{a}_1 = (\sqrt{3}\hat{x}/2 + \hat{y}/2) a$	—	
\mathbf{a}_2	lattice vector	$\mathbf{a}_2 = (\sqrt{3}\hat{x}/2 - \hat{y}/2) a$	—	
\mathbf{b}_1	reciprocal lattice vector	$\mathbf{b}_1 = (\hat{x}/2 + \sqrt{3}\hat{y}/2) 4\pi/(\sqrt{3}a)$	—	
\mathbf{b}_2	reciprocal lattice vector	$\mathbf{b}_2 = (\hat{x}/2 - \sqrt{3}\hat{y}/2) 4\pi/(\sqrt{3}a)$	—	

Nanotube parameters				
symbol	name	formula	range	value
(n, m)	—	—	$0 \leq m \leq n$	(4,2)
d_t	diameter	$d_t = \sqrt{n^2 + nm + m^2} a/\pi$	—	0.41 nm
θ	chiral angle	$\theta = \arctan(\sqrt{3}m/(2n + m))$	$0^\circ \leq \theta \leq 30^\circ$	19°
χ	handedness	$\chi = \text{ZR/AL, ZL/AR}$	—	ZR/AL

Additional coefficients				
symbol	formula	range	value	
d	$d = \text{gcd}^\dagger(n, m)$	$1 \leq d \leq n$	2	
d_R	$d_R = \text{gcd}^\dagger(2n + m, 2m + n)$	$d_R = d$ if $\text{mod}^\ddagger(n - m, 3d) \neq 0$ $d_R = 3d$ if $\text{mod}^\ddagger(n - m, 3d) = 0$	2	
(t_1, t_2)	$t_1 = (2m + n)/d_R$ $t_2 = -(2n + m)/d_R$	—	(4, -5)	
(u, v)	$mu - nv = d$	$0 < t_1v - t_2u < N/d$	(1, 0)	
(p, q)	$t_1q - t_2p = 1$	$0 < mp - nq < N$	(1, -1)	
N	$N = 2(n^2 + nm + m^2)/d_R$	—	28	
W	$W = t_1v - t_2u$	$1 \leq W < N$	5	
M	$M = mp - nq$	$1 < M < N/d$	6	

$^\dagger \text{gcd}(i, j)$ denotes the greatest common divisor of the two integers i and j
 $^\ddagger \text{mod}(i, j)$ is the remainder of the division of i by j

Symmetry vectors				
symbol	name	formula	magnitude	value
\mathbf{C}_h	chiral vector	$\mathbf{C}_h = n\mathbf{a}_1 + m\mathbf{a}_2$	$C_h = \pi d_t$	1.30 nm
\mathbf{C}_h/d	rotational vector	$\mathbf{C}_h/d = n\mathbf{a}_1/d + m\mathbf{a}_2/d$	—	0.65 nm
\mathbf{T}	translational vector	$\mathbf{T} = t_1\mathbf{a}_1 + t_2\mathbf{a}_2$	$T = \sqrt{3}\pi d_t/d_R$	1.13 nm
\mathbf{Z}	screw vector [32]	$\mathbf{Z} = u\mathbf{a}_1 + v\mathbf{a}_2$ $N\mathbf{Z} = W\mathbf{C}_h + d\mathbf{T}$	—	0.246 nm 6.89 nm
\mathbf{R}	screw vector [129]	$\mathbf{R} = p\mathbf{a}_1 + q\mathbf{a}_2$ $N\mathbf{R} = \mathbf{C}_h + M\mathbf{T}$	—	0.246 nm 6.89 nm

Cutting lines

symbol	name	formula	magnitude
\mathbf{K}_1	angular reciprocal lattice vector	$\mathbf{K}_1 = t_1 \mathbf{b}_2/N - t_2 \mathbf{b}_1/N$	$K_1 = 2\pi/C_h$
\mathbf{K}_2	linear reciprocal lattice vector	$\mathbf{K}_2 = m \mathbf{b}_1/N - n \mathbf{b}_2/N$	$K_2 = 2\pi/T$

Helical-helical representation

symbol	name	formula
\mathbf{R}_1	screw lattice vector	$\mathbf{R}_1 = -t_2 \mathbf{C}_h/N + m \mathbf{T}/N$
\mathbf{R}_2	screw lattice vector	$\mathbf{R}_2 = t_1 \mathbf{C}_h/N - n \mathbf{T}/N$
\mathbf{Q}_1	helical reciprocal lattice vector	$\mathbf{Q}_1 = n \mathbf{K}_1 + t_1 \mathbf{K}_2$
\mathbf{Q}_2	helical reciprocal lattice vector	$\mathbf{Q}_2 = m \mathbf{K}_1 + t_2 \mathbf{K}_2$

symbol	name	range	conserved
μ	angular projection	undefined	no
k	linear projection	undefined	no

Angular-helical representation

symbol	name	formula
\mathbf{R}_1	rotational lattice vector	$\mathbf{R}_1 = \mathbf{C}_h/d$
\mathbf{R}_2	screw lattice vector	$\mathbf{R}_2 = \mathbf{Z}$
\mathbf{Q}_1	angular reciprocal lattice vector	$\mathbf{Q}_1 = d \mathbf{K}_1 - W \mathbf{K}_2$
\mathbf{Q}_2	helical reciprocal lattice vector	$\mathbf{Q}_2 = N \mathbf{K}_2/d$

symbol	name	range	conserved
μ	angular momentum	$1 - d/2 \leq \mu \leq d/2$	yes
k	linear projection	$-(N/d)\pi/T < k \leq (N/d)\pi/T$	no

Helical-linear representation

symbol	name	formula
\mathbf{R}_1	screw lattice vector	$\mathbf{R}_1 = \mathbf{R}$
\mathbf{R}_2	translational lattice vector	$\mathbf{R}_2 = \mathbf{T}$
\mathbf{Q}_1	helical reciprocal lattice vector	$\mathbf{Q}_1 = N \mathbf{K}_1$
\mathbf{Q}_2	linear reciprocal lattice vector	$\mathbf{Q}_2 = -M \mathbf{K}_1 + \mathbf{K}_2$

symbol	name	range	conserved
μ	angular projection	$1 - N/2 \leq \mu \leq N/2$	no
k	linear momentum	$-\pi/T < k \leq \pi/T$	yes

Chapter 3

Electronic properties

Using the zone-folding technique developed in Section 2.5, the electronic dispersion relations of SWNTs are derived from those of a graphene sheet. We start this Chapter by reviewing a simple tight-binding (STB) model that provides important insights for understanding the key electronic properties of a graphene sheet and, consequently, of SWNTs. We further develop an extended tight-binding (ETB) model that gives good agreement with recent optical spectroscopy measurements as well as with accurate first-principles calculations.

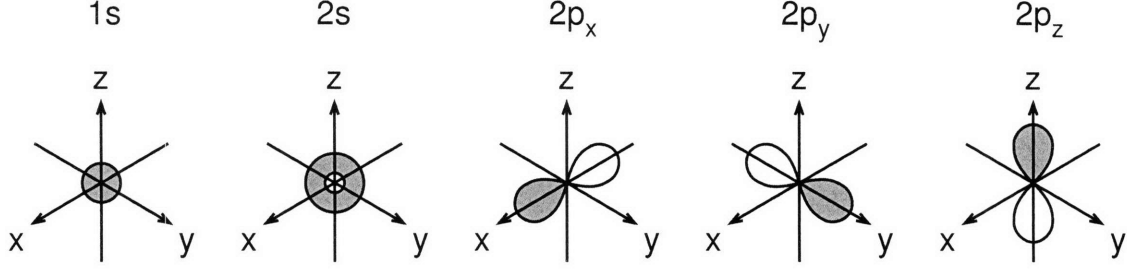


Figure 3-1: A schematic of the $1s$, $2s$, $2p_x$, $2p_y$, and $2p_z$ atomic orbitals of the carbon atom. The gray and white shaded areas denote the wavefunction phase difference of π . For example, the gray shaded area corresponds to a positive sign of the wavefunction amplitude, while the white shaded area indicates the negative wavefunction amplitude.

3.1 Tight-binding framework

The electronic dispersion relations of a graphene sheet are obtained by solving the single-particle Schrödinger equation:

$$H\Psi^b(\mathbf{k}, \mathbf{r}, t) = i\hbar\frac{\partial}{\partial t}\Psi^b(\mathbf{k}, \mathbf{r}, t), \quad (3.1)$$

where $H = T + V(\mathbf{r})$ is the single-particle Hamiltonian, $T = \mathbf{p}^2/(2m)$ is the kinetic energy operator, $\mathbf{p} = -i\hbar\nabla$ is the momentum operator, ∇ is the gradient operator, \hbar is Planck's constant, m is the electron mass, $V(\mathbf{r})$ is the effective periodic potential, $\Psi^b(\mathbf{k}, \mathbf{r}, t)$ is the one-electron wavefunction, b is the band index, \mathbf{k} is the electron wavevector, \mathbf{r} is the spatial coordinate, t is time, and i is imaginary unity. The electron wavefunction $\Psi^b(\mathbf{k}, \mathbf{r}, t)$ is approximated by a linear combination of atomic orbitals (LCAO) in terms of Bloch sums [147]:

$$\begin{cases} \Psi^b(\mathbf{k}, \mathbf{r}, t) = \exp(-iE^b(\mathbf{k})t/\hbar) \sum_{so} C_{so}^b(\mathbf{k})\Phi_{so}(\mathbf{k}, \mathbf{r}), \\ \Phi_{so}(\mathbf{k}, \mathbf{r}) = \frac{1}{\sqrt{U}} \sum_u^U \exp(i\mathbf{k}\mathbf{R}_{us}) \phi_o(\mathbf{r} - \mathbf{R}_{us}), \end{cases} \quad (3.2)$$

where $E^b(\mathbf{k})$ is the one-electron energy, $C_{so}^b(\mathbf{k})$ is the Bloch amplitude, $\Phi_{so}(\mathbf{k}, \mathbf{r})$ is the Bloch wavefunction, $\phi_o(\mathbf{r})$ is the atomic orbital, \mathbf{R}_{us} is the atomic coordinate, the

index $u = 1, \dots, U$ spans all the U unit cells in a graphene sheet, the index $s = A, B$ labels the two inequivalent atoms in the unit cell, and the index $o = 1s, 2s, 2p_x, 2p_y, 2p_z$ enumerates the atomic orbitals of a carbon atom schematically shown in Fig. 3-1. Upon multiplying Eq. (3.1) by $\Phi_{s'o'}^*(\mathbf{k}, \mathbf{r})$ of Eq. (3.2) and integrating over \mathbf{r} , we obtain the stationary Schrödinger equation for the Bloch amplitudes $C_{so}^b(\mathbf{k})$ in the matrix form:

$$\sum_{so} H_{s'o'so}(\mathbf{k}) C_{so}^b(\mathbf{k}) = \sum_{so} E^b(\mathbf{k}) S_{s'o'so}(\mathbf{k}) C_{so}^b(\mathbf{k}), \quad (3.3)$$

where the Hamiltonian $H_{s'o'so}(\mathbf{k})$ and overlap $S_{s'o'so}(\mathbf{k})$ matrices are given by:

$$\begin{cases} H_{s'o'so}(\mathbf{k}) = \sum_u^U \exp(i\mathbf{k}(\mathbf{R}_{us} - \mathbf{R}_{u's'})) \int \phi_{o'}^*(\mathbf{r} - \mathbf{R}_{u's'}) H \phi_o(\mathbf{r} - \mathbf{R}_{us}) d\mathbf{r}, \\ S_{s'o'so}(\mathbf{k}) = \sum_u^U \exp(i\mathbf{k}(\mathbf{R}_{us} - \mathbf{R}_{u's'})) \int \phi_{o'}^*(\mathbf{r} - \mathbf{R}_{u's'}) \phi_o(\mathbf{r} - \mathbf{R}_{us}) d\mathbf{r}, \end{cases} \quad (3.4)$$

and the index u' labels the unit cell under consideration. The orthonormality condition for the electron wavefunction of Eq. (3.2) then becomes:

$$\int \Psi^{b' *}(\mathbf{k}, \mathbf{r}, t) \Psi^b(\mathbf{k}, \mathbf{r}, t) d\mathbf{r} = \sum_{s'o'} \sum_{so} C_{s'o'}^{b' *}(\mathbf{k}) S_{s'o'so}(\mathbf{k}) C_{so}^b(\mathbf{k}) = \delta_{b'b}, \quad (3.5)$$

where $\delta_{b'b}$ is the Kronecker delta function [129].

To evaluate the integrals in Eq. (3.4), the effective periodic potential $V(\mathbf{r})$ in the single-particle Hamiltonian H of Eq. (3.1) is expressed by a sum of the effective spherically-symmetric potentials $U(\mathbf{r} - \mathbf{R}_{u''s''})$ centered at the atomic sites $\mathbf{R}_{u''s''}$:

$$V(\mathbf{r}) = \sum_{u''s''} U(\mathbf{r} - \mathbf{R}_{u''s''}). \quad (3.6)$$

The Hamiltonian matrix $H_{s'o'so}(\mathbf{k})$ then contains the three-center integrals that involve two orbitals $\phi_{o'}^*(\mathbf{r} - \mathbf{R}_{u's'})$ and $\phi_o(\mathbf{r} - \mathbf{R}_{us})$ at two different atomic sites $\mathbf{R}_{u's'}$ and \mathbf{R}_{us} , while the potential $U(\mathbf{r} - \mathbf{R}_{u''s''})$ originates from a third atomic site $\mathbf{R}_{u''s''}$. In contrast, the overlap matrix $S_{s'o'so}(\mathbf{k})$ contains two-center integrals only. Neglecting the three-center integrals in $H_{s'o'so}(\mathbf{k})$ [144], the remaining two-center integrals in both

$H_{s'o'so}(\mathbf{k})$ and $S_{s'o'so}(\mathbf{k})$ can be parameterized as functions of the interatomic vector $\mathbf{R} = \mathbf{R}_{us} - \mathbf{R}_{u's'}$ and of the symmetry and relative orientation of the atomic orbitals $\phi_{o'}^*(\mathbf{r})$ and $\phi_o(\mathbf{r})$:

$$\begin{cases} \varepsilon_o = \int \phi_o^*(\mathbf{r}) H \phi_o(\mathbf{r}) d\mathbf{r}, \\ t_{o'o}(\mathbf{R}) = \int \phi_{o'}^*(\mathbf{r}) (T + U(\mathbf{r}) + U(\mathbf{r} - \mathbf{R})) \phi_o(\mathbf{r} - \mathbf{R}) d\mathbf{r}, \\ s_{o'o}(\mathbf{R}) = \int \phi_{o'}^*(\mathbf{r}) \phi_o(\mathbf{r} - \mathbf{R}) d\mathbf{r}, \end{cases} \quad (3.7)$$

where ε_o is the atomic orbital energy,¹ $t_{o'o}(\mathbf{R})$ is the transfer integral, and $s_{o'o}(\mathbf{R})$ is the overlap integral. A numerical calculation of parameters ε_o , $t_{o'o}(\mathbf{R})$, and $s_{o'o}(\mathbf{R})$ defines the non-orthogonal tight-binding model. Within the orthogonal tight-binding model, $s_{o'o}(\mathbf{R})$ is set to zero.

The transfer $t_{o'o}(\mathbf{R})$ and overlap $s_{o'o}(\mathbf{R})$ integrals of Eq. (3.7) depend on the symmetry of the atomic orbitals denoted by indices o' and o . A schematic of the atomic orbitals occupied by electrons in a carbon atom is shown in Fig. 3-1. The ground state electronic configuration of atomic carbon reads as $1s^2 2s^2 2p^2$. When carbon atoms are put together to form a graphene sheet, one of the two $2s$ electrons is excited to the $2p$ state, so that the electronic configuration becomes $1s^2 2s^1 2p^3$. The $1s^2$ atomic orbitals are localized near the nucleus and lie far below the Fermi level on the energy scale, so that they are not involved in chemical bonding and will not be considered thereafter. The $2s$ atomic orbitals mix with the $2p_x$ and $2p_y$ atomic orbitals to form the hybridized σ molecular orbitals. The hybridized σ molecular orbitals produce covalent bonds arranging carbon atoms into the hexagonal lattice. The $2p_z$ atomic orbitals form the π molecular orbitals normal to the graphene plane and therefore are uncoupled from the σ molecular orbitals. The π energy bands lie near the Fermi level on the energy scale, and thus are most relevant for transport and optical properties of a graphene sheet and SWNTs [129].

The transfer $t_{o'o}(\mathbf{R})$ and overlap $s_{o'o}(\mathbf{R})$ integrals of Eq. (3.7) depend on the relative orientation of the atomic orbitals o' and o with respect to the interatomic vector \mathbf{R} .

¹Note that ε_o differs from the atomic orbital energy of the free atom because of the effective periodic potential $V(\mathbf{r})$ in the single-particle Hamiltonian H in Eq. (3.1).

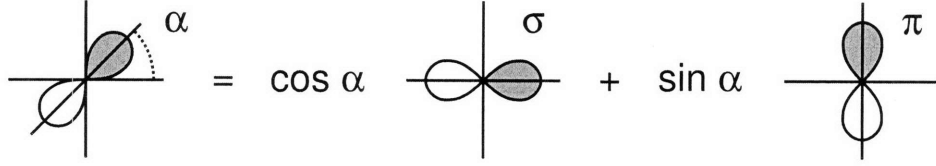


Figure 3-2: The σ and π projections of the $2p$ atomic orbital. The $2p$ atomic orbital makes an angle α with respect to the interatomic vector \mathbf{R} represented by the horizontal line. The coefficients $\cos \alpha$ and $\sin \alpha$ follow from the projections of the spherical harmonic $Y_{21}(\theta, \phi)$ of the $2p$ atomic orbital and therefore are not valid for other atomic orbitals.

While the $2s$ atomic orbital is spherically symmetric, the $2p$ atomic orbital has the symmetry of the spherical harmonic $Y_{21}(\theta, \phi)$. The spherical harmonic $Y_{21}(\theta, \phi)$ can be decomposed along two mutually orthogonal directions, parallel and perpendicular to the interatomic vector \mathbf{R} , as shown in Fig. 3-2. We refer to these two projections of the $2p$ atomic orbital as σ and π , respectively, in accordance with the above definitions of the σ and π molecular orbitals, while the $2s$ atomic orbital is referred to as s for brevity. It is therefore sufficient to determine the transfer $t_{o'o}(R)$ and overlap $s_{o'o}(R)$ integrals between the pairs of $o' = s, \sigma, \pi$ and $o = s, \sigma, \pi$ atomic orbitals as functions of the interatomic distance $R = |\mathbf{R}|$. Among of nine possible pairs, five ($o'o = ss, s\sigma, \sigma s, \sigma\sigma, \pi\pi$) shown in Fig. 3-3 (a) give nonvanishing transfer and overlap integrals. For the remaining four pairs ($o'o = s\pi, \pi s, \sigma\pi, \pi\sigma$) shown in Fig. 3-3 (b), the transfer and overlap integrals are identically zero by symmetry requirements. Considering that the two pairs $o'o = s\sigma$ and σs , connected by a dashed line in Fig. 3-3 (a), yield transfer and overlap integrals of equivalent magnitudes and opposite signs, we conclude that there are a total of four independent pairs ($o'o = ss, s\sigma, \sigma\sigma, \pi\pi$). The number of tight-binding parameters is therefore reduced to ten, namely, the two atomic orbital energies ($\varepsilon_{2s}, \varepsilon_{2p}$), the four transfer integrals ($t_{ss}(R), t_{s\sigma}(R), t_{\sigma\sigma}(R), t_{\pi\pi}(R)$), and the four overlap integrals ($s_{ss}(R), s_{s\sigma}(R), s_{\sigma\sigma}(R), s_{\pi\pi}(R)$).

The Hamiltonian $H_{s'o'so}(\mathbf{k})$ and overlap $S_{s'o'so}(\mathbf{k})$ matrices of Eq. (3.4) can now be constructed for a given lattice geometry. For each pair of carbon atoms, the $2p$ atomic orbitals are decomposed into three mutually orthogonal projections, one of which is parallel to the interatomic distance. The integrals in Eq. (3.4) for this atom pair are

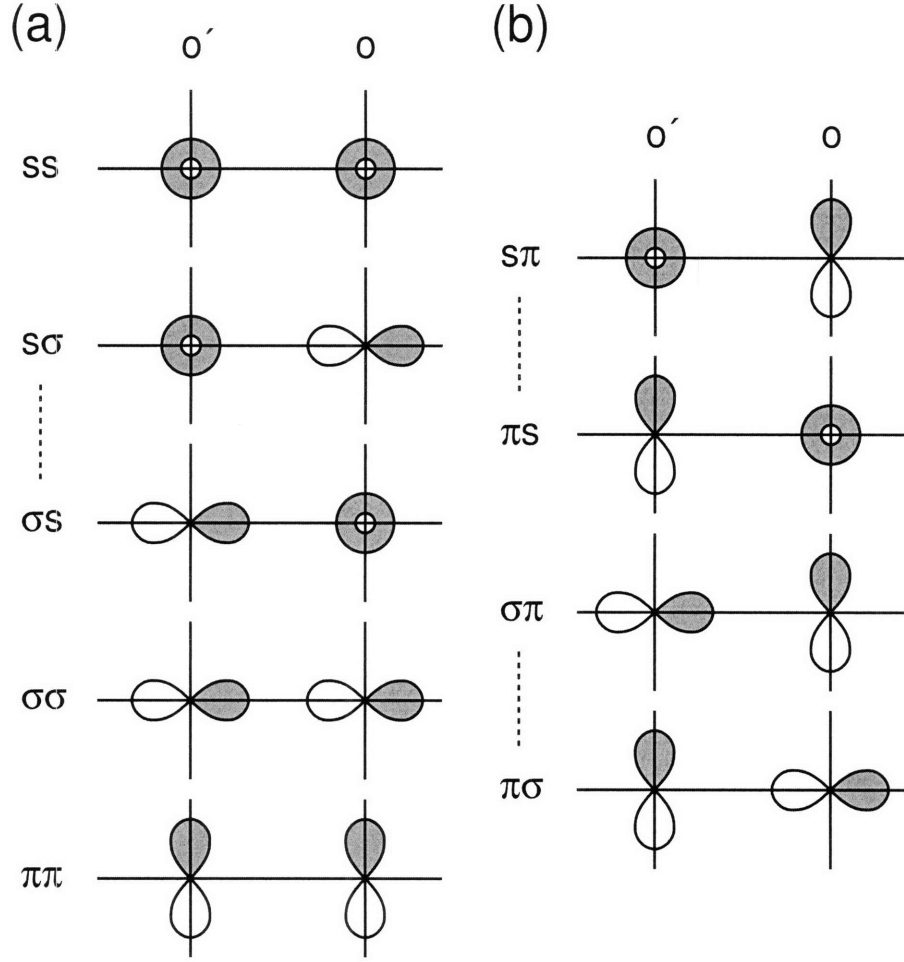


Figure 3-3: (a) Five molecular orbital configurations $o'o = ss, s\sigma, \sigma s, \sigma\sigma, \pi\pi$ that give nonvanishing transfer $t_{o'o}(R)$ and overlap $s_{o'o}(R)$ integrals. The two configurations $o'o = s\sigma, \sigma s$ connected by a dashed line yield the transfer and overlap integrals of equivalent magnitudes and opposite signs. (b) The remaining four configurations $o'o = s\pi, \pi s, \sigma\pi, \pi\sigma$ for which the transfer and overlap integrals are identically zero by symmetry requirements. The dashed lines connect the equivalent configurations.

then written as linear combinations of the transfer ($t_{ss}(R)$, $t_{s\sigma}(R)$, $t_{\sigma\sigma}(R)$, $t_{\pi\pi}(R)$) and overlap ($s_{ss}(R)$, $s_{s\sigma}(R)$, $s_{\sigma\sigma}(R)$, $s_{\pi\pi}(R)$) integrals. Considering that there are four atomic orbitals per carbon atom ($o', o = 2s, 2p_x, 2p_y, 2p_z$) and two carbon atoms per unit cell ($s', s = A, B$), we obtain the 8×8 Hamiltonian $H_{s'o'so}(\mathbf{k})$ and overlap $S_{s'o'so}(\mathbf{k})$ matrices. In a flat graphene sheet, these matrices are partitioned into the 6×6 and 2×2 subblocks corresponding to the σ and π molecular orbitals, respectively. In Section 3.2, we solve for the 2×2 subblock to determine the dispersion relations

and the Bloch amplitudes for the π electrons in a flat graphene sheet.

3.2 Simple tight-binding model

Within the framework of the simple tight-binding (STB) model [129], we neglect the σ molecular orbitals and the long-range atomic interactions, $R > a_{CC}$. The STB model thus employs three parameters, the atomic orbital energy ε_{2p} , the transfer integral $t_{\pi\pi}(a_{CC})$, and the overlap integral $s_{\pi\pi}(a_{CC})$. Thereafter we refer to these parameters as ε , t , and s , respectively.

To construct the Hamiltonian $H_{s'o'so}(\mathbf{k})$ and overlap $S_{s'o'so}(\mathbf{k})$ matrices of Eq. (3.3), let us consider the nearest-neighbor interactions ($R = a_{CC}$) in the unit cell of a graphene sheet shown in Fig. 2-1 (a). The unit cell contains two atoms, A and B, each of which has three nearest neighbors of the opposite atom type. The absence of nearest-neighbor interactions within the same A or B sublattice yields the diagonal Hamiltonian and overlap matrix elements, $H_{A\pi A\pi} = H_{B\pi B\pi} = \varepsilon$ and $S_{A\pi A\pi} = S_{B\pi B\pi} = 1$, independent of the transfer t and overlap s integrals. For the $H_{A\pi B\pi}$ and $S_{A\pi B\pi}$ matrix elements, the interatomic vectors \mathbf{R} from atom A to its three nearest-neighbors in Eq. (3.3) are given by $(\mathbf{a}_1 + \mathbf{a}_2)/3$, $(\mathbf{a}_1 - 2\mathbf{a}_2)/3$, and $(\mathbf{a}_2 - 2\mathbf{a}_1)/3$, as one can see in Fig. 2-1 (a). Substituting these vectors from Eq. (2.1) into Eq. (3.3), we obtain $H_{A\pi B\pi} = tf(\mathbf{k})$ and $S_{A\pi B\pi} = sf(\mathbf{k})$, where $f(\mathbf{k})$ is the sum of the phase factors over the nearest neighbors given by:

$$f(\mathbf{k}) = \exp\left(+i\frac{k_x a}{\sqrt{3}}\right) + \exp\left(-i\frac{k_x a}{2\sqrt{3}} + i\frac{k_y a}{2}\right) + \exp\left(-i\frac{k_x a}{2\sqrt{3}} - i\frac{k_y a}{2}\right). \quad (3.8)$$

The $H_{B\pi A\pi}$ and $S_{B\pi A\pi}$ matrix elements are derived in a similar fashion. The interatomic vectors \mathbf{R} have the opposite signs, implying that $H_{B\pi A\pi} = tf^*(\mathbf{k})$ and $S_{B\pi A\pi} = sf^*(\mathbf{k})$. The Hamiltonian and overlap matrices are thus Hermitian. The Schrödinger equation in the matrix form, Eq. (3.3), can then be written as follows:

$$\begin{pmatrix} \varepsilon & tf(\mathbf{k}) \\ tf^*(\mathbf{k}) & \varepsilon \end{pmatrix} \begin{pmatrix} C_{A\pi}^b(\mathbf{k}) \\ C_{B\pi}^b(\mathbf{k}) \end{pmatrix} = E^b(\mathbf{k}) \begin{pmatrix} 1 & sf(\mathbf{k}) \\ sf^*(\mathbf{k}) & 1 \end{pmatrix} \begin{pmatrix} C_{A\pi}^b(\mathbf{k}) \\ C_{B\pi}^b(\mathbf{k}) \end{pmatrix}. \quad (3.9)$$

Solving the secular equation yields the energy eigenvalues:

$$\begin{cases} E^v(\mathbf{k}) = \frac{\varepsilon + tw(\mathbf{k})}{1 + sw(\mathbf{k})}, \\ E^c(\mathbf{k}) = \frac{\varepsilon - tw(\mathbf{k})}{1 - sw(\mathbf{k})}, \end{cases} \quad (3.10)$$

where the band index $b = v, c$ indicates the valence and conduction bands, taking into account that $t < 0$, and $w(\mathbf{k})$ is the absolute value of the phase factor $f(\mathbf{k})$, that is, $w(\mathbf{k}) = \sqrt{f^*(\mathbf{k})f(\mathbf{k})}$. For $f(\mathbf{k})$ given by Eq. (3.8) we obtain:

$$w(\mathbf{k}) = \sqrt{1 + 4 \cos \frac{\sqrt{3}k_x a}{2} \cos \frac{k_y a}{2} + 4 \cos^2 \frac{k_y a}{2}}. \quad (3.11)$$

According to Eq. (3.10), the atomic orbital energy ε is an arbitrary reference point in the orthogonal STB model ($s = 0$), while ε is a relevant parameter in the non-orthogonal STB model ($s \neq 0$).

Substituting the energy eigenvalues $E^b(\mathbf{k})$ of Eq. (3.10) into Eq. (3.9) yields the wavefunction amplitudes $C_{A\pi}^b(\mathbf{k})$ and $C_{B\pi}^b(\mathbf{k})$ for the valence ($b = v$) and conduction ($b = c$) electrons. Using the orthonormality condition of Eq. (3.5), we obtain the Bloch amplitudes for the valence band:

$$\begin{cases} C_{A\pi}^v(\mathbf{k}) = +\sqrt{\frac{f(\mathbf{k})}{2w(\mathbf{k})(1 + sw(\mathbf{k}))}}, \\ C_{B\pi}^v(\mathbf{k}) = +\sqrt{\frac{f^*(\mathbf{k})}{2w(\mathbf{k})(1 + sw(\mathbf{k}))}}, \end{cases} \quad (3.12)$$

and for the conduction band:

$$\begin{cases} C_{A\pi}^c(\mathbf{k}) = +\sqrt{\frac{f(\mathbf{k})}{2w(\mathbf{k})(1 - sw(\mathbf{k}))}}, \\ C_{B\pi}^c(\mathbf{k}) = -\sqrt{\frac{f^*(\mathbf{k})}{2w(\mathbf{k})(1 - sw(\mathbf{k}))}}. \end{cases} \quad (3.13)$$

The Bloch amplitudes thus vary with the phase of square root of $f(\mathbf{k})$. The phase

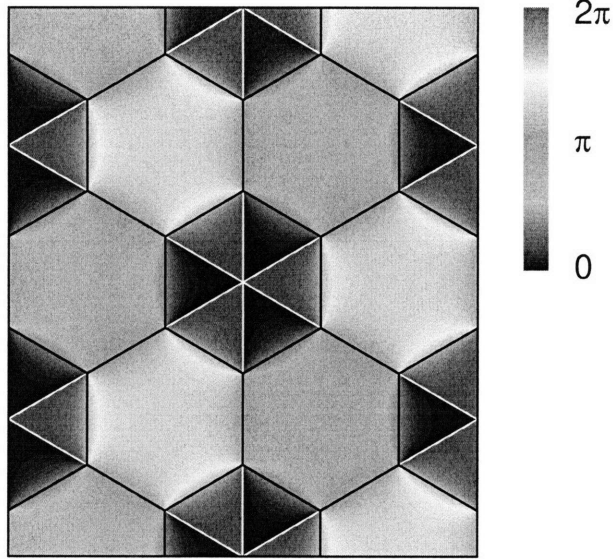


Figure 3-4: The phase of $f(\mathbf{k})$ given by Eq. (3.8) in the reciprocal space of the graphene sheet shown in Fig. 2-1. The color scale from blue to red represents the phase from 0 to 2π . The sharp boundaries between the blue and red regions correspond to small phase oscillations around the zero value.

of $f(\mathbf{k})$ in the reciprocal space of the graphene sheet is shown in Fig. 3-4. There are three types of Brillouin zones in Fig. 3-4, blue-red, cyan-green, and green-yellow, where the phase of $f(\mathbf{k})$ is about 0, $2\pi/3$, and $4\pi/3$, respectively. By going around the K point in Fig. 3-4 along the blue-cyan-green-yellow-red color direction, the phase of $f(\mathbf{k})$ changes from 0 to 2π . The phases of the Bloch amplitudes, however, change from 0 to π and from π to 0 because of the square roots in Eqs. (3.12) and (3.13). This phase change of π is known as Berry's phase. Berry's phase of π leads to a half-integer quantum Hall effect in the graphene sheet [103, 176].

Fitting the dispersion relations of the graphene sheet given by Eq. (3.10) to the energy values obtained from an *ab initio* variational approach [109], yields the values of the transfer $t = -3.033$ eV and overlap $s = 0.129$ integrals, after setting the atomic orbital energy equal to zero of the energy scale, $\varepsilon = 0$ eV [129]. Figures 3-5 (a) and (b) show the dispersion relations of the graphene sheet given by Eq. (3.10) with the above parameters throughout the entire first Brillouin zone and along the high-symmetry directions in the first Brillouin zone, respectively, where the first Brillouin

zone is shown in Fig. 2-1 (b). The lower band is completely filled with electrons in the ground state and is labeled by v as the valence band in Fig. 3-5 (b). The upper band is completely empty of electrons in the ground state and is labeled by c as the conduction band in Fig. 3-5 (b). The formation of the valence and conduction bands can be understood from the Bloch amplitudes given by Eqs. (3.12) and (3.13) and from the phase of $f(\mathbf{k})$ shown in Fig. 3-4. At the Γ point, $\mathbf{k} = 0$ and $C_{A\pi}^v = C_{B\pi}^v$, while $C_{A\pi}^c = -C_{B\pi}^c$. The wavefunctions given by Eq. (3.2) then become $\Psi^v \propto \Phi_{A\pi} + \Phi_{B\pi}$ and $\Psi^c \propto \Phi_{A\pi} - \Phi_{B\pi}$. The wavefunction Ψ^v represents the electron density concentrated between the A and B atoms, and thus is identified as the bonding π molecular orbital with the lower energy. The wavefunction Ψ^c represents the electron density concentrated at the A and B atoms, and thus is identified as the antibonding π^* molecular orbital with the higher energy. Away from the Γ point, $\mathbf{k} \neq 0$ and the Bloch wavefunctions for the A and B sublattices, $\Phi_{A\pi}(\mathbf{k}, \mathbf{r})$ and $\Phi_{B\pi}(\mathbf{k}, \mathbf{r})$, have, in general, different phase factors. Therefore, the standing wave modulation patterns shown in Fig. 2-6 (a) by solid and dashed curves represent the envelope functions given by the exponential factors in the Bloch wavefunctions $\Phi_{so}(\mathbf{k}, \mathbf{r})$ of Eq. (3.2). To obtain the actual standing wavefunctions $\Psi^b(\mathbf{k}, \mathbf{r}, t)$, these envelope functions must be multiplied by the atomic orbitals $\phi_o(\mathbf{r} - \mathbf{R}_{us})$, by Bloch amplitudes $C_{so}^b(\mathbf{k})$, and by the phase factors $\exp(-iE^b(\mathbf{k})t/\hbar)$, according to Eq. (3.2).

The valence and conduction bands of a graphene sheet touch each other at the K and K' points, as one can see in Fig. 3-5. The touching points defined by the condition $w(\mathbf{k}) = 0$ are referred to as the Fermi points, \mathbf{k}_F and \mathbf{k}'_F , respectively. The Fermi level E_F passes through the \mathbf{k}_F and \mathbf{k}'_F points, as shown by the horizontal line in Fig. 3-5 (b) lying at zero energy, since the atomic orbital energy ε is set to zero. The density of electronic states (DOS) shown in Fig. 3-5 (c) goes to zero at the Fermi level, indicating that a graphene sheet is a zero-gap semiconductor [165]. Unlike for most semiconductors, the band structure of a graphene sheet shows a linear dispersion relations around the K and K' points near the Fermi level, as one can see in Fig. 3-5. Indeed, we can write the electron wavevector around the K point in the first Brillouin zone of Fig. 2-1 (b) in the form $k_x = \Delta k_x$ and $k_y = -4\pi/(3a) + \Delta k_y$,

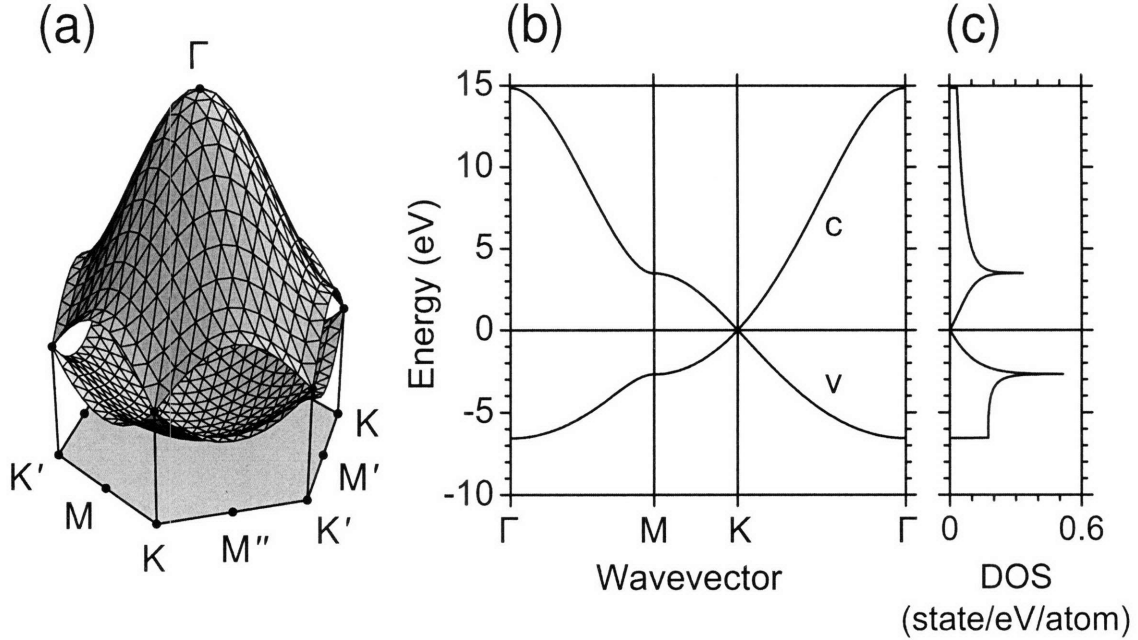


Figure 3-5: Electronic dispersion relations of a graphene sheet given by Eq. (3.10) with STB parameters $t = -3.033$ eV, $s = 0.129$, and $\varepsilon = 0$ eV (a) throughout the entire first Brillouin zone shown in Fig. 2-1 and (b) along the high-symmetry directions in the first Brillouin zone. The valence and conduction bands are labeled by v and c , respectively. (c) The density of electronic states (DOS). The Fermi level is shown by the horizontal line at zero energy.

where Δk_x and Δk_y are small compared to $1/a$. Substituting this wavevector into Eq. (3.11) and making the expansion in a power series in $\Delta k_x a$ and $\Delta k_y a$ up to the second order, we obtain $w = \frac{\sqrt{3}}{2} \Delta k a$, where $\Delta k = \sqrt{\Delta k_x^2 + \Delta k_y^2}$ is the distance from the electron wavevector to the K point. Substituting w into Eq. (3.10) yields the electronic dispersion relations in the valence and conduction bands:

$$\begin{cases} E^v(\Delta k) = \varepsilon - \frac{\sqrt{3}}{2} (\varepsilon s - t) a \Delta k, \\ E^c(\Delta k) = \varepsilon + \frac{\sqrt{3}}{2} (\varepsilon s - t) a \Delta k, \end{cases} \quad (3.14)$$

which are linear in Δk . The linear dispersion relations near the Fermi level imply that the effective mass approximation of the non-relativistic Schrödinger equation used for conventional semiconductors with parabolic energy bands is not applicable to a graphene sheet. The conducting π electrons in a graphene sheet mimic massless

particles whose behavior is governed by the relativistic Dirac equation. Note that Berry's phase of Dirac fermions is equal to π , in accordance with the above discussion of Fig. 3-4. Furthermore, the linear dispersion relations increase the mobility of the conducting π electrons in a graphene sheet compared to conventional semiconductors [69]. In contrast to the π electrons, the σ electrons are involved in covalent bonds, and therefore are not mobile. Indeed, the σ energy bands lie several eV away from the Fermi level, as obtained by solving Eq. (3.3) for the σ molecular orbitals [129].

3.3 Metallicity

As discussed in Section 3.2, a graphene sheet is a zero-gap semiconductor with the valence and conduction bands touching at the K and K' points of the first Brillouin zone. Let us consider the electron wavefunction defined by Eq. (3.2) at the K point. The electron wavevector \mathbf{k} is given by the Γ K distance in reciprocal space. The wavevector \mathbf{k} points towards the zigzag (Z) direction in a graphene sheet of Fig. 2-1 (a), and its magnitude $k = 4\pi/(3a)$ can be obtained from Fig. 2-1 (b) and Eq. (2.3). The adjacent unit cells in the Z direction of the graphene sheet are separated by distance $a/2$, as one can see in Fig. 2-1 (a). Therefore, the metallic wavefunction phase factor takes three distinct values: 0, $ka/2 = 2\pi/3$, and $ka = 4\pi/3$, at the three adjacent unit cells. We thus conclude that the metallic wavefunction is periodic over the three unit cells. The metallic wavefunction periodicity is described by the supercell of six carbon atoms, as shown in dark gray in Fig. 3-6 (a). The supercell is spanned by the vectors \mathbf{c}_1 and \mathbf{c}_2 defined as follows:

$$\begin{cases} \mathbf{c}_1 = \frac{\sqrt{3}a}{2} \hat{\mathbf{x}} + \frac{3a}{2} \hat{\mathbf{y}}, \\ \mathbf{c}_2 = \frac{\sqrt{3}a}{2} \hat{\mathbf{x}} - \frac{3a}{2} \hat{\mathbf{y}}, \end{cases} \quad (3.15)$$

similar to Eq. (2.1) for the lattice vectors \mathbf{a}_1 and \mathbf{a}_2 . These vectors are shown by arrows in Fig. 3-6 (a) along with \mathbf{a}_1 and \mathbf{a}_2 . Using the definition of Eq. (2.2), we construct the reciprocal supercell vectors \mathbf{d}_1 and \mathbf{d}_2 by analogy with the reciprocal

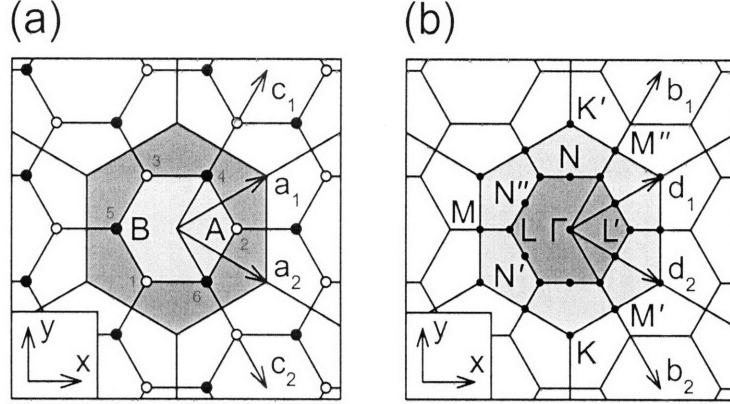


Figure 3-6: (a) A single graphene sheet. The two-atom unit cell (in light gray) and the six-atom supercell at the K point (in dark gray). The open and solid dots indicate the A and B sublattices, respectively. The lattice vectors \mathbf{a}_1 and \mathbf{a}_2 and the supercell vectors \mathbf{c}_1 and \mathbf{c}_2 are shown by arrows. (b) The reciprocal lattice of a single graphene sheet. The first Brillouin zone (in light gray) and the supercell Brillouin zone of the K point supercell (in dark gray). The dots labeled by Γ , K, K', M, M', M'', L, L', N, N', and N'' indicate the high-symmetry points. The reciprocal lattice vectors \mathbf{b}_1 and \mathbf{b}_2 and the reciprocal supercell vectors \mathbf{d}_1 and \mathbf{d}_2 are shown by arrows.

lattice vectors \mathbf{b}_1 and \mathbf{b}_2 given by Eq. (2.3):

$$\begin{cases} \mathbf{d}_1 = \frac{2\pi}{\sqrt{3}a} \hat{\mathbf{x}} + \frac{2\pi}{3a} \hat{\mathbf{y}}, \\ \mathbf{d}_2 = \frac{2\pi}{\sqrt{3}a} \hat{\mathbf{x}} - \frac{2\pi}{3a} \hat{\mathbf{y}}. \end{cases} \quad (3.16)$$

The reciprocal supercell vectors \mathbf{d}_1 and \mathbf{d}_2 form the supercell Brillouin zone of a graphene sheet shown in dark gray in Fig. 3-6 (b). The supercell Brillouin zone (the dark gray hexagon in Fig. 3-6 (b)) is obtained by cutting the first Brillouin zone (the light gray hexagon in Fig. 3-6 (b)) along six M–L lines and folding it along six L–L lines into one third of its actual size. The supercell Brillouin zone is therefore triple-folded, with both the K and K' points mapped to the Γ point. The K point metallic wavefunction thus appears at the Γ point of the supercell Brillouin zone, indicating that the supercell approach establishes the periodicity of a graphene sheet at the K point. Note the visual correspondence in Fig. 3-6 between the unit cell and the supercell Brillouin zone, as well as between the supercell and the first Brillouin zone.

This correspondence arises from the choice of the supercell vectors \mathbf{c}_1 and \mathbf{c}_2 making an angle of 120° , as discussed in Section 2.1.

When a graphene sheet is rolled into a SWNT, the SWNT becomes either metallic or semiconducting, depending on whether the metallic wavefunction of a graphene sheet is commensurate with the SWNT circumference or not, respectively [127]. For the SWNT to be metallic, its chiral vector must connect the two supercells shown in Fig. 3-6 (a) or, in other words, it must span an integer number of the supercell vectors \mathbf{c}_1 and \mathbf{c}_2 . According to Eq. (2.4), the chiral vector is defined by its projections on the lattice vectors \mathbf{a}_1 and \mathbf{a}_2 . By comparing Eq. (3.15) with Eq. (2.1), we can express \mathbf{a}_1 and \mathbf{a}_2 in terms of \mathbf{c}_1 and \mathbf{c}_2 as follows, $\mathbf{a}_1 = (2\mathbf{c}_1 + \mathbf{c}_2)/3$ and $\mathbf{a}_2 = (2\mathbf{c}_2 + \mathbf{c}_1)/3$. Substituting \mathbf{a}_1 and \mathbf{a}_2 into Eq. (2.4) yields $\mathbf{C}_h = (2n + m)\mathbf{c}_1/3 + (2m + n)\mathbf{c}_2/3$. We thus conclude that for metallic SWNTs, quantities $(2n + m)/3$ and $(2m + n)/3$ must be integers. The latter two conditions are equivalent between themselves, taking into account that $(2n + m)/3 = n + m - (2m + n)/3$. Therefore, we find that a SWNT is metallic if $\text{mod}(2n + m, 3) = 0$ and semiconducting otherwise, where $\text{mod}(i, j)$ is the remainder of the division of i by j . The latter condition implies that there are twice as many semiconducting SWNTs ($\text{mod}(2n + m, 3) = 1$ or 2) as metallic SWNTs ($\text{mod}(2n + m, 3) = 0$). Indeed, considering that the supercell is three times larger than the unit cell, only one-third of all SWNTs have an integer number of supercells around their circumference, thus being commensurate with the metallic wavefunction of a graphene sheet.

The classification of SWNTs by their metallicity can also be obtained by considering the cutting lines defined by Eq. (2.14) in the reciprocal space of a graphene sheet. The SWNT can be either metallic or semiconducting, depending on whether one of the cutting lines crosses the K point or not, respectively [50, 131]. Considering the cutting lines in the helical-helical representation shown in Fig. 2-7, we can evaluate the projection of the $\Gamma\mathbf{K}$ vector pointing towards the K point on the \mathbf{K}_1 direction normal to the cutting lines. Choosing the right top corner of the dark gray hexagon in Fig. 2-7 gives $\Gamma\mathbf{K} = (2\mathbf{b}_1 + \mathbf{b}_2)/3$. Using the expression for \mathbf{K}_1 given in Table 2.1, we then find the projection $(\Gamma\mathbf{K} \cdot \mathbf{K}_1)/(\mathbf{K}_1 \cdot \mathbf{K}_1) = (2n + m)/3$. If $(2n + m)/3$ is an

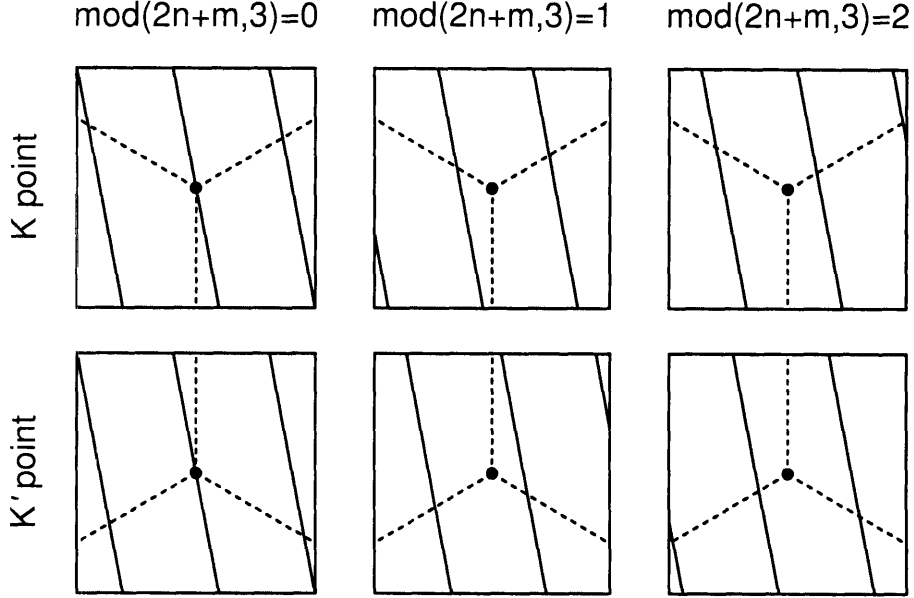


Figure 3-7: Three possible configurations of the cutting lines in the vicinity of the K and K' points depending on the value of $\text{mod}(2n + m, 3)$. The solid lines represent the cutting lines, the solid dots show the K and K' points, and the dashed lines indicate the KM directions which are the boundaries of the first Brillouin zone.

integer, $\Gamma\mathbf{K}$ has an integer number of \mathbf{K}_1 components, so that one of the cutting lines crosses the K point, and the SWNT turns out to be metallic. If $(2n + m)/3$ is a fractional number, namely $1/3$ or $2/3$, none of the cutting lines crosses the K point and the SWNT becomes semiconducting. Thus, a SWNT is metallic if $\text{mod}(2n + m, 3) = 0$ and semiconducting if $\text{mod}(2n + m, 3) = 1$ or 2 , in agreement with the results of the previous paragraph. These three types of SWNTs are referred to as M0, S1, and S2, respectively. Different configurations of the cutting lines in the vicinity of the K and K' points, depending on the value of $\text{mod}(2n + m, 3)$, are shown in Fig. 3-7.

The chiral vector \mathbf{C}_h forms different patterns for M0, S1, and S2 SWNTs in the rightmost gray sector in Fig. 2-2. We redraw this sector in Fig. 3-8 where the hexagons to which the chiral vectors for M0, S1, and S2 SWNTs point are shaded in white, light gray, and dark gray, respectively. The hexagons of each color form a triangular sublattice in the graphene sheet, as one can see in Fig. 3-8. Within each triangular sublattice, the adjacent hexagons are connected by the lines of constant

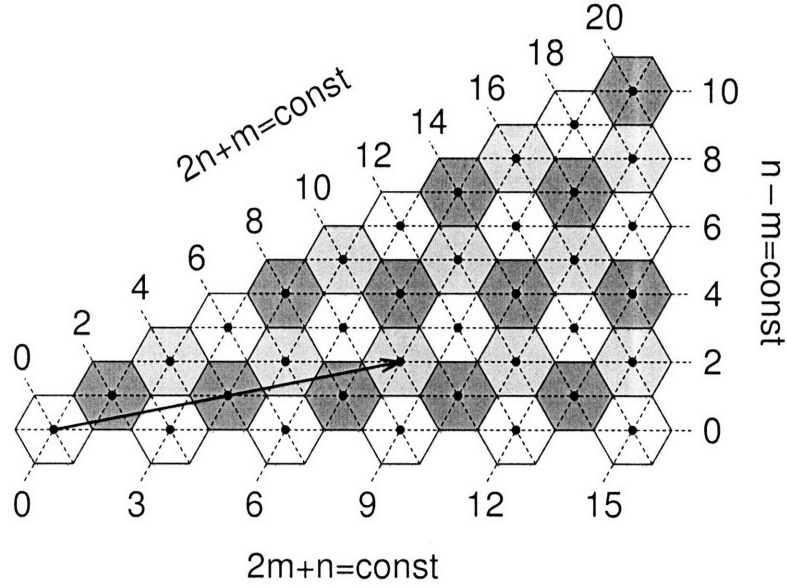


Figure 3-8: The 30° -sector in a graphene sheet identical to the rightmost gray sector in Fig. 2-2 where the chiral vector is defined. The solid dots indicate the centers of the hexagons to which the chiral vectors point. The white, light gray, and dark gray hexagons correspond to the chiral vectors of M0, S1, and S2 SWNTs, respectively. The dashed lines represent the families of constant $2n + m$, $n - m$, and $2m + n$. The numbers give the values of constant $2n + m$, $n - m$, and $2m + n$ for each family. The chiral vector of a (4, 2) SWNT is shown by an arrow.

$2n + m$, $n - m$, and $2m + n$ in three different directions, as shown by the dashed lines in Fig. 3-8. These lines are called the family lines, and all M0, S1, or S2 SWNTs along the same dashed line in Fig. 3-8 are said to belong to the same family. Each family line in Fig. 3-8 is labeled by a number that indicates the value of constant $2n + m$, $n - m$, or $2m + n$. As an example, the chiral vector of a (4, 2) SWNT is shown by an arrow in Fig. 3-8. The arrow points to a light gray hexagon that belongs to families $2n + m = 10$, $n - m = 2$, and $2m + n = 8$, as one can see in Fig. 3-8. The light gray color of the hexagon implies that the (4, 2) SWNT is of S1 type, since $\text{mod}(2n + m, 3) = \text{mod}(10, 3) = 1$. Note, however, that for the same (4, 2) SWNT, $\text{mod}(n - m, 3) = \text{mod}(2, 3) = 2$ and $\text{mod}(2m + n, 3) = \text{mod}(8, 3) = 2$. The definition of S1 and S2 types thus depends on the choice of the family lines, $2n + m$, $n - m$, or $2m + n$. For a general semiconducting (n, m) SWNTs, the value of $\text{mod}(2n + m, 3)$ is always opposite to the values of $\text{mod}(n - m, 3)$ and $\text{mod}(2m + n, 3)$, where the

latter two are equivalent between themselves. This can be seen in Fig. 3-8, and it also follows from the aforementioned relation $(2n + m)/3 = n + m - (2m + n)/3$ taking into account that $(n - m)/3 = (2n + m)/3 - (2m + n)/3$. Furthermore, S1 and S2 types switch when going to SWNTs of the opposite handedness defined in the rightmost white sector in Fig. 2-2. Indeed, by hypothetically drawing this sector in Fig. 3-8, we find that the two semiconducting SWNTs of the same (n, m) indices but opposite handedness correspond to the two hexagons of different shades of gray in the two sectors in Fig. 3-8. In what follows, we stick with the definition of S1 and S2 types according to the values of $\text{mod}(2n + m, 3)$ within the sector shown in Fig. 3-8. Our choice is based on the fact that the $2n + m$ family lines group together M0, S1, and S2 SWNTs of the closest diameters, compared to the $n - m$ and $2m + n$ family lines. This can be seen in Fig. 3-8, taking into account that the diameter is proportional to the magnitude of the chiral vector, and the latter is measured from the leftmost hexagon in Fig. 3-8 labeled by the zero family numbers.

The M0/S1/S2 classification of SWNTs can be further developed [136]. In Section 2.3, we classified SWNTs according to whether $d_R = 3d$ or $d_R = d$, and we showed that $d_R = 3d$ if $\text{mod}(n - m, 3d) = 0$ and $d_R = d$ otherwise. Since $\text{mod}(n - m, 3d) = 0$ implies $\text{mod}(n - m, 3) = 0$, we conclude that for M0 SWNTs either one of the two conditions, $d_R = 3d$ or $d_R = d$, can be satisfied, while for S1 and S2 SWNTs the condition $d_R = d$ is always maintained. Thus, M0 SWNTs divide into M1 and M2 subtypes for which $d_R = d$ and $d_R = 3d$, respectively [136]. Furthermore, M1 SWNTs can be classified as M1+ and M1- depending upon $\text{mod}((2n + m)/d, 3) = 1$ or 2 , respectively [136]. Similarly, M2 SWNTs can be either M2+ or M2- according to whether $\text{mod}(3m/d_R, 3) = 1$ or 2 [136]. Finally, SWNTs of S1 (S2) type divide into S1+ and S1- (S2+ and S2-) subtypes for which $\text{mod}(N, 3) = 1$ and 2 , correspondingly [136]. We, however, do not go into details of these classifications. While SWNTs of M0, S1, and S2 types have shown distinct optical properties in various spectroscopic measurements, there was no experimental evidence of any difference between M1 and M2, M1+ and M1-, M2+ and M2-, S1+ and S1-, or S2+ and S2- subtypes of SWNTs. We therefore stick with the M0/S1/S2 classification.

3.4 Density of electronic states

As we showed above in Section 3.3, SWNTs become metallic if one of the cutting lines defined by Eq. (2.14) crosses the K point. The electronic dispersion relations around the K point of a graphene sheet can be approximated by a linear function of the electron wavevector measured from the K point, according to Eq. (3.14). We plot these linear dispersion relations in the vicinity of the K point in Fig. 3-9 (a), where the lower and upper cones represent the valence and conduction bands, respectively. The solid lines superimposed on the dispersion relations in Fig. 3-9 (a) are the cutting lines for a metallic (15, 0) SWNT. Following the zone-folding technique, the energy dispersion along the cutting lines is projected into the 1D Brillouin zone of the (15, 0) SWNT. The resulting 1D dispersion relations are shown in Fig. 3-9 (b). The horizontal axis of Fig. 3-9 (b) represents the 1D wavevector k of the (15, 0) SWNT, or the 2D wavevector \mathbf{k} of the graphene sheet along the cutting lines in Fig. 3-9 (a), according to Eq. (2.14). The 1D wavevector changes in the range $-\pi/T < k \leq \pi/T$, where $T = \sqrt{3}a$ is the translational length of the (15, 0) SWNT, according to Table 2.1. Each cutting line in Fig. 3-9 (a) generates an energy subband in Fig. 3-9 (b). These energy subbands are labeled by band index $b = v, c$ and by subband number i progressively increasing away from the Fermi level $E_F = 0$ eV shown by the horizontal line in Fig. 3-9 (b). The density of electronic states (DOS) of the (15, 0) SWNT derived from the dispersion relations of Fig. 3-9 (b) is shown in Fig. 3-9 (c).

Since one of the cutting lines in Fig. 3-9 (a) goes through the K point, the corresponding $i = 0$ valence and conduction subbands in Fig. 3-9 (b) touch at the 1D Fermi point $k_F = 0$ making the (15, 0) SWNT metallic. These subbands exhibit linear dispersion around the Fermi level $E_F = 0$ eV resembling that of a graphene sheet from Fig. 3-5 (b). Nevertheless, the DOSs of the (15, 0) SWNT and of the graphene sheet show quite different behavior near E_F . The DOS of the graphene sheet vanishes at E_F , as shown in Fig. 3-5 (c), thus making the graphene sheet a zero-gap semiconductor, as discussed in Section 3.2. In contrast, the (15, 0) SWNT has a finite DOS at E_F , as one can see in Fig. 3-9 (c). The finite DOS at E_F arises from the 1D nature of the

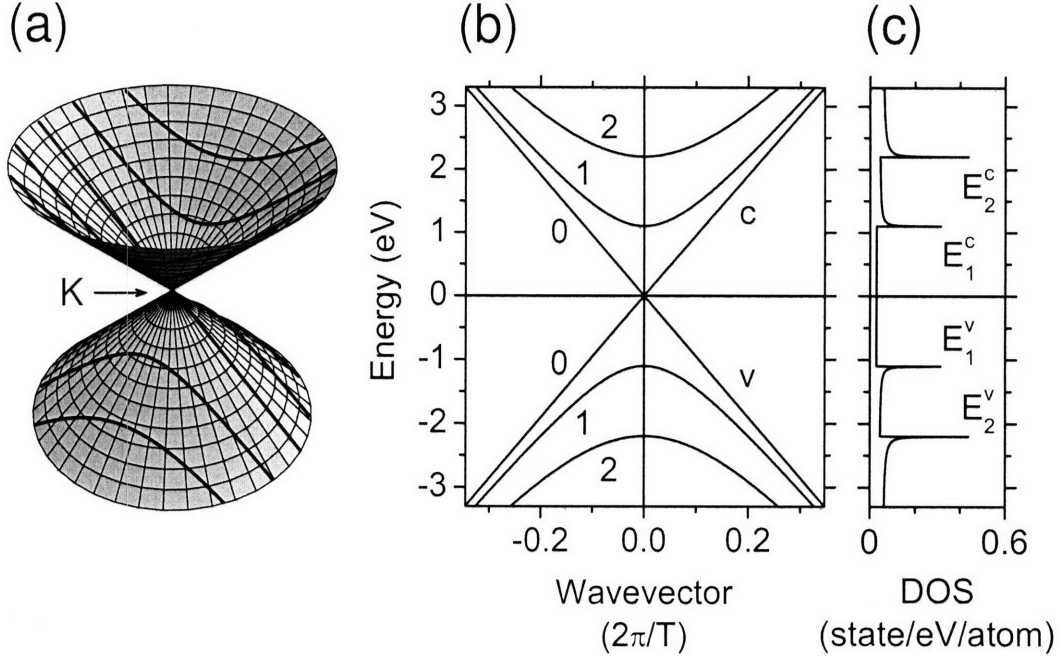


Figure 3-9: (a) The electronic dispersion relations of a graphene sheet around the K point, as approximated by Eq. (3.14). The lower and upper cones represent the valence and conduction bands, respectively. The solid lines are the cutting lines for a metallic (15, 0) SWNT. (b) The electronic dispersion relations of the (15, 0) SWNT when different cutting lines are folded together into the 1D Brillouin zone. The length of the 1D Brillouin zone is $2\pi/T$. The energy subbands are labeled by band index $b = v, c$ and by subband number i progressively increasing away from the Fermi level $E_F = 0$ eV shown by the horizontal line. The vertical line denotes the Fermi point $k_F = 0$ and the critical wavevectors $k_i^b = 0$. (c) The density of electronic states (DOS) of the (15, 0) SWNT. A finite DOS at E_F indicates that the SWNT is metallic. The sharp spikes in the DOS typical for 1D systems are known as Van Hove singularities (VHSs). The VHSs associated with different subband edges are labeled by E_i^b .

SWNT. As a result, the (15, 0) SWNT is a true metal, unlike the graphite sheet, and so are all other M0 SWNTs. In fact, however, the curvature of the SWNT sidewall breaks the nearest-neighbor bond symmetry of a graphene sheet, changing the phase factors in $f(\mathbf{k})$ of Eq. (3.8) and correspondingly shifting the 2D Fermi points, \mathbf{k}_F and \mathbf{k}'_F , away from the K and K' points [75]. This shift opens a mini band gap at the Fermi level in M0 SWNTs [75]. The width of the mini band gap is given by:

$$E_g = \frac{(\varepsilon s - t) a^2 \cos 3\theta}{4d_i^2}. \quad (3.17)$$

For the (15,0) SWNT, the mini band gap width $E_g = 33 \text{ meV}$ is comparable to the thermal energy $k_B T = 26 \text{ meV}$ at room temperature $T = 300 \text{ K}$, where $k_B = 0.086173 \text{ meV/K}$ is the Boltzmann constant. The mini band gap width scales inversely with the square of the diameter, which is a measure of the curvature-induced bond asymmetry in the SWNTs sidewall. The mini band gap width also depends on the chiral angle θ , vanishing for armchair SWNTs and reaching its maximum value for zigzag SWNTs, in which cases \mathbf{k}_F and \mathbf{k}'_F move parallel and perpendicular to the cutting lines, respectively [75]. This result agrees with the group theory prediction that the linear energy bands in armchair SWNTs have different symmetry and therefore are not split by the curvature of the SWNT sidewall [12]. We thus conclude that among M0 SWNTs, only armchair SWNTs are truly metallic, while the other M0 SWNTs have mini band gaps of width about the thermal energy at room temperature. Since the concept of zone-folding excludes the curvature of the SWNT sidewall, the zone-folding technique fails to predict the mini band gap opening for the (15,0) SWNT, as one can see in Fig. 3-9 (c). The curvature effects and the limitations of zone-folding will be considered in more detail in Section 3.6.

While the $i = 0$ subbands in Fig. 3-9 (b) demonstrate a linear dependence on the 1D wavevector k , the dispersion relations for the $i = 1$ and 2 subbands show a hyperbolic behavior:

$$E_i^b(k) = \varepsilon \mp \frac{\sqrt{3}}{2} (\varepsilon s - t) a \sqrt{\left(\frac{2i}{d_t}\right)^2 + k^2}, \quad (3.18)$$

as obtained by superimposing the cutting lines of Eq. (2.14) on the linear dispersion relations of a graphene sheet given by Eq. (3.14) and taking into account the separation between the adjacent cutting lines expressed by the reciprocal lattice vector \mathbf{K}_1 listed in Table 2.1. The hyperbolic dispersion relations present some flat regions in Fig. 3-9 (b) close to the subband edges:

$$E_i^b = \varepsilon \mp i\sqrt{3} (\varepsilon s - t) \frac{a}{d_t}, \quad (3.19)$$

at the critical angular and linear momenta, μ_i^b and k_i^b , where $k_i^b = 0$ in Fig. 3-9 (b).

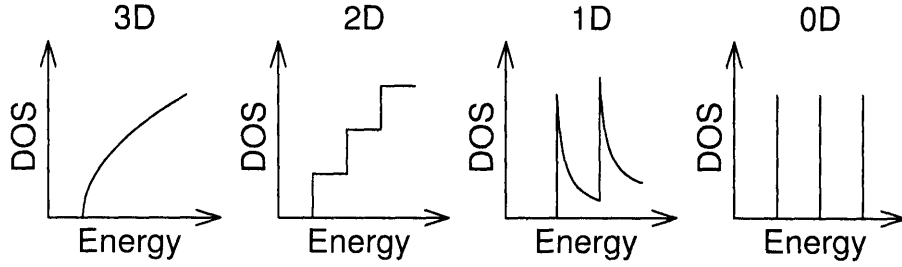


Figure 3-10: The density of electronic states (DOS) of typical 3D, 2D, 1D, and 0D systems. The DOSs of 3D and 2D systems are both monotonously increasing functions of energy. The DOSs of 1D and 0D systems both exhibit singularities at certain values of energy.

The flat dispersion regions give rise to the spikes in the density of electronic states, as one can see in Fig. 3-9 (c), where each spike is labeled with the corresponding subband edge E_i^b . These spikes are known as Van Hove singularities (VHSs).

The Van Hove singularities (VHSs) typically dominate the density of electronic states (DOS) of one-dimensional (1D) systems. The DOS profiles for systems of different dimensionality are usually very different from one another, as one can see in Fig. 3-10. Given the parabolic dispersion relations, the DOS dependence on energy is governed by $g(E) \propto (E - E_0)^{d/2-1}$, where d is an integer that denotes the dimensionality, assuming the values 1, 2, and 3 for 1D, 2D, and 3D systems, respectively. Here E_0 can be considered as a critical energy in the DOS. For a 3D system, E_0 might correspond to an energy threshold for the onset of optical transitions, or to a band edge state in a semiconductor. For a 2D system, E_0 would correspond to the energy at which a new subband or a quantum confinement level is formed. For a 1D system, E_0 is equal to the subband edge energy E_i^b given by Eq. (3.19), where the magnitude of the DOS becomes very large. One can see from Fig. 3-10 that 1D systems exhibit DOS profiles which are quite similar to the case of 0D systems, having very sharp maxima at certain energies, in contrast to the DOS profiles for 2D and 3D systems, which show a more monotonic increase with energy. However, the 1D DOS is different from the 0D DOS in that the 1D DOS has a sharp threshold and a decaying tail, so that the 1D DOS does not go to zero between the sharp maxima, as the 0D DOS does (see Fig. 3-10). Also, the values of the DOS at the peak positions

are generally much higher for 1D objects (nanotubes and nanowires) than for 0D objects (molecules and quantum dots), because of much larger number of atoms in 1D objects. The extremely high values of the DOS at the VHSs allow the observation of the resonance Raman spectra from individual SWNTs grown by chemical vapor deposition (CVD) on a Si/SiO₂ substrate, where the Raman bands of the SWNT and those of Si have comparable intensities, even though the ratio of the number of carbon atoms to the number of silicon atoms in the laser spot is as low as 10⁻⁶ [65]. The VHSs along with the mini band gaps in the DOS of individual metallic SWNTs on an Au substrate are observed by scanning tunneling spectroscopy [107].

The critical wavevectors k_i^b at which the VHSs E_i^b are observed appear at the center of the 1D Brillouin zone of the (15,0) SWNT, $k_i^b = 0$, as one can see in Fig. 3-9 (b). The Fermi point k_F that can be considered as a critical wavevector k_0^v or k_0^c also appears at the zone center, $k_F = 0$. A question arises, whether the same conditions $k_i^b = 0$ and $k_F = 0$ are maintained for a general (n, m) SWNT. Assuming the isotropic dispersion relations around the K point, as approximated by Eq. (3.14) and plotted in Fig. 3-9, we need to evaluate the projection of the $\Gamma\mathbf{K}$ vector pointing towards the K point in the \mathbf{K}_2 direction parallel to the cutting lines, according to Eq. (2.14). Choosing the right top corner of the dark gray hexagon in Fig. 2-7 gives $\Gamma\mathbf{K} = (2\mathbf{b}_1 + \mathbf{b}_2)/3$. Using the expression for \mathbf{K}_2 given in Table 2.1, we then find the projection $(\Gamma\mathbf{K} \cdot \mathbf{K}_2)/(\mathbf{K}_2 \cdot \mathbf{K}_2) = m/d_R$. Since $d_R = d$ in the case of M1, S1, and S2 SWNTs, the ratio m/d_R is an integer, and therefore the critical wavevectors k_i^b and the Fermi point k_F appear at the center of the 1D Brillouin zone, $k_i^b = 0$ and $k_F = 0$. For M2 SWNTs, however, $d_R = 3d$, which implies $\text{mod}(m, d_R) = 1$ or 2. The critical wavevectors k_i^b and the Fermi point k_F thus appear at two-third of the distance from the center Γ to the edge X of the 1D Brillouin zone, $\pm K_2/3$, which is related to the shortening of the translational length T by a factor of 3, as explained in Section 2.3. Due to time-reversal symmetry, each VHS E_i^b is doubly degenerate, with two critical wavevectors k_i^b and $k_i^{b'}$ near the K and K' points in the 2D Brillouin zone of a graphene sheet, and the same is true for the Fermi points, k_F and k_F' . It follows that $k_i^b = k_F = +K_2/3$ and $k_i^{b'} = k_F' = -K_2/3$ for M2+ SWNTs,

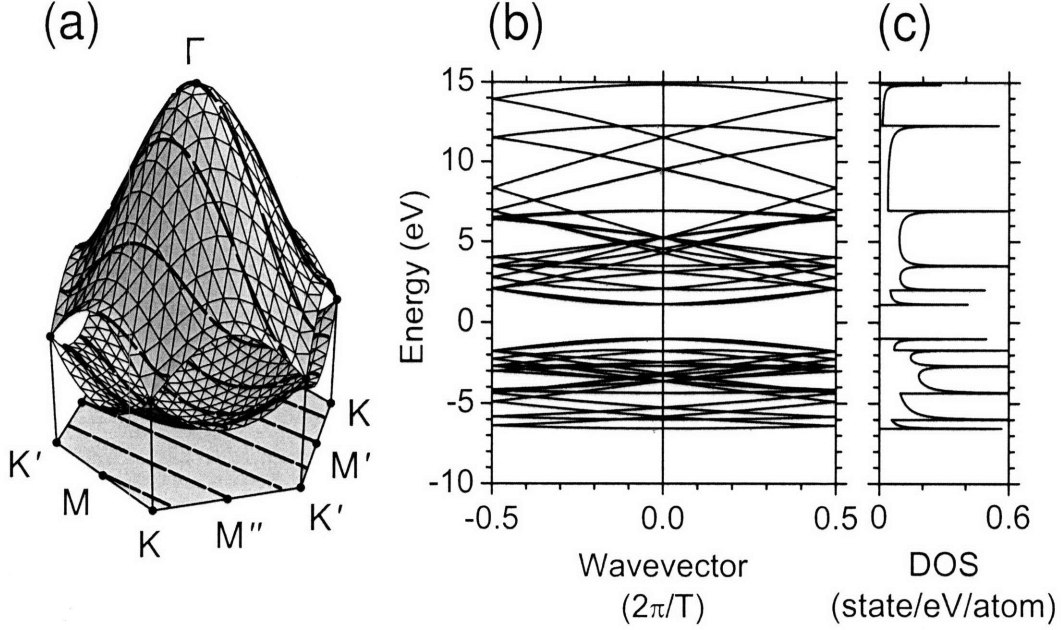


Figure 3-11: (a) The electronic dispersion relations of a graphene sheet within the STB model replicated from Fig. 3-5. The solid lines are the cutting lines for a semiconducting (4, 2) SWNT in the helical-helical representation. (b) The electronic dispersion relations of the (4, 2) SWNT when different cutting lines are folded together into the 1D Brillouin zone. The length of the 1D Brillouin zone is given by $2\pi/T$. (c) The density of electronic states (DOS) of the (4, 2) SWNT. Vanishing DOS at the Fermi level $E_F = 0$ eV indicates that the SWNT is semiconducting. The sharp spikes in the DOS typical for 1D systems are known as Van Hove singularities.

while $k_i^b = k_F = -K_2/3$ and $k_i^{b'} = k'_F = +K_2/3$ for M2- SWNTs [136]. On the other hand, the critical wavevectors for S1 and S2 SWNTs, as well as the Fermi points for M1 SWNTs, are doubly degenerate, $k_i^b = k_i^{b'} = 0$ and $k_F = k'_F = 0$, given the isotropic dispersion relations around the K and K' points. In a similar fashion, the expressions for the critical angular momenta μ_i^b and $\mu_i^{b'}$ can be derived for different types of SWNTs [136].

The degeneracy of the critical wavevectors, k_i^b and $k_i^{b'}$, only holds for achiral SWNTs due to the presence of a horizontal mirror plane [12]. For chiral SWNTs, the anisotropy of the electronic dispersion relations around the K point of a graphene sheet lifts the degeneracy, $k_i^b = -k_i^{b'} \neq 0$. The anisotropy also shifts the critical points for M2 SWNTs, $k_i^b = -k_i^{b'} \neq \pm K_2/3$. While the anisotropy is neglected under the linear approximation of Eq. (3.14), it appears within the exact STB solution given

by Eq. (3.10). In Fig. 3-11 (a), we replicate the STB electronic dispersion relations of a graphene sheet shown in Fig. 3-5 (a), and we superimpose the cutting lines defined by Eq. (2.14) in the helical-helical representation for the (4, 2) SWNT over the dispersion surface, similar to Fig. 3-9 (a). We then construct the 1D dispersion relations and the DOS of the (4, 2) SWNT in Figs. 3-11 (b) and (c), respectively, by analogy with Figs. 3-9 (b) and (c). The critical wavevectors k_i^b corresponding to the subband extrema in Fig. 3-11 (b) are slightly shifted from the center Γ of the 1D Brillouin zone, $k_i^b \neq 0$. The shift of the critical wavevectors is induced by the anisotropy of the electronic dispersion relations around the K point of a graphene sheet. This anisotropy is in fact naturally embedded into the STB model, and it is known as the trigonal warping effect [130]. We will discuss the trigonal warping effect in more detail in Section 3.5. Also, one can see in Figs. 3-11 (b) and (c) that a band gap opens up at the Fermi level $E_F = 0$ eV of the (4, 2) SWNT. Indeed, the (4, 2) SWNT is a semiconductor of S2 type, according to the definitions in Section 3.3. The width of the band gap E_g can be estimated similar to Eq. (3.19) from the linear approximation of Eq. (3.14) shown in Fig. 3-9. A more accurate estimate of E_g implementing the trigonal warping effect is obtained from the exact STB solution of Eq. (3.10) shown in Fig. 3-11. The latter, however, ignores the curvature of the SWNT sidewall. The curvature shifts the subband edges E_i^b and the critical wavevectors k_i^b (and the Fermi points k_F for M2 SWNTs) even further than the trigonal warping effect does, especially in small diameter SWNTs such as (4, 2). We will consider the curvature effects in more detail in Section 3.6.

3.5 Trigonal Warping Effect

The presence of VHSs in the DOS of SWNTs has a great impact on their physical properties, such as optical absorption, transport dynamics, thermal conductivity, etc. Generally speaking, a significant enhancement in the SWNT response is observed when the excitation energy for the probe matches one of the VHSs in the DOS in the valence and conduction bands of the SWNT. For example, optical absorption is

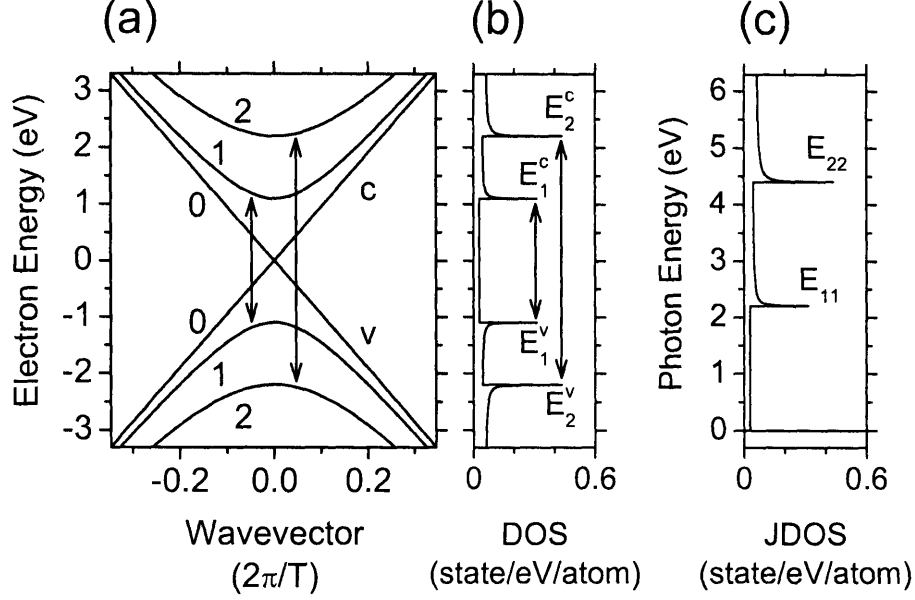


Figure 3-12: (a) The electronic dispersion relations and (b) the density of electronic states (DOS) of the (15, 0) SWNT replicated from Figs. 3-9 (b) and (c). The vertical arrows show the allowed optical transitions between the first and second valence and conduction subbands. (c) The joint density of electronic states (JDOS) of the (15, 0) SWNT. The VHS labeled by E_{11} (E_{22}) corresponds to the transition between E_1^v and E_1^c (E_2^v and E_2^c) shown by an arrow in (b).

strongly enhanced when the photon energy is in resonance with the allowed transition between two VHSs in the valence and conduction bands. This enhancement is generally interpreted in terms of the joint density of electronic states (JDOS) which takes into account the dipole selection rules. The dipole selection rules can be derived from the optical dipole transition matrix elements using the zone-folding technique expressed by Eq. (2.14) [2, 48, 133], or from group theory [12, 14], as discussed in Section 5.1.1. The slope of the electronic dispersion relations in the graphene sheet is given by $\pm \frac{\sqrt{3}}{2} (\epsilon s - t) a$ according to Eq. (3.14), while the slope of the photon dispersion relations is equal to $\hbar c$, where \hbar is Planck's constant and c is the speed of light. Taking into account that $\sqrt{3} (\epsilon s - t) a \ll \hbar c$ suggests that $|\boldsymbol{\kappa}| \ll |\mathbf{k}^v - \Gamma\mathbf{K}|$ and $|\boldsymbol{\kappa}| \ll |\mathbf{k}^c - \Gamma\mathbf{K}|$, where $\boldsymbol{\kappa}$ is the photon wavevector and \mathbf{k}^v and \mathbf{k}^c are the electron wavevectors in the valence and conduction bands. The momentum conservation $\mathbf{k}^v - \mathbf{k}^c = \pm \boldsymbol{\kappa}$ for light absorption and emission then implies $\mathbf{k}^v = \mathbf{k}^c$, or in other

words, the optical transitions in the graphene sheet are vertical. Upon substituting the relation $\mathbf{k}^v = \mathbf{k}^c$ into Eq. (2.14), we express the dipole selection rules in SWNTs in the form $\mu^v = \mu^c$ and $k^v = k^c$ within the zone-folding approximation. The optical transitions thus conserve both angular and linear momenta in SWNTs. For illustrative purposes, we replicate in Fig. 3-12, the electronic dispersion relations and the DOS of the (15,0) SWNT from Fig. 3-9. The allowed optical transitions are shown in Figs. 3-12 (a) and (b) by the vertical arrows (conservation of the linear momentum k) connecting the mirror subbands (conservation of the angular momentum μ). In Fig. 3-12 (c), we show the density of allowed optical transitions as a function of the photon energy (the length of the vertical arrows in Figs. 3-12 (a) and (b)), which is known as the joint density of electronic states (JDOS). The VHSs in the JDOS labeled by E_{ii} ($i = 1, 2$) in Fig. 3-12 (c) correspond to transitions between the mirror valence E_i^v and conduction E_i^c VHSs in the DOS shown by the vertical arrows in Fig. 3-12 (b), implying that $E_{ii} = E_i^c - E_i^v$.

The optical response of SWNTs is thus dominated by the VHSs in the JDOS labeled by E_{ii} . The optical transition energies E_{ii} for $i = 1, 2, 3, \dots$ and for all the possible (n, m) SWNTs are summarized in the Kataura plot [71] as a function of the SWNT diameter d_t . The Kataura plot is a useful tool for analyzing Raman spectra of SWNTs, since the frequency of the Raman-active radial-breathing phonon mode ω^{RBM} is inversely proportional to d_t , as will be shown in Chapter 4. In Fig. 3-13 (a), we show the Kataura plot calculated within the STB model of Section 3.2. The same STB Kataura plot is shown in Fig. 3-13 (b) as a function of the inverse SWNT diameter $1/d_t$, which is more convenient for direct comparison with experiments, since $1/d_t$ is proportional to ω^{RBM} . Furthermore, the $1/d_t$ scale allows us to explore the small d_t region ($d_t < 1.2$ nm), which has a lower density of (n, m) indices and the more pronounced 1D character. As one can see from Fig. 3-13, the E_{ii} energies for M0, S1, and S2 SWNTs show distinct behavior, while there is no obvious difference between M1 and M2 subtypes of M0 type, and neither between the other subtypes discussed in Section 3.3. Within the M0, S1, and S2 types, the E_{ii} energies that belong to the families of constant $2n + m$ group together in the Kataura plot. Indeed, as we recall

from Section 3.3, the members of the families of constant $2n + m$ have the closest diameters compared to the members of the families of constant $n - m$ or constant $2m + n$. The E_{ii} energies within each family of constant $2n + m$ are connected by gray lines labeled by $2n + m$ values in Fig. 3-13.

Within the isotropic dispersion relations of Eq. (3.14), the VHSs in the DOS for M SWNTs are given by Eq. (3.19). A similar expression can be derived for S SWNTs, where i is substituted with $[i/2 + \text{mod}(i, 2)/6 - 1/3]$, taking into account that the K point appears at the $1/3$ or $2/3$ distance between the cutting lines, as shown in Fig. 3-7. This suggests that the E_{ii} energies for M and S SWNTs are given by:

$$\begin{cases} E_{ii}^{\text{M}} = \frac{\sqrt{3}(\varepsilon s - t)a}{d_t} [2i], \\ E_{ii}^{\text{S}} = \frac{\sqrt{3}(\varepsilon s - t)a}{d_t} [i + \text{mod}(i, 2)/3 - 2/3]. \end{cases} \quad (3.20)$$

Indeed, the E_{ii} energies group into bands labeled by E_{11}^{S} , E_{22}^{S} , and E_{11}^{M} in Fig. 3-13. These bands exhibit a hyperbolic dependence on d_t and a linear dependence on $1/d_t$ in Figs. 3-13 (a) and (b), respectively, in accordance with Eq. (3.20). However, in the small d_t region of the Kataura plot in Fig. 3-13, the E_{ii} energies deviate from the simple hyperbolic (linear) dependence given by Eq. (3.20). This is a manifestation of the trigonal warping effect [130], which introduces anisotropy in the electronic dispersion relations around the K point, omitted in the linear approximation of Eq. (3.14).

When deriving Eq. (3.14), we expressed the electron wavevector near the K point in the graphene sheet as $\mathbf{k} = (k_x, k_y) = (\Delta k_x, -4\pi/(3a) + \Delta k_y)$. Making the expansion of Eq. (3.11) in a power series in $a\Delta k_x$ and $a\Delta k_y$ up to the second order, we obtained $w = \sqrt{3}a\Delta k/2$, where $\Delta k = \sqrt{\Delta k_x^2 + \Delta k_y^2}$ is the electron wavevector measured from the K point. Now we expand Eq. (3.11) up to the third order:

$$w = \frac{\sqrt{3}}{2} a\Delta k + \frac{1}{8} a^2 \frac{\Delta k_y^3 - 3\Delta k_x \Delta k_y^2}{\Delta k}. \quad (3.21)$$

Referring to the angle between the wavevector $(\Delta k_x, \Delta k_y)$ and the direction $\text{K}\Gamma$ as φ , we express Δk_x and Δk_y in the form $\Delta k_x = \Delta k \sin \varphi$ and $\Delta k_y = \Delta k \cos \varphi$. Sub-

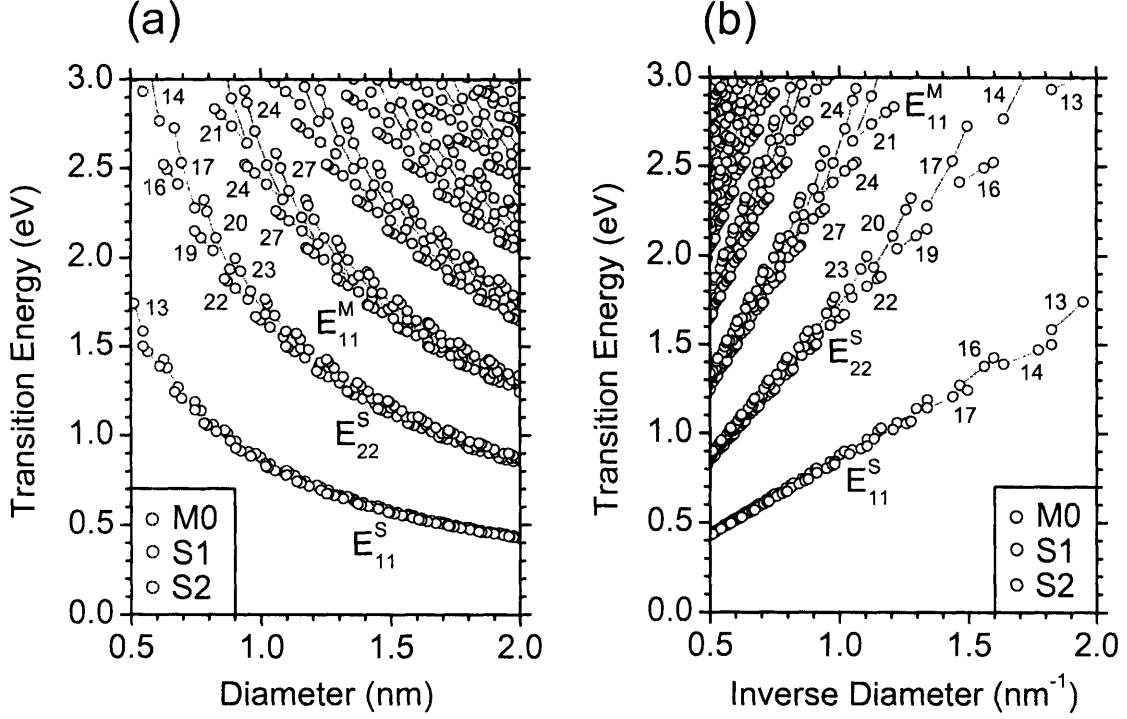


Figure 3-13: The optical transition energies E_{ii} for $i = 1, 2, 3, \dots$ and for all possible (n, m) SWNTs calculated within the STB model of Section 3.2 as a function of (a) the SWNT diameter d_t and (b) the inverse diameter $1/d_t$, known as the Kataura plot. The red, green, and blue dots correspond to M0, S1, and S2 SWNTs, respectively. The bands of E_{ii} for M and S SWNTs are labeled by E_{ii}^M and E_{ii}^S , accordingly. The families of constant $2n+m$ are connected by gray lines and labeled by $2n+m$ values.

stituting Δk_x and Δk_y into Eq. (3.21) yields

$$w = \frac{\sqrt{3}}{2} a \Delta k + \frac{1}{8} \cos 3\varphi a^2 \Delta k^2, \quad (3.22)$$

taking into account that $\cos 3\varphi = \cos^3\varphi - 3\sin^2\varphi \cos\varphi$. Substituting Eq. (3.22) into Eq. (3.10) yields the electronic dispersion relations of the graphene sheet:

$$\begin{cases} E^v(\Delta k, \varphi) = \varepsilon - \frac{\sqrt{3}}{2} (\varepsilon s - t) a \Delta k - \frac{1}{8} (\varepsilon s - t) \cos 3\varphi a^2 \Delta k^2 - \frac{3}{4} s t a^2 \Delta k^2, \\ E^c(\Delta k, \varphi) = \varepsilon + \frac{\sqrt{3}}{2} (\varepsilon s - t) a \Delta k + \frac{1}{8} (\varepsilon s - t) \cos 3\varphi a^2 \Delta k^2 - \frac{3}{4} s t a^2 \Delta k^2. \end{cases} \quad (3.23)$$

Eq. (3.23) describes the distortion of the isotropic electronic dispersion relations of

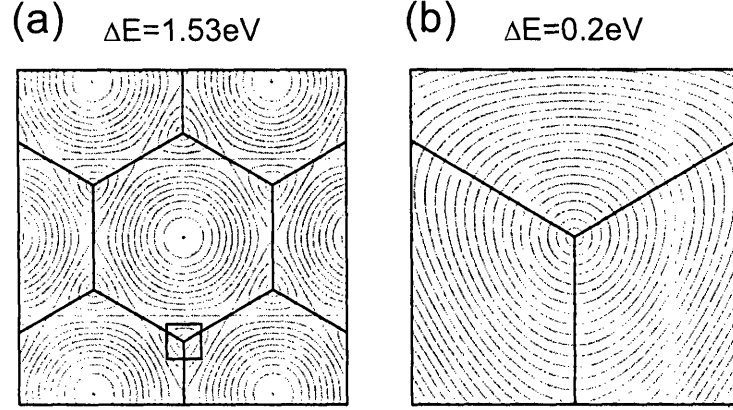


Figure 3-14: (a) The contours of constant transition energy $E^c - E^v$ in the first Brillouin zone of the graphene sheet shown in Fig. 2-1 calculated within the STB model described in Section 3.2. The square box indicates the area of linear dimensions $K\Gamma/3 = 4\pi/(9a)$ centered at the K point. (b) A zoom in of area within the square box in (a). The transition energy difference between the adjacent contours $\Delta E = 1.53$ eV and $\Delta E = 0.2$ eV are shown above the figures.

Eq. (3.14), referred to as the trigonal warping effect [130]. This distortion has a triangular symmetry around the K point in the reciprocal space of the graphene sheet, because of the factor $\cos 3\varphi$ in Eq. (3.23). The triangular distortion is clearly seen in Fig. 3-14 where we plot the electronic equi-energy contours around the K point in the reciprocal space of the graphene sheet calculated within the STB model.

The critical angular and linear momenta, μ_i^b and k_i^b , introduced in Section 3.4 after Eq. (3.19) for M SWNTs, correspond to the critical wavevector in the reciprocal space of the graphene sheet, $\mathbf{k}_i = (\pm 2i \sin \theta/d_t, -4\pi/(3a) \pm 2i \cos \theta/d_t)$, where θ is the chiral angle, according to Eq. (2.14). A similar expression can be obtained for S SWNTs, where i is substituted with $[i + \text{mod}(i, 2)/3 - 2/3]$, as follows from Eq. (3.20) and discussion therein. The trigonal warping effect shifts the critical linear momenta k_i^b along the cutting lines away from the 0 and $\pm K_2/3$ points, as discussed in Section 3.4, thus affecting \mathbf{k}_i . However, the changes to \mathbf{k}_i are quadratic in $1/d_t$, that yield the cubic in Δk corrections in the band energy of Eq. (3.23). These corrections can therefore be neglected. Substituting $\Delta k = 2i/d_t$ and $\varphi = \theta$ or $\theta + \pi$ into Eq. (3.23)

yields the transition energies for M and S SWNTs:

$$\left\{ \begin{array}{l} E_{ii}^M = -\frac{\sqrt{3}(\varepsilon s - t)a}{d_t} [2i] + M \frac{(\varepsilon s - t)a^2}{4d_t^2} \cos 3\theta [2i]^2, \\ E_{ii}^S = -\frac{\sqrt{3}(\varepsilon s - t)a}{d_t} \left[i + \frac{\text{mod}(i, 2)}{3} - \frac{2}{3} \right] + [1 - 2 \text{mod}(S + i, 2)] \\ \quad \times \frac{(\varepsilon s - t)a^2}{4d_t^2} \cos 3\theta \left[i + \frac{\text{mod}(i, 2)}{3} - \frac{2}{3} \right]^2, \end{array} \right. \quad (3.24)$$

where $M = -1, +1$ for the lower and higher components of E_{ii}^M usually labeled by E_{ii}^{ML} and E_{ii}^{MH} , and $S = 1, 2$ for S1 and S2 SWNTs. Equation (3.24) describes the deviation of the families of constant $2n + m$ from a pure hyperbolic dependence on d_t and a pure linear dependence on $1/d_t$ given by Eq. (3.20), as shown in Figs. 3-13 (a) and (b), respectively. This deviation, known as the family spread, can be understood from the trigonal warping of the electronic equi-energy contours shown in Fig. 3-14. For a given family of constant $2n + m$, the chiral angle θ of the family members changes from armchair (A) to zigzag (Z), thus rotating the cutting lines superimposed on the reciprocal space of the graphene sheet shown in Fig. 3-14. For A SWNTs, the cutting lines in Fig. 3-14 are vertical, and the critical wavevectors \mathbf{k}_i on the two sides of the K point ($\varphi = \pm\pi/2$) give rise to the same E_{ii} value that appears at the mean hyperbolic curves in Fig. 3-13 (a) and at the mean straight lines in Fig. 3-13 (b). For Z SWNTs, the cutting lines in Fig. 3-14 are horizontal, and the critical wavevectors \mathbf{k}_i on the opposite sides of the K point ($\varphi = 0$ and π) give rise to the two distinct E_{ii} values that deviate from the mean hyperbolic curves in Fig. 3-13 (a) and from the mean straight lines in Fig. 3-13 (b). The family spread then appears in Fig. 3-13.

To better illustrate the effect of the trigonal warping on the $2n+m$ family patterns, we construct three distinct Kataura plots: (1) for the isotropic dispersion relations of Eq. (3.14) yielding Eq. (3.20), (2) for the trigonally distorted dispersion relations of Eq. (3.23) yielding Eq. (3.24), and (3) for the purely triangular equi-energy contours described by Eq. (3.14) multiplied by $2 \cos \varphi$ in the range $|\varphi| \leq \pi/3$. The three Kataura plots along with the corresponding equi-energy contours are shown in Fig. 3-15. One can see from Fig. 3-15 how the family patterns in the Kataura plot are affected

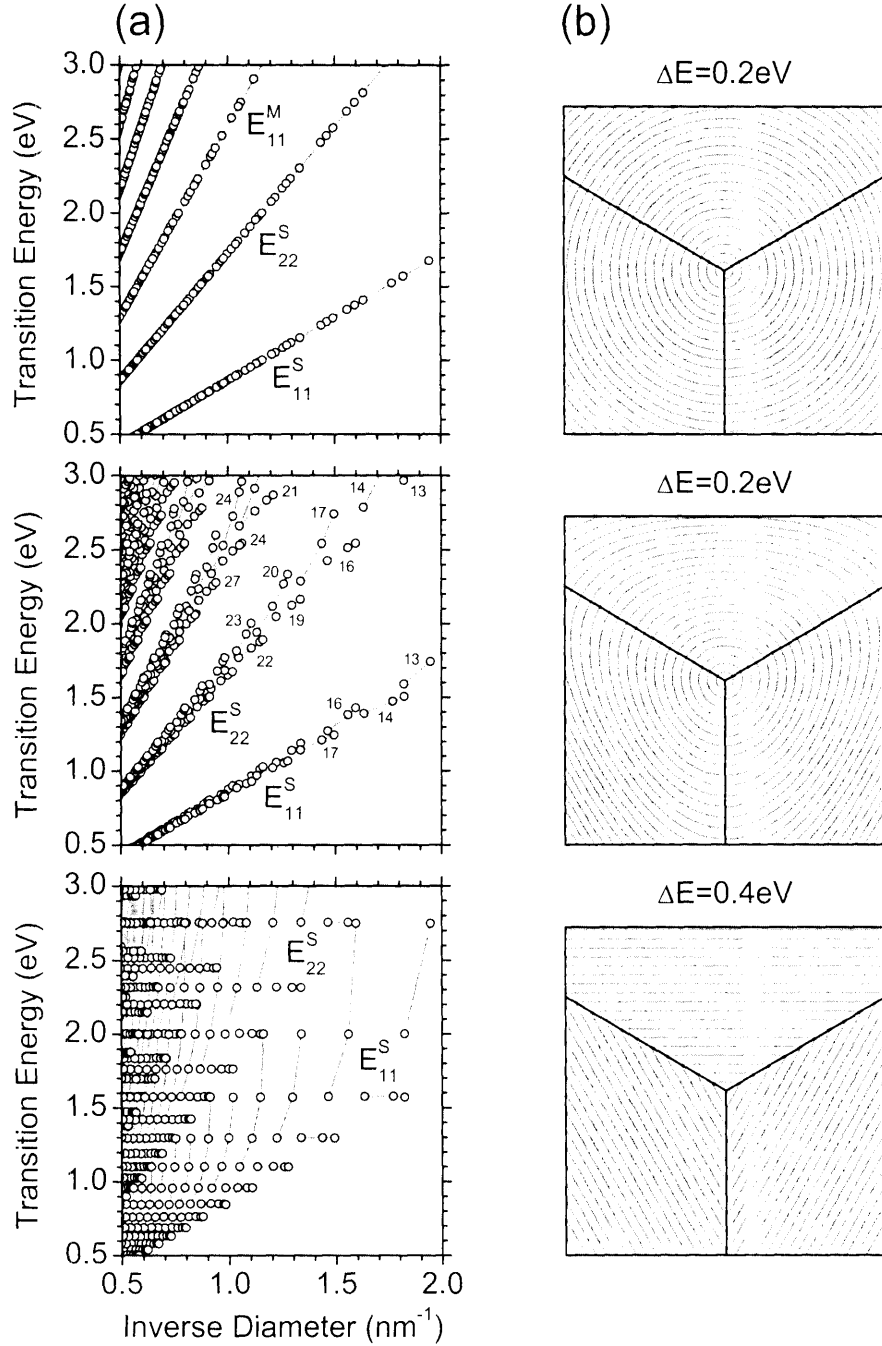


Figure 3-15: (a) The model Kataura plots similar to the STB Kataura plot in Fig. 3-13(b). Panels from top to bottom correspond to the isotropic, trigonally distorted, and completely trigonal dispersion relations. See text for details. (b) The corresponding equi-energy contours around the K point in the reciprocal space of the graphene sheet within the square box in Fig. 3-14 (a). The transition energy difference between the adjacent contours $\Delta E = 0.2 \text{ eV}$ and $\Delta E = 0.4 \text{ eV}$ are shown above the figures.

by the trigonal warping effect. For the isotropic dispersion relations (the top trace in Fig. 3-15 (a)), the $2n + m$ families follow a linear dependence on $1/d_t$. When the trigonal distortion develops (the middle trace in Fig. 3-15 (a)), the $2n + m$ families deviate below and above the mean line, similar to Fig. 3-13. For the completely trigonal dispersion relations (the bottom trace in Fig. 3-15 (a)), the higher $2n + m$ families rapidly increase in energy, while the lower $2n + m$ families become flat.

3.6 Extended tight-binding model

Early resonance Raman studies of SWNT bundles [125] were interpreted in terms of the STB Kataura plot described in Section 3.5. Later on, resonance Raman scattering (RRS) from individual CVD SWNTs on a Si/SiO₂ substrate was observed [65], and the Kataura plot was calibrated by adjusting the STB parameters [65]. The fitted STB parameters, $\varepsilon = 0$ eV, $t = -2.89$ eV, and $s = 0$, scale the Kataura plot as a whole, maintaining the relative positioning of the E_{ii} bands and the family patterns in Fig. 3-13. All these studies were carried out on samples of SWNTs with large diameters ($d_t > 1.2$ nm), where the curvature of the SWNT sidewall is small. The electronic properties of large diameter SWNTs resemble those of the graphene sheet, thus validating the use of the zone-folding technique for constructing the STB Kataura plot. The electronic properties of SWNTs start to deviate from the graphene-like behavior in the small diameter region ($d_t < 1.2$ nm), and the STB Kataura plot fails to explain resonance Raman spectra of small diameter SWNTs.

An experimental Kataura plot in the small diameter region was recently obtained by the band gap photoluminescence (PL) measurements [8] on SWNTs synthesized by high-pressure CO decomposition (HiPCO) [15] and suspended by sodium dodecyl sulfate (SDS) surfactant in deuterium oxide (D₂O) [104]. The excitation-emission density map from Ref. [8] is shown in Fig. 3-16 (a), where each bright spot corresponds to a distinct pair of (n, m) indices. For each bright spot, the excitation and emission wavelengths are resonant with the E_{22}^S and E_{11}^S transitions, respectively. The E_{11}^S and E_{22}^S energies extracted from Fig. 3-16 (a) are summarized in Fig. 3-16 (b) in the form

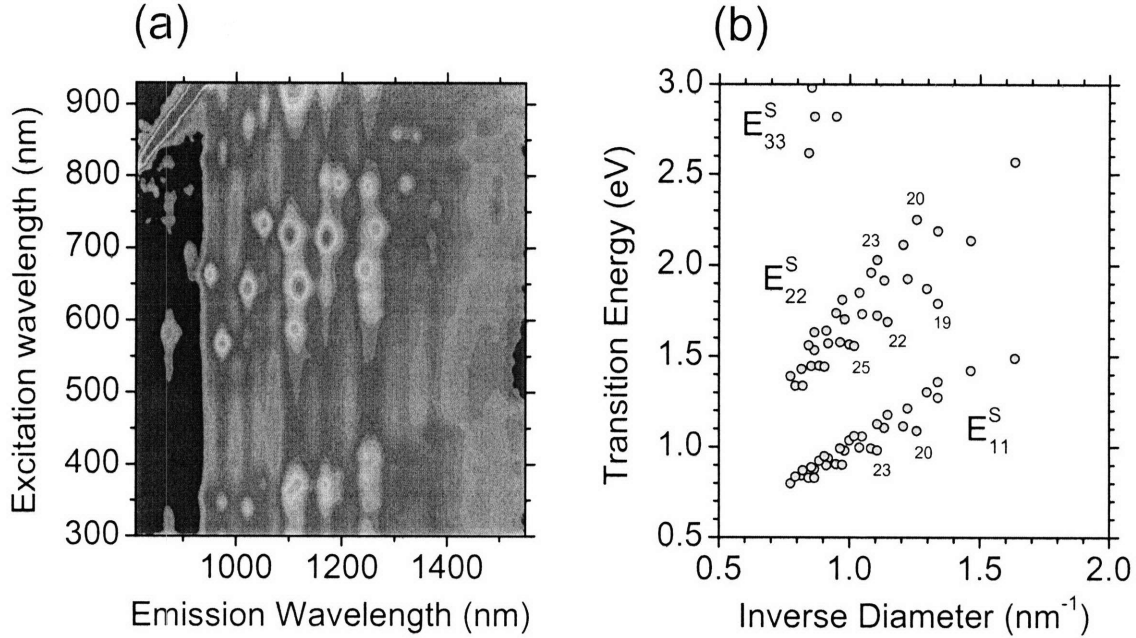


Figure 3-16: (a) The photoluminescence excitation-emission density map measured on wrapped HiPCO SWNTs suspended by SDS surfactant in aqueous solution [8]. (b) The experimental Kataura plot derived from the density map in (a) [168]. The numbers show the families of constant $2n + m$.

of the Kataura plot [168], that is, as a function of the inverse SWNT diameter.

Later on, resonance Raman studies were performed on the same sample using a quasi-continuous set of excitation laser lines [42]. The excitation-emission density map in the frequency range of the radial-breathing mode (RBM) taken from Ref. [42] is shown in Fig. 3-17(a). Again, the bright spots in Fig. 3-17(a) are associated with individual (n, m) SWNTs. For each bright spot, the excitation laser energy is resonant with E_{11}^S , E_{22}^S , or E_{11}^M , while the RBM frequency is inversely proportional to the SWNT diameter, as discussed in Section 3.5. The excitation-emission density map thus directly gives the experimental Kataura plot [63]. For clarity, we replicate the E_{ii} energies from Fig. 3-17(a) in Fig. 3-17(b) as a function of the inverse SWNT diameter.

Comparison of Figs. 3-16(b) and 3-17(b) indicates that both techniques, PL and RRS, give the same E_{ii} energies for the same SWNT sample. However, the experimental Kataura plots in Figs. 3-16(b) and 3-17(b) differ from the theoretical STB

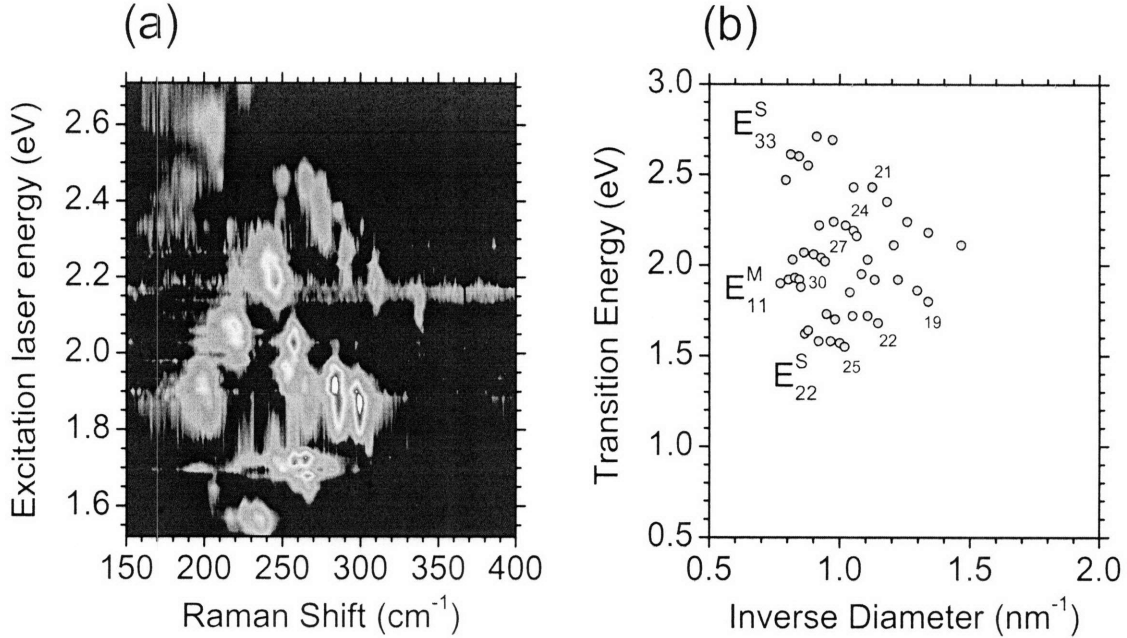


Figure 3-17: (a) The resonance Raman excitation-emission density map in the frequency range of the RBM measured on wrapped HiPCO SWNTs suspended by SDS surfactant in aqueous solution [42]. (b) The experimental Kataura plot derived from the density map in (a) [63]. The numbers show the families of constant $2n + m$.

Kataura plot in Fig. 3-13 (b) in the two different ways, in the large diameter limit and in the small diameter limit. In the large d_t limit, the ratio of E_{22}^S to E_{11}^S reaches 1.8 in the experimental Kataura plots, while the same ratio goes to 2 in the theoretical Kataura plot [8]. The ratio problem is an indication of the many-body interactions in SWNTs [70] that will be discussed in Section 3.7. In the small d_t limit, the families of constant $2n + m$ deviate from the mean E_{ii} energy bands in the experimental Kataura plots, while the family spread in the theoretical Kataura plot remains relatively moderate [168]. The family spread is related to the trigonal warping effect, as shown in Section 3.5 and particularly in Fig. 3-13. However, even the ultimate trigonal warping illustrated in the bottom trace of Fig. 3-15 (b) cannot reproduce the family patterns found in the experimental Kataura plots in Figs. 3-16 (b) and 3-17 (b). A half of the $2n + m$ families bends down with increasing the inverse diameter in Figs. 3-16 (b) and 3-17 (b), while the same families appear as straight horizontal lines in the bottom trace of Fig. 3-15 (a). In fact, the trigonal warping effect can never bend the

families down with increasing inverse diameter. On the other hand, the second half of the $2n + m$ families rapidly increase with the inverse diameter in the bottom trace of Fig. 3-15 (a), but they show very little spread away from the mean E_{ii} bands in Figs. 3-16 (b) and 3-17 (b). It is therefore clear that the trigonal warping effect alone cannot explain the family spread observed by PL and RRS measurements.

In search for the origin of the family spread, we reconsider the limitations of the STB model introduced in Section 3.2. Within the framework of the STB model, we neglected the long-range atomic interactions and the σ molecular orbitals. Meanwhile, the long-range atomic interactions are known to alternate the electronic band structure of the graphene sheet and SWNTs [126]. On the other hand, the σ molecular orbitals are irrelevant in the graphene sheet and large diameter SWNTs as they lie far away in energy from the Fermi level. In small diameter SWNTs, however, the curvature of the SWNT sidewall changes the lengths of the interatomic bonds and the angles between them. This leads to the rehybridization of the σ and π molecular orbitals, which affects the band structure of π electrons near the Fermi level. Furthermore, the σ - π rehybridization suggests that the geometrical structure of a small diameter SWNT deviates from the rolled up graphene sheet. A geometrical structure optimization must thus be performed to allow for atomic relaxation to equilibrium positions. This in turn affects the E_{ii} energies of the small diameter SWNTs.

We extend the STB model introduced in Section 3.2 by including the long-range atomic interactions and the σ molecular orbitals, and by optimizing the geometrical structure. The resulting model is thereafter referred to as the extended tight-binding model (ETB). Within the framework of the ETB model, we use the tight-binding parametrization determined from density-functional theory (DFT) employing the local-density approximation (LDA) and using a local orbital basis set [122]. The ETB model makes use of all the ten tight-binding parameters introduced in Section 3.1. The two atomic orbital energies are given by $\varepsilon_{2s} = -0.4988$ and $\varepsilon_{2p} = -0.1974$ (in units of the Hartree energy E_h ; $E_h = 27.21138$ eV). The four transfer integrals ($t_{ss}(R)$, $t_{s\sigma}(R)$, $t_{\sigma\sigma}(R)$, $t_{\pi\pi}(R)$) and the four overlap integrals ($s_{ss}(R)$, $s_{s\sigma}(R)$, $s_{\sigma\sigma}(R)$, $s_{\pi\pi}(R)$) are functions of the interatomic distance R . These integrals are fitted to the

Table 3.1: Coefficients C_n of the Chebyshev polynomial expansion according to Eqs. (3.25) and (3.26) for the ETB transfer $t_{o'o}(R) = S(R)$ (in units of the Hartree energy E_h ; $E_h = 27.21138$ eV) and overlap $s_{o'o}(R) = S(R)$ (dimensionless) integrals as functions of the interatomic distance R . Boundaries of R are at $R_1 = 1.0$ and $R_2 = 7.0$ (in units of the Bohr radius a_0 ; $a_0 = 0.052917721$ nm). The molecular orbital configurations $o'o = ss, s\sigma, \sigma\sigma, \pi\pi$ are shown in Fig. 3-3. The calculated $t_{o'o}(R)$ and $s_{o'o}(R)$ dependencies are shown in Fig. 3-18 [122].

	t_{ss}	$t_{s\sigma}$	$t_{\sigma\sigma}$	$t_{\pi\pi}$
C_0	-0.4663805	+0.3395418	+0.2422701	-0.3793837
C_1	+0.3528951	-0.2250358	-0.1315258	+0.3204470
C_2	-0.1402985	+0.0298224	-0.0372696	-0.1956799
C_3	+0.0050519	+0.0653476	+0.0942352	+0.0883986
C_4	+0.0269723	-0.0605786	-0.0673216	-0.0300733
C_5	-0.0158810	+0.0298962	+0.0316900	+0.0074465
C_6	+0.0036716	-0.0099609	-0.0117293	-0.0008563
C_7	+0.0010301	+0.0020609	+0.0033519	-0.0004453
C_8	-0.0015546	+0.0001264	-0.0004838	+0.0003842
C_9	+0.0008601	-0.0003381	-0.0000906	-0.0001855

	s_{ss}	$s_{s\sigma}$	$s_{\sigma\sigma}$	$s_{\pi\pi}$
C_0	+0.4728644	-0.3662838	-0.1359608	+0.3715732
C_1	-0.3661623	+0.2490285	+0.0226235	-0.3070867
C_2	+0.1594782	-0.0431248	+0.1406440	+0.1707304
C_3	-0.0204934	-0.0584391	-0.1573794	-0.0581555
C_4	-0.0170732	+0.0492775	+0.0753818	+0.0061645
C_5	+0.0096695	-0.0150447	-0.0108677	+0.0051460
C_6	-0.0007135	-0.0010758	-0.0075444	-0.0032776
C_7	-0.0013826	+0.0027734	+0.0051533	+0.0009119
C_8	+0.0007849	-0.0011214	-0.0013747	-0.0001265
C_9	-0.0002005	+0.0002303	+0.0000751	-0.0000227

functional form:

$$S(R) = \sum_{n=0}^9 C_n T_n \left(\frac{2R - R_2 - R_1}{R_2 - R_1} \right), \quad (3.25)$$

where R_1 and R_2 are the boundaries of R , and $T_n(x)$ are the modified Chebyshev polynomials of the first kind:

$$\begin{cases} T_0(x) = \frac{1}{2}, & T_1(x) = x, & T_2(x) = 2x^2 - 1, \\ T_n(x) = 2xT_{n-1}(x) - T_{n-2}(x) & \text{for } n = 3, \dots, 9. \end{cases} \quad (3.26)$$

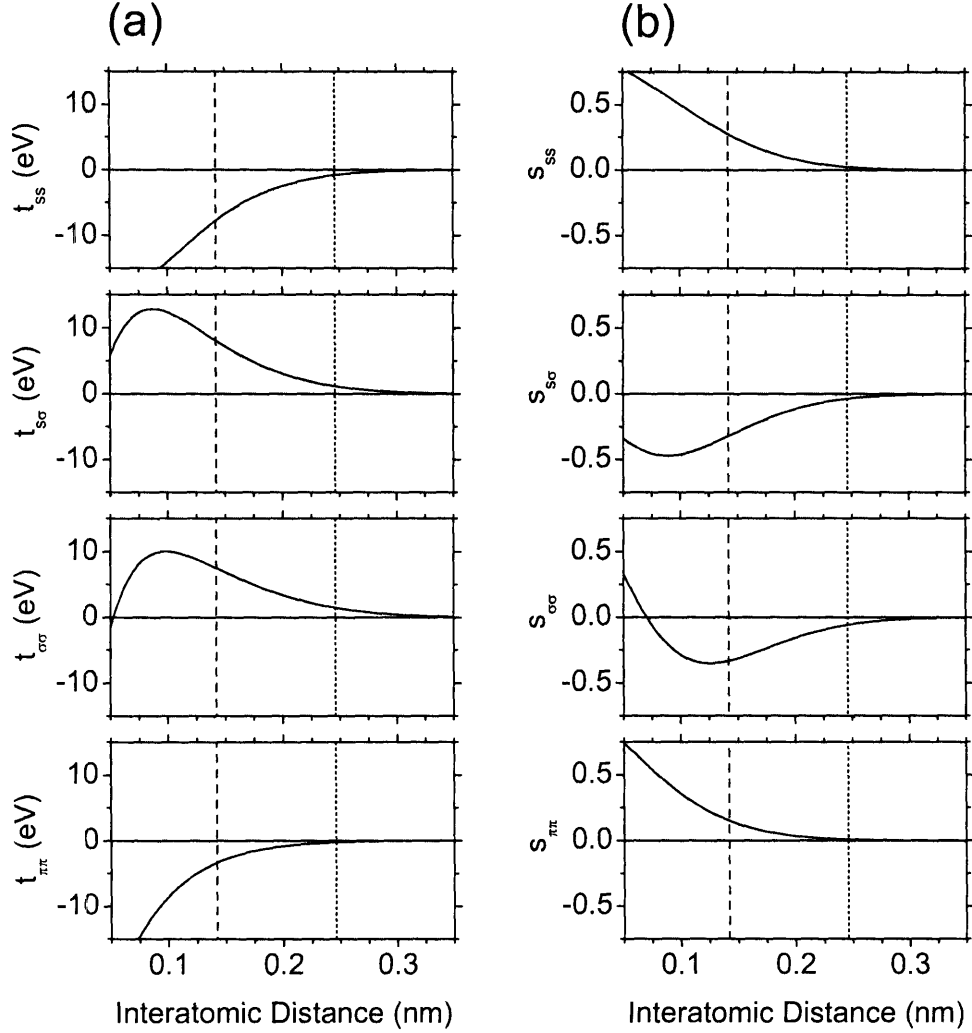


Figure 3-18: The ETB (a) transfer $t_{o'o}(R)$ and (b) overlap $s_{o'o}(R)$ integrals as functions of the interatomic distance R calculated by the Chebyshev polynomial expansions given in Table 3.1. The molecular orbital configurations $o'o = ss, s\sigma, \sigma\sigma, \pi\pi$ are shown in Fig. 3-3. The dashed and dotted vertical lines indicate the first- and second-neighbor interatomic distances, $a_{CC} = 0.142$ nm and $a = \sqrt{3}a_{CC} = 0.246$ nm, respectively.

The coefficients C_n and boundaries (R_1, R_2) for the transfer $t_{o'o}(R) = S(R)$ and overlap $s_{o'o}(R) = S(R)$ integrals are listed in Table 3.1.² The dependence of the transfer and overlap integrals on the interatomic distance is shown in Fig. 3-18. At

²The function $S(R)$ of Eqs. (3.25) and (3.26) with coefficients C_n from Table 3.1 exhibits discontinuities at the cutoff distance $R = R_2$. These lead to discontinuities in the total energy that prevent finding its absolute minimum during optimization of the geometrical structure. To avoid this problem, we extrapolate $S(R)$ with exponential tails at $R > R_2$.

Table 3.2: Coefficients C_n of the Chebyshev polynomial expansion according to Eqs. (3.25) and (3.26) for the ETB short-range repulsive potential $v(R) = S(R)$ (in units of the Hartree energy E_h ; $E_h = 27.21138$ eV) as a function of the interatomic distance R . Boundaries of R are at $R_1 = 1.0$ and $R_2 = 4.1$ (in units of the Bohr radius a_0 ; $a_0 = 0.052917721$ nm) The calculated $v(R)$ dependency is shown in Fig. 3-19 [122].

	v
C_0	+2.2681036
C_1	-1.9157174
C_2	+1.1677745
C_3	-0.5171036
C_4	+0.1529242
C_5	-0.0219294
C_6	-0.0000002
C_7	-0.0000001
C_8	-0.0000005
C_9	+0.0000009

the nearest neighbor interatomic distance $R = a_{CC} = 0.142$ nm shown by the dashed lines in Fig. 3-18, the ETB transfer and overlap integrals $t_{\pi\pi}(a_{CC}) = -3.351$ eV and $s_{\pi\pi}(a_{CC}) = 0.150$ differ slightly from the STB integrals $t_{\pi\pi}(a_{CC}) = -3.033$ eV and $s_{\pi\pi}(a_{CC}) = 0.129$ introduced in Section 3.2. At the second neighbor distance $R = a = \sqrt{3}a_{CC} = 0.246$ nm shown by the dotted lines in Fig. 3-18, the ETB transfer and overlap integrals $t_{\pi\pi}(a) = -0.248$ eV and $s_{\pi\pi}(a) = 0.008$ decrease significantly, and the STB integrals are neglected. While the STB integrals are defined at a fixed interatomic distance $R = a_{CC}$, the ETB integrals shown in Fig. 3-18 are continuous functions of R vanishing at $R \approx 0.3$ nm. The continuous dependence of the transfer and overlap integrals on the interatomic distance is essential for performing the geometrical structure optimization.

The geometrical structure optimization is performed by minimizing the total energy of the system. The total energy within the ETB model is given by a sum of the band structure energy and the repulsive energy [122]. The band structure energy is obtained by summing the electronic band energy over all occupied states on the Monkhorst-Pack grid in the first Brillouin zone [97], taking into account the twofold

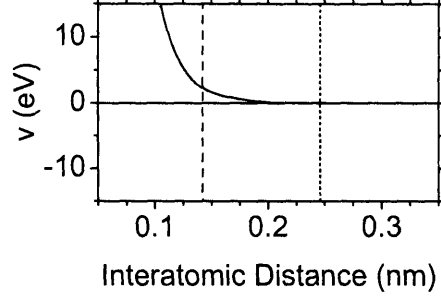


Figure 3-19: The ETB short-range repulsive potential $v(R)$ as a function of the interatomic distance R calculated by the Chebyshev polynomial expansions given in Table 3.2. The dashed and dotted lines show the first- and second-neighbor interatomic distances, $a_{CC} = 0.142$ nm and $a = \sqrt{3}a_{CC} = 0.246$ nm, respectively.

spin degeneracy. The repulsive energy is equal to a sum of the short-range repulsive potentials between pairs of atoms. The short-range repulsive potential $v(R)$ as a function of the interatomic distance R is calculated with the help of DFT-LDA and is fitted to the functional form of Eq. (3.25) [122]. The coefficients C_n and boundaries (R_1, R_2) for the short-range repulsive potential $v(R) = S(R)$ are listed in Table 3.2. The dependence of the short-range repulsive potential on the interatomic distance is shown in Fig. 3-19. At the first and second neighbor distances $R = a_{CC}$ and a shown by the dashed and dotted lines in Fig. 3-19, the short-range repulsive potential is given by $v(a_{CC}) = 2.331$ eV and $v(a) = 0$ eV. The short-range repulsive potential is thus restricted to the nearest neighbor interactions.

The total energy per carbon atom of a graphene sheet is given by:

$$E = \frac{1}{2W} \sum_w \sum_b^8 n^b(\mathbf{k}_w) E^b(\mathbf{k}_w) + \frac{1}{4U} \sum_{u'} \sum_{s'}^2 \sum_{us}^3 v(|\mathbf{R}_{us} - \mathbf{R}_{u's'}|), \quad (3.27)$$

where W is the number of the Monkhorst-Pack mesh points \mathbf{k}_w in the first Brillouin zone of the graphene sheet, $n^b(\mathbf{k}_w)$ is the electron occupation number, $E^b(\mathbf{k}_w)$ is the electronic band energy, U is the number of the two-atom unit cells in the graphene sheet, and the summation on atomic site s in unit cell u is carried out over the three nearest neighbors of atomic site s' in unit cell u' . The factors of $\frac{1}{2}$ and $\frac{1}{4}$ arise from the facts that there are two atoms per unit cell and that each atomic pair in the second

term of in Eq. (3.27) is counted twice. At zero temperature $T = 0$ K, the valence bands are filled and the conduction bands are empty, $n^b(\mathbf{k}_w) = 2$ for $b = 1, \dots, 4$ and $n^b(\mathbf{k}_w) = 0$ for $b = 5, \dots, 8$. The summation on band index b in the first term of Eq. (3.27) is thus performed over the valence bands.

Minimization of the total energy given by Eq. (3.27) with respect to the atomic coordinates $\mathbf{R}_{u's'}$ requires knowledge of the forces acting on the atoms. The electronic part of the interatomic forces is given by the partial derivatives of the electronic band energy $E^b(\mathbf{k}_w)$ with respect to $\mathbf{R}_{u's'}$. Upon differentiating Eq. (3.3) with respect to $\mathbf{R}_{u's'}$, multiplying it by $C_{s'o'}^{b*}(\mathbf{k}_w)$ and summing it over indices s' and o' , we find:

$$\frac{\partial E^b(\mathbf{k}_w)}{\partial \mathbf{R}_{u's'}} = \sum_{s'o'}^8 \sum_{so}^8 C_{s'o'}^{b*}(\mathbf{k}_w) \left(\frac{\partial H_{s'o'so}(\mathbf{k}_w)}{\partial \mathbf{R}_{u's'}} - E^b(\mathbf{k}_w) \frac{\partial S_{s'o'so}(\mathbf{k}_w)}{\partial \mathbf{R}_{u's'}} \right) C_{so}^b(\mathbf{k}_w), \quad (3.28)$$

where the second term arises from the rigid movement of the atomic orbitals along with the atoms, taking into account the nonorthogonality of the atomic orbitals. The interatomic forces are thus determined by the partial derivatives of the Hamiltonian $H_{s'o'so}(\mathbf{k}_w)$ and overlap $S_{s'o'so}(\mathbf{k}_w)$ matrices, but are independent of the partial derivatives of the Bloch amplitudes $C_{so}^b(\mathbf{k}_w)$, which is known as the Hellmann-Feynman theorem. The partial derivatives of $n^b(\mathbf{k}_w)$ with respect to $\mathbf{R}_{u's'}$ vanish at $T = 0$ K because the graphene sheet and M SWNTs are zero-gap semiconductors. Finally, the repulsive part of the interatomic forces is given by the derivatives of the short-range repulsive potential $v(|\mathbf{R}_{us} - \mathbf{R}_{u's'}|)$ with respect to $\mathbf{R}_{u's'}$. We thus express the interatomic forces in terms of the derivatives of $t_{o'o}(R)$, $s_{o'o}(R)$, and $v(R)$ with respect to R . These derivatives can be solved analytically from Eqs. (3.25) and (3.26) and Tables 3.1 and 3.2. Alternatively, a finite difference technique can be used to numerically compute the partial derivatives of the total energy given by Eq. (3.27) with respect to $\mathbf{R}_{u's'}$. For systems with large unit cells, the numerical calculation is considerably slower than the analytical Hellman-Feynman approach. However, both methods are equally applicable for the two-atom unit cell of the graphene sheet.

The two-atom unit cell of the graphene sheet has six degrees of freedom. However, the symmetry of the graphene sheet described by the point group D_{6h} reduces the

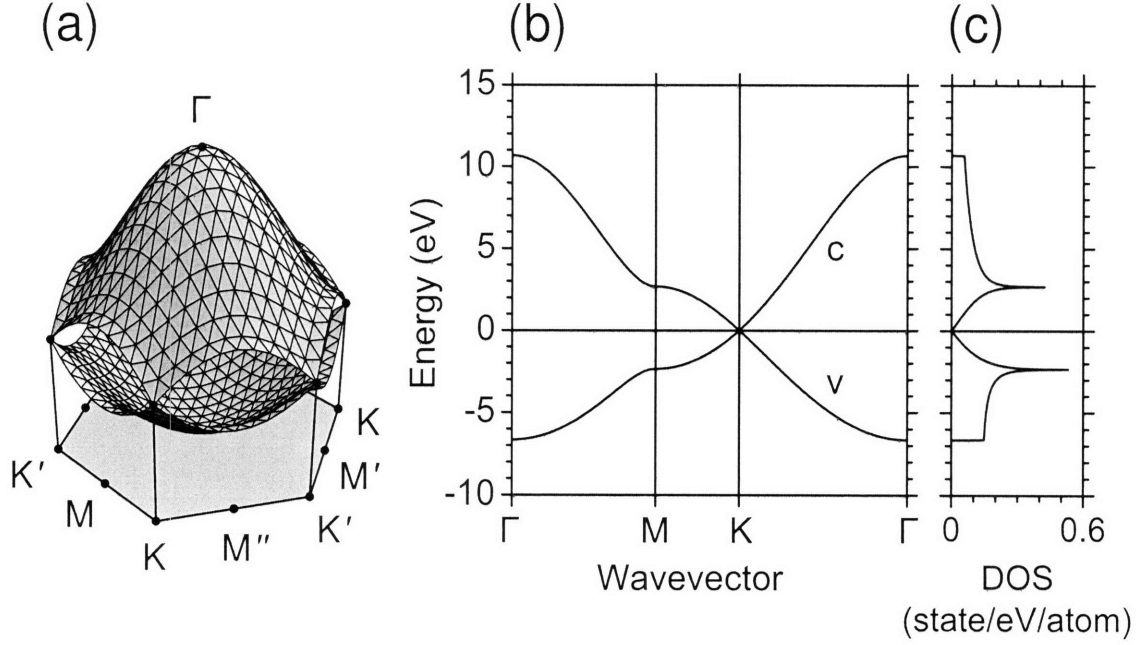


Figure 3-20: The ETB electronic dispersion relations of the optimized graphene sheet with $a_{CC} = 0.141751$ nm (a) throughout the entire first Brillouin zone shown in Fig. 2-1 and (b) along the high-symmetry directions in the first Brillouin zone. The valence and conduction bands are labeled by v and c , respectively. (c) The density of electronic states (DOS). The Fermi level is shown by the horizontal line at zero energy.

number of independent degrees of freedom to one. Namely, the interatomic distance a_{CC} (or, equivalently, the lattice constant a) should be optimized to minimize the total energy given by Eq. (3.27). The total energy of the graphene sheet as a function of a_{CC} is shown in Fig. 3 of Ref. [122]. The total energy reaches its minimum value at $a_{CC} = 0.141751$ nm, and that value should be used instead of $a_{CC} = 0.142$ nm for calculating the electronic structure of the graphene sheet at $T = 0$ K within the ETB model. The ETB parameters for the nearest and second neighbor interatomic distances change slightly to the new values, $t_{\pi\pi}(a_{CC}) = -3.370$ eV, $s_{\pi\pi}(a_{CC}) = 0.151$, $v(a_{CC}) = 2.357$ eV, $t_{\pi\pi}(a) = -0.251$ eV, $s_{\pi\pi}(a) = 0.009$, and $v(a) = 0$ eV.

At finite temperature $T > 0$ K, the geometrical structure is optimized by minimizing the Helmholtz free energy $F = E - TS$, where E is the total energy given by Eq. (3.27) and S is the vibrational entropy [99]. The electron occupation number

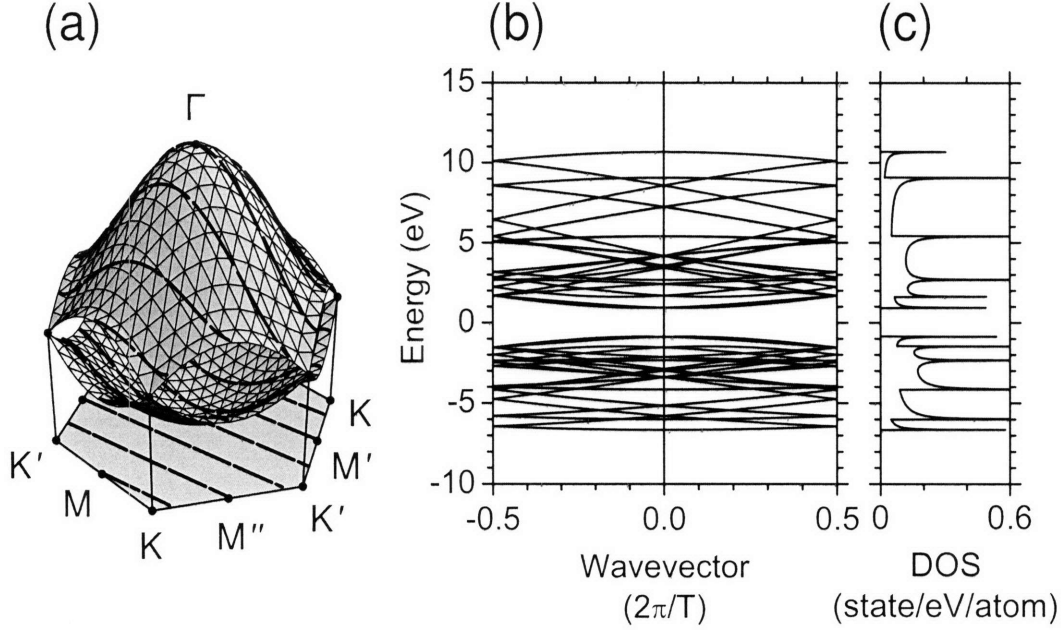


Figure 3-21: (a) The ETB electronic dispersion relations of the optimized graphene sheet with $a_{CC} = 0.141751$ nm replicated from Fig. 3-20. The solid lines are the cutting lines for a semiconducting (4, 2) SWNT in the helical-helical representation. (b) The electronic dispersion relations of the (4, 2) SWNT when different cutting lines are folded together into the 1D Brillouin zone. The length of the 1D Brillouin zone is given by $2\pi/T$. (c) The density of electronic states (DOS) of the (4, 2) SWNT. Vanishing DOS at the Fermi level $E_F = 0$ eV indicates that the SWNT is semiconducting. The sharp spikes in the DOS typical for 1D systems are known as Van Hove singularities.

$n^b(\mathbf{k}_w)$ in E is now given by the Fermi-Dirac distribution:

$$n^b(\mathbf{k}_w) = \frac{1}{\exp \frac{E^b(\mathbf{k}_w) - E_F}{k_B T} + 1}. \quad (3.29)$$

The vibrational entropy S is determined by the out-of-plane transverse acoustic (oTA) phonon mode that has the lowest frequency (ω^{oTA}) in the graphene sheet, as will be shown in Chapter 4. Considering that ω^{oTA} increases with increasing a_{CC} , S decreases and the minimum of F shifts to the lower value of a_{CC} [99]. Hence, the graphene sheet exhibits an anomalous contraction upon heating [99]. However, finite temperature phenomena are beyond the scope of this Thesis. We therefore limit our consideration to the graphene sheet with $a_{CC} = 0.141751$ nm optimized at $T = 0$ K.

In Figs. 3-20 (a) and (b), we plot the ETB electronic dispersion relations of the optimized graphene sheet with $a_{CC} = 0.141751$ nm throughout the entire first Brillouin zone and along the high-symmetry directions in the first Brillouin zone, respectively. The corresponding density of electronic states (DOS) is shown in Fig. 3-20 (c). By comparing Fig. 3-20 with the analogous Fig. 3-5 calculated within the STB model, we find little difference between the two except for the overall redshift of the top of the conduction band in Fig. 3-20 associated with the long-range atomic interactions in the graphene sheet [126]. In Fig. 3-21 (a), we replicate the ETB electronic dispersion relations of the optimized graphene sheet with $a_{CC} = 0.141751$ nm shown in Fig. 3-20 (a), and we superimpose the cutting lines defined by Eq. (2.14) in the helical-helical representation for the (4, 2) SWNT over the dispersion surface, similar to Fig. 3-11 (a) for the STB dispersion relations. We then construct the 1D dispersion relations and the DOS of the (4, 2) SWNT in Figs. 3-21 (b) and (c), respectively, analogous to the STB dispersion relations in Figs. 3-11 (b) and (c). Again, comparison of Figs. 3-21 (b) and 3-11 (b) reveals an overall redshift of the top of the conduction band within the ETB model.

3.6.1 Long-range interactions

Similar to the VHSs in Fig. 3-21 (c) for the (4, 2) SWNT, the entire ETB Kataura plot is constructed by applying the zone-folding technique defined by Eq. (2.14) to the ETB electronic dispersion relations of the optimized graphene sheet with $a_{CC} = 0.141751$ nm shown in Fig. 3-20 (a). The resulting ETB Kataura plot is shown in Fig. 3-22. By comparing Figs. 3-22 and 3-13, we observe the overall blueshift of the ETB Kataura plot from the STB Kataura plot, while the family spread in the ETB Kataura plot is similar to the family spread in the STB Kataura plot. Since the zone-folding technique neglects the curvature of the SWNT sidewall and the optimized geometrical structure of the SWNT, the ETB Kataura plot in Fig. 3-22 only differs from the STB Kataura plot in Fig. 3-13 by including the long-range atomic interactions. Hence, the family spread in the ETB Kataura plot arises from the trigonal warping effect. The trigonal warping effect in the ETB model is illustrated in

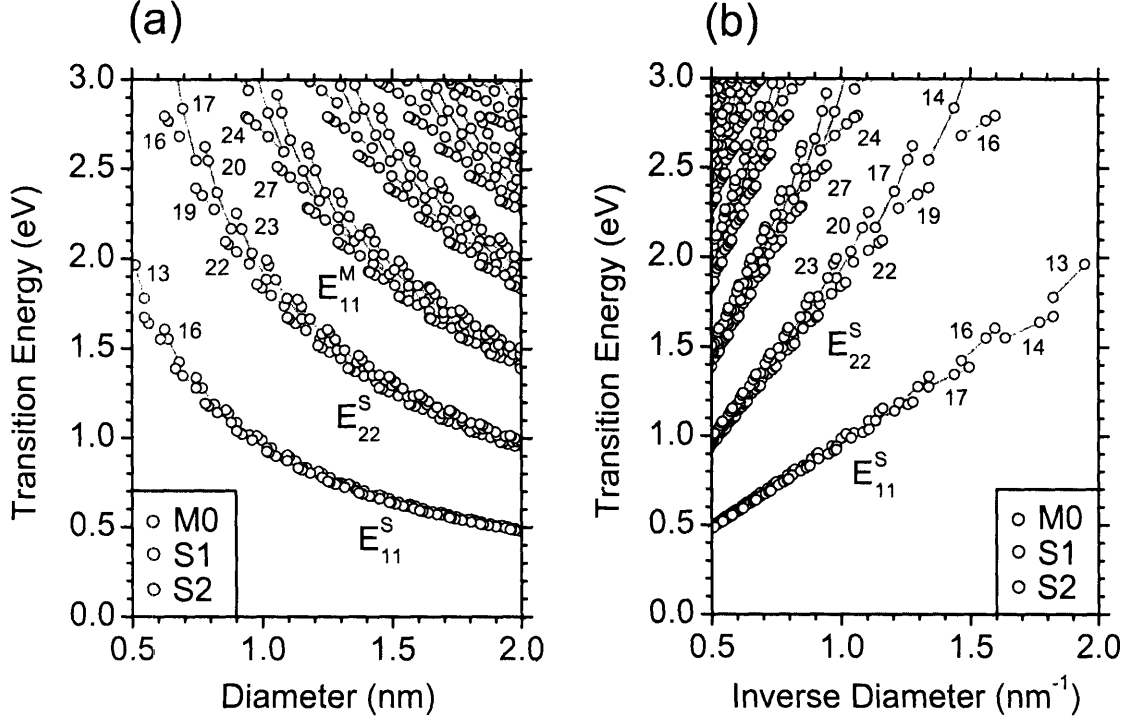


Figure 3-22: The ETB Kataura plot as a function of (a) the SWNT diameter d_t and (b) the inverse diameter $1/d_t$ similar to the STB Kataura plot in Fig. 3-13. The ETB Kataura plot is calculated by applying the zone-folding technique to the ETB electronic dispersion relations of the optimized graphene sheet with $a_{CC} = 0.141751$ nm. This approach takes into account the long-range atomic interactions in the graphene sheet. The red, green, and blue dots correspond to M0, S1, and S2 SWNTs, respectively. The families of constant $2n + m$ are connected by gray lines and labeled by $2n + m$ values.

Fig. 3-23 where we show the electronic equi-energy contours around the K point in the reciprocal space of the graphene sheet. By comparing Fig. 3-23 with the analogous Fig. 3-14 calculated within the STB model, we find that the trigonal warping effect in the ETB model is similar to the trigonal warping effect in the STB model. Both are described by Eq. (3.23) with different sets of tight-binding parameters (ϵ, s, t) , neglecting the long-range atomic interactions. The ETB Kataura plot obtained by the zone-folding technique is thus similar to the STB Kataura plot. To take into account the effects of curvature and relaxation within the framework of the ETB model, we must go beyond the zone-folding approximation.

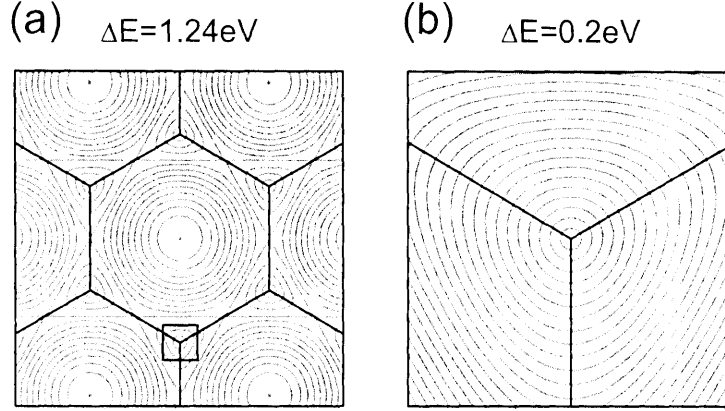


Figure 3-23: (a) The contours of constant transition energy $E^c - E^v$ in the first Brillouin zone of the graphene sheet shown in Fig. 2-1 calculated within the ETB model similar to the STB contours in Fig. 3-14. The square box indicates the area of linear dimensions $K\Gamma/3 = 4\pi/(9a)$ centered at the K point. (b) A zoom in of area within the square box in (a). The transition energy difference between the adjacent contours $\Delta E = 1.24$ eV and $\Delta E = 0.2$ eV are shown above the figures.

3.6.2 Curvature-induced rehybridization

Within the zone-folding approximation, the electronic dispersion relations of SWNTs are obtained by solving the stationary Schrödinger equation, Eq. (3.3), with the Hamiltonian and overlap matrices of Eq. (3.4) calculated for the planar geometry of the graphene sheet with the 1D angular and linear momenta, μ and k , substituted for the 2D momentum \mathbf{k} , according to Eq. (2.14). Calculation for the cylindrical geometry of SWNTs involves the translational unit cell of $2N$ carbon atoms, yielding the $8N \times 8N$ Hamiltonian and overlap matrices. Alternatively, the two-atom unit cell of the graphene sheet can be used, and the cylindrical geometry of the SWNT is taken into account by aligning the atomic orbitals $\phi_o(\mathbf{r} - \mathbf{R}_{us})$ in Eq. (3.4) along the tangential and normal directions to the SWNT sidewall [119]. Upon aligning the z -axis with the SWNT axis, the atomic coordinates \mathbf{R}_{us} are expressed in the cylindrical coordinate system as follows:

$$\mathbf{R}_{us} = \left(\frac{1}{2} d_{us}, \frac{1}{2} d_{us} \phi_{us}, z_{us} \right), \quad (3.30)$$

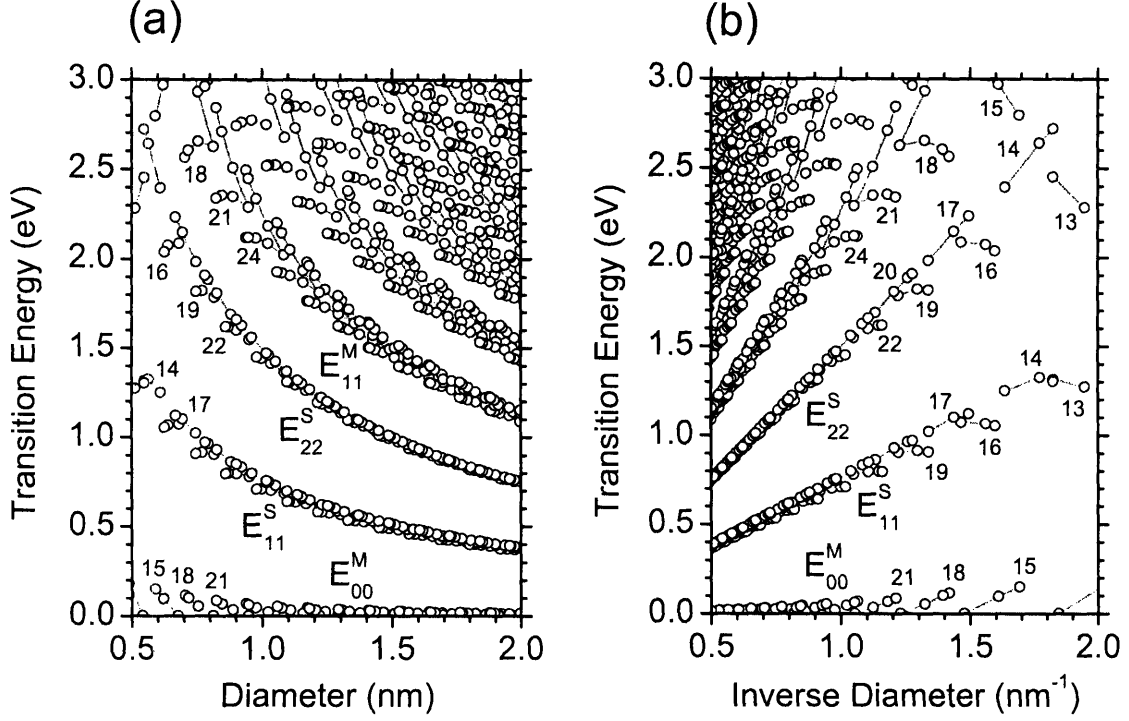


Figure 3-24: The ETB Kataura plot as a function of (a) the SWNT diameter d_t and (b) the inverse diameter $1/d_t$ similar to the STB Kataura plot in Fig. 3-13. The ETB Kataura plot is calculated directly from the ETB electronic dispersion relations of the SWNTs rolled up from the optimized graphene sheet with $a_{CC} = 0.141751$ nm. This approach takes into account the long-range atomic interactions and the curvature of the SWNT sidewall. The red, green, and blue dots correspond to M0, S1, and S2 SWNTs, respectively. The families of constant $2n + m$ are connected by gray lines and labeled by $2n + m$ values.

where the SWNT diameter d_t is an average value of the atomic coordinate d_{us} . The $2p$ atomic orbitals $\phi_o(\mathbf{r} - \mathbf{R}_{us})$ in Eq. (3.4) are then rotated around the z -axis by angles ϕ_{us} . The rotation operation consists of multiplying the argument of $\phi_o(\mathbf{r} - \mathbf{R}_{us})$ in Eq. (3.4) by the rotation matrix $R^z(\phi_{us})$ defined by:

$$R^z(\phi_{us}) = \begin{pmatrix} \cos \phi_{us} & \sin \phi_{us} & 0 \\ -\sin \phi_{us} & \cos \phi_{us} & 0 \\ 0 & 0 & 1 \end{pmatrix}. \quad (3.31)$$

The electronic dispersion relations of SWNTs are calculated by solving Eq. (3.3)

within the framework of the ETB model upon substituting Eqs. (2.14) and (3.31) into Eq. (3.4) and using the atomic coordinates \mathbf{R}_{us} of SWNTs rolled up from the optimized graphene sheet with $a_{CC} = 0.141751$ nm. The ETB Kataura plot obtained from these dispersion relations is shown in Fig. 3-24. This approach takes into account not only the long-range atomic interactions but also the curvature of the SWNT sidewall, but omits the optimized geometrical structures of the SWNTs. By comparing Figs. 3-24 and 3-13, we find the overall redshift of the ETB Kataura plot from the STB Kataura plot. Besides, the curvature opens the mini band gaps in M SWNTs labeled by E_{00}^M in Fig. 3-24, in accordance with Eq. (3.17). Finally, the family spread in the ETB Kataura plot is slightly enhanced compared with the family spread in the STB Kataura plot, and the family patterns for S1 and S2 SWNTs within the E_{11}^S band switch their behavior. However, the family spread in Fig. 3-24 is still much less than the family spread observed in the experimental Kataura plots of Figs. 3-16 (b) and 3-17 (b). To investigate the origin of the experimentally observed family spread, we perform an optimization of the geometrical structures of the SWNTs.

3.6.3 Geometrical structure relaxation

The geometrical structure optimization of SWNTs is performed by minimizing the total energy of SWNTs with respect to the atomic degrees of freedom. The two-atom unit cell of the SWNT has six degrees of freedom. Because of the translational symmetry of the two-atom unit cell of the SWNT described by the lattice vectors \mathbf{a}_1 and \mathbf{a}_2 projected on the cylinder surface, it is convenient to express the unit cell degrees of freedom in the cylindrical coordinate system. The cylindrical degrees of freedom are illustrated in Fig. 3-25 where we replicate the translational unit cell of the (4, 2) ZR/AL SWNT shown in Fig. 2-3. The three degrees of freedom are described by the relative positions of the A and B atoms within the two-atom unit cell along the axial, angular, and radial directions, T_{AB} , φ_{AB} , and d_{AB} , respectively, as shown in Fig. 3-25 (a). In terms of Eq. (3.30), $T_{AB} = z_{uA} - z_{uB}$, $\varphi_{AB} = \phi_{uA} - \phi_{uB}$, and $d_{AB} = d_{uA} - d_{uB}$. The three other degrees of freedom are described by the macroscopic deformations of the SWNT, the axial strain ε , the torsion angle τ , and the radial

expansion ϱ . The macroscopic deformations are associated with microscopic changes in the dimensions of the translational unit cell. The dimensions of the translational unit cell in the axial and radial directions, T and d_t , are shown in Fig. 3-25 (b). The axial and angular projections of the lattice vectors \mathbf{a}_1 and \mathbf{a}_2 are shown in Fig. 3-25 (c) labeled by T_{a1} , T_{a2} , φ_{a1} , and φ_{a2} , correspondingly. These projections are determined by the SWNT chiral angle θ that specifies the orientation of the \mathbf{a}_1 and \mathbf{a}_2 vectors with respect to the \mathbf{C}_h and \mathbf{T} vectors in the unrolled graphene sheet shown in Fig. 2-4. The changes in the unit cell parameters are determined by the macroscopic deformations:

$$\begin{cases} \Delta T = \varepsilon T, & \Delta T_{AB} = \varepsilon T_{AB}, & \Delta T_{a1} = \varepsilon T_{a1}, & \Delta T_{a2} = \varepsilon T_{a2}, \\ \Delta \varphi_{AB} = \tau T_{AB}, & \Delta \varphi_{a1} = \tau T_{a1}, & \Delta \varphi_{a2} = \tau T_{a2}, \\ \Delta d_t = \varrho d_t, & \Delta d_{AB} = \varrho d_{AB}. \end{cases} \quad (3.32)$$

Hence, the independent degrees of freedom are identified as:

$$\varepsilon, \quad \tau, \quad \varrho, \quad \tilde{T}_{AB} = \frac{T_{AB}}{1 + \varepsilon}, \quad \tilde{\varphi}_{AB} = \varphi_{AB} - \frac{\tau T_{AB}}{1 + \varepsilon}, \quad \tilde{d}_{AB} = \frac{d_{AB}}{1 + \varrho}, \quad (3.33)$$

where we decouple the internal changes of the unit cell structure ($\tilde{T}_{AB}, \tilde{\varphi}_{AB}, \tilde{d}_{AB}$) from the macroscopic deformations of the SWNT ($\varepsilon, \tau, \varrho$). The remaining unit cell parameters ($T, d_t, T_{a1}, T_{a2}, \varphi_{a1}, \varphi_{a2}$) are determined from Eq. (3.32).

The symmetry of the SWNT reduces the number of independent degrees of freedom given by Eq. (3.33). The C'_2 and C''_2 rotational axes perpendicular to the SWNT axis [12] exchange the A and B atoms. Hence, the minimum of the total energy is reached at $d_{AB} = 0$, implying that all the A and B atoms lie on the same cylindrical surface. For achiral SWNTs, the σ'_v and σ''_v mirror planes parallel to the SWNT axis [12] change τ to $-\tau$, suggesting that $\tau = 0$ at the equilibrium. We thus conclude that there are four independent degrees of freedom for achiral SWNTs ($\varepsilon, \varrho, \tilde{T}_{AB}, \tilde{\varphi}_{AB}$) and five for chiral SWNTs ($\varepsilon, \tau, \varrho, \tilde{T}_{AB}, \tilde{\varphi}_{AB}$). In chiral SWNTs, however, ε and τ are coupled to each other [83].

There is no residual torsion, $\tau = 0$, in chiral SWNTs rolled up from the optimized graphene sheet, since the latter exhibits no shear deformation. Yet, the value

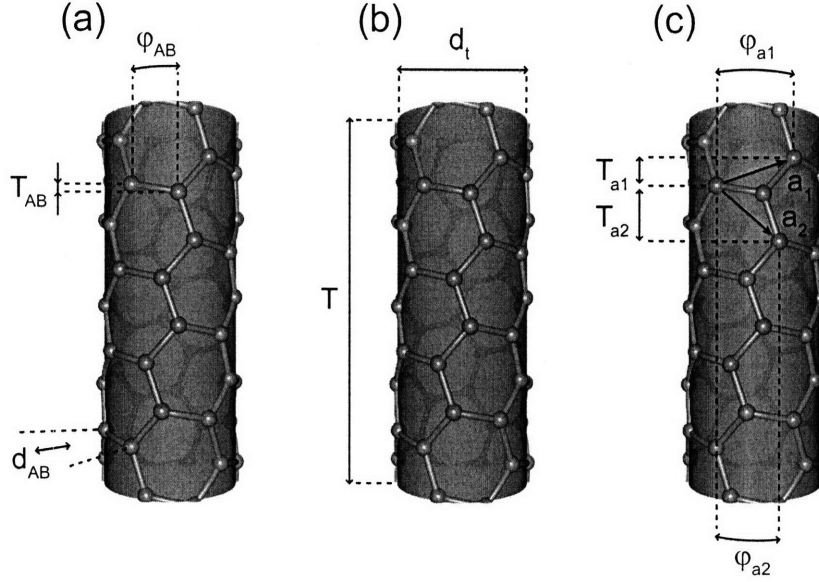


Figure 3-25: The (4, 2) ZR/AL SWNT replicated from Fig. 2-3. (a) The relative positions of the A and B atoms within the SWNT unit cell along the axial, angular, and radial directions, T_{AB} , φ_{AB} , and d_{AB} , respectively. (b) The dimensions of the translational unit cell in the axial and radial directions, T and d_t . (c) The lattice vectors \mathbf{a}_1 and \mathbf{a}_2 and their axial and angular projections T_{a1} , T_{a2} , φ_{a1} , and φ_{a2} , correspondingly. The projections are determined by the SWNT chiral angle θ .

of τ at the equilibrium geometry may not go to zero in chiral SWNTs. The residual torsion, $\tau \neq 0$, is, in general, incommensurate with the translational unit cells of chiral SWNTs. Such incommensurability breaks the translation symmetry of chiral SWNTs, thus invalidating the use of the helical-linear representation. The geometrical structure of chiral SWNTs should therefore be optimized in the angular-helical representation, allowing τ to vary. Study of this optimization will be the subject of future work.

In the present study, we fixed the value of $\tau = 0$ to maintain the translational symmetry of chiral SWNTs. We performed the geometrical structure optimization by minimizing the total energy with respect to the four degrees of freedom (ε , ϱ , \tilde{T}_{AB} , $\tilde{\varphi}_{AB}$) at $T = 0\text{ K}$ for all (n, m) SWNTs within the diameter range $0.3\text{ nm} < d_t < 3.0\text{ nm}$. The total energy of the SWNT is obtained from Eq. (3.27) where the summation over the 2D momentum \mathbf{k} is instead carried out over the 1D angular and linear momenta, μ and k , according to Eq. (2.14). The total energy is calculated on a 1D Monkhorst-

Pack grid of $(1 \mu\text{m}/T)$ k -points (884 k -points for $(4, 2)$ SWNT) along the cutting lines in the helical-linear representation. The minimization of the total energy is performed by the steepest decent algorithm with a relative convergence tolerance of 10^{-10} . The Hellmann-Feynman forces are calculated numerically by a central finite difference approximation for the partial derivatives of the total energy with the step $\Delta R = 10^{-6}$ nm.

Among the four optimized degrees of freedom $(\varepsilon, \varrho, \tilde{T}_{AB}, \tilde{\varphi}_{AB})$, ϱ shows the largest deviation from the initial value corresponding to the rolled up optimized graphene sheet. While ϱ increases with decreasing d_t , the dependence of ϱ on the chiral angle θ is rather weak. We thus fit ϱ as a function of d_t to the form $\varrho = 1 + 0.0063 \text{ nm}^2/d_t^2$. For the $(4, 2)$ SWNT rolled up from the optimized graphene sheet, we obtain $d_t = 0.41$ nm. This yields $\varrho = 1.04$ suggesting that the optimized diameter increases by 4 %, $d_t + \Delta d_t = 0.43$ nm. The optimized values of ε and ϱ as functions of d_t for all (n, m) SWNTs are shown in Fig. 2 of Ref. [119].

The ETB Kataura plot calculated for the optimized geometrical structures of the SWNTs is shown in Fig. 3-26. The family spread in the ETB Kataura plot of Fig. 3-26 is strongly enhanced compared with the family spread in the STB Kataura plot of Fig. 3-13. The ETB family spread turns out to be very sensitive to the geometrical structures of the SWNTs. Changing the geometrical structure by 1 % causes the E_{ii} energies to shift by 10 %. Thus, the small variations in the geometrical structures of the optimized SWNTs give rise to the large family spread in the ETB Kataura plot of Fig. 3-26. The geometrical structure optimization of chiral SWNTs over the torsion degree of freedom is likely to distort the family patterns in the ETB Kataura plot of Fig. 3-26. However, both ends of the family curves correspond to achiral armchair and zigzag SWNTs and therefore are fixed under the torsion optimization. The finite temperature also shifts the family patterns by distorting the relaxed geometrical structure, as discussed earlier in this Section.

The ETB family spread shows a good agreement with the results of first-principles calculations for several small diameter zigzag semiconducting SWNTs [155]. The ETB family spread also matches nearly perfectly the family spread found in the PL and

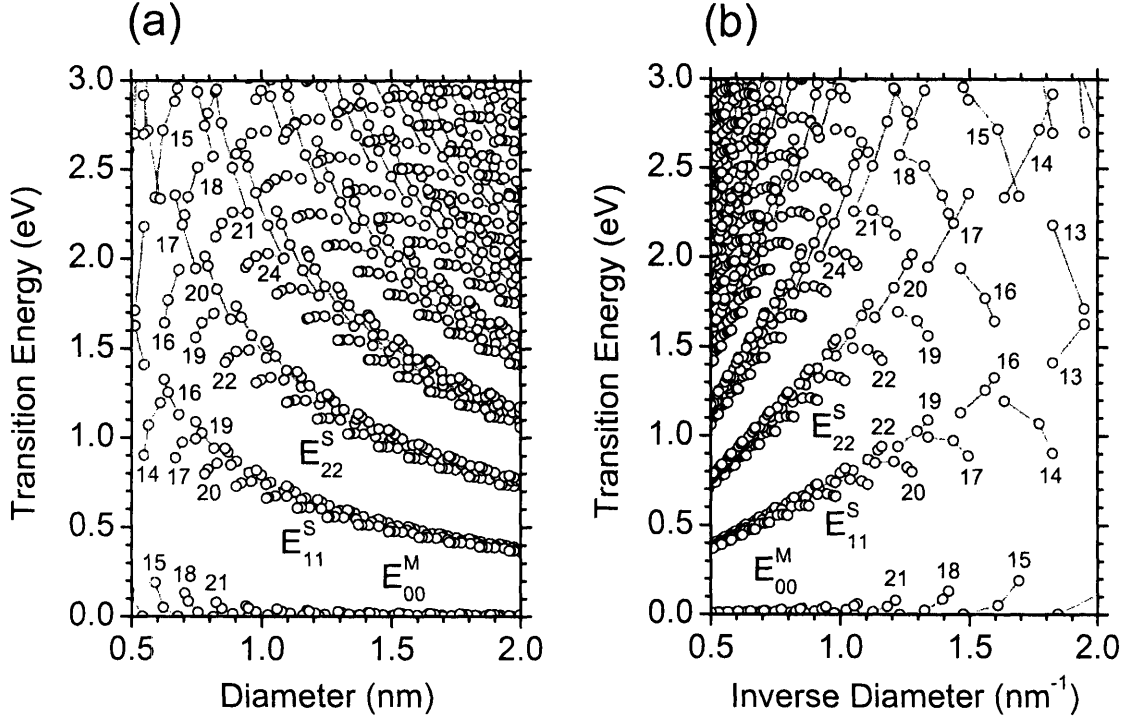


Figure 3-26: The ETB Kataura plot as a function of (a) the SWNT diameter d_t and (b) the inverse diameter $1/d_t$ similar to the STB Kataura plot in Fig. 3-13. The ETB Kataura plot is calculated directly from the ETB electronic dispersion relations of the optimized SWNTs. This approach takes into account the long-range atomic interactions, the curvature of the SWNT sidewall, and the optimized geometrical structures of the SWNTs. The red, green, and blue dots correspond to M0, S1, and S2 SWNTs, respectively. The families of constant $2n + m$ are connected by gray lines and labeled by $2n + m$ values.

RRS experimental Kataura plots of Figs. 3-16 (b) and 3-17 (b). The experimental family spread is thus attributed to the relaxation of the geometrical structures of the SWNTs [139, 143]. In spite of a good agreement in the family spread, the PL and RRS experimental Kataura plots exhibit an overall blueshift by about 200—300 meV from the ETB Kataura plot. Also, the E_{22}^S to E_{11}^S ratio in the PL and RRS experimental Kataura plots goes to 1.8 in the large d_t limit, while the E_{22}^S to E_{11}^S ratio in the ETB Kataura plot reaches the value of 2 at $d_t = 2$ nm where the family spread is small. Both the blueshift problem and the ratio problem originate from the many-body interactions in SWNTs, as discussed in Section 3.7.

3.7 Many-body effects

Because of the spatial confinement of electrons in one dimension, the Coulomb interaction between photoexcited electrons and electrons in the ground state in SWNTs is strongly enhanced compared to bulk semiconductors. The electron-electron interaction increases the single-particle transition energies by the quasiparticle self-energies. At the same time, photoexcited electrons and photogenerated holes form excitons whose binding energies are comparable but slightly smaller than the quasiparticle self-energies. Thus, the single-particle transition energies are moderately blueshifted by the Coulomb electron-electron repulsion and the exciton electron-hole attraction, together referred to as the many-body interactions.

The effect of the many-body interactions on the E_{ii} transition energies in SWNTs was first predicted theoretically using the effective-mass approximation [4]. Later on, numerous theoretical studies based on different models [70, 112, 113, 177], first-principles calculations [24, 155], ETB approximations [21, 58], and group theory [11, 12] were carried out exploring the physics of quasiparticles and excitons in SWNTs. SWNTs have a rich excitonic structure because quasiparticles near the K and K' points of the Brillouin zone have the same group velocity, and thus can form excitons [35]. Most of the oscillator strength, however, is collected by the lowest energy bright (optically active) exciton [155], which manifests itself in the PL and RRS spectra of SWNTs.

To summarize the key findings of the aforementioned works, we write the optical transition energies in SWNTs in the form:

$$E_{ii} = E_{ii}^e + {}^{2D}E_{ii}^{ee} + {}^{1D}E_{ii}^{ee} - {}^{2D}E_{ii}^{eh} - {}^{1D}E_{ii}^{eh}, \quad (3.34)$$

where E_{ii}^e is the single-particle transition energy, E_{ii}^{ee} is the quasiparticle self-energy, and E_{ii}^{eh} is the binding energy of the lowest bright exciton. Both E_{ii}^{ee} and E_{ii}^{eh} can be split into two terms, ${}^{2D}E_{ii}$ which arises from short-range interactions on scales smaller than πd_t , and ${}^{1D}E_{ii}$ which arises from long-range interactions on scales larger than πd_t [70]. Let us consider each term of Eq. (3.34) independently.

The E_{ii}^e transition energies are summarized in the ETB Kataura plot of Fig. 3-26. The ${}^{2D}E_{ii}^{ee}$ self-energy is given by the logarithmic correction term:

$${}^{2D}E_{ii}^{ee} = \frac{\sqrt{3}}{2} (\varepsilon s - t) \Delta k_i a \frac{g}{4} \ln \frac{\Lambda}{\Delta k_i}, \quad (3.35)$$

where ($\varepsilon = -5.372$ eV, $s = 0.151$, $t = -3.370$ eV) are the ETB parameters introduced in Section 3.6, g is the Coulomb interaction parameter, and Λ is an ultraviolet interaction cutoff, all of which depend on the dielectric constant κ of the SWNT environment, and Δk_i is the critical wavevector measured from the K point in the 2D Brillouin zone [70]. The latter is given by $\Delta k_1^S = 2/(3d_t)$, $\Delta k_2^S = 4/(3d_t)$, and $\Delta k_1^M = 6/(3d_t)$ for the E_{11}^S , E_{22}^S , and E_{11}^M transition energies, respectively, as discussed in Sections 3.4 and 3.5. The ${}^{2D}E_{ii}^{eh}$ binding energy in Eq. (3.34) vanishes due to the absence of excitons in the graphene sheet. The ${}^{1D}E_{ii}^{ee}$ and ${}^{1D}E_{ii}^{eh}$ terms in Eq. (3.34) scale with the SWNT diameter d_t , the reduced mass of the exciton μ_{ii} , and the dielectric constant κ of the SWNT environment [21, 113]. The reduced mass μ_{ii} is determined by the effective masses of the electron and the hole, m_i^e and m_i^v , at the critical wavevectors k_i^c and k_i^v , respectively. The effective masses m_i^e and m_i^v show a strong dependence on the SWNT diameter d_t and chiral angle θ , revealed by the ETB calculations [63]. Thus, the ${}^{1D}E_{ii}^{ee}$ and ${}^{1D}E_{ii}^{eh}$ energies develop family patterns [21, 58, 113].

In small diameter SWNTs, the ${}^{1D}E_{ii}^{ee}$ and ${}^{1D}E_{ii}^{eh}$ terms significantly exceed the ${}^{2D}E_{ii}^{ee}$ self-energy of Eq. (3.35) due to a strong spatial confinement of the Coulomb interaction. Nevertheless, ${}^{1D}E_{ii}^{ee}$ and ${}^{1D}E_{ii}^{eh}$ nearly perfectly cancel each other [58, 70]. This implies that E_{ii}^{ee} moderately exceeds E_{ii}^{eh} , and the experimental E_{ii} values are slightly blueshifted from the ETB E_{ii}^e values [4]. Such behavior is contrary to that observed in bulk semiconductors where the self-energy is small and excitonic resonances are redshifted from the band edge. If we assume that the ${}^{1D}E_{ii}^{ee}$ and ${}^{1D}E_{ii}^{eh}$ energies completely cancel out (which is a good approximation), then Eq. (3.34) reads as $E_{ii} = E_{ii}^e + {}^{2D}E_{ii}^{ee}$. Considering that ${}^{2D}E_{ii}^{ee}$ only depends on d_t and is independent of θ , the experimental family patterns in E_{ii} are entirely determined by the ETB family patterns in E_{ii}^e , with which they show a good agreement. In Fig. 3-27 (a), we

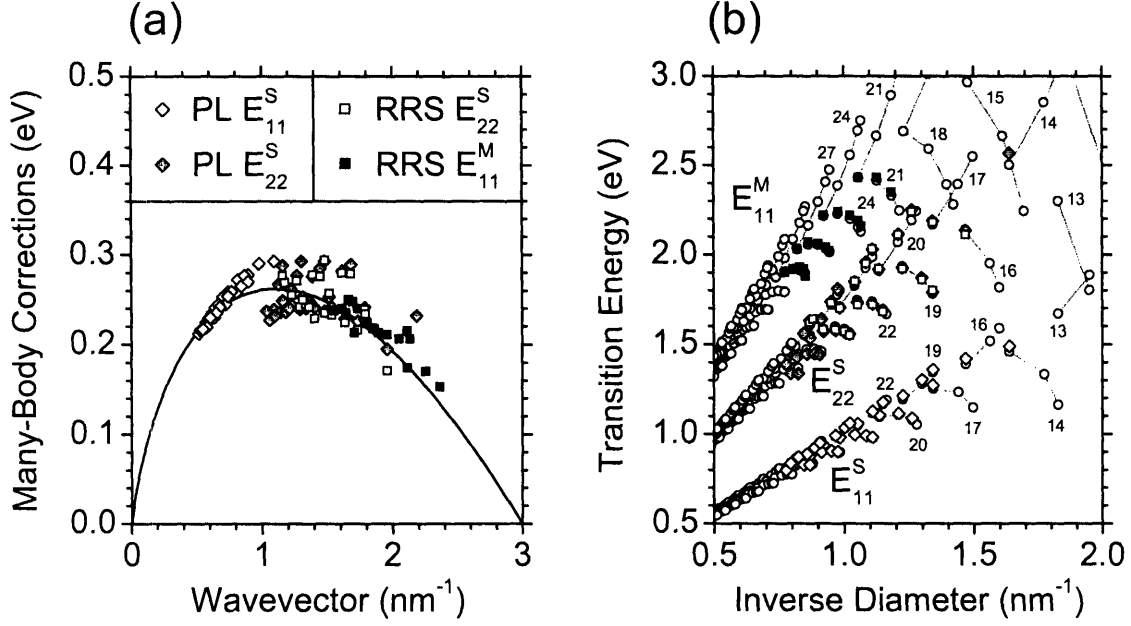


Figure 3-27: (a) The difference between the PL and RRS experimental E_{ii} and the ETB E_{ii}^e transition energies from Fig. 3-26 as a function of the wavevector Δk_i from Eq. (3.35). The light and dark diamonds show the PL E_{11}^S and E_{22}^S values from Fig. 3-16. The light and dark squares show the RRS E_{22}^S and E_{11}^M values from Fig. 3-17. The solid curve shows the best fit using Eq. (3.35) with parameters $g = 1.7$ and $\Lambda = 3 \text{ nm}^{-1}$. (b) The ETB+MB Kataura plot obtained by applying the logarithmic correction given by the solid curve in (a) to the ETB Kataura plot of Fig. 3-26. The red, green, and blue dots correspond to M0, S1, and S2 SWNTs, respectively. The families of constant $2n + m$ are connected by gray lines and labeled by their $2n + m$ values.

show the difference between the experimental E_{ii} and the ETB E_{ii}^e transition energies as a function of the wavevector Δk_i from Eq. (3.35). Fitting this difference to the functional form of Eq. (3.35) yields the parameters $g = 1.7$ and $\Lambda = 3 \text{ nm}^{-1}$, in good agreement with the previously reported values [63, 70, 139]. By applying the logarithmic correction of Eq. (3.35) to the ETB Kataura plot of Fig. 3-26, we obtain the ETB+MB Kataura plot as shown by dots in Fig. 3-27 (b). We only show the E_{11}^S , E_{22}^S , and E_{11}^M transition energies for which the PL and RRS experiments are performed. For comparison, the PL and RRS experimental E_{ii} values are shown in Fig. 3-27 (b) by diamonds and squares, respectively. One can here see a good agreement between the ETB+MB Kataura plot and the experimental data points in

Fig. 3-27(b). Note, however, that the experimental data points are extracted from PL and RRS spectra of SDS-encapsulated HiPCO SWNTs in D₂O. For the same HiPCO SWNTs wrapped with various surfactants, polymers, and single-stranded DNA molecules and suspended in aqueous media [7, 98], for HiPCO SWNTs suspended in air [105, 148, 173], and for HiPCO SWNTs aggregated into bundles [42], the experimental data points are redshifted from those shown in Fig. 3-27(b) by 10–20 meV, 70–90 meV, and 100 meV, respectively. The logarithmic correction of Eq. (3.35) should then be fitted separately for each SWNT environment, revealing the dependence of the parameters g and Λ on the dielectric constant κ of the SWNT environment. The ETB+MB Kataura plot in Fig. 3-27(b) scales accordingly with κ .

3.8 Summary and future work

In this Chapter, we reviewed the basic electronic properties of SWNTs on the basis of the simple tight-binding (STB) model. In the light of recent progress in the photoluminescence (PL) and resonance Raman spectroscopy (RRS) of small diameter SWNTs, we develop the extended tight-binding (ETB) model that shows an excellent agreement with the experimental data. The ETB model is based on the DFT-LDA calculation of the tight-binding parameters for carbon [122]. It is worth mentioning that an alternative tight-binding parameterization for carbon [110] does not fit well the PL and RRS experimental data. We demonstrate that the geometrical structure optimization of small diameter SWNTs has a significant impact on their electronic properties and, accordingly, on their PL and RRS spectra.

While performing the geometrical structure optimization of SWNTs, we fixed the torsion degree of freedom to ensure the translational symmetry of SWNTs. The geometrical structure of chiral SWNTs, however, should be optimized over the torsion degree of freedom. This will be the subject of future work. The dependence of the ETB transition energies E_{ii}^e on temperature [23, 30, 81], doping [151, 164], axial strain [29, 75, 153, 171], torsional strain [75, 171], hydrostatic pressure from the SWNT environment [22], and the dependence of the many-body corrections E_{ii}^{ee} and

E_{ii}^{eh} on the dielectric constant of the SWNT environment [7, 42, 98, 173] should be studied further. The higher-energy optical transitions (E_{33}^S , E_{44}^S , and E_{22}^M) in larger diameter SWNTs need to be considered separately [5]. The effects of incommensurability, metallicity, and diameter difference between inner and outer tubes on the optical transitions in double-wall carbon nanotubes (DWNTs) require special consideration [115].

As the ETB model has been proven to accurately predict the electronic properties of SWNTs, we use it to explore the vibrational properties of SWNTs in Chapter 4, and the electron-photon and electron-phonon interactions in SWNTs in Chapter 5. Within the ETB framework, we solve for the quasiparticle self-energy, the quasiparticle wavefunction, the exciton binding energy, and the exciton wavefunction [58]. We then investigate the exciton-photon and exciton-phonon interactions in SWNTs [59]. We further plan to calculate the PL and RRS intensities in SWNTs within the excitonic picture.

Chapter 4

Vibrational properties

We start this Chapter by reviewing the force-constant models widely used to obtain the phonon dispersion relations of the graphene sheet. We compare the predictions of these models against first-principles calculations and the results of various experiments. We then derive the phonon dispersion relations of SWNTs both from the force-constant models and by direct calculations of the dynamical matrix within the ETB framework. We consider in particular the electron-phonon interactions which soften the frequencies of certain phonons in the graphene sheet and in SWNTs, and we review the experimental evidence for such softening.

4.1 Force-constant framework

In Chapter 3, we discussed the optimized geometrical structure of the graphene sheet. When carbon atoms are displaced from their equilibrium positions, the restoring force drives them back. The dynamics of carbon atoms around their equilibrium positions is described by the equation of motion in the harmonic approximation:

$$M \frac{d^2 r_{u's'\alpha'}^\nu}{dt^2} = \sum_u \sum_s \sum_\alpha \phi_{u's'\alpha'us\alpha} (r_{us\alpha}^\nu - r_{u's'\alpha}^\nu), \quad (4.1)$$

where M is the mass of a carbon atom, \mathbf{r}_{us}^ν is the displacement vector of the atomic site us from its equilibrium position \mathbf{R}_{us} , $u = 1, \dots, U$ spans all the unit cells in the graphene sheet, $s = A, B$ labels the atomic sites within the unit cell, $\alpha = x, y, z$ are the Cartesian coordinates, ν is the phonon mode index, t is time, and $\phi_{u's'\alpha'us\alpha}$ is the interatomic force constant. The atomic displacement vector \mathbf{r}_{us}^ν is expressed by the Fourier transform:

$$\mathbf{r}_{us}^\nu = \frac{\sqrt{2}}{W} \sum_w \exp(i\mathbf{q}_w \mathbf{R}_{us} - i\omega^\nu(\mathbf{q}_w)t) \rho^\nu(\mathbf{q}_w) \mathbf{e}_s^\nu(\mathbf{q}_w), \quad (4.2)$$

where $\mathbf{e}_s^\nu(\mathbf{q}_w)$ is the normal mode displacement, $\rho^\nu(\mathbf{q}_w)$ is the amplitude of the atomic displacements, $\omega^\nu(\mathbf{q}_w)$ is the phonon frequency, \mathbf{q}_w is the phonon wavevector, $W = U$ is the number of the sampling \mathbf{q}_w points in the first Brillouin zone, and the factor of $\sqrt{2}$ comes from the orthonormality condition for the two atoms per unit cell:

$$\sum_s \sum_\alpha e_{s\alpha}^{\nu'*}(\mathbf{q}_w) e_{s\alpha}^\nu(\mathbf{q}_w) = \delta_{\nu'\nu}, \quad (4.3)$$

where $\delta_{\nu'\nu}$ is the Kronecker delta function. The normal mode displacements $\mathbf{e}_s^\nu(\mathbf{q}_w)$ are additionally constrained by the condition:

$$\mathbf{e}_s^{\nu'*}(\mathbf{q}_w) = \mathbf{e}_s^\nu(-\mathbf{q}_w), \quad (4.4)$$

to ensure that the displacement vector \mathbf{r}_{us}^ν given by Eq. (4.2) is real at the initial moment of time $t = 0$.

Substituting Eq. (4.2) into Eq. (4.1) yields:

$$\begin{aligned}
& \sum_u^U \sum_s^2 \sum_\alpha^3 \sum_w^W \phi_{u's'\alpha'us\alpha} \exp(i\mathbf{q}_w \mathbf{R}_{u's'} - i\omega^\nu(\mathbf{q}_w)t) e_{s'\alpha}^\nu(\mathbf{q}_w) \\
& - \sum_u^U \sum_s^2 \sum_\alpha^3 \sum_w^W \phi_{u's'\alpha'us\alpha} \exp(i\mathbf{q}_w \mathbf{R}_{us} - i\omega^\nu(\mathbf{q}_w)t) e_{s\alpha}^\nu(\mathbf{q}_w) \\
& = \sum_w^W M\omega^{\nu 2}(\mathbf{q}_w) \exp(i\mathbf{q}_w \mathbf{R}_{u's'} - i\omega^\nu(\mathbf{q}_w)t) e_{s'\alpha}^\nu(\mathbf{q}_w).
\end{aligned} \tag{4.5}$$

Upon multiplying Eq. (4.5) by $\exp(-i\mathbf{q}_{w'} \mathbf{R}_{u's'} + i\omega^\nu(\mathbf{q}_{w'})t)$, taking a summation over $u' = 1, \dots, U$, and using the orthogonality condition:

$$\sum_{u'}^U \exp(i(\mathbf{q}_w - \mathbf{q}_{w'}) \mathbf{R}_{u's'}) = U\delta_{ww'}, \tag{4.6}$$

we obtain the equation of motion in the matrix form:

$$\sum_s^2 \sum_\alpha^3 D_{s'\alpha's\alpha}(\mathbf{q}_{w'}) e_{s\alpha}^\nu(\mathbf{q}_{w'}) = M\omega^{\nu 2}(\mathbf{q}_{w'}) e_{s'\alpha'}^\nu(\mathbf{q}_{w'}), \tag{4.7}$$

where $D_{s'\alpha's\alpha}(\mathbf{q}_{w'})$ is the dynamical matrix defined by:

$$D_{s'\alpha's\alpha}(\mathbf{q}_{w'}) = \sum_u^U \left(\delta_{s's} \sum_{s''}^2 \phi_{u's''\alpha'us\alpha} - \exp(i\mathbf{q}_{w'} (\mathbf{R}_{us} - \mathbf{R}_{u's'})) \phi_{u's'\alpha'us\alpha} \right), \tag{4.8}$$

with the index u' labeling the unit cell under consideration [129].

The lattice dynamics of the graphene sheet is described by Eq. (4.7) with the 6×6 dynamical matrix of Eq. (4.8). Diagonalizing this matrix gives the phonon dispersion curves $\omega^\nu(\mathbf{q}_w)$ and the normal mode displacements $\mathbf{e}_s^\nu(\mathbf{q}_w)$ labeled by the index $\nu = 1, \dots, 6$. Solving for $\omega^\nu(\mathbf{q}_w)$ requires a knowledge of the interatomic force constants $\phi_{u's'\alpha'us\alpha}$, which will be discussed later on in Sections 4.2 and 4.3. On the other hand, the form of $\mathbf{e}_s^\nu(\mathbf{q}_w)$ is determined by the symmetry of the graphene sheet, independent on the force constant parameters. Below, we derive the normal mode displacements in the graphene sheet at the Γ and K points of the first Brillouin zone, $\mathbf{e}_s^\nu(\Gamma)$ and $\mathbf{e}_s^\nu(\text{K})$, following a common group theory procedure [34].

The group of the wavevector at the Γ point (G_Γ) is isomorphic to the point group

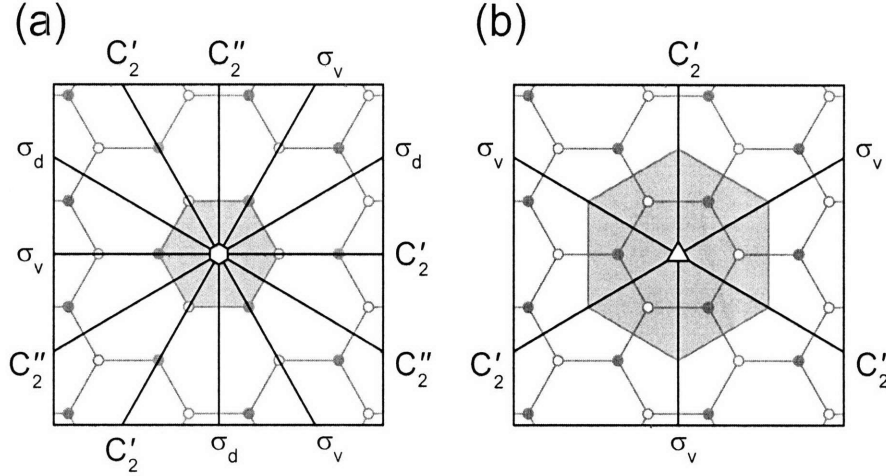


Figure 4-1: A single graphene sheet. The open and solid dots indicate the A and B sublattices, respectively. (a) The two-atom unit cell at the Γ point from Fig. 2-1 and (b) the six-atom supercell at the K point from Fig. 3-6 are shaded in gray. The symmetry of the unit cell in (a) and the supercell in (b) are described by the point groups D_{6h} and D_{3h} , correspondingly. The symmetry operations of the point groups D_{6h} and D_{3h} are shown in (a) and (b). The high-symmetry rotation axes C_6 and C_3 are indicated by a small hexagon in (a) and a small triangle in (b), accordingly. The rotation axes C_2' and C_2'' and the mirror planes σ_v and σ_d are shown by black lines. The mirror plane σ_h coincides with the image plane. The character tables of the point groups D_{6h} and D_{3h} are given in Tables 4.1 and 4.2.

D_{6h} . The symmetry operations and the character table for the point group D_{6h} are shown in Fig. 4-1 (a) and Table 4.1, respectively. By applying the symmetry operations to the atomic sites (a.s.) in Fig. 4-1 (a), we find the characters for the equivalence transformation, $\chi_{a.s.}$, which represents the number of atoms that are invariant under the symmetry operations of the point group D_{6h} . Using Table 4.1, we decompose $\chi_{a.s.}$ into the characters of irreducible representations, yielding the representation for the equivalence transformation, $\Gamma_{a.s.} = A_{1g} + B_{1u}$. The representation for a vector is given by $\Gamma_{vec.} = A_{2u} + E_{1u}$, according to Table 4.1. We then find the characters for the molecular vibrations, $\chi_{m.v.}$, by taking the direct product of $\chi_{a.s.}$ with the characters $\chi_{vec.}$ for a vector. Again, we decompose $\chi_{m.v.}$ into the characters of irreducible representations. Finally, we express the representation for the molecular vibrations in terms of irreducible representations, $\Gamma_{m.v.} = A_{2u} + B_{2g} + E_{1u} + E_{2g}$.

We now construct the normal mode displacements for each irreducible representa-

Table 4.1: The character table for the point group D_{6h} which describes the symmetry of the two-atom unit cell of the graphene sheet at the Γ point shown in Fig. 4-1 (a). The top row consists of the symmetry operations shown in Fig. 4-1 (a). The first two columns give the symmetries of the first and second order combinations of Cartesian coordinates. Infinitesimal rotations are listed as R_x , R_y , and R_z .

D_{6h} ($6/mmm$)		E	$2C_6$	$2C_3$	C_2	$3C_2'$	$3C_2''$	I	$2S_3$	$2S_6$	σ_h	$3\sigma_d$	$3\sigma_v$
x^2+y^2, z^2	A_{1g}	1	1	1	1	1	1	1	1	1	1	1	1
—	A_{1u}	1	1	1	1	1	1	-1	-1	-1	-1	-1	-1
—	A_{2g}	1	1	1	1	-1	-1	1	1	1	1	-1	-1
—	A_{2u}	1	1	1	1	-1	-1	-1	-1	-1	-1	1	1
—	B_{1g}	1	-1	1	-1	1	-1	1	-1	1	-1	1	-1
—	B_{1u}	1	-1	1	-1	1	-1	-1	-1	-1	1	-1	1
—	B_{2g}	1	-1	1	-1	-1	1	1	-1	1	-1	-1	1
—	B_{2u}	1	-1	1	-1	-1	1	-1	1	-1	1	1	-1
—	E_{1u}	2	1	-1	-2	0	0	-2	-1	1	2	0	0
xz, yz	E_{1g}	2	1	-1	-2	0	0	2	1	-1	-2	0	0
—	E_{2u}	2	-1	-1	2	0	0	-2	1	1	-2	0	0
x^2-y^2, xy	E_{2g}	2	-1	-1	2	0	0	2	-1	-1	2	0	0

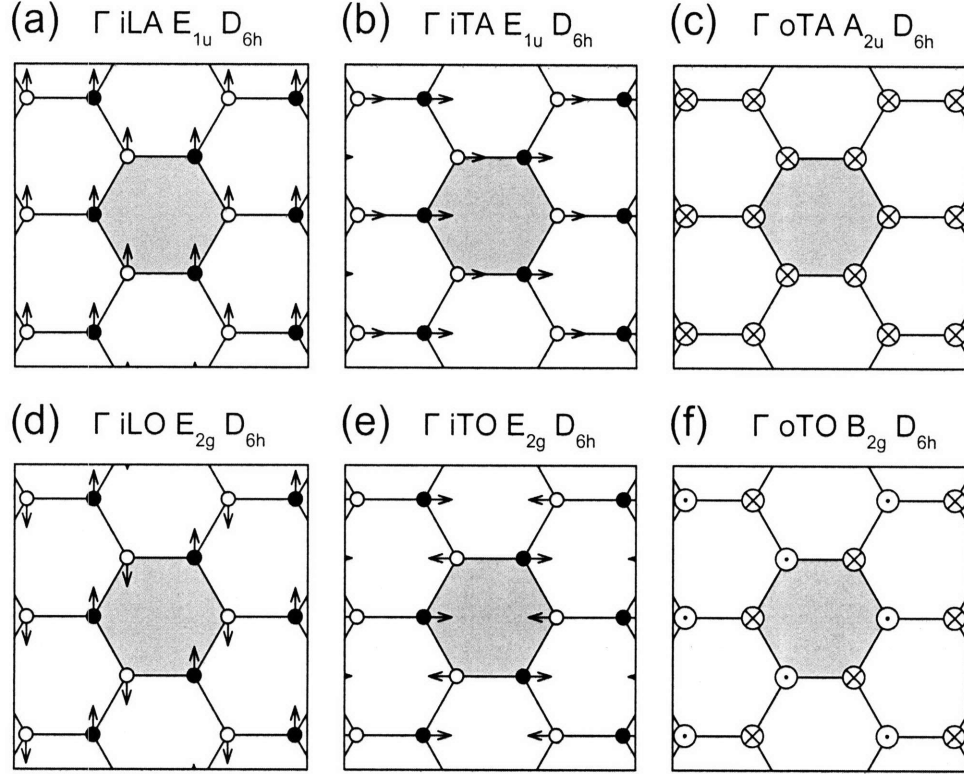


Figure 4-2: A single graphene sheet. The open and solid dots indicate the A and B sublattices, respectively. The arrows show directions of the normal mode displacements for the six phonon modes of the graphene sheet at the Γ point, $\mathbf{e}_s^\nu(\Gamma)$, obtained from the character table for the point group D_{6h} given in Table 4.1. The labels of the phonon modes are explained in the text. The dotted and crossed points in (c) and (f) represent the vectors pointing in and out of the image plane.

tion in $\Gamma_{m.v.}$. By applying the projector algebra [34] to the motion of the atomic sites in Fig. 4-1 (a) along the directions of the Cartesian coordinates, we find the characters and, accordingly, the irreducible representations, of which the motion of the atomic sites consists. The atomic motion of the normal modes is shown in Figs. 4-2 (a) to (f). Each of the modes in Fig. 4-2 is labeled by an irreducible representation of $\Gamma_{m.v.}$. We also label these modes as the in-plane and out-of-plane, the longitudinal and transverse, and the acoustic and optical (iLA, iTA, oTA, iLO, iTO, oTO) modes, according to the directions of the atomic displacements within the unit cell.

The lattice distortions caused by the K point phonon modes are incommensurate with the two-atom unit cell of the graphene sheet. The six-atom supercell is thus

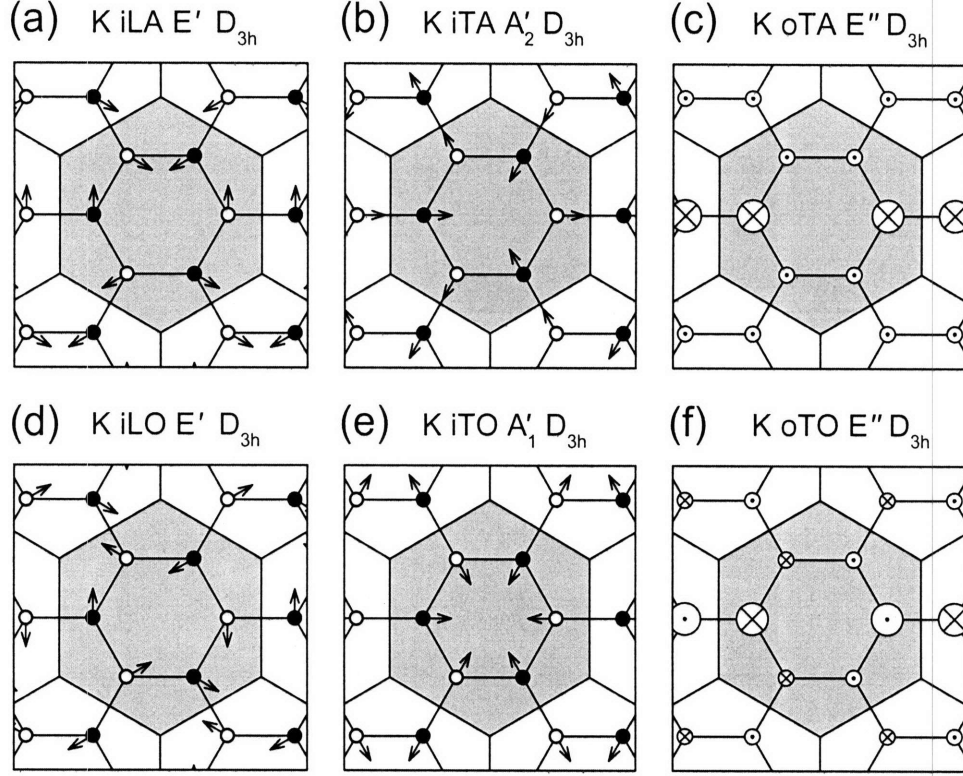


Figure 4-3: A single graphene sheet. The open and solid dots indicate the A and B sublattices, respectively. The arrows show directions of the atomic displacements for the six stationary phonon modes of the graphene sheet at the K point, $\mathbf{e}'_s(\mathbf{K})$, obtained by rotating the arrows shown in Fig. 4-2 by angles $\pm 2\pi/3$. The labels of the phonon modes are explained in the text. The dotted and crossed points in (c) and (f) represent the vectors pointing in and out of the image plane. The large and small points in (c) and (f) indicate the magnitudes of the vectors equal to $\sqrt{2}$ and $1/\sqrt{2}$, respectively, of the magnitudes of the vectors in (a), (b), (d), and (e).

introduced in Fig. 4-2, as discussed in Section 3.3 of Chapter 3. The normal mode displacements $\mathbf{e}'_s(\mathbf{K})$ differ from those in Fig. 4-2 by the phase factor $\exp(i\mathbf{q}\mathbf{R}_{us})$, where $\mathbf{q} = (0, -4\pi/(3a))$ at the K point and $\mathbf{R}_{us} \cdot \hat{\mathbf{y}} = \pm a/2$ within the six-atom supercell. The normal mode displacements $\mathbf{e}'_s(\mathbf{K})$ are thus obtained by rotating $\mathbf{e}'_s(\Gamma)$ in Fig. 4-2 by angles $\pm 2\pi/3$, as shown in Fig. 4-3. In contrast to the Γ point, the longitudinal and transverse components, as well as the acoustic and optical components, are completely mixed at the K point. Nevertheless, we label the modes in Fig. 4-4 as the (iLA, iTA, oTA, iLO, iTO, oTO) to identify the branch of the phonon dispersion relations at the Γ point from which they arise.

Table 4.2: The character table for the point group D_{3h} which describes the symmetry of the six-atom supercell of the graphene sheet at the K point shown in Fig. 4-1 (b). The top row consists of the symmetry operations shown in Fig. 4-1 (b). The first two columns give the symmetries of the first and second order combinations of Cartesian coordinates. Infinitesimal rotations are listed as R_x , R_y , and R_z .

$D_{3h} (-6m2)$			E	$2C_3$	$3C'_2$	$2S_3$	σ_h	$3\sigma_v$
x^2+y^2, z^2	—	A'_1	1	1	1	1	1	1
—	R_z	A'_2	1	1	-1	1	1	-1
—	—	A''_1	1	1	1	-1	-1	-1
—	z	A''_2	1	1	-1	-1	-1	1
x^2-y^2, xy	x, y	E'	2	-1	0	-1	2	0
xz, yz	R_x, R_y	E''	2	-1	0	1	-2	0

The normal mode displacements $\mathbf{e}'_s(\mathbf{K})$ can be derived in a more formal way, following the same approach described above for the case of $\mathbf{e}'_s(\Gamma)$. The group of the wavevector at the K point (G_K) is isomorphic to the point group D_{3h} . The symmetry operations and the character table for the point group D_{3h} are shown in Fig. 4-1 (b) and Table 4.2, respectively. We then obtain $\Gamma_{a.s.} = E'$, $\Gamma_{vec.} = A''_2 + E'$, and $\Gamma_{m.v.} = A'_1 + A'_2 + E' + E''$ for the point group D_{3h} . By applying the projector algebra [34] to the atomic displacements shown in Fig. 4-3, we find the characters and, accordingly, the irreducible representations, of which the motion of the atomic sites consists. The atomic motion of the normal modes is shown in Figs. 4-4 (a) to (f). Each of the modes in Fig. 4-4 is labeled by an irreducible representation of $\Gamma_{m.v.}$. While Figs. 4-4 (c) to (f) coincide with Figs. 4-3 (c) to (f), the normal mode displacements in Figs. 4-4 (a) and (b) differ from the atomic displacements in Figs. 4-3 (a) and (b) by phase factors $\exp(\pm i\pi/2)$ that rotate the atomic displacements by angles $\pm\pi/2$. The phonon modes in Figs. 4-4 (a) and (b) thus have higher symmetry than those in Figs. 4-3 (a) and (b).

The A'_1 and A'_2 phonon modes shown in Figs. 4-4 (b) and (e) obey C_6 symmetry, while the E' and E'' phonon modes in Figs. 4-4 (a), (c), (d), and (f) have the C_2 rotation axes. At the same time, the point group D_{3h} contains the C_3 rotation axis, but neither C_6 nor C_2 axes. This contradiction is understood by taking into account

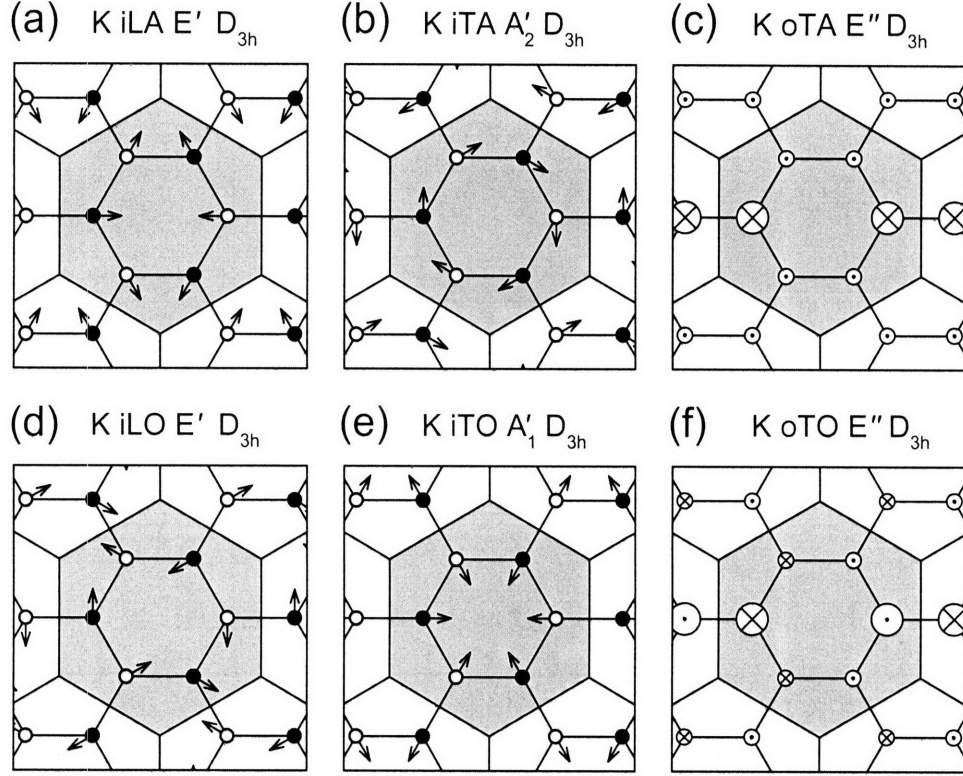


Figure 4-4: A single graphene sheet. The open and solid dots indicate the A and B sublattices, respectively. The arrows show directions of the normal mode displacements for the six stationary phonon modes of the graphene sheet at the K point, $\mathbf{e}_s''(\mathbf{K})$, obtained from the character table for the point group D_{3h} given in Table 4.2. Note that the arrows in (a) and (b) are obtained by rotating the arrows in Figs. 4-3 (a) and (b) by angles $\pm\pi/2$. The labels of the phonon modes are explained in the text. The dotted and crossed points in (c) and (f) represent the vectors pointing in and out of the image plane. The large and small points in (c) and (f) indicate the magnitudes of the vectors equal to $\sqrt{2}$ and $1/\sqrt{2}$, respectively, of the magnitudes of the vectors in (a), (b), (d), and (e).

that the complex traveling phonon modes at the K and K' points only have the C_3 rotation axes. Time-reversal symmetry mixes the complex traveling phonon modes at the K and K' points into the real stationary phonon modes that obey D_{6h} symmetry. The stationary phonon modes shown in Figs. 4-4 thus preserve the C_6 and C_2 rotation axes [86].

4.2 Basic force-constant model

The lattice dynamics of the graphene sheet is described by the equation of motion, Eq. (4.7), with the dynamical matrix of Eq. (4.8) expressed through the interatomic force constants, $\phi_{u's'\alpha'us\alpha}$. For each pair $u's'us$ of carbon atoms, the interatomic force constants $\phi_{u's'\alpha'us\alpha}$ are written in the form of the 3×3 force constant matrix $\Phi_{u's'us}$ over the coordinates α', α defined by $(\Phi_{u's'us})_{\alpha'\alpha} = \phi_{u's'\alpha'us\alpha}$. The force constant matrices are usually constructed using the normal coordinates $\alpha', \alpha = ir, it, ot$, corresponding to the in-plane radial, in-plane tangential, and out-of-plane tangential displacements of carbon atoms, as shown in Fig. 4-5 (a), rather than Cartesian coordinates $\alpha', \alpha = x, y, z$. The force constant matrices are then transformed from $\Phi_{u's'us}^{\text{norm}}$ in the normal coordinates to $\Phi_{u's'us}^{\text{cart}}$ in Cartesian coordinates by means of rotation matrices.

Within the basic force-constant (BFC) model, we consider the force constants up to the fourth shell of the nearest neighbors [129]. The inclusion of the four shells of the nearest neighbors is essential in order to describe the twisted motion of carbon atoms in the graphene sheet [129]. Within the BFC framework, we further neglect off-diagonal elements of the force constant matrices in the normal coordinates [129]. While the in-plane and out-of-plane motions are decoupled in the flat graphene sheet implying $\phi_{u's'\alpha'us\alpha} = 0$ for $(\alpha', \alpha) = (ir, ot), (it, ot), (ot, ir), (ot, it)$, the in-plane off-diagonal matrix elements of the force constant matrices, $\phi_{u's'\alpha'us\alpha}$ for $(\alpha', \alpha) = (ir, it), (it, ir)$, are in fact small but not zero, as will be shown in Section 4.3. Upon neglecting these matrix elements, we label the force constants as $\phi_{u's'us\alpha} = 0$ for brevity, reflecting the fact that $\alpha' = \alpha$.

The four shells of the nearest neighbors of atom A are shown by the circles in Fig. 4-5 (b). Note that the first, third, and fourth shells consist of atoms B of the opposite type than the central A atom, while the same A atoms appear in the second shell. Each atom within the four shells is labeled by a pair of indices, ιj instead of us , where $\iota = 1, \dots, 4$ indicates the shell number and j numerates the atoms in each shell counterclockwise looking down the z -axis. The first atom $j = 1$ within each shell ι appears in the positive direction of the x -axis. The indices $\iota j = 11, 12, 13$ for the

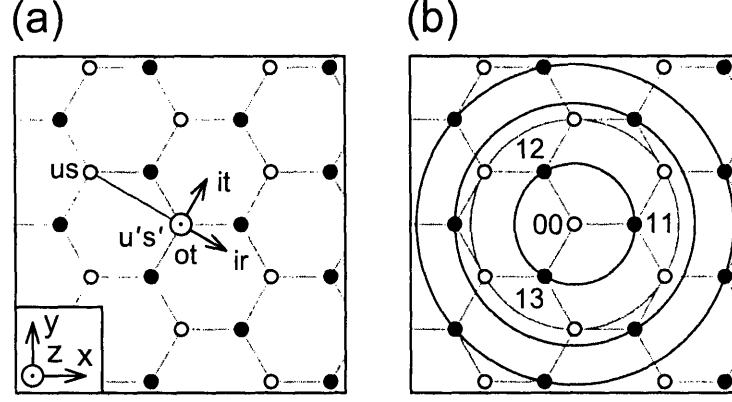


Figure 4-5: A single graphene sheet. The open and solid dots indicate the A and B sublattices, respectively. (a) The normal coordinates (ir, it, ot) for a pair of us and $u's'$ atoms connected by the red line. The dotted points represent the vectors ot and z pointing out of the image plane. (b) The four shells of the nearest neighbors of the central A atom are shown by circles. The shells that consist of the A and B atoms are shown in green and blue, respectively. The central A atom and the three B atoms from the first shell are labeled by indices $\nu_j = 00$ and $\nu_j = 11, 12, 13$, respectively. The nearest neighbor shells of the central B atom can be obtained by rotating the image by 180° .

first shell $\nu = 1$ are shown in Fig. 4-5 (b). The central A atom is referred by $\nu_j = 00$ instead of $u's'$. The indices $\nu_j = 00$ for the central atom are shown in Fig. 4-5 (b). In this notation, the force constant matrices $\Phi_{u's'us}$ and the force constants $\phi_{u's'us\alpha}$ are written as $\Phi_{00\nu_j}$ and $\phi_{00\nu_j\alpha}$, respectively. In the normal coordinates $\alpha = ir, it, ot$, the force constants $\phi_{00\nu_j\alpha}$ within each shell ν are equivalent. Thus, $\phi_{00\nu_j\alpha}$ is independent of index j , and so does $\Phi_{00\nu_j}^{\text{norm}}$. Hence, we label $\phi_{00\nu_j\alpha}$ as $\phi_\alpha^{(\nu)}$, assuming $\alpha = ir, it, ot$.

For the pairs of atoms $00\nu_j$, the normal coordinate system is rotated by the angles $\phi_{00\nu_j}$ from the Cartesian coordinate system around the common axis $ot = z$, as one can see in Fig. 4-5 (a). The force constant matrices in the normal coordinates:

$$\Phi_{00\nu_j}^{\text{norm}} = \begin{pmatrix} \phi_{ir}^{(\nu)} & 0 & 0 \\ 0 & \phi_{it}^{(\nu)} & 0 \\ 0 & 0 & \phi_{ot}^{(\nu)} \end{pmatrix} \quad (4.9)$$

are then transformed to Cartesian coordinates by means of the rotation matrix

$R^z(\phi_{00\iota j})$ given by Eq. (3.31) and its transpose $R^{z\text{T}}(\phi_{00\iota j})$:

$$\Phi_{00\iota j}^{\text{cart}} = R^{z\text{T}}(\phi_{00\iota j})\Phi_{00\iota j}^{\text{norm}}R^z(\phi_{00\iota j}). \quad (4.10)$$

Upon substituting Eq. (3.31) into Eq. (4.10), we obtain the force constant matrices in Cartesian coordinates:

$$\Phi_{00\iota j}^{\text{cart}} = \begin{pmatrix} \phi_{ir}^{(\iota)} \cos^2 \phi_{00\iota j} + \phi_{it}^{(\iota)} \sin^2 \phi_{00\iota j} & (\phi_{ir}^{(\iota)} - \phi_{it}^{(\iota)}) \cos \phi_{00\iota j} \sin \phi_{00\iota j} & 0 \\ (\phi_{ir}^{(\iota)} - \phi_{it}^{(\iota)}) \cos \phi_{00\iota j} \sin \phi_{00\iota j} & \phi_{ir}^{(\iota)} \sin^2 \phi_{00\iota j} + \phi_{it}^{(\iota)} \cos^2 \phi_{00\iota j} & 0 \\ 0 & 0 & \phi_{ot}^{(\iota)} \end{pmatrix}. \quad (4.11)$$

For the first shell of the nearest neighbors $\iota j = 11, 12, 13$, the rotation angles are given by $\phi_{0011} = \pi$, $\phi_{0012} = -\pi/3$, and $\phi_{0013} = \pi/3$, according to Fig. 4-5 (b). Upon substituting these angles into Eq. (4.11), we obtain the force constant matrices in Cartesian coordinates:

$$\Phi_{0011}^{\text{cart}} = \begin{pmatrix} \phi_{ir}^{(1)} & 0 & 0 \\ 0 & \phi_{it}^{(1)} & 0 \\ 0 & 0 & \phi_{ot}^{(1)} \end{pmatrix}, \quad (4.12)$$

$$\Phi_{0012}^{\text{cart}} = \begin{pmatrix} \frac{1}{4}\phi_{ir}^{(1)} + \frac{3}{4}\phi_{it}^{(1)} & -\frac{\sqrt{3}}{4}(\phi_{ir}^{(1)} - \phi_{it}^{(1)}) & 0 \\ -\frac{\sqrt{3}}{4}(\phi_{ir}^{(1)} - \phi_{it}^{(1)}) & \frac{3}{4}\phi_{ir}^{(1)} + \frac{1}{4}\phi_{it}^{(1)} & 0 \\ 0 & 0 & \phi_{ot}^{(1)} \end{pmatrix}, \quad (4.13)$$

$$\Phi_{0013}^{\text{cart}} = \begin{pmatrix} \frac{1}{4}\phi_{ir}^{(1)} + \frac{3}{4}\phi_{it}^{(1)} & \frac{\sqrt{3}}{4}(\phi_{ir}^{(1)} - \phi_{it}^{(1)}) & 0 \\ \frac{\sqrt{3}}{4}(\phi_{ir}^{(1)} - \phi_{it}^{(1)}) & \frac{3}{4}\phi_{ir}^{(1)} + \frac{1}{4}\phi_{it}^{(1)} & 0 \\ 0 & 0 & \phi_{ot}^{(1)} \end{pmatrix}, \quad (4.14)$$

In a similar fashion, the force constant matrices for the shells $\iota = 2, 3, 4$ and those for the central B atom are transformed to Cartesian coordinates using Eq. (4.11). The resulting force constant matrices multiplied by the appropriate phase factors build up the dynamical matrix, according to Eq. (4.8). Thus, the dynamical matrix within the BFC model is determined by 12 force constant parameters $\phi_{\alpha}^{(\iota)}$ with $\iota = 1, \dots, 4$ and $\alpha = ir, it, ot$.

4.2.1 Electron and neutron scattering

The early determination of the phonon dispersion relations of the graphene sheet involved fitting the force constant parameters to experimental data. A widely used set of the force constants [61] was obtained by fitting the BFC model to the phonon dispersion curves along the ΓM direction measured by coherent inelastic neutron scattering from highly oriented pyrolytic graphite (HOPG) [101] and by reflection electron-energy-loss spectroscopy from bulk graphite [106]. The resulting force constant parameters are summarized in Table 4.3. The phonon dispersion relations of the graphene sheet calculated with the help of these force constants are shown in Fig. 4-6 along with the aforementioned experimental data. One can see a good agreement with experiment along the ΓM direction. However, there were no experimental data available around the K point at that time. Later on, the phonon dispersion curves along the ΓK direction were measured by high-resolution electron-energy-loss spectroscopy from a graphite flake [146], yet the experimental data were quite noisy near the K point. We show these data in Fig. 4-6, even though these data were not involved in the determination of the force constant parameters [61].

4.2.2 Resonance Raman scattering

In the light of recent advances in resonance Raman spectroscopy of SWNTs [36], the force constants listed in Table 4.3 were revisited. The double resonance Raman scattering in the graphene sheet involves phonons near the Γ and K points [161]. The detailed theory of the double resonance mechanism will be presented in more detail in Chapter 5. At the moment, it is only essential to mention that the double resonance process allows probing the phonon frequencies at a certain distance from the Γ and K points, which is determined by the excitation laser energy [134]. The strongest double resonance features in the Raman spectra of graphitic materials, the disorder-induced D -band and its overtone, the G' -band, were attributed to the iLO phonon mode near the K point [88]. However, the slope of the iLO phonon curve near the K point shown in Fig. 4-6(b) does not match the dispersion of the D -

Table 4.3: The force constants for a graphene sheet within the BFC model (in units of 10^4 dyn/cm; $1 \text{ dyn/cm} = 6.2415 \text{ meV/nm}^2$) fitted [61] to the results of coherent inelastic neutron scattering (INS) from highly oriented pyrolytic graphite (HOPG) [101] and reflection electron-energy-loss spectroscopy (EELS) from bulk graphite [106]. The corresponding phonon dispersion relations are shown in Fig. 4-6.

	ϕ_{ir}	ϕ_{it}	ϕ_{ot}
$\phi^{(1)}$	+36.50	+24.50	+9.82
$\phi^{(2)}$	+8.80	-3.23	-0.40
$\phi^{(3)}$	+3.00	-5.25	+0.15
$\phi^{(4)}$	-1.92	+2.29	-0.58

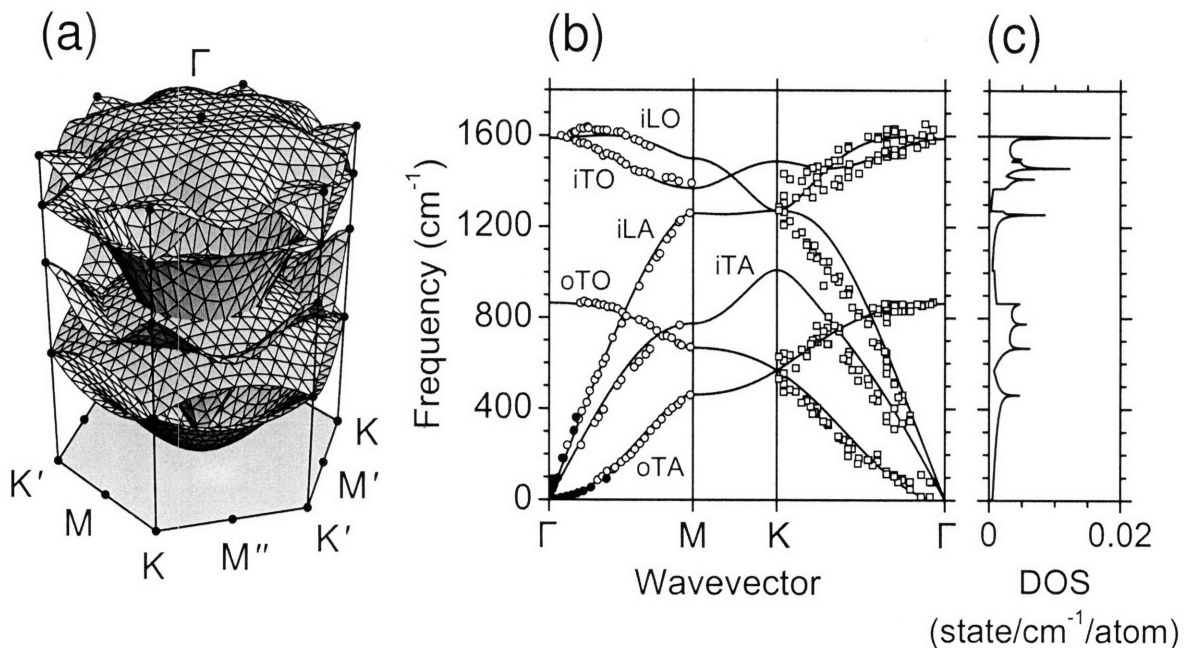


Figure 4-6: Phonon dispersion relations of a graphene sheet according to the BFC model with the force constants [61] given in Table 4.3 (a) throughout the entire first Brillouin zone shown in Fig. 2-1 and (b) along the high-symmetry directions in the first Brillouin zone. The phonon modes are labeled by iLA, iTA, oTA, iLO, iTO, and oTO, as discussed in Section 4.1 and shown in Figs. 4-2 and 4-4. The solid dots, open dots, and open squares show the results of coherent inelastic neutron scattering from highly oriented pyrolytic graphite (HOPG) [101], reflection electron-energy-loss spectroscopy from bulk graphite [106], and high-resolution electron-energy-loss spectroscopy from a graphite flake [146], respectively. (c) The density of phonon states (DOS).

Table 4.4: The force constants for a graphene sheet within the BFC model (in units of 10^4 dyn/cm; 1 dyn/cm = 6.2415 meV/nm²) fitted [47] to the results of resonance Raman scattering (RRS) from highly oriented pyrolytic graphite (HOPG) [73, 74], HOPG and SWNT bundles [160], graphite whisker (GW) [159], and SWNT bundles [79]. The corresponding phonon dispersion relations are shown in Fig. 4-7.

	ϕ_{ir}	ϕ_{it}	ϕ_{ot}
$\phi^{(1)}$	+40.37	+25.18	+9.40
$\phi^{(2)}$	+2.76	+2.22	-0.08
$\phi^{(3)}$	+0.05	-8.99	-0.06
$\phi^{(4)}$	+1.31	+0.22	-0.63

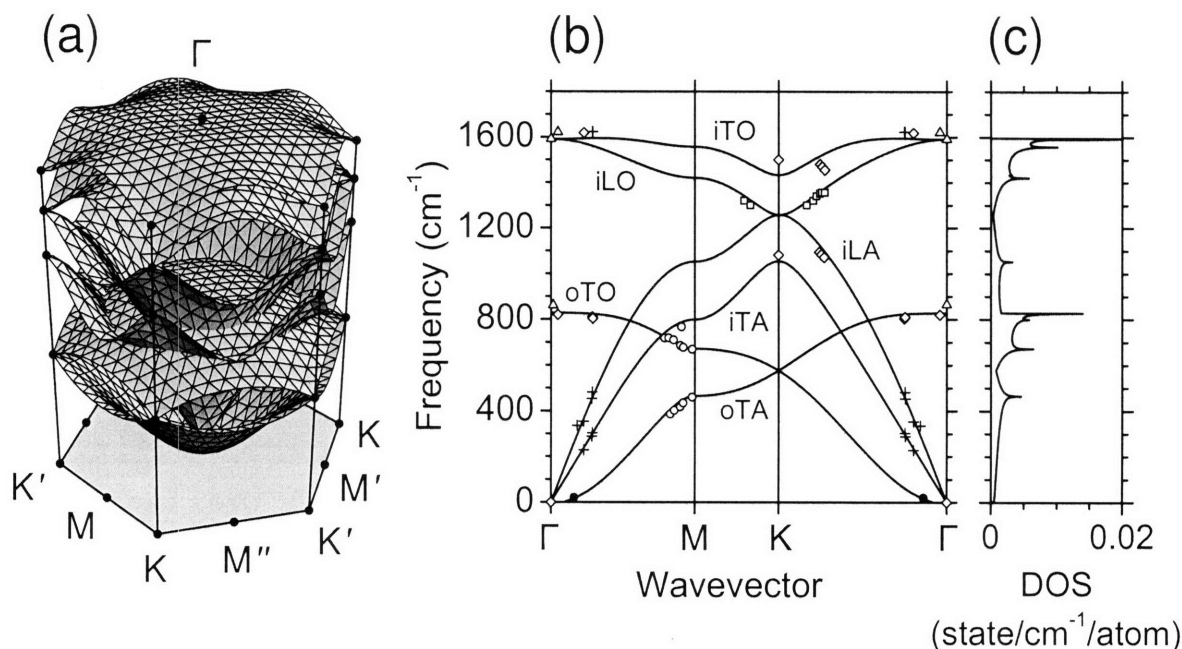


Figure 4-7: Phonon dispersion relations of a graphene sheet according to the BFC model with the force constants [47] given in Table 4.4 (a) throughout the entire first Brillouin zone shown in Fig. 2-1 and (b) along the high-symmetry directions in the first Brillouin zone. The phonon modes are labeled by iLA, iTA, oTA, iLO, iTO, and oTO, as discussed in Section 4.1 and shown in Figs. 4-2 and 4-4. The diamonds, crosses, triangles, and squares show the results of resonance Raman scattering from highly oriented pyrolytic graphite (HOPG) [73, 74], HOPG and SWNT bundles [160], graphite whisker (GW) [159], and SWNT bundles [79], respectively. The solid and open dots are experimental data taken from Fig. 4-6 for a better fit. (c) The density of phonon states (DOS).

band and the G' -band with respect to the excitation laser energy ($\partial\omega/\partial E_{\text{laser}}$) [88]. The force constant parameters shown in Table 4.3 must therefore be refitted to the experimental data near the K point. The corrected set of the force constants [47] was obtained by fitting the BFC model to the results of resonance Raman scattering from highly oriented pyrolytic graphite (HOPG) [73, 74], HOPG and SWNT bundles [160], graphite whisker (GW) [159], and SWNT bundles [79], taken at several different laser excitation energies. The resulting force constant parameters are listed in Table 4.4, and the corresponding phonon dispersion relations of the graphene sheet are shown in Fig. 4-7 along with Raman spectroscopic data. One can see that the slope of the iLO phonon branch around the K point reflects the proper dispersion of the D -band shown by squares in Fig. 4-7 (b). Also, the iLO and iTO phonon modes calculated using a new set of the force constants do not cross each other near the K point and, correspondingly, switch between each other around the Γ point.

4.2.3 Phonon trigonal warping effect

The double resonance process averages out different directions around the Γ and K points in graphite and SWNT bundles. Nevertheless the experimental points in Fig. 4-7 (b) are placed along the high-symmetry directions ΓM , ΓK , KM , and $\text{K}\Gamma$, for simplicity and ease of fitting. The anisotropy of the phonon dispersion relations around the Γ and K points in the first Brillouin zone of a graphene sheet is thus smeared out during the fitting of the Raman spectroscopic data shown in Fig. 4-7 (b). On the other hand, the double resonance process for individual SWNTs is selective not only of the magnitude, but also of the direction of the phonon wavevectors measured from the Γ and K points in the first Brillouin zone of the graphene sheet [142]. To capture the phonon anisotropy within the BFC model [142], we fit the force constants to the frequencies of the G' -band peaks in the resonance Raman spectra of individual CVD SWNTs on a Si/SiO₂ substrate [65]. The resulting set of the force constants along with the phonon dispersion relations are given in Table 4.5 and Fig. 4-8, respectively. The experimental points are shown by dots around the K and K' points on the iLO phonon dispersion surface in Fig. 4-8 (a). The same points

Table 4.5: The force constants for a graphene sheet within the BFC model (in units of 10^4 dyn/cm; $1 \text{ dyn/cm} = 6.2415 \text{ meV/nm}^2$) fitted [142] to the results of resonance Raman scattering (RRS) from individual CVD SWNTs on a Si/SiO₂ substrate revealing the phonon trigonal warping effect (TWE) [65]. The corresponding phonon dispersion relations are shown in Fig. 4-8.

	ϕ_{ir}	ϕ_{it}	ϕ_{ot}
$\phi^{(1)}$	+41.32	+23.65	+9.28
$\phi^{(2)}$	+1.22	+3.98	-0.08
$\phi^{(3)}$	-3.03	-11.50	-0.06
$\phi^{(4)}$	+3.80	+0.93	-0.62

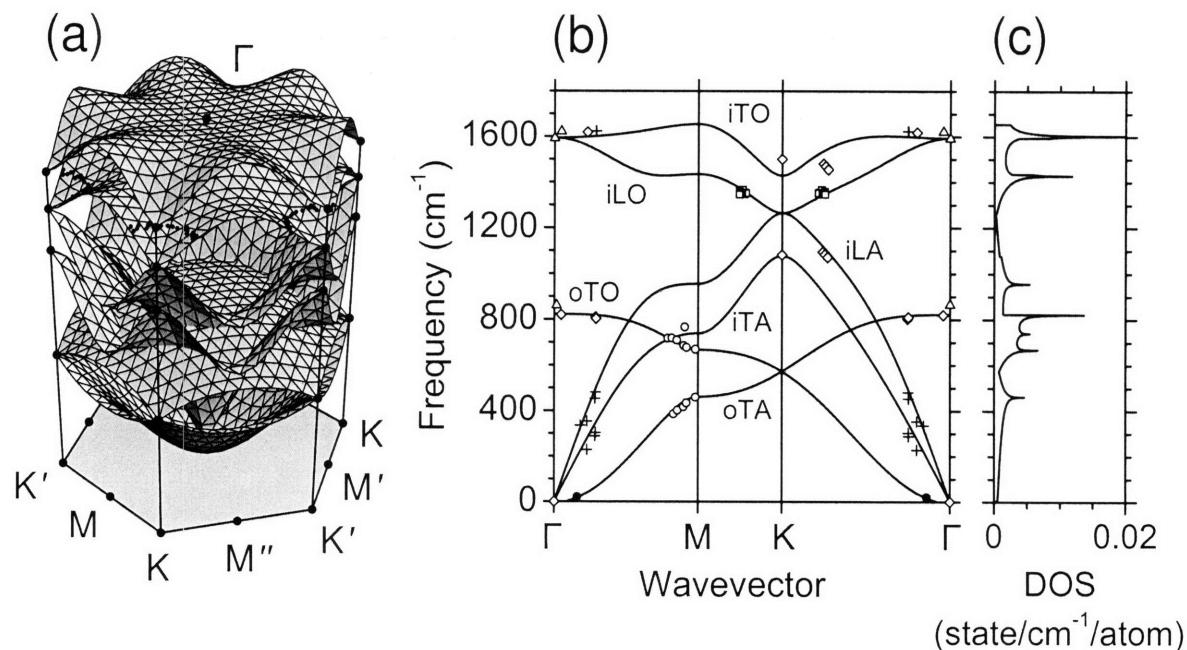


Figure 4-8: Phonon dispersion relations of a graphene sheet according to the BFC model with the force constants [142] given in Table 4.5 (a) throughout the entire first Brillouin zone shown in Fig. 2-1 and (b) along the high-symmetry directions in the first Brillouin zone. The phonon modes are labeled by iLA, iTA, oTA, iLO, iTO, and oTO, as discussed in Section 4.1 and shown in Figs. 4-2 and 4-4. The dots in (a) and squares in (b) show the results of resonance Raman scattering from individual CVD SWNTs on a Si/SiO₂ substrate [65]. The diamonds, crosses, triangles, solid dots, and open dots are experimental data taken from Fig. 4-8 for a better fit. (c) The density of phonon states (DOS).

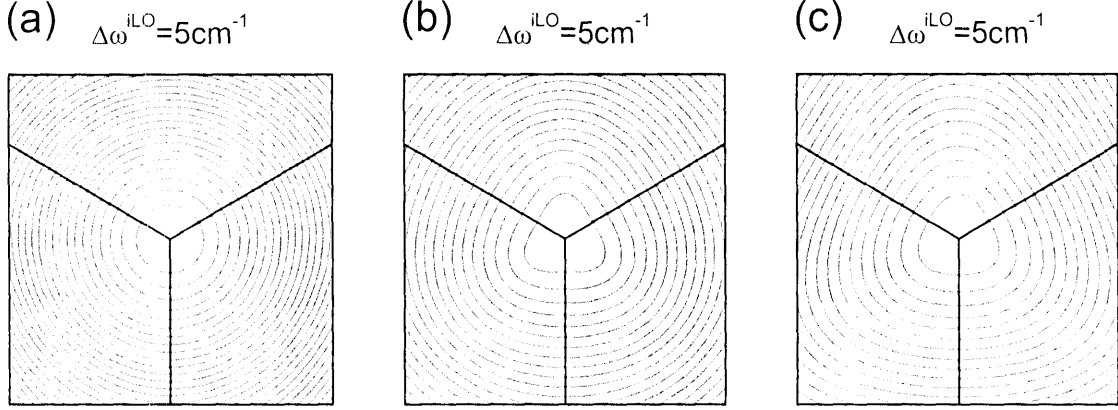


Figure 4-9: The squares show the area of linear dimensions $K\Gamma/3 = 4\pi/(9a)$ from Fig. 3-14 centered at the K point in the first Brillouin zone of a graphene sheet. The contours of constant frequency of the iLO phonon mode calculated within the BFC model with the force constants given in (a) Table 4.3, (b) Table 4.4, and (c) Table 4.5. The corresponding phonon dispersion relations are shown in Figs. 4-6, 4-7, and 4-8, respectively. The phonon frequency difference between the adjacent contours $\Delta\omega^{iLO} = 5 \text{ cm}^{-1}$ is shown above the figures.

projected on the KM and $K\Gamma$ directions appear as squares in Fig. 4-8 (b).

To illustrate the anisotropy of the phonon dispersion relations, we plot in Fig. 4-9 the equi-frequency contours for the iLO phonon mode in the square of linear dimensions $K\Gamma/3 = 4\pi/(9a)$ centered at the K point, by analogy with the trigonal warping effect for electrons shown in Fig. 3-14. The equi-frequency contours in Fig. 4-9 (a) for the phonon dispersion relations in Fig. 4-6 are isotropic around the K point, since the force constants were fitted to the experimental data along the ΓM direction. The inner contours in Fig. 4-9 (b) for the phonon dispersion relations in Fig. 4-7 exhibit a strong anisotropy, while the outer contours show almost isotropic behavior. This is understood considering that the Raman spectroscopic data in Fig. 4-7 (b) was measured using laser excitation energies in the range of 1.58 eV to 2.54 eV, and the outer contours in Fig. 4-9 (b) correspond to the laser excitation energies of 1.65 eV to 2.33 eV [141]. Since the double resonance process averages out different directions around the K point, the outer contours in Fig. 4-9 (b) do not exhibit significant anisotropy. Finally, the equi-frequency contours in Fig. 4-9 (c) for the phonon dispersion relations in Fig. 4-8 demonstrate the actual anisotropy in the phonon dispersion relations of the

graphene sheet. To give a quantitative measure of the phonon anisotropy, we evaluate the frequency difference $\omega^{\text{iLO}}(\text{KM}/2) - \omega^{\text{iLO}}(\text{K}\Gamma/4)$ corresponding to the outermost equi-energy contours in Fig. 4-9 and to the laser excitation energies of 2.41 eV and 2.54 eV. The frequency differences for Figs. 4-9 (a), (b), and (c) are given by -8 cm^{-1} , 0 cm^{-1} , and 25 cm^{-1} , respectively [141].

4.2.4 X-ray scattering

Recently, the optical phonon dispersion curves along the high-symmetry $\Gamma\text{MK}\Gamma$ directions were measured by inelastic x-ray scattering from a graphite flake [92]. By fitting the BFC model to the results of this experiment, we obtain the force constant parameters listed in Table 4.6. The corresponding phonon dispersion relations along with the x-ray scattering data are shown in Fig. 4-10. The qualitative changes in Fig. 4-10 (b) compared to Figs. 4-6 (b), 4-7 (b), and 4-8 (b) are the crossing points between the iLO and iTO phonon modes along the ΓM and ΓK directions, and a considerable softening of the frequency of the iTO phonon mode around the K point. Accordingly, the frequency of the iTA phonon mode at the K point increases, to satisfy the force constant sum rules within the BFC model [47]. These discrepancies with the previous fits indicate wrong assignment of the D - and G' -bands to the iLO phonon mode near the K point [88, 47, 142], while in fact these Raman bands arise from the iTO phonon mode around the K point that strongly couples to electrons, as we will show in Section 4.6 and in Chapter 5. Also, the experimental data points for the iLO phonon mode exhibit an overbending near the Γ point in Fig. 4-10 (b), and the electron-energy-loss spectroscopy data in Fig. 4-6 (b) show a similar behavior. The iLO overbending is an evidence of the strong coupling of the iLO phonon mode at the Γ point to electrons (see Section 4.6). Note that the iLO overbending is not reproduced within the BFC model which yields the flat dispersion of the iLO phonon mode around the Γ point (see Fig. 4-10 (b)). The iLO overbending is an indication of the long-range interatomic interactions in the dynamical matrix, which is beyond the framework of the BFC model.

Table 4.6: The force constants for a graphene sheet within the BFC model (in units of 10^4 dyn/cm; 1 dyn/cm = 6.2415 meV/nm²) fitted to the results of inelastic x-ray scattering (IXS) from a graphite flake [92]. The corresponding phonon dispersion relations are shown in Fig. 4-10.

	ϕ_{ir}	ϕ_{it}	ϕ_{ot}
$\phi^{(1)}$	+39.28	+11.36	+10.18
$\phi^{(1)}$	+6.34	-3.18	-0.36
$\phi^{(1)}$	-6.14	+9.27	-0.46
$\phi^{(1)}$	+2.53	+0.40	-0.44

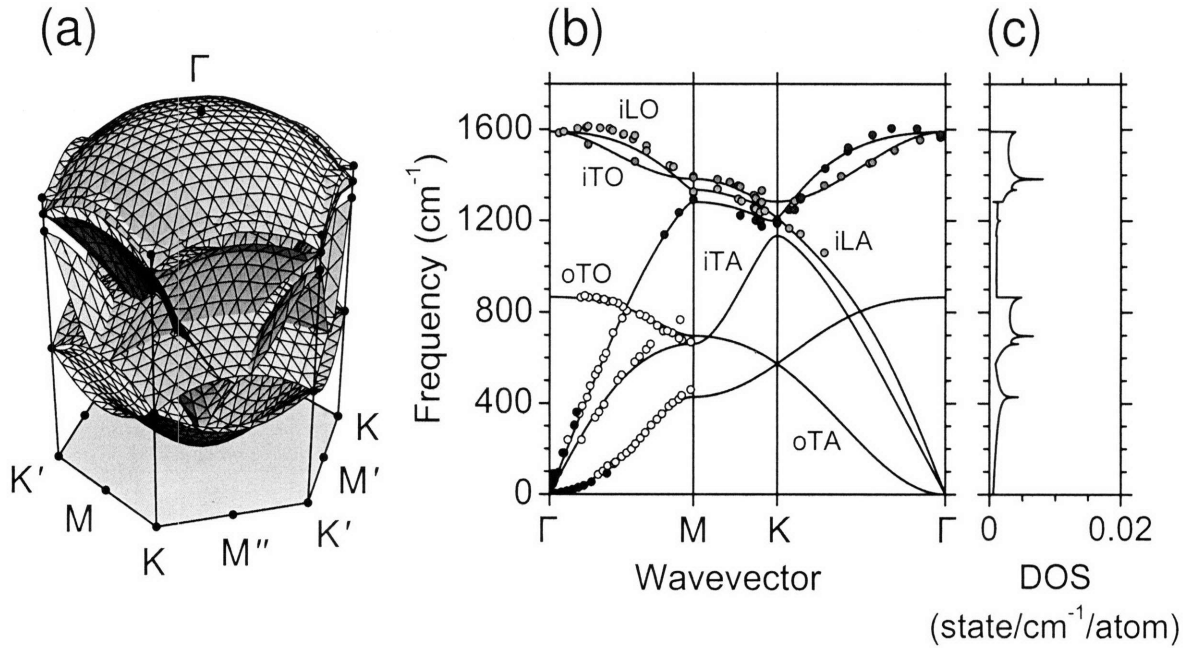


Figure 4-10: Phonon dispersion relations of a graphene sheet according to the BFC model with the force constants given in Table 4.6 (a) throughout the entire first Brillouin zone shown in Fig. 2-1 and (b) along the high-symmetry directions in the first Brillouin zone. The phonon modes are labeled by iLA, iTA, oTA, iLO, iTO, and oTO, as discussed in Section 4.1 and shown in Figs. 4-2 and 4-4. The red, green, and blue dots show the results of inelastic x-ray scattering from a graphite flake [92]. The solid and open dots are experimental data taken from Fig. 4-6 for a better fit. (c) The density of phonon states (DOS).

4.3 Advanced force-constant model

As shown in Section 4.2, the BFC model fails to accurately reproduce the phonon dispersion curves of the graphene sheet observed experimentally. The advanced force-constant (AFC) model is thus introduced. The AFC model involves twenty shells of nearest neighbors and off-diagonal matrix elements of the force constant matrices. The twenty shells and off-diagonal elements are essential in order to reproduce the phonon dispersion relations of the graphene sheet obtained from first-principles calculations on the basis of density-functional theory (DFT) employing the local-density approximation (LDA) for the exchange-correlation potential with a plane-wave expansion of the wavefunctions and using pseudo-potentials for the core electrons [37].

The twenty shells of the nearest neighbors of atom A are shown by circles in Fig. 4-11, where the first four shells coincide with those in Fig. 4-5 (b). The shells 1, 3, 4, 7, 8, 9, 11, 13, 14, 16, 18, 20 consist of atoms B of the opposite type than the central A atom, while the shells 2, 5, 6, 10, 12, 15, 17, 19 contain atoms A of the same type. Note that there are two different types of atoms in shell 20, which we refer to as 20 and 20', shown by black and red dots in Fig. 4-11, respectively. By analogy with the BFC model discussed in Section 4.2, each atom within the twenty shells is labeled by a pair of indices ιj , where $\iota = 1, \dots, 20$ indicates the shell number and j numerates the atoms in each shell counterclockwise looking down the z -axis. The first atom $j = 1$ within each shell ι appears in the positive direction of the x -axis. These atoms are highlighted by a yellow background in Fig. 4-11. The central A atom is referred by $\iota j = 00$.

Let us construct the force constant matrices in the normal coordinates $\Phi_{00\iota j}^{\text{norm}}$. The diagonal matrix elements of $\Phi_{00\iota j}^{\text{norm}}$ are given by $\phi_{ir}^{(\iota)}$, $\phi_{it}^{(\iota)}$, and $\phi_{ot}^{(\iota)}$, similar to Eq. (4.9) for the BFC model. The out-of-plane off-diagonal matrix elements of $\Phi_{00\iota j}^{\text{norm}}$ are zero. The in-plane off-diagonal matrix elements of $\Phi_{00\iota j}^{\text{norm}}$, on the other hand, are determined by the symmetry of the pairs of atoms shown in Fig. 4-11. For the shells $\iota = 1, 3, 5, 8, 11, 15, 20$, the in-plane off-diagonal matrix elements of $\Phi_{00\iota j}^{\text{norm}}$ vanish. For the shells $\iota = 2, 4, 6, 7, 9, 12, 13, 14, 16, 18, 19, 20'$, there is one independent in-plane off-

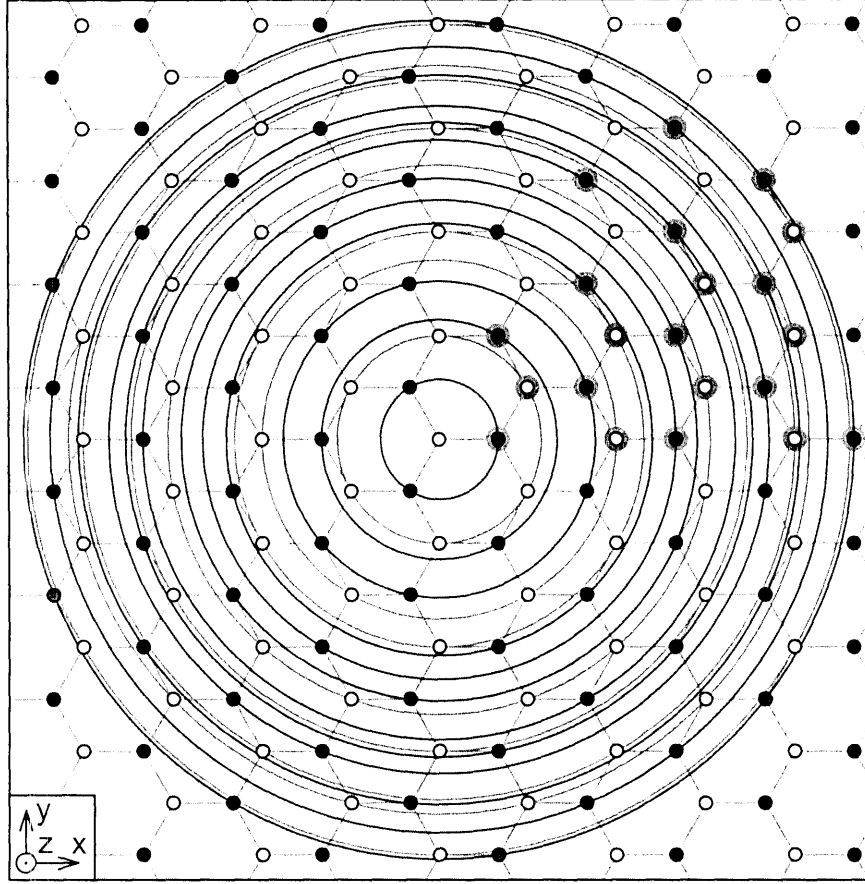


Figure 4-11: A single graphene sheet. The open and solid dots indicate the A and B sublattices, respectively. The twenty shells of the nearest neighbors of the central A atom are shown by the circles. The shells that consist of the A and B atoms are shown in green and blue, respectively. The B atoms that form the shell 20' are shown by red dots. The atoms in each shell are numbered counterclockwise looking down the z -axis. The first atom within each shell is highlighted by a yellow background. The nearest neighbor shells of the central B atom can be obtained by rotating the image by 180° .

diagonal matrix element of $\Phi_{00ij}^{\text{norm}}$, which we refer to as $\phi_{i1}^{(i)}$. For the shells $i = 10, 17$, there are two independent in-plane off-diagonal matrix elements of $\Phi_{00ij}^{\text{norm}}$, which we refer to as $\phi_{i1}^{(i)}$ and $\phi_{i2}^{(i)}$. The in-plane diagonal blocks of the force constant matrices $\Phi_{00ij}^{\text{norm}}$ are then written in the following form:

$$\left\{ \begin{array}{l}
\left(\Phi_{00zj}^{\text{norm}} \right)_{ii} = \begin{pmatrix} +\phi_{ir}^{(z)} & 0 \\ 0 & +\phi_{it}^{(z)} \end{pmatrix} \quad \text{for} \quad \begin{cases} z = 1, 3, 8, 11, 20, \\ j = 1, 2, 3, \end{cases} \\
\left(\Phi_{00zj}^{\text{norm}} \right)_{ii} = \begin{pmatrix} +\phi_{ir}^{(z)} & 0 \\ 0 & +\phi_{it}^{(z)} \end{pmatrix} \quad \text{for} \quad \begin{cases} z = 5, 15, \\ j = 1, 2, 3, 4, 5, 6, \end{cases} \\
\left(\Phi_{00zj}^{\text{norm}} \right)_{ii} = \begin{pmatrix} +\phi_{ir}^{(z)} & +\phi_{i1}^{(z)} \\ -\phi_{i1}^{(z)} & +\phi_{it}^{(z)} \end{pmatrix} \quad \text{for} \quad \begin{cases} z = 2, 6, 12, 19, \\ j = 1, 3, 5, \end{cases} \\
\left(\Phi_{00zj}^{\text{norm}} \right)_{ii} = \begin{pmatrix} +\phi_{ir}^{(z)} & -\phi_{i1}^{(z)} \\ +\phi_{i1}^{(z)} & +\phi_{it}^{(z)} \end{pmatrix} \quad \text{for} \quad \begin{cases} z = 2, 6, 12, 19, \\ j = 2, 4, 6, \end{cases} \\
\left(\Phi_{00zj}^{\text{norm}} \right)_{ii} = \begin{pmatrix} +\phi_{ir}^{(z)} & +\phi_{i1}^{(z)} \\ +\phi_{i1}^{(z)} & +\phi_{it}^{(z)} \end{pmatrix} \quad \text{for} \quad \begin{cases} z = 4, 7, 9, 13, 14, 16, 18, 20', \\ j = 1, 3, 5, \end{cases} \\
\left(\Phi_{00zj}^{\text{norm}} \right)_{ii} = \begin{pmatrix} +\phi_{ir}^{(z)} & -\phi_{i1}^{(z)} \\ -\phi_{i1}^{(z)} & +\phi_{it}^{(z)} \end{pmatrix} \quad \text{for} \quad \begin{cases} z = 4, 7, 9, 13, 14, 16, 18, 20', \\ j = 2, 4, 6, \end{cases} \\
\left(\Phi_{00zj}^{\text{norm}} \right)_{ii} = \begin{pmatrix} +\phi_{ir}^{(z)} & +\phi_{i1}^{(z)} \\ +\phi_{i2}^{(z)} & +\phi_{it}^{(z)} \end{pmatrix} \quad \text{for} \quad \begin{cases} z = 10, 17, \\ j = 1, 5, 9, \end{cases} \\
\left(\Phi_{00zj}^{\text{norm}} \right)_{ii} = \begin{pmatrix} +\phi_{ir}^{(z)} & -\phi_{i1}^{(z)} \\ -\phi_{i2}^{(z)} & +\phi_{it}^{(z)} \end{pmatrix} \quad \text{for} \quad \begin{cases} z = 10, 17, \\ j = 4, 8, 12, \end{cases} \\
\left(\Phi_{00zj}^{\text{norm}} \right)_{ii} = \begin{pmatrix} +\phi_{ir}^{(z)} & +\phi_{i2}^{(z)} \\ +\phi_{i1}^{(z)} & +\phi_{it}^{(z)} \end{pmatrix} \quad \text{for} \quad \begin{cases} z = 10, 17, \\ j = 3, 7, 11, \end{cases} \\
\left(\Phi_{00zj}^{\text{norm}} \right)_{ii} = \begin{pmatrix} +\phi_{ir}^{(z)} & -\phi_{i2}^{(z)} \\ -\phi_{i1}^{(z)} & +\phi_{it}^{(z)} \end{pmatrix} \quad \text{for} \quad \begin{cases} z = 10, 17, \\ j = 2, 6, 10, \end{cases}
\end{array} \right. \quad (4.15)$$

while the out-of-plane diagonal blocks are given by $\left(\Phi_{00zj}^{\text{norm}} \right)_{oo} = \phi_{ot}^{(z)}$, and the off-diagonal blocks $\left(\Phi_{00zj}^{\text{norm}} \right)_{io}$ and $\left(\Phi_{00zj}^{\text{norm}} \right)_{oi}$ vanish. The force constant matrices $\Phi_{00zj}^{\text{norm}}$ given by Eq. (4.15) are then transformed from the normal coordinates to Cartesian coordinates using Eq. (4.11). The force constant matrices for the central B atom are

obtained in a similar fashion. The resulting force constant matrices multiplied by the appropriate phase factors build up the dynamical matrix, according to Eq. (4.8). Thus, the dynamical matrix within the AFC model is determined by 79 force constant parameters $\phi_\alpha^{(\iota)}$, where $\alpha = ir, it, ot$ for $\iota = 1, 3, 5, 8, 11, 15, 20$, $\alpha = ir, it, ot, i1$ for $\iota = 2, 4, 6, 7, 9, 12, 13, 14, 16, 18, 19, 20'$, and $\alpha = ir, it, ot, i1, i2$ for $\iota = 10, 17$.

In Section 4.2, the 12 force constant parameters of the BFC model were fitted to the experimental data. However, the 79 force constant parameters of the AFC model provide too many degrees of freedom for the fitting algorithm. The latter may lead to non-unique solutions, or may have problems to converge. The 79 force constant parameters of the AFC model are thus determined either by first-principles calculations or within the ETB model introduced in Section 3.6.

4.3.1 DFT-LDA calculations

The early first-principles calculations [78, 111] in the framework of DFT-LDA established the key features of the phonon dispersion relations of the graphene sheet, including the crossing points between the iLO and iT0 phonon modes along the ΓM and ΓK directions, the softening of the frequency of the iT0 phonon mode around the K point, and the overbending of the iLO phonon mode near the Γ point, as discussed in Section 4.2 regarding Fig. 4-10 (b). Further first-principles calculations [37, 99, 170] only provided quantitative improvements to the phonon dispersion relations of the graphene sheet.

The force constant parameters within the framework of the AFC model calculated with the help of DFT-LDA [37] are summarized in Table 4.7. The DFT-LDA calculations slightly overestimate the phonon frequencies according to the variational principle. In order to fit the calculated phonon dispersion curves to the well-known experimental data $\omega^{E_{2g}}(\Gamma) = 1582 \text{ cm}^{-1}$ and $\omega^{B_{2g}}(\Gamma) = 868 \text{ cm}^{-1}$ [170], the frequencies of the in-plane and out-of-plane phonon modes are multiplied by 0.9915 and 0.9754, respectively. The in-plane and out-of-plane force constants in Table 4.7 are scaled by factors 0.9915^2 and 0.9754^2 , respectively. The phonon dispersion relations of the graphene sheet calculated with the force constants from Table 4.7 are shown

Table 4.7: The force constants for a graphene sheet within the AFC model (in units of 10^4 dyn/cm; 1 dyn/cm = 6.2415 meV/nm²) calculated with the help of DFT-LDA [37]. The in-plane and out-of-plane force constants are scaled by factors 0.9915^2 and 0.9754^2 , respectively, in order to fit the Γ point optical phonon frequencies to the well-known experimental data $\omega^{E_{2g}}(\Gamma) = 1582$ cm⁻¹ and $\omega^{B_{2g}}(\Gamma) = 868$ cm⁻¹ [170]. The corresponding phonon dispersion relations are shown in Fig. 4-12.

	ϕ_{ir}	ϕ_{it}	ϕ_{ot}	ϕ_{i1}	ϕ_{i2}
$\phi^{(1)}$	+43.0374	+16.0741	+9.6310	—	—
$\phi^{(2)}$	+7.3805	-4.1183	-0.7718	+0.4415	—
$\phi^{(3)}$	-1.3043	+3.1505	+0.6341	—	—
$\phi^{(4)}$	-0.6390	+0.3681	-0.7535	+1.0211	—
$\phi^{(5)}$	+0.8245	+0.1673	+0.1058	—	—
$\phi^{(6)}$	+0.1737	-0.4310	-0.0180	-0.0109	—
$\phi^{(7)}$	-0.3062	+0.2356	-0.0127	+0.1669	—
$\phi^{(8)}$	-0.7099	+0.0203	+0.0982	—	—
$\phi^{(9)}$	+0.0128	+0.1167	+0.0395	-0.0512	—
$\phi^{(10)}$	+0.1764	-0.0838	-0.0099	+0.2299	-0.0940
$\phi^{(11)}$	-0.1364	+0.1983	+0.0029	—	—
$\phi^{(12)}$	+0.0975	+0.0096	+0.0020	-0.0306	—
$\phi^{(13)}$	-0.0496	-0.0335	-0.0063	+0.0356	—
$\phi^{(14)}$	-0.1200	-0.0283	-0.0127	+0.0542	—
$\phi^{(15)}$	+0.1428	+0.0212	+0.0020	—	—
$\phi^{(16)}$	-0.0835	+0.0220	+0.0028	-0.0073	—
$\phi^{(17)}$	+0.0301	-0.0203	+0.0006	+0.0246	-0.0069
$\phi^{(18)}$	-0.0687	+0.0220	-0.0010	+0.0330	—
$\phi^{(19)}$	+0.0426	-0.0141	+0.0002	+0.0000	—
$\phi^{(20)}$	-0.1368	-0.0552	+0.0028	—	—
$\phi^{(20')}$	-0.0120	+0.0104	+0.0020	+0.0033	—

in Fig. 4-12. The off-diagonal force constants ϕ_{i1} and ϕ_{i2} turn out to significantly influence the phonon dispersion relations of the graphene sheet. If we omit the last two columns in Table 4.7, the iTA and iT0 phonon modes at the M point in Fig. 4-12 (b) appear to have very close frequencies, similar to Fig. 5 of Ref. [99].

To verify the results of DFT-LDA calculations, the experimental data points from Fig. 4-10 (b) are replicated in Fig. 4-12 (b). One can see a good agreement between the calculated and experimental phonon dispersion curves in Fig. 4-12 (b). In particular, the DFT-LDA calculations closely reproduce the iLO-iTO crossing near the M

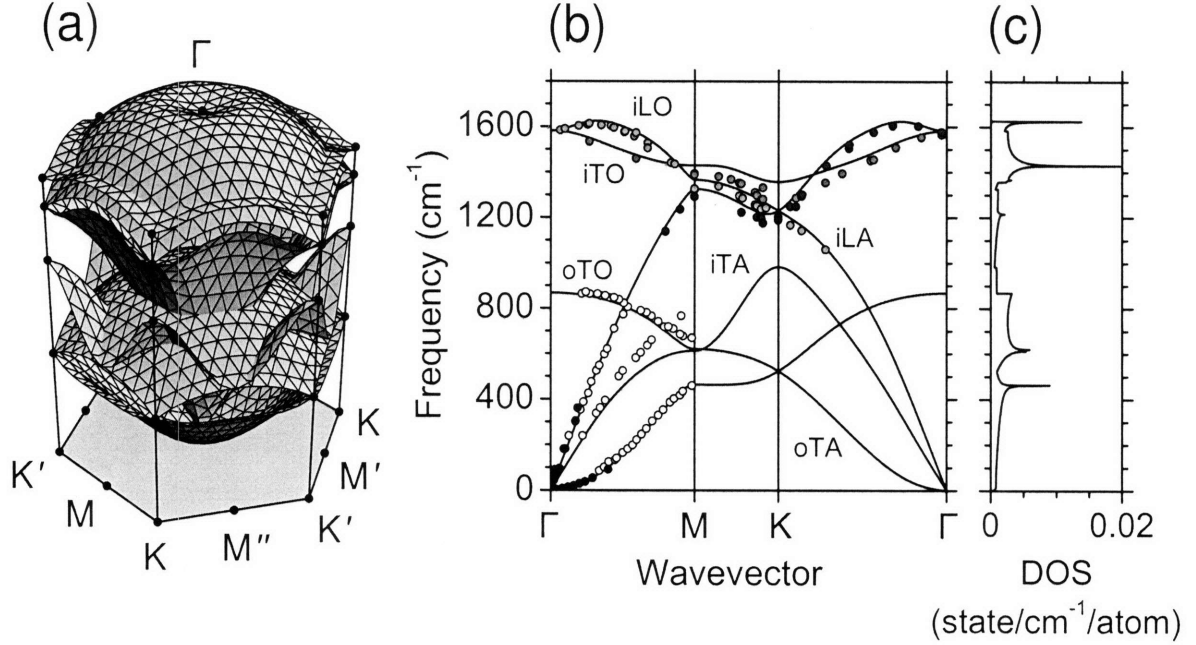


Figure 4-12: Phonon dispersion relations of a graphene sheet according to the AFC model with the force constants [37] given in Table 4.7 (a) throughout the entire first Brillouin zone shown in Fig. 2-1 and (b) along the high-symmetry directions in the first Brillouin zone. The in-plane and out-of-plane force constants are calculated with the help of DFT-LDA [37] and scaled by factors 0.9915^2 and 0.9754^2 , respectively, to fit experimental data $\omega^{E_{2g}}(\Gamma) = 1582 \text{ cm}^{-1}$ and $\omega^{B_{2g}}(\Gamma) = 868 \text{ cm}^{-1}$ [170]. The phonon modes are labeled by iLA, iTA, oTA, iLO, iTO, and oTO, as discussed in Section 4.1 and shown in Figs. 4-2 and 4-4. The red, green, blue, solid, and open dots are experimental data taken from Fig. 4-10. (c) The density of phonon states (DOS).

and K points and the iLO overbending around the Γ point. On the other hand, the DFT-LDA calculations overestimate the iTO frequency at the K point and underestimate the iTA frequency at the M point. The overestimation of the iTO frequency at the K point is due to anharmonic effects, as we will show in Section 4.6. The large finite difference step size used for the DFT-LDA calculations of the force constants [37] smears out the softening of the iTO phonon mode around the K point. The underestimation of the iTA frequency at the M point is related to the long-range character of the dynamical matrix [172]. The long-range interaction cut-off at the twentieth nearest neighbor induces errors in the low-frequency iTA phonon mode at the M point [172].

The 1D phonon dispersion relations of SWNTs in the zone-folding approximation

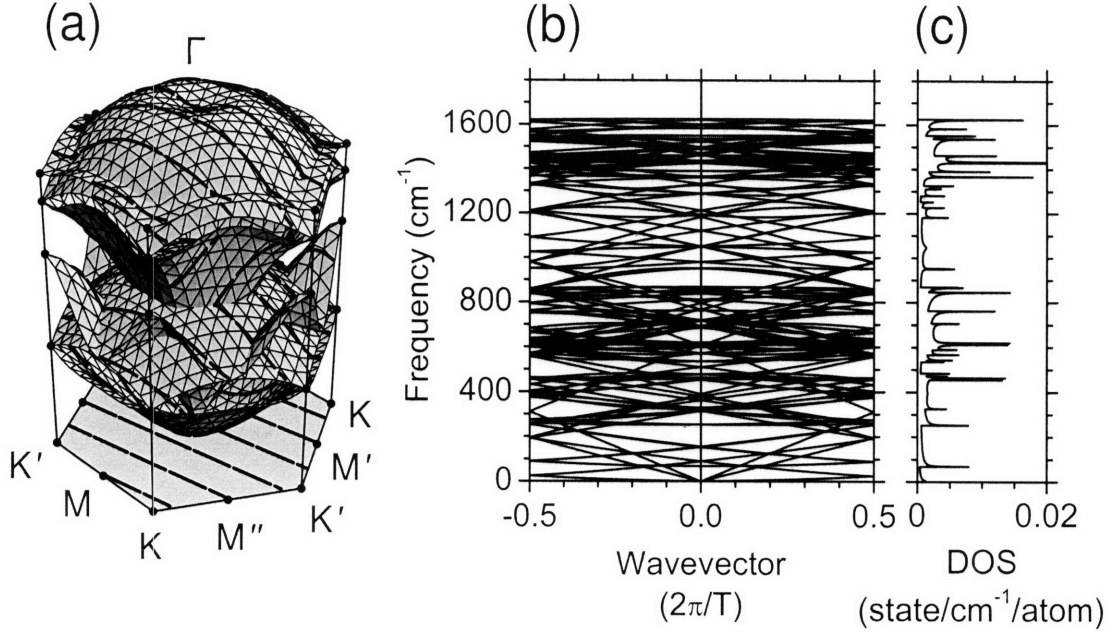


Figure 4-13: (a) The phonon dispersion relations of a graphene sheet within the STB model replicated from Fig. 4-12. The solid lines are the cutting lines for a semiconducting (4, 2) SWNT in the helical-helical representation. (b) The phonon dispersion relations of the (4, 2) SWNT when different cutting lines are folded together into the 1D Brillouin zone. The length of the 1D Brillouin zone is given by $2\pi/T$. (c) The density of phonon states (DOS) of the (4, 2) SWNT. The sharp spikes in the DOS typical for 1D systems are known as Van Hove singularities.

are obtained by superimposing the cutting lines over the 2D phonon dispersion surfaces shown in Fig. 4-12 (a). The cutting lines for phonons are defined by the following relation:

$$\mathbf{q} = \eta \mathbf{K}_1 + q \frac{\mathbf{K}_2}{K_2}, \quad (4.16)$$

similar to Eq. (2.14) for electrons, where \mathbf{q} is the 2D wavevector of the graphene sheet, while η and q are the 1D angular and linear momenta in SWNTs. In Fig. 4-13 (a), we superimpose the cutting lines given by Eq. (4.16) in the helical-helical representation for the (4, 2) SWNT over the 2D phonon dispersion surfaces of a graphene sheet replicated from Fig. 4-12 (a). We then construct the 1D phonon dispersion curves and the phonon DOS of the (4, 2) SWNT in Figs. 4-13 (b) and (c), respectively. The applicability of the zone-folding technique to phonons will be discussed in Section 4.4.

4.3.2 ETB calculations

To clarify the origin of the aforementioned discrepancies between the theoretical and experimental results, we calculate the force constants for a graphene sheet within the framework of the ETB model. The force constant matrix between the two atoms in a graphene sheet is given by the Hessian (the matrix of second partial derivatives [94]) of the total energy with respect to the coordinates of these atoms. The Hessian is obtained either by analytical derivation, or by a central finite difference approximation for the first derivative of the Hellmann-Feynman forces, or by a central finite difference approximation for the second derivative of the total energy. The large supercell is used for the total energy calculations in order to minimize interactions between the pairs of atoms in the adjacent supercells.

We have chosen the supercell bounded by the $15\mathbf{a}_1$ and $15\mathbf{a}_2$ translational vectors that encloses the 225 two-atom unit cells or 450 carbon atoms. The total energy was calculated from Eq. (3.27) on a 4×4 Monkhorst-Pack grid in reciprocal space. A small number (namely, sixteen) of the sampling \mathbf{k} -points does not spoil the accuracy of the calculation due to the large size of the supercell. The Hessian was calculated by a central finite difference approximation for the second derivative of the total energy with the step $\Delta R = 10^{-4}$ nm. For each pair of carbon atoms, the normal directions ir, it, ot are determined as shown in Fig. 4-5 (a), the two atoms are displaced from their equilibrium positions by $\pm\frac{1}{2}\Delta R$ along the normal directions, and the total energy is calculated for the distorted geometries.

However, the total energy approach is time consuming and numerically inaccurate, as it involves numerous calculations of the total energy for different distorted geometries. Hence, we obtain the Hessian by a central finite difference approximation for the first derivative of the Hellmann-Feynman forces. The Hellmann-Feynman forces are calculated analytically from Eq. (3.28). In this case, we only need to shift the central atom of the supercell from its equilibrium position by $\pm\frac{1}{2}\Delta R$ along three orthogonal directions. The Hellmann-Feynman forces acting on all atoms in the supercell are calculated for the distorted geometries. Compared to the Hellmann-Feynman

Table 4.8: The force constants for a graphene sheet within the AFC model (in units of 10^4 dyn/cm; 1 dyn/cm = 6.2415 meV/nm²) calculated within the ETB model. The in-plane and out-of-plane force constants are scaled by factors 0.8841^2 and 1.0292^2 , respectively, in order to fit the Γ point optical phonon frequencies to the well-known experimental data $\omega^{E_{2g}}(\Gamma) = 1582$ cm⁻¹ and $\omega^{B_{2g}}(\Gamma) = 868$ cm⁻¹ [170]. The corresponding phonon dispersion relations are shown in Fig. 4-14.

	ϕ_{ir}	ϕ_{it}	ϕ_{ot}	ϕ_{i1}	ϕ_{i2}
$\phi^{(1)}$	+43.2925	+16.2138	+9.8923	—	—
$\phi^{(2)}$	+7.5365	-4.4769	-0.5488	+1.5358	—
$\phi^{(3)}$	-2.0163	+4.1265	+0.7946	—	—
$\phi^{(4)}$	-0.6857	+0.0062	-0.9717	+1.0180	—
$\phi^{(5)}$	+1.0928	+0.1444	+0.0974	—	—
$\phi^{(6)}$	+0.1315	-0.4157	+0.0098	-0.0433	—
$\phi^{(7)}$	-0.3464	+0.2683	-0.0117	+0.2698	—
$\phi^{(8)}$	-0.8798	+0.1550	+0.1119	—	—
$\phi^{(9)}$	-0.0309	+0.1130	+0.0351	-0.1376	—
$\phi^{(10)}$	+0.1809	-0.1439	-0.0072	+0.2792	-0.1300
$\phi^{(11)}$	-0.2019	+0.2839	+0.0047	—	—
$\phi^{(12)}$	+0.1478	+0.0475	-0.0011	-0.0157	—
$\phi^{(13)}$	-0.0038	-0.0596	-0.0049	+0.0192	—
$\phi^{(14)}$	-0.0890	-0.0279	-0.0114	+0.0776	—
$\phi^{(15)}$	+0.1765	+0.0393	+0.0012	—	—
$\phi^{(16)}$	-0.1154	+0.0664	+0.0040	+0.0332	—
$\phi^{(17)}$	+0.0030	-0.0646	+0.0003	-0.0220	+0.0288
$\phi^{(18)}$	-0.0466	+0.0277	-0.0001	+0.0653	—
$\phi^{(19)}$	+0.0425	-0.0416	+0.0000	+0.0544	—
$\phi^{(20)}$	-0.1576	+0.0459	+0.0025	—	—
$\phi^{(20')}$	-0.0458	+0.0532	+0.0006	-0.0366	—

approach, the analytical derivation of the Hessian does not provide significant improvement in the computation time or numerical accuracy. We therefore stick with the Hellmann-Feynman approach as involving simpler analytical expressions.

The force constants calculated within the Hellmann-Feynman approach using the aforementioned parameters (450 atom supercell, 16 sampling \mathbf{k} -points, and $\Delta R = 10^{-4}$ nm central difference step) are summarized in Table 4.8. The ETB calculation overestimates the in-plane phonon frequencies by about 10% due to the limited basis set used in the tight-binding calculations [121]. Hence, the in-plane and out-of-plane

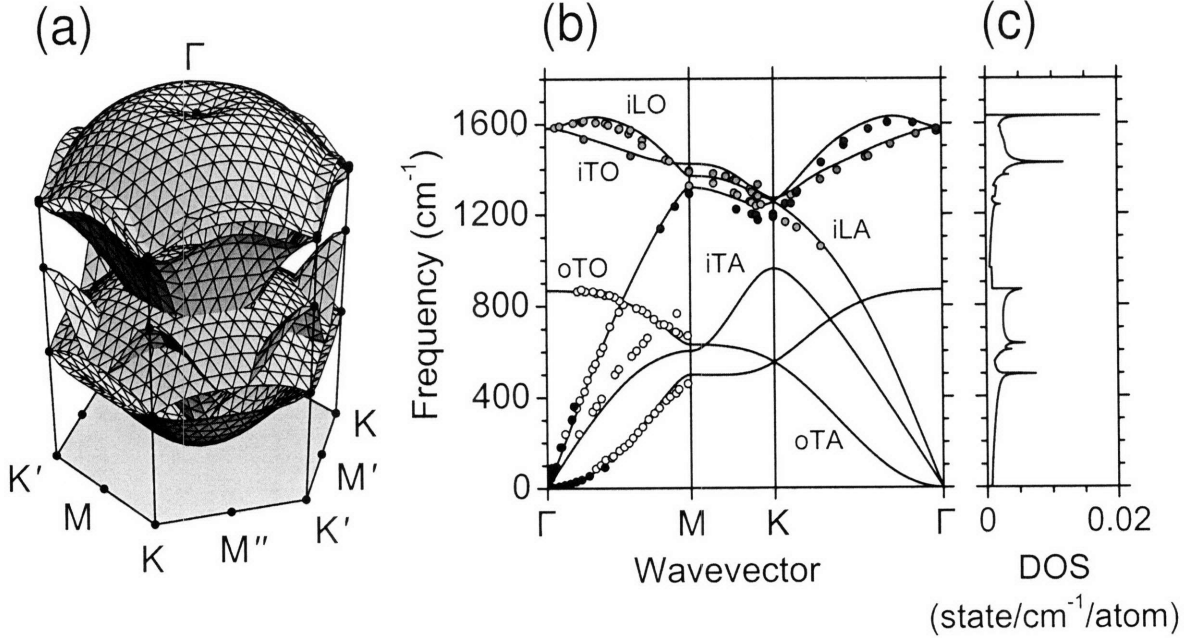


Figure 4-14: Phonon dispersion relations of a graphene sheet according to the AFC model with the force constants given in Table 4.8 (a) throughout the entire first Brillouin zone shown in Fig. 2-1 and (b) along the high-symmetry directions in the first Brillouin zone. The in-plane and out-of-plane force constants are calculated within the ETB model and scaled by factors 0.8841^2 and 1.0292^2 , respectively, to fit experimental data $\omega^{E_{2g}}(\Gamma) = 1582 \text{ cm}^{-1}$ and $\omega^{B_{2g}}(\Gamma) = 868 \text{ cm}^{-1}$ [170]. The phonon modes are labeled by iLA, iTA, oTA, iLO, iTO, and oTO, as discussed in Section 4.1 and shown in Figs. 4-2 and 4-4. The red, green, blue, solid, and open dots are experimental data taken from Fig. 4-10. (c) The density of phonon states (DOS).

force constants in Table 4.8 are scaled by factors 0.8841^2 and 1.0292^2 , respectively, to fit the experimental frequencies $\omega^{E_{2g}}(\Gamma) = 1582 \text{ cm}^{-1}$ and $\omega^{B_{2g}}(\Gamma) = 868 \text{ cm}^{-1}$ [170]. The phonon dispersion relations of the graphene sheet calculated with the force constants from Table 4.8 are shown in Fig. 4-14, where we also replicate the experimental data points from Fig. 4-10 (b).

By comparing Figs. 4-14 (b) and 4-12 (b), one finds that the ETB calculations nicely fit the experimentally observed behavior of the iTO phonon mode near the K point, in contrast to the DFT-LDA calculations. We will discuss the softening of the iTO phonon mode around the K point in more detail in Section 4.6. Also, the ETB calculations closely reproduce the iLO-iTO crossing near the M and K points and the iLO overbending around the Γ point, similar to the DFT-LDA calculations.

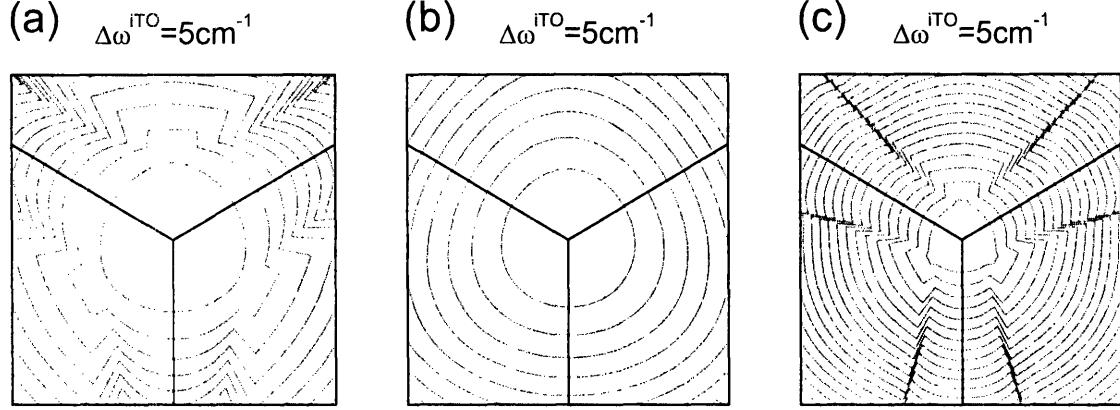


Figure 4-15: The squares show the area of linear dimensions $K\Gamma/3 = 4\pi/(9a)$ from Fig. 3-14 centered at the K point in the first Brillouin zone of a graphene sheet. The contours of constant frequency of the iTO phonon mode calculated (a) within the BFC model with the force constants from Table 4.6 and within the AFC model with the force constants from (b) Table 4.7 and (c) Table 4.8, similar to the iLO contours in Fig. 4-9. The corresponding phonon dispersion relations are shown in Figs. 4-10, 4-12, and 4-14, respectively. The phonon frequency difference between the adjacent contours $\Delta\omega^{iTO} = 5 \text{ cm}^{-1}$ is shown above the figures.

At the same time, the ETB calculations underestimate the iTA frequency at the M point, which is understood from the long-range interaction cut-off in the dynamical matrix [172], similar to the DFT-LDA calculations.

To illustrate the anisotropy of the phonon dispersion relations within the AFC model, we plot in Fig. 4-15 the equi-frequency contours for the iTO phonon mode around the K point, by analogy with Fig. 4-9 for the BFC model. Note that Fig. 4-9 shows the equi-frequency contours for the iLO phonon mode, due to the wrong assignment of the D and G' Raman bands to the iLO phonon mode within the BFC model, as discussed in Section 4.2.4. While the iLO and iTO phonon modes in Figs. 4-10(b) and 4-14(b) cross each other along the high-symmetry direction $K\Gamma$ near the K point, they anti-cross along a general direction in reciprocal space, resulting in discontinuities along the equi-frequency contours in Figs. 4-15 (a) and (c), respectively. The equi-frequency contours in Fig. 4-15 (b) do not exhibit discontinuities because the DFT-LDA calculations overestimate the frequency of the iTO phonon mode around the K point, as one can see from Fig. 4-12 (b). To give a quantitative measure of the

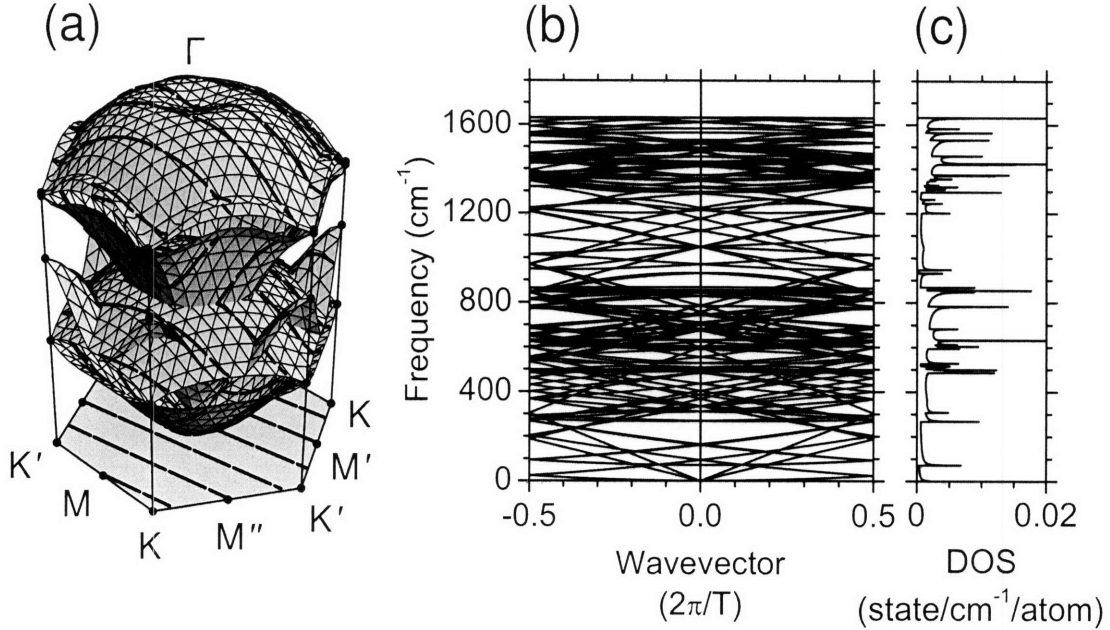


Figure 4-16: (a) The phonon dispersion relations of a graphene sheet within the STB model replicated from Fig. 4-14. The solid lines are the cutting lines for a semiconducting (4, 2) SWNT in the helical-helical representation. (b) The phonon dispersion relations of the (4, 2) SWNT when different cutting lines are folded together into the 1D Brillouin zone. The length of the 1D Brillouin zone is given by $2\pi/T$. (c) The density of phonon states (DOS) of the (4, 2) SWNT. The sharp spikes in the DOS typical for 1D systems are known as Van Hove singularities.

phonon anisotropy, we evaluate the frequency difference $\omega^{i\text{TO}}(\text{KM}/2) - \omega^{i\text{TO}}(\text{K}\Gamma/4)$ corresponding to the outermost equi-energy contours in Fig. 4-15 and to the laser excitation energies of 2.41 eV and 2.54 eV. The frequency differences for Figs. 4-15 (a), (b), and (c) are given by 12 cm^{-1} , 7 cm^{-1} , and 10 cm^{-1} , respectively. Comparison of these values with the experimental frequency difference of 25 cm^{-1} reported in Section 4.2.3 suggests that further theoretical and experimental studies are needed to obtain a quantitative measure of the phonon trigonal warping effect.

The 1D phonon dispersion relations of SWNTs are obtained by applying the zone-folding technique to the 2D phonon dispersion relations of a graphene sheet, as described in Section 4.3.1. In Fig. 4-16 (a), we superimpose the cutting lines defined by Eq. (4.16) in the helical-helical representation for the (4, 2) SWNT over the 2D phonon dispersion surfaces of a graphene sheet replicated from Fig. 4-14 (a), by anal-

ogy with Fig. 4-13 (a). We then construct the 1D phonon dispersion curves and the phonon DOS of the (4, 2) SWNT in Figs. 4-16 (b) and (c), respectively, similar to Figs. 4-13 (b) and (c). The applicability of the zone-folding technique to phonons is discussed below in Section 4.4.

4.4 Curvature-adapted force-constant model

Fig. 4-16 (b) shows the 1D phonon dispersion curves for the (4, 2) SWNT. Given the six phonon modes $\nu = \text{iLA, iTA, oTA, iLO, iTO, oTO}$ and the $N = 28$ distinct values of the angular momentum $\eta = 1 - N/2, \dots, N/2$ (associated with the N non-equivalent cutting lines in Eq. (4.16)), we conclude that there are a total of $6N = 168$ phonon dispersion curves in Fig. 4-16 (b). Nevertheless, group theory predicts that there are only 14 (6) Raman-active and 6 (3) infrared-active phonon modes with angular and linear momenta $\mu = 0, \pm 1, \pm 2$ and $k = 0$ in chiral (achiral) SWNTs [3, 12]. Among them, only 3 (2) Raman-active phonon modes with angular momentum $\mu = 0$ are strongly coupled to electrons. These phonon modes belong to the irreducible representation A_1 (A_{1g}) of point group D_N (D_{2nh}) [3, 12]. They are known as the radial breathing mode (RBM), the G^T mode, and the G^L mode, after the RBM and the G Raman bands to which they give rise [125]. The RBM, G^T , and G^L phonon modes in SWNTs correspond to the oTA, iTO, and iLO phonon modes in the graphene sheet whose atomic displacements are shown in Figs. 4-2 (c), (e), and (d), respectively.

4.4.1 Zone-folding technique

The 1D phonon dispersion curves for the (4, 2) SWNT shown in Fig. 4-16 (b) are obtained within the zone-folding approximation by superimposing the cutting lines given by Eq. (4.16) on the 2D phonon dispersion surfaces of the graphene sheet shown in Fig. 4-16 (a) calculated from the ETB model. Figure 4-16 (b) is replicated in Figure 4-17 (a) where the dispersion curves associated with the RBM, G^T , and G^L phonon modes are highlighted. The RBM, G^T , and G^L phonon modes appear

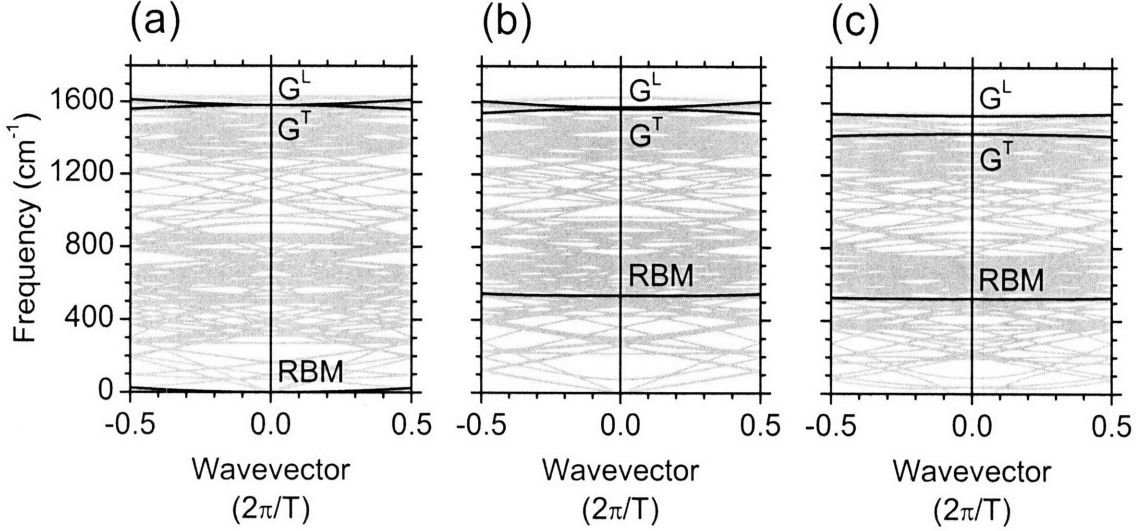


Figure 4-17: The phonon dispersion relations of the (4, 2) SWNT: (a) identical to Fig. 4-16 obtained by the zone-folding technique using the force constants from Table 4.8, (b) calculated using the curvature-adapted model with the force constants from Table 4.8, and (c) obtained from the force constants calculated explicitly for the (4, 2) SWNT within the ETB framework and scaled by factors 0.8841^2 , 1.0292^2 , and 0.8841×1.0292 , as in Table 4.8. Shown in black are the dispersion curves associated with the RBM, G^T , and G^L phonon modes corresponding to the oTA, iTO, and iLO phonon modes in the graphene sheet shown in Figs. 4-2 (c), (e), and (f), respectively. The frequencies of the RBM, G^T , and G^L phonon modes are given by (a) 0 cm^{-1} , 1582 cm^{-1} , and 1582 cm^{-1} , (b) 535 cm^{-1} , 1564 cm^{-1} , and 1573 cm^{-1} , (c) 522 cm^{-1} , 1430 cm^{-1} , and 1531 cm^{-1} , respectively.

at the 1D Γ point in these dispersion curves indicated by the vertical line in Fig. 4-17(a). The frequencies of the phonon modes where the dispersion curves cross the vertical line in Fig. 4-17(a) are given by $\omega^{\text{RBM}}(\Gamma) = 0 \text{ cm}^{-1}$, $\omega^{G^T}(\Gamma) = 1582 \text{ cm}^{-1}$, and $\omega^{G^L}(\Gamma) = 1582 \text{ cm}^{-1}$. The normal mode displacements for the RBM, G^T , and G^L phonon modes obtained by rolling up Figs. 4-2 (c), (e), and (d) are shown in Figs. 4-18 (a), (b), and (c), respectively. While the normal mode displacements for the RBM mode are aligned with the radial direction of the SWNT, the normal mode displacements for the G^T and G^L phonon modes are perpendicular and parallel to one of the sp^2 bonds in the SWNT sidewall, and are not aligned with the circumferential and axial directions of the SWNT, because the (4, 2) SWNT is chiral.

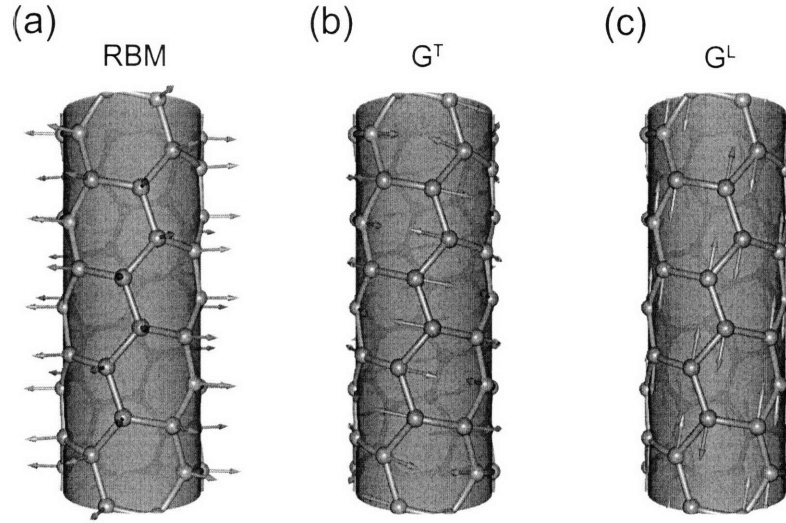


Figure 4-18: The (4, 2) ZR/AL SWNT replicated from Fig. 2-3. The arrows indicate the normal mode displacements for the (a) RBM, (b) G^T , and (c) G^L phonon modes shown in Fig. 4-17 (a). The normal mode displacements are obtained by applying the zone-folding technique to the oTA, iTO, and iLO phonon modes in the graphene sheet shown in Figs. 4-2 (c), (e), and (f), respectively. The normal mode displacements for the RBM, G^T , and G^L phonon modes are aligned with the radial direction of the SWNT and parallel and normal to one of the sp^2 bonds in the SWNT sidewall.

4.4.2 Curvature-adapted model

According to Section 4.4.1, the zone-folding technique predicts a vanishing frequency of the RBM mode, since the RBM originates from the oTA, which is the acoustic phonon mode in the graphene sheet. In fact, however, the curvature of the SWNT sidewall mixes the in-plane and out-of-plane motions of carbon atoms, yielding a finite frequency for the RBM mode [80, 82, 129]. The curvature effect is understood by considering the atomic displacements in the circumferential direction of the SWNT associated with the oTA phonon mode in the graphene sheet, as shown by the red and green curves in Fig. 2-6. The oTA $\mu = 0$ phonon mode has a zero frequency in the graphene sheet, but it involves bond-stretching atomic displacements yielding a finite frequency of the RBM in SWNTs [80, 82, 129]. The oTA $\mu = \pm 1$ phonon modes have a finite frequency in the graphene sheet, while in SWNTs they become the acoustic modes with vanishing frequencies and atomic displacements perpendicular to the SWNT axis [82, 129]. The oTA $\mu = \pm 2$ phonon modes have even higher frequencies

in the graphene sheet, yet they correspond to the low frequency squashing modes in SWNTs [82, 129]. Hence, the curvature of the SWNT sidewall has the strongest effect on the low frequency acoustic phonon modes [61, 129].

The curvature of the SWNT sidewall is incorporated into the force-constant model either by constructing the $6N \times 6N$ dynamical matrix for the translational unit cell of $2N$ carbon atoms [129], or by transforming the 6×6 dynamical matrix for the two-atom unit cell given by Eq. (4.8) to cylindrical coordinates [82], similar to the case of electrons in Section 3.6.2. The 6×6 dynamical matrix in cylindrical coordinates is obtained upon substituting the normal mode displacements $\mathbf{e}_s^\nu(\mathbf{q})$ with $R^z(\phi_{us})\mathbf{e}_s^\nu(\eta, q)$ in the equation of motion, Eq. (4.7):

$$D_{s'\alpha's\alpha}(\eta, q) = \sum_u \left(\delta_{s's} \sum_{s''}^2 \sum_{\beta'}^3 \sum_{\beta}^3 R_{\alpha'\beta'}^z{}^T(\phi_{u's'}) \phi_{u's''\beta'us\beta} R_{\beta\alpha}^z(\phi_{u's'}) - \sum_{\beta'}^3 \sum_{\beta}^3 \exp(i\eta(\phi_{us} - \phi_{u's'}) + iq(z_{us} - z_{u's'})) R_{\alpha'\beta'}^z{}^T(\phi_{u's'}) \phi_{u's'\beta'us\beta} R_{\beta\alpha}^z(\phi_{us}) \right), \quad (4.17)$$

where η and q are the 1D angular and linear momenta substituted for the 2D momentum \mathbf{q} according to Eq. (4.16), ϕ_{us} and z_{us} are the cylindrical projections of the atomic coordinate \mathbf{R}_{us} from Eq. (3.30), $R^z(\phi_{us})$ is the rotation matrix given by Eq. (3.31), and the index u' labels the unit cell under consideration [82].

The force constant matrices Φ_{00rj} for SWNTs are constructed in the normal coordinates (ir, it, ot) according to Eq. (4.15) from the force constant parameters $\phi_\alpha^{(i)}$ for the flat graphene sheet calculated within the ETB framework and listed in Table 4.8. The force constant matrices Φ_{00rj} are then transformed to Cartesian coordinates (x, y, z) using Euler angles (ϕ, θ, ψ) [6]. In order to determine the Euler angles for SWNTs, we depict the (4, 2) ZR/AL SWNT in Fig. 4-19 (a), where the two red spheres represent a pair of us and $u's'$ atoms in the flat graphene sheet connected by the red line in Fig. 4-5 (a). The normal coordinates (ir, it, ot) for the two red atoms are shown by arrows in Fig. 4-19 (a), where ir is a chord connecting the two red atoms, ot is orthogonal to both ir and the SWNT axis, and it is orthogonal to both ir and ot . The two red atoms from Fig. 4-19 (a) are replotted in Fig. 4-19 (b) along with the normal (ir, it, ot) and

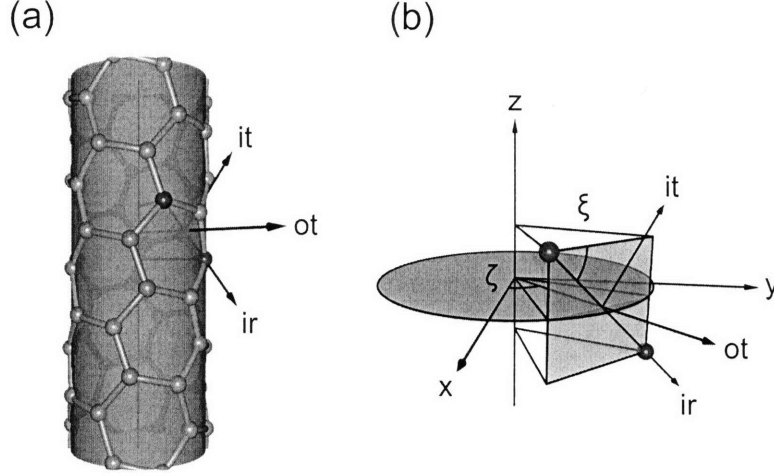


Figure 4-19: (a) The (4,2) ZR/AL SWNT replicated from Fig. 2-3. The two red spheres represent a pair of us and $u's'$ atoms in the flat graphene sheet connected by the red line in Fig. 4-5. The normal coordinates (ir, it, ot) are shown by arrows, where ir is a chord connecting the two red atoms, ot is orthogonal to both ir and the SWNT axis, and it is orthogonal to both ir and ot . (b) The orientation of the normal coordinates (ir, it, ot) for the pair of the red spheres with respect to Cartesian coordinates (x, y, z) determined by angles ζ and ξ . The disc represents the circumferential cross-section of the SWNT.

Cartesian (x, y, z) coordinates. The relative orientation of the two coordinate systems is described by angles ζ and ξ that define the direction of ot in the xy plane and the direction of ir in the normal to the ot plane, as shown in Fig. 4-19 (b). For each pair of us and $u's'$ atoms, the angles ζ and ξ are found from the atomic coordinates \mathbf{R}_{us} and $\mathbf{R}_{u's'}$, the Euler angles are expressed as $(\phi, \theta, \psi) = (\zeta + \pi/2, \pi/2, -\xi)$, and the force constant transformation reads as follows:

$$\Phi_{00ij}^{\text{cart}} = R^{zz}{}^T \left(\zeta + \frac{\pi}{2}, \frac{\pi}{2}, -\xi \right) \Phi_{00ij}^{\text{norm}} R^{zz} \left(\zeta + \frac{\pi}{2}, \frac{\pi}{2}, -\xi \right), \quad (4.18)$$

where $R^{zz}(\zeta + \pi/2, \pi/2, -\xi)$ is the Euler rotation matrix given by [6]:

$$R^{zz} \left(\zeta + \frac{\pi}{2}, \frac{\pi}{2}, -\xi \right) = \begin{pmatrix} -\sin \zeta \cos \xi & \cos \zeta \cos \xi & -\sin \xi \\ -\sin \zeta \sin \xi & \cos \zeta \sin \xi & \cos \xi \\ \cos \zeta & \sin \zeta & 0 \end{pmatrix}, \quad (4.19)$$

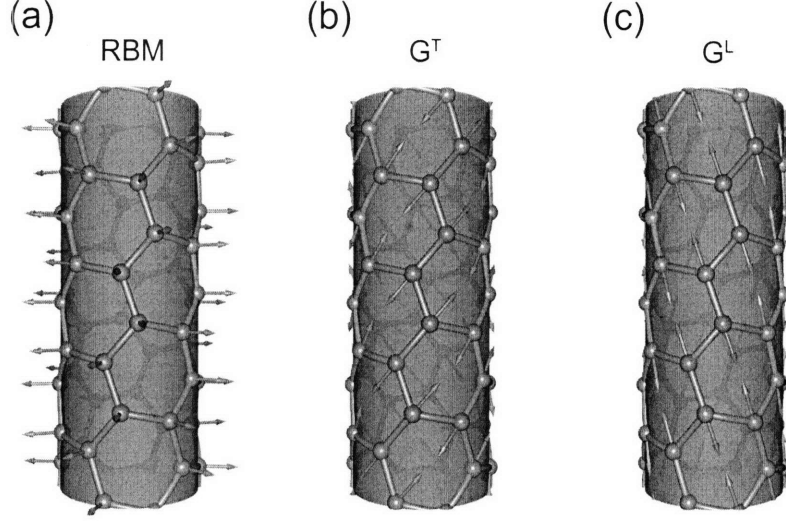


Figure 4-20: The (4, 2) ZR/AL SWNT replicated from Fig. 2-3. The arrows indicate the normal mode displacements for the (a) RBM, (b) G^T , and (c) G^L phonon modes shown in Fig. 4-17 (b). The normal mode displacements are calculated using the curvature-adapted force constant matrices given by Eq. (4.18) with the force constant parameters for the flat graphene sheet taken from Table 4.8. The normal mode displacements for the RBM, G^T , and G^L phonon modes are approximately aligned within a few degrees with the radial direction of the SWNT and with two different sp^2 bonds in the SWNT sidewall [128].

and $R^{zzx^T}(\zeta + \pi/2, \pi/2, -\xi)$ is the transpose of $R^{zzx}(\zeta + \pi/2, \pi/2, -\xi)$. For the flat graphene sheet shown in Fig. 4-5 (a), the Euler angles are given by $(\phi, \theta, \psi) = (\phi_{00ij}, 0, 0)$, the rotation matrix $R^{zzx}(\phi_{00ij}, 0, 0)$ of Eq. (4.19) is equivalent to $R^z(\phi_{00ij})$ from Eq. (3.31), and Eq. (4.18) coincides with Eq. (4.10).

Diagonalizing the dynamical matrix $D_{s'\alpha's\alpha}(\eta, q)$ of Eq. (4.17) yields the phonon dispersion relations $\omega^\nu(\eta, q)$ and the normal mode displacements $e_{s'\alpha'}^\nu(\eta, q)$ of SWNTs. The phonon dispersion relations for the (4, 2) SWNT are shown in Fig. 4-17 (b). The frequencies of the RBM, G^T , and G^L phonon modes are given by $\omega^{\text{RBM}}(\Gamma) = 535 \text{ cm}^{-1}$, $\omega^{G^T}(\Gamma) = 1564 \text{ cm}^{-1}$, and $\omega^{G^L}(\Gamma) = 1573 \text{ cm}^{-1}$. Upon comparing with Section 4.4.1, one finds that the curvature of the SWNT sidewall significantly upshifts the frequency of the RBM phonon mode and slightly downshifts and splits the frequencies of the G^T and G^L phonon modes, in agreement with the above discussion in the first paragraph of Section 4.4.2. The normal mode displacements for the RBM, G^T , and G^L phonon

modes of the (4, 2) SWNT are shown in Fig. 4-20. The normal mode displacements for the RBM mode are approximately aligned with the radial direction of the SWNT (within a few degrees), and the normal mode displacements for the G^T and G^L phonon modes are approximately aligned within a few degrees with two different sp^2 bonds in the SWNT sidewall [128], according to Fig. 4-20, in contrast to the normal mode displacements for the G^T and G^L phonon modes obtained using the zone-folding technique and shown in Figs. 4-18 (b) and (c).

4.4.3 Force constant corrections

The curvature of the SWNT sidewall not only changes the directions of the normal coordinates (ir, it, ot) , as shown in Section 4.4.2, but also affects the values of the force constants [129]. Instead of using the force constant parameters for the flat graphene sheet listed in Table 4.8, different sets of force constants must be calculated explicitly within the ETB framework for specific (n, m) SWNTs along the directions of the normal coordinates (ir, it, ot) shown in Fig. 4-19 (b). The calculation method is identical to the one described in Section 4.3 for the flat graphene sheet. For the (4, 2) SWNT, we have chosen the supercell that contains 3 translational unit cells or 84 two-atom unit cells or 168 carbon atoms. The force constants are obtained by a central finite difference approximation for the first derivative of the Hellmann-Feynman forces with the step $\Delta R = 10^{-4}$ nm. The Hellmann-Feynman forces are calculated from Eq. (3.28) on a 1D Monkhorst-Pack grid of 58 k -points along the cutting lines in the helical-linear representation. The calculated in-plane and out-of-plane force constants are scaled by factors 0.8841^2 and 1.0292^2 , respectively, similar to the force constants for the graphene sheet listed in Table 4.8. The calculated off-diagonal force constants that mix the in-plane and out-of-plane components, $\phi_{u's'\alpha'us\alpha}$ with $(\alpha', \alpha) = (ir, ot), (it, ot), (ot, ir), (ot, it)$, are scaled by a factor of 0.8841×1.0292 . According to the ETB calculations, the circumferential and axial force constants for the (4, 2) SWNT are lowered by about 20% and 4%, respectively, compared to the force constants for the flat graphene sheet listed in Table 4.8.

The phonon dispersion relations and the normal mode displacements obtained

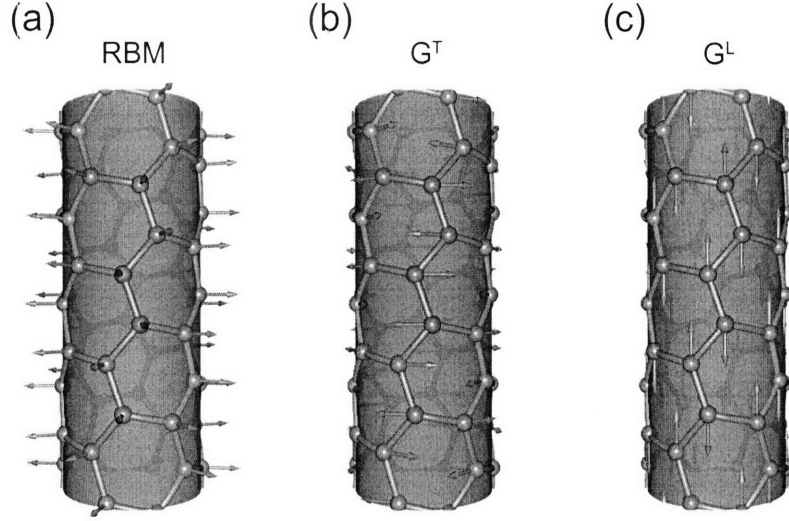


Figure 4-21: The (4, 2) ZR/AL SWNT replicated from Fig. 2-3. The arrows indicate the normal mode displacements for the (a) RBM, (b) G^T , and (c) G^L phonon modes shown in Fig. 4-17 (c). The normal mode displacements are calculated using the curvature-adapted force constant matrices given by Eq. (4.18) with the force constant parameters calculated explicitly for the (4, 2) SWNT within the ETB framework and scaled by factors 0.8841^2 , and 1.0292^2 , and 0.8841×1.0292 , as in Table 4.8. The normal mode displacements for the RBM, G^T , and G^L phonon modes are approximately aligned with the radial, circumferential, and axial directions of the SWNT within a few degrees [82].

from Eqs. (4.17), (4.18), and (4.19) with the aforementioned force constant parameters calculated within the ETB framework for the (4, 2) SWNT are shown in Figs. 4-17 (c) and 4-21, respectively. The normal mode displacements for the RBM, G^T , and G^L phonon modes are approximately aligned with the radial, circumferential, and axial directions of the SWNT within a few degrees [121], according to Fig. 4-21, in contrast to the normal mode displacements for the G^T and G^L phonon modes obtained with the force constant parameters for the flat graphene sheet and shown in Figs. 4-20 (b) and (c). In achiral armchair and zigzag SWNTs, the sp^2 bonds are aligned with the circumferential and axial directions, so that the G^T and G^L phonon modes decouple into pure circumferential and axial components, as follows from group theory. For chiral SWNTs such as (4, 2), the sp^2 bonds are misaligned with the circumferential and axial directions, thus coupling circumferential and axial atomic displacements, according to the symmetry considerations. Early first-principles calculations revealed

a considerable mixing between circumferential and axial atomic motions associated with the G^T and G^L phonon modes in chiral SWNTs [128], whose atomic displacements are approximately aligned with two different sp^2 bonds in the SWNT sidewall, as shown in Figs. 4-20 (b) and (c). Recent calculations within the ETB framework discussed in Section 4.5, on the other hand, indicate a small departure from the pure circumferential and axial character of the G^T and G^L phonon modes in chiral SWNTs [121], as shown in Figs. 4-21 (b) and (c). The directions of the normal mode displacements are thus very sensitive to the values of the interatomic force constants. Further investigations are expected to clarify this issue.

The frequencies of the RBM, G^T , and G^L phonon modes shown in Fig. 4-17 (c) are given by $\omega^{\text{RBM}}(\Gamma) = 522 \text{ cm}^{-1}$, $\omega^{G^T}(\Gamma) = 1430 \text{ cm}^{-1}$, and $\omega^{G^L}(\Gamma) = 1531 \text{ cm}^{-1}$. Upon comparing Fig. 4-17 (c) with Fig. 4-17 (b), we find that the curvature of the SWNT sidewall splits the frequencies of the G^T and G^L phonon modes. This splitting can be understood taking into account that the G^T and G^L phonon modes involve atomic displacements in the circumferential and axial directions, respectively, as shown in Figs. 4-21 (b) and (c). The circumferential and axial force constants scale by the factors of 0.80 and 0.96, respectively, according to the ETB calculations. The frequencies of the G^T and G^L phonon modes are then expected to scale as $\sqrt{0.80} = 0.89$ and $\sqrt{0.96} = 0.98$, respectively. In fact, however, the frequency scaling factors are given by $1430/1582 = 0.90$ and $1531/1582 = 0.97$, as follows from comparing Figs. 4-17 (a) and (c). The small difference between the force constant scaling factors and the frequency scaling factors indicates the small contributions of the circumferential (axial) force constants to the axial G^L (circumferential G^T) phonon mode.

4.5 Direct calculation of the dynamical matrix

A different set of force constants must be calculated for each (n, m) SWNT within the ETB framework, as shown in Section 4.4.3. Such calculations are time consuming, as they involve large supercells in order to minimize interactions between the pairs of atoms in the adjacent supercells. Furthermore, the Fourier transform of the force

constants in Eq. (4.8) eliminates singularities in the dynamical matrix and, accordingly, in the phonon dispersion relations, because of the long-range interaction cut-off at the twentieth nearest neighbor. Such singularities in fact appear in the phonon dispersion relations of the graphene sheet and metallic SWNTs, as discussed below in Section 4.6. Also, the force constant approach developed in Section 4.1 excludes anharmonic corrections to the dynamical matrix, which become essential for certain phonon modes, as will be shown in Section 4.6. In this section, we directly calculate the dynamical matrix within the ETB framework without using the force constant approximation.

4.5.1 Supercell method

The frequencies of the optical phonon modes at the Γ point of the graphene sheet are expressed from the equation of motion, Eq. (4.7), in the following form:

$$\omega^\nu(\mathbf{q}) = \sqrt{\frac{1}{M} \sum_{s'}^2 \sum_{\alpha'}^3 \sum_s^2 \sum_\alpha^3 e_{s'\alpha'}^{\nu*}(\mathbf{q}) D_{s'\alpha's\alpha}(\mathbf{q}) e_{s\alpha}^\nu(\mathbf{q})}, \quad (4.20)$$

where the dynamical matrix $D_{s'\alpha's\alpha}(\mathbf{q})$ is obtained from the second variation $\delta^2 E$ of the total energy E per carbon atom with respect to the normal mode displacements:

$$\delta^2 E = \frac{1}{2} \rho^{\nu^2}(\mathbf{q}) \sum_{s'}^2 \sum_{\alpha'}^3 \sum_s^2 \sum_\alpha^3 e_{s'\alpha'}^{\nu*}(\mathbf{q}) D_{s'\alpha's\alpha}(\mathbf{q}) e_{s\alpha}^\nu(\mathbf{q}), \quad (4.21)$$

the factor of $\frac{1}{2}$ stands for two atoms per unit cell, and $\mathbf{q} = 0$ at the Γ point. Upon substituting Eq. (4.21) into Eq. (4.20), the frequencies of the phonon modes are written as follows:

$$\omega^\nu(\mathbf{q}) = \sqrt{\frac{2 \delta^2 E}{M \rho^{\nu^2}(\mathbf{q})}}, \quad (4.22)$$

where $\delta^2 E$ is calculated within the framework of the ETB model.

The normal mode displacements $e_{s\alpha}^\nu(\mathbf{q})$ in Eq. (4.21) for the optical phonon modes $\nu = \text{iLO, iT0, oTO}$ at the Γ point of the graphene sheet are determined by group theory, as shown in Figs. 4-2 (d) to (f). The second variation of the total energy $\delta^2 E$

in Eq. (4.22) is evaluated by a central finite difference approximation for the second derivative of the total energy along the aforementioned normal mode displacements with the step $\Delta R = 10^{-4}$ nm. The total energy E for the two-atom unit cell is calculated from Eq. (3.27) on a 60×60 Monkhorst-Pack grid in reciprocal space. The frequencies $\omega^{\text{iLO}}(\Gamma) = \omega^{\text{iTO}}(\Gamma) = 1797 \text{ cm}^{-1}$ and $\omega^{\text{oTO}}(\Gamma) = 825 \text{ cm}^{-1}$ obtained from Eq. (4.22) deviate from the experimental data $\omega^{\text{iLO}}(\Gamma) = \omega^{\text{iTO}}(\Gamma) = 1582 \text{ cm}^{-1}$ and $\omega^{\text{oTO}}(\Gamma) = 868 \text{ cm}^{-1}$ [170] by factors of 0.8841 and 1.0292, respectively, in accordance with the force constants listed in Table 4.8.

In a similar fashion, the frequencies of the RBM, G^{T} , and G^{L} phonon modes in SWNTs are expressed by Eqs. (4.21) and (4.22) upon substituting the 1D angular η and linear q momenta from Eq. (4.16) for the 2D momentum \mathbf{q} and switching to cylindrical coordinates represented by the rotation matrices $R^z(\phi_{u's'})$ in the dynamical matrix $D_{s'\alpha's\alpha}(\eta, q)$ of Eq. (4.17). However, the normal mode displacements $e_{s'\alpha'}^{\nu}(\eta, q)$ in Eq. (4.21) for the RBM, G^{T} , and G^{L} phonon modes in SWNTs are not known from group theory, as opposed to the graphene sheet, because of the lower symmetry of SWNTs than that of the graphene sheet. For achiral armchair and zigzag SWNTs, even though the circumferential and axial components of the atomic displacements are decoupled by symmetry considerations, they are still allowed to mix with the radial component [80]. For chiral SWNTs, the circumferential and axial components are allowed to mix not only with the radial component but also with each other [128]. The normal mode displacements for the RBM, G^{T} , and G^{L} phonon modes thus deviate from the pure radial, circumferential, and axial directions by a few degrees [121], as shown in Fig. 4-21. The small deviations of the normal mode displacements lead to significant changes in the frequencies of the phonon modes. Hence, the normal mode displacements need to be determined along with the frequencies of the phonon modes at the Γ point by diagonalizing the 6×6 dynamical matrix for SWNTs.

The 6×6 dynamical matrix for SWNTs is given by the Hessian of the total energy E in cylindrical coordinates, as follows from Eq. (4.21) upon substituting η and q from Eq. (4.16) for \mathbf{q} :

$$D_{s'\alpha's\alpha}(\eta, q) = \frac{1}{2} \frac{\partial^2 E}{\partial R_{u's'\alpha'} \partial R_{u's\alpha}}, \quad (4.23)$$

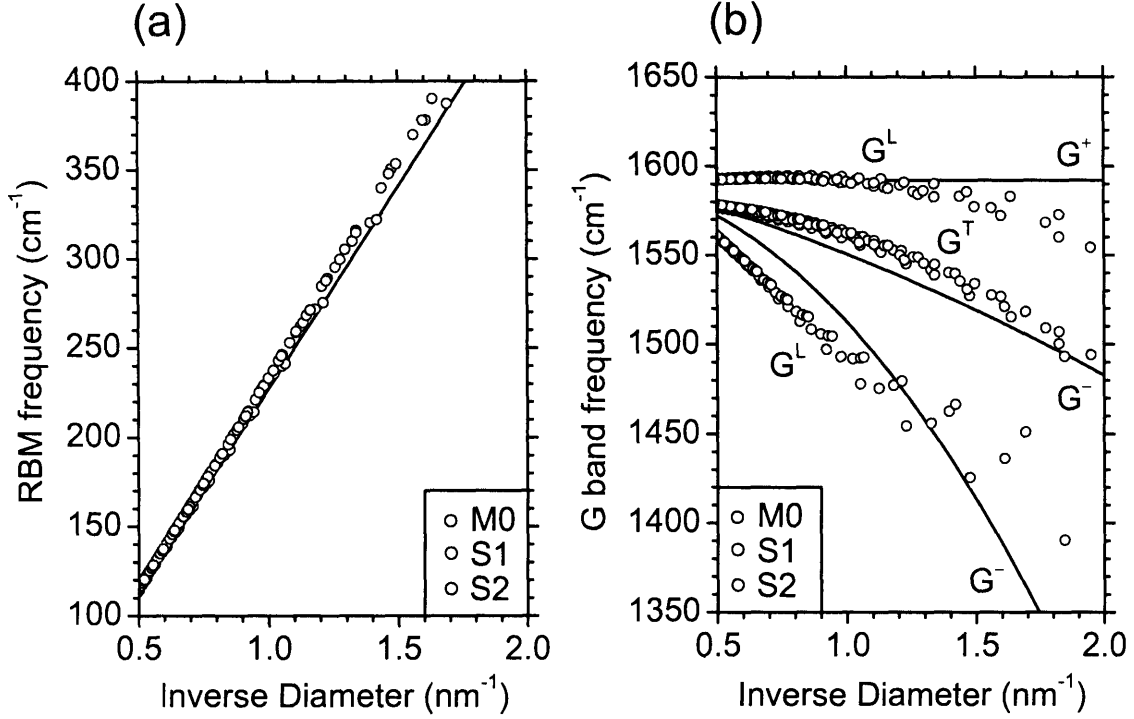


Figure 4-22: The dots show the frequencies of the (a) RBM, (b) G^T , and G^L phonon modes for all possible (n, m) SWNTs obtained by diagonalizing the dynamical matrix of Eq. (4.23) calculated within the ETB framework and scaled by a factor of 0.8841^2 , as in Table 4.8. For the $(4, 2)$ SWNT, the frequencies of the RBM, G^T , and G^L phonon modes are given by 524 cm^{-1} , 1433 cm^{-1} , and 1536 cm^{-1} , respectively. The red, green, and blue dots correspond to M0, S1, and S2 SWNTs, respectively. The curves show the least-square fits to the experimentally observed frequencies of the RBM, G^- , and G^+ Raman modes according to Eq. (4.24).

where $\alpha', \alpha = r, \phi, z$ correspond to the radial, circumferential, and axial directions, according to Eq. (3.30), the factor of $\frac{1}{2}$ is associated with the second partial derivative of the total energy E , while $\frac{1}{2}$ from Eq. (4.21) is compensated by the orthonormality condition of Eq. (4.3), $\eta = 0$ and $q = 0$ at the Γ point, and the index u' labels the unit cell under consideration. The second partial derivatives of the total energy E in Eq. (4.23) are evaluated by a central finite difference approximation with the step $\Delta R = 10^{-4} \text{ nm}$. The total energy E is calculated from Eq. (3.27) on a 1D Monkhorst-Pack grid of $(1 \mu\text{m}/T)$ k -points along the cutting lines in the helical-linear representation and scaled by a factor of 0.8841^2 , as in Table 4.8. For the $(4, 2)$ SWNT, the 1D Monkhorst-Pack grid consists of 884 k -points.

Diagonalizing the dynamical matrix of Eq. (4.23) yields the frequencies and the normal mode displacements for the RBM, G^T , and G^L phonon modes in SWNTs. The frequencies of the RBM, G^T , and G^L phonon modes as functions of the inverse SWNT diameter are shown in Fig. 4-22. Note that for M0 SWNTs, the frequencies of the G^L phonon modes are softened below the frequencies of the G^T phonon modes. The softening mechanism will be discussed in Section 4.6. For the (4, 2) SWNT, the frequencies of the RBM, G^T , and G^L phonon modes are given by $\omega^{\text{RBM}}(\Gamma) = 524 \text{ cm}^{-1}$, $\omega^{G^T}(\Gamma) = 1433 \text{ cm}^{-1}$, and $\omega^{G^L}(\Gamma) = 1536 \text{ cm}^{-1}$, in good agreement with the results of the curvature-adapted force-constant model shown in Figs. 4-17 (c). The normal mode displacements for the RBM, G^T , and G^L phonon modes are approximately aligned with the radial, circumferential, and axial directions of the SWNT within a few degrees [121], as shown in Fig. 4-21 for the (4, 2) SWNT.

The frequencies of the RBM, G^T , and G^L phonon modes shown in Fig. 4-22 can be directly compared with the experimental results. The resonance Raman spectra of SWNTs show three main peaks, the RBM and the G -band whose lower and higher frequency components are referred to as G^- and G^+ , as will be discussed in Section 5.3. The least-square fits to the experimentally observed frequencies of the RBM, G^- , and G^+ Raman modes from SDS-wrapped HiPCO SWNTs in D_2O [63] and individual CVD SWNTs on a Si/SiO_2 substrate [64, 67] as functions of the SWNT diameter yield the following dependencies:

$$\left\{ \begin{array}{l} \omega^{\text{RBM}}(\Gamma) = \frac{227 \text{ cm}^{-1}\text{nm}}{d_t}, \\ \omega^{G^-}(\Gamma) = 1592 \text{ cm}^{-1} - \frac{79.5 \text{ cm}^{-1}\text{nm}^2}{d_t^2} \quad \text{for M0,} \\ \omega^{G^-}(\Gamma) = 1592 \text{ cm}^{-1} - \frac{41.4 \text{ cm}^{-1}\text{nm}^{1.4}}{d_t^{1.4}} \quad \text{for S1 and S2,} \\ \omega^{G^+}(\Gamma) = 1592 \text{ cm}^{-1}, \end{array} \right. \quad (4.24)$$

shown by the curves in Fig. 4-22. Upon comparing theoretical dots with experimental curves in Fig. 4-22, we find a good agreement for the RBM frequencies. For S1 and S2 SWNTs, the G^- and G^+ Raman bands are attributed to the G^T and G^L phonon

modes, respectively. For M0 SWNTs, the softened G^L phonon mode fits nicely the G^- Raman band. However, there is a significant frequency mismatch between the theoretical G^T phonon mode and the experimental G^+ Raman band in M0 SWNTs. The origin of the G^+ Raman band in M0 SWNTs requires further theoretical and experimental studies.

For a general phonon wavevector away from the Γ point in the graphene sheet and SWNTs, the proper supercell commensurate with the lattice distortion should be brought into consideration, as shown in Section 3.3 for the K point. The dynamical matrix of proper dimension is then constructed, similar to the 6×6 dynamical matrix of Eq. (4.22) for the Γ point. The supercell approach is thus very efficient for the phonon modes at high symmetry points in the first Brillouin zones of the graphene sheet and SWNTs, when the dynamical matrix has a small dimension. However, the size of the supercell and, accordingly, the dimension of the dynamical matrix drastically increases away from the high symmetry points, making the supercell method impractical. To overcome this complexity, in Section 4.5.2 we employ the linear response approach originally developed within the framework of density-functional perturbation theory (DFPT) [10] and recently implemented for the ETB framework [121]. Within the linear response theory, the dynamical matrix for a general phonon wavevector is calculated on a single two-atom unit cell of the graphene sheet and SWNTs [10, 121].

4.5.2 Linear response method

Within the linear response method, the dynamical matrix $D_{s'\alpha's\alpha}(\mathbf{q})$ for the graphene sheet is associated with the second variation $\delta^2 E$ of the total energy E per carbon atom with respect to the normal mode displacements $e_{s\alpha}^\nu(\mathbf{q})$, according to Eq. (4.21). The variation $\delta^2 E$ is obtained by second-order perturbation theory with respect to a static lattice deformation:

$$\mathbf{r}_{us}^\nu = \frac{1}{\sqrt{2}} \rho^\nu(\mathbf{q}) \left(\exp(+i\mathbf{q}\mathbf{R}_{us}) \mathbf{e}_s^\nu(\mathbf{q}) + \exp(-i\mathbf{q}\mathbf{R}_{us}) \mathbf{e}_s^{\nu*}(\mathbf{q}) \right), \quad (4.25)$$

emphasizing a specific phonon wavevector \mathbf{q} from Eq. (4.2) [10]. The second variation of the total energy $\delta^2 E$ consists of four terms [121]:

$$\delta^2 E = \delta^2 E^{(1)} + \delta^2 E^{(2)} + \delta^2 E^{(3)} + \delta^2 E^{(4)}, \quad (4.26)$$

taking into account the nonorthogonality of the ETB basis set [93]. The term $\delta^2 E^{(1)}$ in Eq. (4.26) is similar to the expression for the Hellmann-Feynman force, substituting the first partial derivatives of the Hamiltonian $H_{s'o'so}(\mathbf{k}_w)$ and overlap $S_{s'o'so}(\mathbf{k}_w)$ matrices in Eq. (3.28) with the second partial derivatives:

$$\begin{aligned} \delta^2 E^{(1)} &= \frac{1}{2} \rho^{\nu^2}(\mathbf{q}) \sum_{s'}^2 \sum_{\alpha'}^3 \sum_s^2 \sum_\alpha^3 \frac{1}{W} \sum_w^W \sum_b^8 n^b(\mathbf{k}_w) \\ &\times \sum_u^U \sum_{o'}^4 \sum_o^4 C_{s'o'}^{b*}(\mathbf{k}_w) \left(\frac{\partial^2 [\exp(+i\mathbf{k}_w(\mathbf{R}_{us} - \mathbf{R}_{u's'})) t_{oo'}(|\mathbf{R}_{us} - \mathbf{R}_{u's'}|)]}{\partial(R_{us\alpha'} - R_{u's'\alpha'}) \partial(R_{us\alpha} - R_{u's'\alpha})} \right. \\ &- E^b(\mathbf{k}_w) \frac{\partial^2 [\exp(+i\mathbf{k}_w(\mathbf{R}_{us} - \mathbf{R}_{u's'})) s_{oo'}(|\mathbf{R}_{us} - \mathbf{R}_{u's'}|)]}{\partial(R_{us\alpha'} - R_{u's'\alpha'}) \partial(R_{us\alpha} - R_{u's'\alpha})} \left. \right) C_{so}^b(\mathbf{k}_w) \\ &\times \left(e_{s\alpha'}^{\nu*}(\mathbf{q}) - \exp(+i\mathbf{q}(\mathbf{R}_{us} - \mathbf{R}_{u's'})) e_{s'\alpha'}^{\nu*}(\mathbf{q}) \right) \\ &\times \left(e_{s\alpha}^\nu(\mathbf{q}) - \exp(-i\mathbf{q}(\mathbf{R}_{us} - \mathbf{R}_{u's'})) e_{s'\alpha}^\nu(\mathbf{q}) \right). \end{aligned} \quad (4.27)$$

The terms $\delta^2 E^{(2)}$ and $\delta^2 E^{(3)}$ in Eq. (4.26) involve the first partial derivatives of the Bloch amplitudes $C_{so}^b(\mathbf{k}_w)$ decomposed into the Bloch amplitudes $C_{so}^b(\mathbf{k}_w + \mathbf{q})$ and $C_{so}^b(\mathbf{k}_w - \mathbf{q})$, respectively, describing the scattering between the electrons with

wavevectors \mathbf{k}_w and $\mathbf{k}_w \pm \mathbf{q}$ by the phonons with wavevector \mathbf{q} :

$$\begin{aligned}
\delta^2 E^{(2)} &= \frac{1}{2} \rho^{\nu^2}(\mathbf{q}) \sum_{s'}^2 \sum_{\alpha'}^3 \sum_s^2 \sum_{\alpha}^3 \frac{1}{W} \sum_w^W \sum_{b'}^8 \sum_b^8 \frac{n^b(\mathbf{k}_w)(2 - n^{b'}(\mathbf{k}_w + \mathbf{q}))}{E^b(\mathbf{k}_w) - E^{b'}(\mathbf{k}_w + \mathbf{q})} \\
&\times \left[\sum_u^U \sum_{o'}^4 \sum_o^4 C_{s'o'}^{b'*}(\mathbf{k}_w) \left(\frac{\partial [\exp(+i\mathbf{k}_w(\mathbf{R}_{us} - \mathbf{R}_{u's'}))t_{oo'}(|\mathbf{R}_{us} - \mathbf{R}_{u's'}|)]}{\partial (R_{us\alpha'} - R_{u's'\alpha'})} \right. \right. \\
&- E^b(\mathbf{k}_w) \frac{\partial [\exp(+i\mathbf{k}_w(\mathbf{R}_{us} - \mathbf{R}_{u's'}))s_{oo'}(|\mathbf{R}_{us} - \mathbf{R}_{u's'}|)]}{\partial (R_{us\alpha'} - R_{u's'\alpha'})} \left. \left. \right) C_{so}^{b'}(\mathbf{k}_w + \mathbf{q}) \right. \\
&\times \left. \left(\exp(-i\mathbf{q}(\mathbf{R}_{us} - \mathbf{R}_{u's'}))e_{s\alpha'}^{\nu^*}(\mathbf{q}) - e_{s'\alpha'}^{\nu^*}(\mathbf{q}) \right) \right] \tag{4.28} \\
&\times \left[\sum_u^U \sum_{o'}^4 \sum_o^4 C_{s'o'}^{b'*}(\mathbf{k}_w + \mathbf{q}) \left(\frac{\partial [\exp(+i\mathbf{k}_w(\mathbf{R}_{us} - \mathbf{R}_{u's'}))t_{oo'}(|\mathbf{R}_{us} - \mathbf{R}_{u's'}|)]}{\partial (R_{us\alpha} - R_{u's'\alpha})} \right. \right. \\
&- E^b(\mathbf{k}_w) \frac{\partial [\exp(+i\mathbf{k}_w(\mathbf{R}_{us} - \mathbf{R}_{u's'}))s_{oo'}(|\mathbf{R}_{us} - \mathbf{R}_{u's'}|)]}{\partial (R_{us\alpha} - R_{u's'\alpha})} \left. \left. \right) C_{so}^b(\mathbf{k}_w) \right. \\
&\times \left. \left(e_{s\alpha}^{\nu}(\mathbf{q}) - \exp(-i\mathbf{q}(\mathbf{R}_{us} - \mathbf{R}_{u's'}))e_{s'\alpha}^{\nu}(\mathbf{q}) \right) \right],
\end{aligned}$$

and

$$\begin{aligned}
\delta^2 E^{(3)} &= \frac{1}{2} \rho^{\nu^2}(\mathbf{q}) \sum_{s'}^2 \sum_{\alpha'}^3 \sum_s^2 \sum_{\alpha}^3 \frac{1}{W} \sum_w^W \sum_{b'}^8 \sum_b^8 \frac{n^b(\mathbf{k}_w)(2 - n^{b'}(\mathbf{k}_w - \mathbf{q}))}{E^b(\mathbf{k}_w) - E^{b'}(\mathbf{k}_w - \mathbf{q})} \\
&\times \left[\sum_u^U \sum_{o'}^4 \sum_o^4 C_{s'o'}^{b'*}(\mathbf{k}_w) \left(\frac{\partial [\exp(+i\mathbf{k}_w(\mathbf{R}_{us} - \mathbf{R}_{u's'}))t_{oo'}(|\mathbf{R}_{us} - \mathbf{R}_{u's'}|)]}{\partial (R_{us\alpha'} - R_{u's'\alpha'})} \right. \right. \\
&- E^b(\mathbf{k}_w) \frac{\partial [\exp(+i\mathbf{k}_w(\mathbf{R}_{us} - \mathbf{R}_{u's'}))s_{oo'}(|\mathbf{R}_{us} - \mathbf{R}_{u's'}|)]}{\partial (R_{us\alpha'} - R_{u's'\alpha'})} \left. \left. \right) C_{so}^{b'}(\mathbf{k}_w - \mathbf{q}) \right. \\
&\times \left. \left(\exp(+i\mathbf{q}(\mathbf{R}_{us} - \mathbf{R}_{u's'}))e_{s\alpha'}^{\nu}(\mathbf{q}) - e_{s'\alpha'}^{\nu}(\mathbf{q}) \right) \right] \tag{4.29} \\
&\times \left[\sum_u^U \sum_{o'}^4 \sum_o^4 C_{s'o'}^{b'*}(\mathbf{k}_w - \mathbf{q}) \left(\frac{\partial [\exp(+i\mathbf{k}_w(\mathbf{R}_{us} - \mathbf{R}_{u's'}))t_{oo'}(|\mathbf{R}_{us} - \mathbf{R}_{u's'}|)]}{\partial (R_{us\alpha} - R_{u's'\alpha})} \right. \right. \\
&- E^b(\mathbf{k}_w) \frac{\partial [\exp(+i\mathbf{k}_w(\mathbf{R}_{us} - \mathbf{R}_{u's'}))s_{oo'}(|\mathbf{R}_{us} - \mathbf{R}_{u's'}|)]}{\partial (R_{us\alpha} - R_{u's'\alpha})} \left. \left. \right) C_{so}^b(\mathbf{k}_w) \right. \\
&\times \left. \left(e_{s\alpha}^{\nu^*}(\mathbf{q}) - \exp(+i\mathbf{q}(\mathbf{R}_{us} - \mathbf{R}_{u's'}))e_{s'\alpha}^{\nu^*}(\mathbf{q}) \right) \right].
\end{aligned}$$

The term $\delta^2 E^{(4)}$ in Eq. (4.26) arises from the second derivatives of the short-range

repulsive potential $v(|\mathbf{R}_{us} - \mathbf{R}_{u's'}|)$ between pairs of carbon atoms in the total energy given by Eq. (3.27):

$$\begin{aligned} \delta^2 E^{(4)} &= \frac{1}{2} \rho^{\nu^2}(\mathbf{q}) \sum_{s'}^2 \sum_{\alpha'}^3 \sum_s^2 \sum_{\alpha}^3 \frac{1}{2} \sum_u^U \frac{d^2 v(|\mathbf{R}_{us} - \mathbf{R}_{u's'}|)}{d(R_{us\alpha'} - R_{u's'\alpha'}) d(R_{us\alpha} - R_{u's'\alpha})} \\ &\times \left(e_{s\alpha'}^{\nu^*}(\mathbf{q}) - \exp(+i\mathbf{q}(\mathbf{R}_{us} - \mathbf{R}_{u's'})) e_{s'\alpha'}^{\nu^*}(\mathbf{q}) \right) \\ &\times \left(e_{s\alpha}^{\nu}(\mathbf{q}) - \exp(-i\mathbf{q}(\mathbf{R}_{us} - \mathbf{R}_{u's'})) e_{s'\alpha}^{\nu}(\mathbf{q}) \right). \end{aligned} \quad (4.30)$$

By comparing Eq. (4.21) with Eqs. (4.26) to (4.30), the dynamical matrix $D_{s'\alpha's\alpha}(\mathbf{q})$ for the graphene sheet is obtained. Diagonalizing $D_{s'\alpha's\alpha}(\mathbf{q})$ yields the phonon dispersion relations identical to those shown in Fig. 4-14 [121]. The linear response method thus gives the same results for the graphene sheet as the AFC model.

The dynamical matrix $D_{s'\alpha's\alpha}(\eta, q)$ for SWNTs is obtained upon multiplying \mathbf{e}_s^{ν} by $R^z(\phi_{us})$ and substituting $\mathbf{q}\mathbf{R}_{us}$ with $(\eta\phi_{us} + qz_{us})$ and $\mathbf{k}_w\mathbf{R}_{us}$ with $(\mu_w\phi_{us} + k_wz_{us})$ in Eqs. (4.26) to (4.30), by analogy with Eq. (4.17). Diagonalizing $D_{s'\alpha's\alpha}(0, 0)$ yields the frequencies of the RBM, G^- , and G^+ phonon modes identical to those shown in Fig. 4-22 [121]. The linear response method predicts the frequency softening for the G^+ phonon modes in metallic SWNTs [121], similar to the supercell method in Section 4.5.1. Furthermore, the linear response method also predicts the frequency softening for certain phonon modes away from the Γ point in metallic SWNTs [121], where the supercell method becomes impractical, as discussed in Section 4.5.1. The mechanism of the frequency softening in metallic SWNTs will be discussed below in Section 4.6. For the RBM, G^- , and G^+ phonon modes, the linear response method yields the normal mode displacements aligned with the radial, circumferential, and axial directions of the SWNT within a few degrees [121], as shown in Fig. 4-20 for the (4, 2) SWNT. This contradicts the results of the early first-principles calculations [128], but on the other hand, these early calculations did not predict the frequency softening in metallic SWNTs. Future studies are expected to clarify the present debate about the directions of the normal mode displacements in SWNTs.

4.6 Phonon frequency softening

The frequency softening of the G^+ phonon mode in metallic SWNTs predicted by the ETB calculations in Sections 4.4 and 4.5 has in fact been observed by resonance Raman scattering from SWNT bundles [116]. Similarly, the overbending of the iLO phonon mode around the Γ point and the softening of the iT0 phonon mode around the K point in the graphene sheet obtained within the ETB framework in Section 4.3 have recently been measured by inelastic x-ray scattering from a graphite flake [92]. The frequency softening is attributed to Peierls instabilities in metallic SWNTs [38] and to Kohn anomalies in the graphene sheet [117]. The Peierls instability, analogous to the Jahn-Teller effect in molecular systems, occurs when a phonon mode opens a dynamical (oscillating with the phonon frequency) band gap at the Fermi level E_F in a graphene sheet [162] and in metallic SWNTs [38]. The Kohn anomaly occurs when electrons at the Fermi surface screen the phonon mode in a graphene sheet [117] and in metallic SWNTs [9, 13, 27, 121]. The two aforementioned phenomena are manifestations of the same underlying electron-phonon coupling mechanism. When a phonon mode opens a dynamical band gap, all the valence electrons lie in states whose energy is lowered, thus reducing the total energy and softening the phonon frequency. On the other hand, the soft phonon mode induces electron scattering at the Fermi surface, which in turn generates charge density waves, opening a dynamical band gap [137].

4.6.1 Peierls instability

The Fermi surface for the graphene sheet is reduced to the K and K' points in the first Brillouin zone, as shown in Chapter 3. The electrons at the Fermi surface are thus scattered either within the same K or K' point by the phonon modes around the Γ point, or between different K and K' points by the phonon modes near the K or K' point, as will be discussed in Section 5.3. The normal mode displacements for the phonon modes of the graphene sheet at the Γ and K points are shown in Figs. 4-2 and 4-4, respectively. Among these phonon modes, only the iLO and iT0 at the Γ

point and the iLA, iLO, and iT0 at the K point are strongly coupled to π -electrons, while the other 7 phonon modes do not change the interatomic distances in the first order approximation, and therefore they are only weakly coupled to π -electrons (though 4 of them are strongly coupled to σ -electrons by changing the bond angles).

The STB Hamiltonian of Eq. (3.9) for the graphene sheet distorted by the iLO and iT0 phonon modes at the Γ point takes the form:

$$H = \begin{pmatrix} \varepsilon + \lambda h^\nu(\mathbf{k}) & t f^\nu(\mathbf{k}) + \alpha g^\nu(\mathbf{k}) \\ t f^{\nu*}(\mathbf{k}) + \alpha g^{\nu*}(\mathbf{k}) & \varepsilon + \lambda h^\nu(\mathbf{k}) \end{pmatrix}, \quad (4.31)$$

with terms $f^\nu(\mathbf{k})$, $g^\nu(\mathbf{k})$, and $h^\nu(\mathbf{k})$ being defined as follows:

$$\begin{cases} f^\nu(\mathbf{k}) = \sum_j^3 \exp\left(i\mathbf{k} \left(\mathbf{R}_{jB} - \mathbf{R}_{0A} + \mathbf{r}_{jB}^\nu - \mathbf{r}_{0A}^\nu\right)\right), \\ g^\nu(\mathbf{k}) = \sum_j^3 \exp\left(i\mathbf{k} \left(\mathbf{R}_{jB} - \mathbf{R}_{0A} + \mathbf{r}_{jB}^\nu - \mathbf{r}_{0A}^\nu\right)\right) \frac{(\mathbf{R}_{jB} - \mathbf{R}_{0A}) \cdot (\mathbf{r}_{jB}^\nu - \mathbf{r}_{0A}^\nu)}{a_{CC}}, \\ h^\nu(\mathbf{k}) = \sum_j^3 \frac{(\mathbf{R}_{jB} - \mathbf{R}_{0A}) \cdot (\mathbf{r}_{jB}^\nu - \mathbf{r}_{0A}^\nu)}{a_{CC}}, \end{cases} \quad (4.32)$$

instead of Eq. (3.8). The overlap matrix in Eq. (3.9) is omitted for simplicity, the transfer integral t is renormalized to $(t - \varepsilon s)$ and s is set to zero, according to Eq. (3.14). Employing the ETB parameters from Section 3.6, we find $\varepsilon = -5.372$ eV, $s = 0$, and $t = -3.370 + 5.372 \times 0.151$ eV = -2.56 eV. The on-site λ and off-site α electron-phonon coupling (EPC) coefficients are given by the derivatives of ε and t with respect to the interatomic distance yielding $\alpha = 76.6 - 5.372 \times 3.43$ eV/nm = 58.2 eV/nm. Within the ETB framework, the atomic orbital energy ε is a constant parameter and λ is approximated by $\frac{3}{8}$ of the derivative of the short-range repulsive potential v , so that $\lambda = -\frac{3}{8} \times 106.3$ eV/nm = -39.9 eV/nm.

The coordinates \mathbf{R}_{js} and displacements \mathbf{r}_{js}^ν of the atomic sites within the two-atom unit cell and their first nearest neighbors are numbered by index j from 0 to 3, as shown by the red numbers in Fig. 2-1 (a). The atomic displacements are written in the following form:

$$\mathbf{r}_{js}^\nu = \frac{1}{\sqrt{2}} \rho \left(\exp(-i\omega t) \mathbf{e}_s^\nu(\mathbf{0}) + \exp(+i\omega t) \mathbf{e}_s^{\nu*}(\mathbf{0}) \right), \quad (4.33)$$

emphasizing the Γ point phonon modes from Eq. (4.2), where the subscript ν and the argument $\mathbf{q} = \mathbf{0}$ of the amplitude of the normal mode displacements ρ and the frequency of the phonon modes ω are omitted for brevity. Substituting the normal mode displacements $\mathbf{e}_s^\nu(\Gamma)$ shown in Figs. 4-2 (d) and (e) into Eqs. (4.33), (4.32) and (4.31) and setting the determinant of H to zero, we find that the Fermi points \mathbf{k}_F and \mathbf{k}'_F oscillate at the phonon frequency with displacement amplitudes $\Delta\mathbf{k}_F$ and $\Delta\mathbf{k}'_F$ around the K and K' points [38]:

$$\begin{cases} \Delta\mathbf{k}_F = -\frac{2\sqrt{3}\alpha\rho}{ta} \cos\omega t \hat{\mathbf{x}} & \text{and} & \Delta\mathbf{k}'_F = -\Delta\mathbf{k}_F & \text{for the iLO } E_{2g} \text{ mode,} \\ \Delta\mathbf{k}_F = +\frac{2\sqrt{3}\alpha\rho}{ta} \cos\omega t \hat{\mathbf{y}} & \text{and} & \Delta\mathbf{k}'_F = -\Delta\mathbf{k}_F & \text{for the iT0 } E_{2g} \text{ mode,} \end{cases} \quad (4.34)$$

determined by the off-site EPC coefficient α , since the terms in Eq. (4.31) with the on-site EPC λ coefficient that are linear in ρ/a cancel out for the normal mode displacements shown in Figs. 4-2 (d) and (e).

Since the lattice distortions caused by the phonon modes at the K point are incommensurate with the two-atom unit cell, the six-atom supercell must be introduced as described in Section 3.3. The first Brillouin zone of the supercell is triple-folded, with both the K and K' points (\mathbf{k}_F and \mathbf{k}'_F) mapped to the Γ point. The electronic states at the Γ point are therefore four-fold degenerate, which, however, is lifted by the lattice distortions caused by the K point phonon modes. To study the degeneracy-lifting mechanism we employ group theory.

The group of the wavevector G_k (G_Γ or G_K) is isomorphic to the group D_{2h} when the graphene sheet is distorted by the E_{2g} Γ or E' K point phonon modes shown in Figs. 4-2 (d), 4-2 (e), 4-4 (a), and 4-4 (d). The four-fold degenerate electronic state at the Γ point thus consists of the four one-dimensional (1D) irreducible representations of group D_{2h} : two B_{1u} (valence bands) and two B_{2g} (conduction bands). This state therefore splits into two two-fold degenerate states $B_{1u}+B_{2g}$ below and above the

Fermi level E_F . Such a splitting shifts the band-crossing points \mathbf{k}_F and \mathbf{k}'_F away from the Γ point to states \mathbf{k} and $-\mathbf{k}$, respectively, maintaining the time-reversal symmetry requirement $\mathbf{k}'_F = -\mathbf{k}_F$. This shift is allowed by group theory because the star of a general wavevector $\mathbf{k} \neq 0$ (the set of wavevectors generated from \mathbf{k} by point group operations) consists of two states, \mathbf{k} and $-\mathbf{k}$. The magnitude of this shift is determined by the off-site EPC coefficient α for the E_{2g} Γ point phonon modes, according to Eq. (4.34), and by the on-site EPC coefficient λ for the E' K point phonon modes, for which $\Delta\mathbf{k}_F$ and $\Delta\mathbf{k}'_F$ are similar to Eq. (4.34), but with $\frac{1}{2}\lambda$ substituted for α .

The group of the wavevector G_K is isomorphic to the group D_{6h} when the graphene sheet is distorted by the A'_1 K point phonon mode shown in Fig. 4-4 (b). The four-fold degenerate electronic state at the Γ point consists of the two 2D irreducible representations of group D_{6h} : E_{2u} (valence bands) and E_{1g} (conduction bands). This state is therefore not required to split by group theory. If it splits, however, a band gap will be opened at the Γ point. Indeed, there are only two inequivalent Fermi points, \mathbf{k}_F and \mathbf{k}'_F , while the star of a general wavevector $\mathbf{k} \neq 0$ consists of six states. Thus, \mathbf{k}_F and \mathbf{k}'_F cannot move away from the Γ point.

To check whether the A'_1 K point phonon mode opens a dynamical band gap at the Γ point, we construct the 6×6 STB Hamiltonian at $\mathbf{k} = 0$ for the six-atom supercell. Labeling atoms in the supercell as shown by the red numbers 1 to 6 in Fig. 3-6 (a), so that atoms 1 to 3 (4 to 6) belong to the A (B) sublattice, the Hamiltonian for an ideal graphene sheet takes the following block diagonal form:

$$H_0 = \begin{pmatrix} \varepsilon & 0 & 0 & t & t & t \\ 0 & \varepsilon & 0 & t & t & t \\ 0 & 0 & \varepsilon & t & t & t \\ t & t & t & \varepsilon & 0 & 0 \\ t & t & t & 0 & \varepsilon & 0 \\ t & t & t & 0 & 0 & \varepsilon \end{pmatrix}. \quad (4.35)$$

Setting the determinant of the Hamiltonian to zero yields the following electronic

states at the Γ point:

$$E_0^b = (\varepsilon + 3t, \varepsilon, \varepsilon, \varepsilon, \varepsilon - 3t). \quad (4.36)$$

The four states $E_0^b = \varepsilon$ (band index $b = 2, 3, 4, 5$) are found to be degenerate, in agreement with the aforementioned predictions by group theory.

For the graphene sheet distorted by the A'_1 symmetry K point phonon mode, we construct the STB Hamiltonian considering the atomic displacements shown in Fig. 4-4 (e). Keeping only terms linear in ρ/a , the λ -terms in the diagonal terms of the Hamiltonian cancel out, while the α -terms in the off-diagonal blocks survive:

$$H = H_0 + \alpha\rho\cos\omega t \begin{pmatrix} 0 & 0 & 0 & 2 & -1 & -1 \\ 0 & 0 & 0 & -1 & 2 & -1 \\ 0 & 0 & 0 & -1 & -1 & 2 \\ 2 & -1 & -1 & 0 & 0 & 0 \\ -1 & 2 & -1 & 0 & 0 & 0 \\ -1 & -1 & 2 & 0 & 0 & 0 \end{pmatrix}. \quad (4.37)$$

Setting the determinant of Eq. (4.37) to zero yields the following electronic states:

$$E^b = E_0^b + \alpha\rho\cos\omega t (0, -3, -3, 3, 3, 0). \quad (4.38)$$

The A'_1 K point phonon mode thus splits the four-fold degenerate electronic state described by Eq. (4.36), $E_0^b = \varepsilon$ ($b = 2, 3, 4, 5$), into the two two-fold degenerate states, $E^b = \varepsilon - 3\alpha\rho\cos\omega t$ ($b = 2, 3$) and $E^b = \varepsilon + 3\alpha\rho\cos\omega t$ ($b = 4, 5$), according to Eq. (4.38). This splitting opens up a dynamical band gap of width [162]:

$$\Delta E_g = 6\alpha\rho\cos\omega t \quad \text{for the iTO } A'_1 \text{ mode,} \quad (4.39)$$

determined by the off-site EPC coefficient α , since the terms in Eq. (4.37) with the on-site EPC λ coefficient that are linear in ρ/a cancel out for the normal mode displacements shown in Fig. 4-4 (e). The Peierls instability induced by the dynamical band gap of Eq. (4.39) is analogous to the dimerization of benzene.

For a general phonon wavevector \mathbf{q} away from the Γ , K , and K' points, the size of the supercell increases significantly, thereby making the supercell method impractical, as discussed in Section 4.5.1. We thus implement the linear-response method reviewed in Section 4.5.2 which operates within the two-atom unit cell of the graphene sheet [10, 121]. In the first order approximation, the amplitudes $\Delta\mathbf{k}_F$, $\Delta\mathbf{k}'_F$, and ΔE_g scale with the phonon wavevector \mathbf{q} as follows:

$$\begin{cases} \Delta\mathbf{k}_F(\mathbf{q}_\Gamma) = \left(1 - \frac{3q_\Gamma}{2\pi a}\right) \Delta\mathbf{k}_F(\mathbf{0}) & \text{and } \Delta\mathbf{k}'_F(\mathbf{q}_\Gamma) = -\Delta\mathbf{k}_F(\mathbf{q}_\Gamma), \\ \Delta E_g(\mathbf{q}_K) = \left(1 - \frac{3q_K}{2\pi a}\right) \Delta E_g(\mathbf{0}) & \text{and } \Delta E_g(\mathbf{q}_{K'}) = \Delta E_g(-\mathbf{q}_K), \end{cases} \quad (4.40)$$

where $\mathbf{q}_\Gamma = \mathbf{q} - \Gamma$, $\mathbf{q}_K = \mathbf{q} - K$, and $\mathbf{q}_{K'} = \mathbf{q} - K'$ are the phonon wavevectors measured from the Γ , K , and K' points, respectively, and the values with the argument $\mathbf{0}$ are given by Eqs. (4.34) and (4.39). The amplitudes $\Delta\mathbf{k}_F$, $\Delta\mathbf{k}'_F$, and ΔE_g thus reach their maximum values at the Γ , K , and K' points, vanishing halfway between the Γ , K , and K' points.

Let us estimate the numerical values of $\Delta\mathbf{k}_F$ and ΔE_g given by Eqs. (4.34) and (4.39), respectively. Within the second quantization formalism, the amplitude of the normal mode displacements is given by:

$$\rho = \sqrt{\frac{\sqrt{3}\hbar a^2 n}{4M\omega}}, \quad (4.41)$$

where n is the phonon occupation number, M is the mass of a carbon atom, and $\omega = 1582 \text{ cm}^{-1}$ and $\omega \approx 1300 \text{ cm}^{-1}$ are the frequencies of the E_{2g} Γ and A'_1 K point phonon modes [37, 99, 121, 170]. The Bose-Einstein distribution:

$$n^\nu(\mathbf{q}_w) = \frac{1}{\exp\left(\frac{\hbar\omega^\nu(\mathbf{q}_w)}{k_B T}\right) - 1} \quad (4.42)$$

at room temperature $T = 300 \text{ K}$ takes values $n = 5 \times 10^{-4}$ for the E_{2g} Γ and $n = 2 \times 10^{-3}$ for the A'_1 K point phonon modes. The density of phonon states in the graphene sheet is given by $1/A$ per phonon mode, where $A = \sqrt{3}a^2/2 = 0.052 \text{ nm}^2$

is an area of the unit cell. On averaging the scaling factors in Eq. (4.40) over the first Brillouin zone, the effective density of phonon states contributing to $\Delta\mathbf{k}_F$ and ΔE_g is reduced by a factor of $\pi/(\sqrt{3} \times 18) = 0.1$ for each of the iLO E_{2g} Γ , iTTO E_{2g} Γ , iTTO A'_1 K, and iTTO A'_1 K' point phonon modes. Putting all the factors together yields $n = 10^{-4} \text{ nm}^{-2}$ for the E_{2g} Γ and $n = 8 \times 10^{-4} \text{ nm}^{-2}$ for the A'_1 K point phonon modes. We then obtain from Eq. (4.41) $\rho = 0.7 \times 10^{-5} \text{ nm}$ for the E_{2g} Γ and $\rho = 2.1 \times 10^{-5} \text{ nm}$ for the A'_1 K point phonon modes. Substituting these values into Eqs. (4.34) and (4.39) yields $|\Delta\mathbf{k}_F| = 1.3 \times 10^{-4} |\mathbf{K}|$ along the \hat{x} and \hat{y} directions for the iLO and iTTO components of the E_{2g} Γ point phonon mode, and $\Delta E_g = 10 \text{ meV}$ for the A'_1 symmetry K and K' point phonon modes, where $|\mathbf{K}| = 4\pi/(3a)$.

4.6.2 Kohn anomaly

The electronic dispersion relations of an ideal graphene sheet and the graphene sheet distorted by the A'_1 K point phonon mode at $T=300 \text{ K}$ calculated within the ETB framework are shown in Fig. 4-23 (a) by dashed and solid curves, respectively. Considering that the amplitude of the dynamical band gap ΔE_g is less than the thermal energy $k_B T = 26 \text{ meV}$ at room temperature $T = 300 \text{ K}$, the former does not affect the transport properties of the graphene sheet, though it softens the frequency ω of the A'_1 phonon mode at the K point by reducing the electronic contribution to the second variation of the total energy $\delta^2 E$, according to Eq. (4.22). In the harmonic approximation, $\delta^2 E = \frac{1}{2} \phi_0 \rho^2 \cos^2 \omega t$, where ϕ_0 is the effective force constant for the A'_1 phonon mode at the K point. By integrating the valence band structure of the graphene sheet with the dynamical band gap of amplitude ΔE_g over the 2D Brillouin zone, we find that the decrease in ϕ_0 at $T = 0 \text{ K}$ is proportional to ΔE_g^2 . Substituting ΔE_g from Eq. (4.40) yields the Kohn anomaly linear in q_K around the K point [117]:

$$\begin{cases} \delta^2 E = \frac{1}{2} \left(\phi_0 - \phi_1 \left(1 - \frac{3q_K a}{2\pi} \right)^2 \right) \rho^2 \cos^2 \omega t, \\ \omega = \sqrt{\frac{1}{M} \left(\phi_0 - \phi_1 \left(1 - \frac{3q_K a}{2\pi} \right)^2 \right)} \approx \sqrt{\frac{\phi_0}{M} \left(1 + \frac{\phi_1}{\phi_0} \frac{3q_K a}{2\pi} \right)}, \end{cases} \quad (4.43)$$

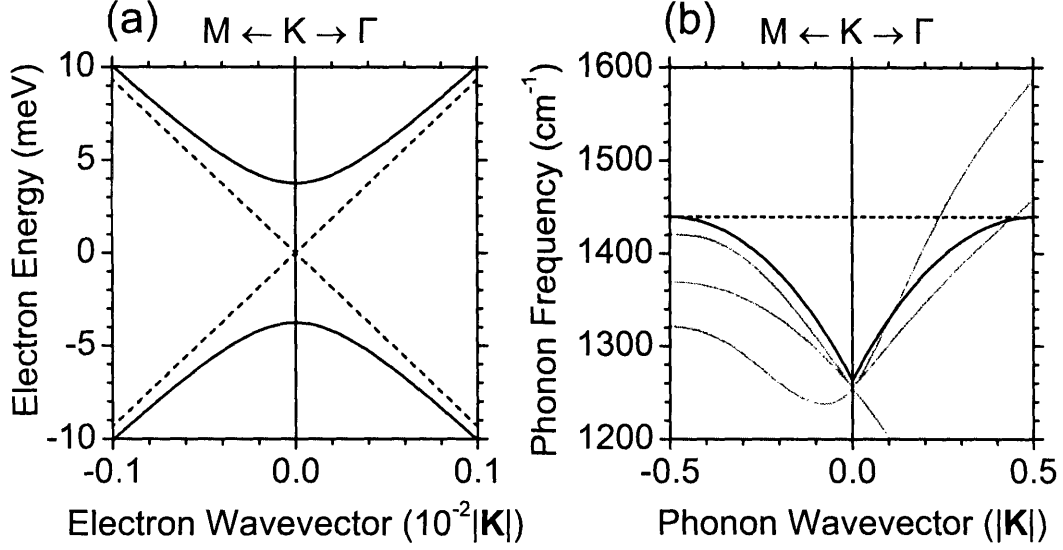


Figure 4-23: (a) The electronic dispersion relations of an ideal graphene sheet (dashed curves) and the graphene sheet distorted by the A'_1 K point phonon mode at $T=300$ K (solid curves) calculated within the ETB framework. (b) The phonon dispersion relations of the graphene sheet calculated within the ETB framework at $T=0$ K (gray curves) and from Eq. (4.43) (solid black curves). The dashed black line shows the leading term in Eq. (4.43). The wavevector units are $|\mathbf{K}| = 4\pi/(3a)$.

where ϕ_1 is the force constant softening associated with $\Delta E_g(\mathbf{0})$ from Eq. (4.39). Upon fitting the phonon dispersion relations in Fig. 4-14 (b) calculated within the ETB framework to the functional form of Eq. (4.43), we obtain $\phi_0 = 163 \times 10^4$ dyn/cm and $\phi_1 = 37 \times 10^4$ dyn/cm. The phonon dispersion relations defined by Eq. (4.43) around the K point and those from Fig. 4-14 (b) are shown in Fig. 4-23 (b) by black and gray curves, respectively. In a similar fashion, the E_{2g} phonon mode at the Γ point exhibits a Kohn anomaly for which ϕ_1 in Eq. (4.43) arises from $\Delta \mathbf{k}_F(\mathbf{0})$ instead of $\Delta E_g(\mathbf{0})$ and q_Γ is substituted for q_K . This results in the phonon dispersion relations linear in q_Γ that reproduce the overbending of the iLO phonon mode around the Γ point shown in Fig. 4-14 (b) [117].

The Kohn anomaly is governed by the electronic contribution to the total energy E , which in turn depends on the doping level and the thermal distribution of electrons. As the Fermi level E_F is moved into the valence or conduction band, the dynamical band gap ΔE_g induced by the A'_1 K point phonon mode in the graphene sheet has

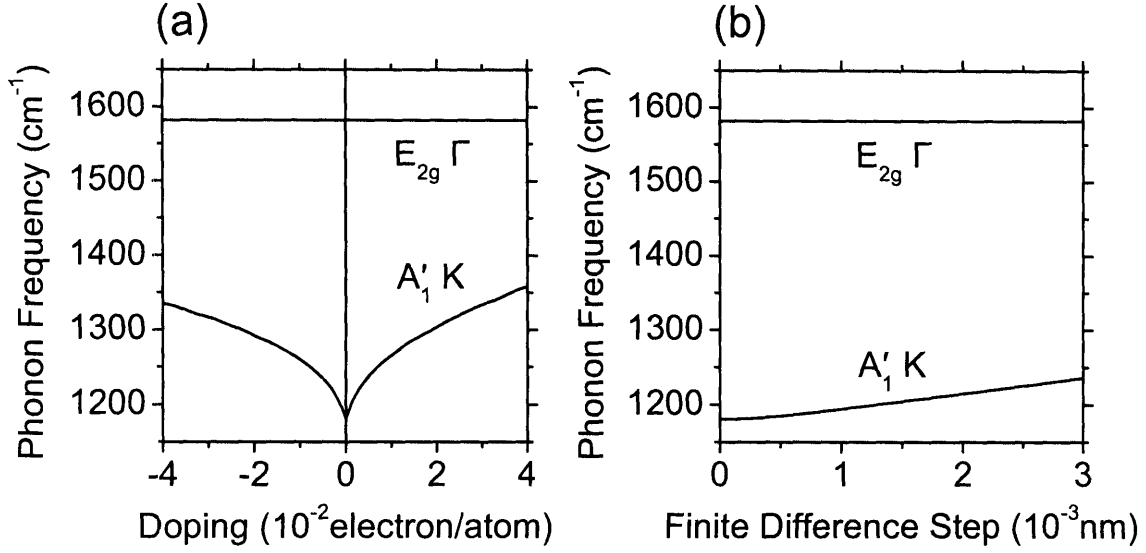


Figure 4-24: The frequencies of the E_{2g} Γ and A'_1 K point phonon modes in the graphene sheet in a central finite difference approximation for the second derivative of the total energy calculated within the ETB framework as functions of (a) doping level and (b) central finite difference step size. The frequency dependence on (a) doping and (b) step arises from (a) the dynamical band gap and (b) cubic anharmonicity in the total energy, which is in turn attributed to the dynamical band gap.

less contribution to E , or in other words, ϕ_1 decreases, so that the Kohn anomaly is smeared out in Eq. (4.43). This is seen in Fig. 4-24 (a) where we show the frequency of the A'_1 phonon mode at the K point as a function of the doping level calculated in a central finite difference approximation with the step $\Delta R = 10^{-4}$ nm for the second derivative of the total energy within the ETB framework on a 34×34 Monkhorst-Pack grid in reciprocal space and scaled by a factor of 0.8841 as in Table 4.8. In contrast, the Kohn anomaly associated with the E_{2g} Γ point phonon mode does not induce the dynamical band gap and consequently is not smeared out by the doping. The frequency of the E_{2g} phonon mode at the Γ point calculated on a 60×60 Monkhorst-Pack grid only changes by a few wavenumbers with the doping level, as shown in Fig. 4-24 (a). In a similar fashion, temperature T smears out the Kohn anomaly in the A'_1 phonon mode at the K point [117].

Furthermore, the dynamical band gap ΔE_g induced by the A'_1 K point phonon mode in the graphene sheet gives rise to a large anharmonic term proportional to ρ^3

in the second variation of the total energy $\delta^2 E$ of Eq. (4.43). Indeed, the frequency of the A'_1 phonon mode at the K point shows a strong dependence on the central finite difference step size ΔR , according to Fig. 4-24 (b), and ΔR is equivalent to ρ for the frequency calculations. In contrast, the frequency of the E_{2g} phonon mode at the Γ point also shown in Fig. 4-24 (b) only changes by a few wavenumbers with ΔR , even though the E_{2g} Γ point phonon mode undergoes a Kohn anomaly. The anharmonicity suggests the importance of the A'_1 K point phonon mode for thermal conductivity in the graphene sheet and SWNTs. It also implies that the overestimation of the frequency of the A'_1 phonon mode around the K point in Fig. 4-12 arises from the large step size $\Delta R = 3 \times 10^{-3}$ nm used for calculations of the force constants in Table 4.7. The step size of $\Delta R = 3 \times 10^{-3}$ nm corresponds to $T = 31000$ K for the A'_1 K and $T = 43000$ K for the E_{2g} Γ point phonon modes, according to Eqs. (4.41) and (4.42). A formal treatment of vibrational anharmonicity in the graphene sheet and SWNTs involves calculations of the phonon-phonon scattering matrix elements within the ETB framework, following the conceptual approach of Chapter 5, that will be the subject of future work.

For metallic SWNTs, the iTO K point phonon mode induces oscillations of the optical transition energies E_{ii} around equilibrium values with amplitude ΔE_g given by Eqs. (4.39) and (4.40). The iLO Γ point phonon mode in metallic SWNTs (involving atomic vibrations along the SWNT axis, as shown in Fig. 4-21 (c)) also causes E_{ii} to oscillate since $\Delta \mathbf{k}_F$ and $\Delta \mathbf{k}'_F$ are perpendicular to the cutting lines [38]. Integration of the valence subbands along the cutting lines at $T = 0$ K yields two terms per subband in $\delta^2 E$, the first is proportional to $-E_{ii}^2$ analogous to the term containing ϕ_1 in Eq. (4.43), and the second given by $E_{ii}^2 \ln E_{ii}$ arises from the 1D nature of ΔE_g in SWNTs. For truly metallic armchair SWNTs, $E_{00} = 0$ at equilibrium and ΔE_g gives rise to the Kohn anomaly logarithmic in q_K and q_Γ around the K and Γ points:

$$\begin{cases} \delta^2 E = \frac{1}{2} \left(\phi_0 + 2\phi_1 \ln \frac{3q_z a}{2\pi} \right) \rho^2 \cos^2 \omega t, \\ \omega = \sqrt{\frac{1}{M} \left(\phi_0 + 2\phi_1 \ln \frac{3q_z a}{2\pi} \right)} \approx \sqrt{\frac{\phi_0}{M}} \left(1 + \frac{\phi_1}{\phi_0} \ln \frac{3q_z a}{2\pi} \right), \end{cases} \quad (4.44)$$

where $Z = K$ or Γ . For mini band gap semiconducting chiral and zigzag SWNTs, $E_{00} \neq 0$ yet $E_{00} \ll E_{11}$, and we can express $\delta^2 E$ in a series expansion with respect to ΔE_g assuming $\Delta E_g \ll E_{00}$. Summing contributions from all the valence subbands, terms linear in E_g cancel out, and $\delta^2 E$ is determined by ΔE_g^2 similar to Eq. (4.43).

The Kohn anomalies at the K and Γ points in both truly metallic armchair and mini band gap semiconducting chiral and zigzag SWNTs are smeared out when the Fermi level crosses the 1D dynamical band gap ΔE_g . The frequencies of the G - and G' -bands measured by resonance Raman spectroscopy from SWNT bundles [123, 124] show a dependence on the doping level similar to the one shown in Fig. 4-24 (a) for the graphene sheet. The logarithmic divergence of the iTO K and iLO Γ point phonon modes in Eq. (4.44) induces the static Peierls distortions in truly metallic armchair SWNTs at low T [9, 13, 27, 121], while the mini band gap semiconducting chiral and zigzag SWNTs do not exhibit the static Peierls distortions. With increasing T , the logarithmic divergence is removed by the electron screening [27], which is only partially included in the ETB framework. The frequencies of the iTO K and iLO Γ point phonon modes show a pronounced anharmonic behavior in truly metallic armchair SWNTs, similar to the frequency of the iTO A'_1 K point phonon mode in the graphene sheet shown in Fig. 4-24 (b). A more detailed study of vibrational anharmonicity in SWNTs will be the subject of future work.

4.7 Summary

We started this chapter by reviewing the basic force-constant (BFC) models for the flat graphene sheet commonly used to study the vibrational properties of SWNTs. We showed that these models do not show satisfactory agreement with the experimental data acquired over the years by various experimental techniques. The phonon dispersion relations calculated within the BFC models also diverge from the results of first-principles calculations. In particular, Kohn anomalies in the phonon dispersion relations of the graphene sheet and metallic SWNTs are smeared out by the Fourier transform of the force constants due to the long-range interaction cut-off within the

BFC framework.

To overcome the aforementioned limitations, we develop an advanced force-constant (AFC) model by including the long-range atomic interactions and incorporating the curvature of the SWNT sidewall. The force constant parameters for the AFC model are calculated within the extended tight-binding (ETB) framework developed in Chapter 3. Even though the AFC model shows good agreement with experiments and first-principles calculations, the force-constant approach still partially smears out Kohn anomalies and does not include anharmonic corrections. A direct calculation of the reciprocal-space dynamical matrix without utilizing the real-space force constants is thus preferable. Such a calculation is performed within the ETB framework using either the supercell method for the high symmetry points in reciprocal space or the linear response method adopted for the ETB framework.

The supercell method and especially the linear response method provide a powerful tool to study the vibrational properties of SWNTs under controlled conditions. Electrochemical doping [28, 123, 124] and uniaxial or torsional strain [29] cause the RBM, D , G^- , G^+ , and G' Raman bands to shift in their frequencies and relative intensities. These frequency shifts can be calculated within the supercell or linear response method, though more systematic experimental studies are needed to check the computational results. A detailed comparison of the theoretical and experimental frequency shifts is the subject of future work.

Chapter 5

Interaction with light

This Chapter presents a quantum-mechanical framework for calculating the intensities of light scattering, absorption, and emission by the graphene sheet and SWNTs. We start this section by deriving the electron-photon and electron-phonon transition matrix elements within the ETB framework. We then calculate the second-order resonance Raman spectra of the graphene sheet using time-dependent perturbation theory. The calculated spectra show good agreement with the experimental spectra and allow us to identify the origin of the previously unassigned Raman modes. We also review the current progress and suggest future directions in the calculations of resonance Raman and photoluminescence spectra of SWNTs.

5.1 Electron-photon interaction

The optical dipole transitions in the visible range occur between the π bonding and π^* antibonding molecular orbitals in the graphene sheet and SWNTs. The dipole selection rules prohibit an optical transition between the $2p$ orbitals of a carbon atom. However, the optical transition between the $2p$ orbitals on adjacent carbon atoms within the graphene sheet and on the walls of SWNTs is allowed by the dipole selection rules. Within first-order time-dependent perturbation theory, the optical dipole transition matrix element between the initial i and final f electronic states in the graphene sheet is given by [48, 133, 138]:

$$M^{b'\lambda b}(\mathbf{k}_f, \boldsymbol{\kappa}, \mathbf{k}_i) = \left\langle \Psi^{b'}(\mathbf{k}_f, \mathbf{r}, t) \left| i \frac{e\hbar}{m} \mathbf{A}^\lambda(\boldsymbol{\kappa}, \mathbf{r}, t) \cdot \nabla \right| \Psi^b(\mathbf{k}_i, \mathbf{r}, t) \right\rangle, \quad (5.1)$$

where b is the band index, λ is the polarization index, \mathbf{k} is the electron wavevector, $\boldsymbol{\kappa}$ is the photon wavevector, e is an elementary charge ($e > 0$), \hbar is Planck's constant, m is the electron mass, $\mathbf{A}^\lambda(\boldsymbol{\kappa}, \mathbf{r}, t)$ is the vector potential of the electromagnetic field, ∇ is the gradient operator, $\Psi^b(\mathbf{k}, \mathbf{r}, t)$ is the one-electron wavefunction of Eq. (3.2), \mathbf{r} is the spatial coordinate, and t is time.

Within the second quantization formalism, the vector potential of the electromagnetic field takes the following form:

$$\begin{aligned} \mathbf{A}^\lambda(\boldsymbol{\kappa}, \mathbf{r}, t) = \sqrt{\frac{\hbar}{2\kappa\kappa_0 V \omega(\boldsymbol{\kappa})}} & \left(\sqrt{n^\lambda(\boldsymbol{\kappa})} \exp(+i\boldsymbol{\kappa}\mathbf{r} - i\omega(\boldsymbol{\kappa})t) \mathbf{P}^\lambda \right. \\ & \left. + \sqrt{n^\lambda(\boldsymbol{\kappa}) + 1} \exp(-i\boldsymbol{\kappa}\mathbf{r} + i\omega(\boldsymbol{\kappa})t) \mathbf{P}^{\lambda*} \right), \end{aligned} \quad (5.2)$$

where κ is the dielectric constant, κ_0 is the dielectric permittivity of free space, V is the quantization volume for the electromagnetic field, $n^\lambda(\boldsymbol{\kappa})$ is the photon occupation number, $\omega(\boldsymbol{\kappa})$ is the photon frequency, and \mathbf{P}^λ is the photon polarization vector.

The optical transition rate is determined by Fermi's Golden Rule:

$$W^{b'\lambda b}(\mathbf{k}_f, \boldsymbol{\kappa}, \mathbf{k}_i) = \frac{1}{\hbar^2 t_l} \left| \int_0^{t_l} dt M^{b'\lambda b}(\mathbf{k}_f, \boldsymbol{\kappa}, \mathbf{k}_i) \right|^2, \quad (5.3)$$

where t_l is the electron-photon interaction time. Integration over time t in Eq. (5.3) gives the delta function $\delta(E^{b'}(\mathbf{k}_f) \mp \hbar\omega(\boldsymbol{\kappa}) - E^b(\mathbf{k}_i))$ that expresses the energy conservation. We thus conclude that the two terms in Eq. (5.2) describe the light absorption and emission processes, respectively. For the light absorption process, the electron is scattered from the π valence to the π^* conduction band, $b = v$ and $b' = c$, and *vice versa* for the light emission process. The induced and spontaneous emission processes are represented by the terms $n^\lambda(\boldsymbol{\kappa})$ and 1 under the square root in Eq. (5.2), respectively.

Equipped with the energy conservation, we can now examine the spatial integral in Eq. (5.1), usually expressed in the form of the dipole vector:

$$\mathbf{D}^{b'b}(\mathbf{k}_f, \pm\boldsymbol{\kappa}, \mathbf{k}_i) = \langle \Psi^{b'}(\mathbf{k}_f, \mathbf{r}, 0) | \exp(\pm i\boldsymbol{\kappa}\mathbf{r}) \nabla | \Psi^b(\mathbf{k}_i, \mathbf{r}, 0) \rangle. \quad (5.4)$$

The dipole vector of Eq. (5.4) can be simplified by taking into account that the slope of the electronic dispersion relations $\sqrt{3}(\varepsilon s - t)a$ given by Eq. (3.14) is much smaller than the slope of the photon dispersion relations $\hbar c/\sqrt{\kappa}$, where c is the speed of light in vacuum. Implementing the energy conservation, the above relation leads to the inequalities $\kappa \ll |\mathbf{k}_i - \mathbf{K}|$ and $\kappa \ll |\mathbf{k}_f - \mathbf{K}|$. Accordingly, the phase factor $\exp(\pm i\boldsymbol{\kappa}\mathbf{r})$ in Eq. (5.4) is approximated with $\exp(\pm i\boldsymbol{\kappa}\mathbf{R}_{u's'})$. Substituting the spatial phase factors from Eq. (3.2) into Eq. (5.4) and summing over the unit cell index u' then yields the momentum conservation, $(-\mathbf{k}_f \pm \boldsymbol{\kappa} + \mathbf{k}_i) = \mathbf{0}$, for the light absorption and emission processes, respectively. In the dipole approximation, $\boldsymbol{\kappa}$ is neglected, $\boldsymbol{\kappa} = \mathbf{0}$, and the optical dipole transitions are vertical, $\mathbf{k}_i = \mathbf{k}_f \equiv \mathbf{k}$.

In the dipole approximation, the optical dipole transition matrix elements for the light absorption and spontaneous emission processes, $M_a^{c\lambda v}(\mathbf{k}, \mathbf{0}, \mathbf{k})$ and $M_e^{v\lambda c}(\mathbf{k}, \mathbf{0}, \mathbf{k})$, respectively, are obtained upon substituting Eqs. (3.2) and (5.2) into Eq. (5.1):

$$\begin{cases} M_a^{c\lambda v}(\mathbf{k}, \mathbf{0}, \mathbf{k}) = i \frac{e\hbar}{m\omega} \sqrt{\frac{I}{2\sqrt{\kappa}\kappa_0 c}} \mathbf{P}^\lambda \cdot \mathbf{D}^{cv}(\mathbf{k}, \mathbf{0}, \mathbf{k}), \\ M_e^{v\lambda c}(\mathbf{k}, \mathbf{0}, \mathbf{k}) = i \frac{e\hbar}{m\omega} \sqrt{\frac{\hbar\omega}{2\kappa\kappa_0 V}} \mathbf{P}^\lambda \cdot \mathbf{D}^{vc}(\mathbf{k}, \mathbf{0}, \mathbf{k}), \end{cases} \quad (5.5)$$

where I is the radiant flux density for the incoming light beam:

$$I = \frac{c}{\sqrt{\kappa V}} \sum_w^W \hbar \omega(\boldsymbol{\kappa}_w) \sum_\lambda^2 n^\lambda(\boldsymbol{\kappa}_w), \quad (5.6)$$

where the sum is taken over the W phonon wavevectors and the two polarizations.

By substituting the one-electron wavefunctions $\Psi^b(\mathbf{k}, \mathbf{r}, 0)$ from Eq. (3.2) into Eq. (5.4), we express the dipole vector $\mathbf{D}^{b'b}(\mathbf{k}, \mathbf{0}, \mathbf{k})$ in the following form:

$$\mathbf{D}^{b'b}(\mathbf{k}, \mathbf{0}, \mathbf{k}) = \sum_{s'o'} \sum_{so} C_{s'o'}^{b'*}(\mathbf{k}) \mathbf{D}_{s'o'so}(\mathbf{k}, \mathbf{0}, \mathbf{k}) C_{so}^b(\mathbf{k}), \quad (5.7)$$

where $\mathbf{D}_{s'o'so}(\mathbf{k}, \mathbf{0}, \mathbf{k})$ is the dipole matrix:

$$\mathbf{D}_{s'o'so}(\mathbf{k}, \mathbf{0}, \mathbf{k}) = \frac{1}{U} \sum_u^U \exp(i\mathbf{k}(\mathbf{R}_{us} - \mathbf{R}_{u's'})) \mathbf{d}_{o'o}(\mathbf{R}_{us} - \mathbf{R}_{u's'}), \quad (5.8)$$

and $\mathbf{d}_{o'o}(\mathbf{R})$ is the atomic dipole transition vector:

$$\mathbf{d}_{o'o}(\mathbf{R}) = \int \phi_{o'}^*(\mathbf{r}) \nabla \phi_o(\mathbf{r} - \mathbf{R}) d\mathbf{r}. \quad (5.9)$$

Here, $\phi_o(\mathbf{r})$ is the atomic orbital, $\mathbf{R} = \mathbf{R}_{us} - \mathbf{R}_{u's'}$ connects the two interacting atoms, and u' labels the unit cell under consideration.

While the $o = 2s$ atomic orbitals are spherically symmetric, the $o = 2p$ atomic orbitals should be projected into the σ and π molecular orbitals along and perpendicular to \mathbf{R} , as shown in Fig. 3-2. The atomic dipole transition vectors of Eq. (5.9) are then decomposed into the nine components for the different configurations of molecular orbitals. These configurations are shown in Fig. 5-1 along with the gradient operator that enters Eq. (5.9). The directions of $\mathbf{d}_{o'o}(\mathbf{R})$ can be either parallel or perpendicular to \mathbf{R} , as shown by arrows in Fig. 5-1, according to the symmetry of the spherical harmonic $Y_{21}(\theta, \phi)$. Along these directions, the magnitudes $d_{o'o} = |\mathbf{d}_{o'o}|$ only depend on the interatomic distances $R = |\mathbf{R}|$. The configurations of the molecular orbitals that have the same $d_{o'o}(R)$ are connected by dashed lines in Fig. 5-1. For the five inequivalent configurations $o'o = ss, s\sigma, \sigma\sigma, \pi\pi, s\pi$ in Fig. 5-1, the atomic dipole tran-

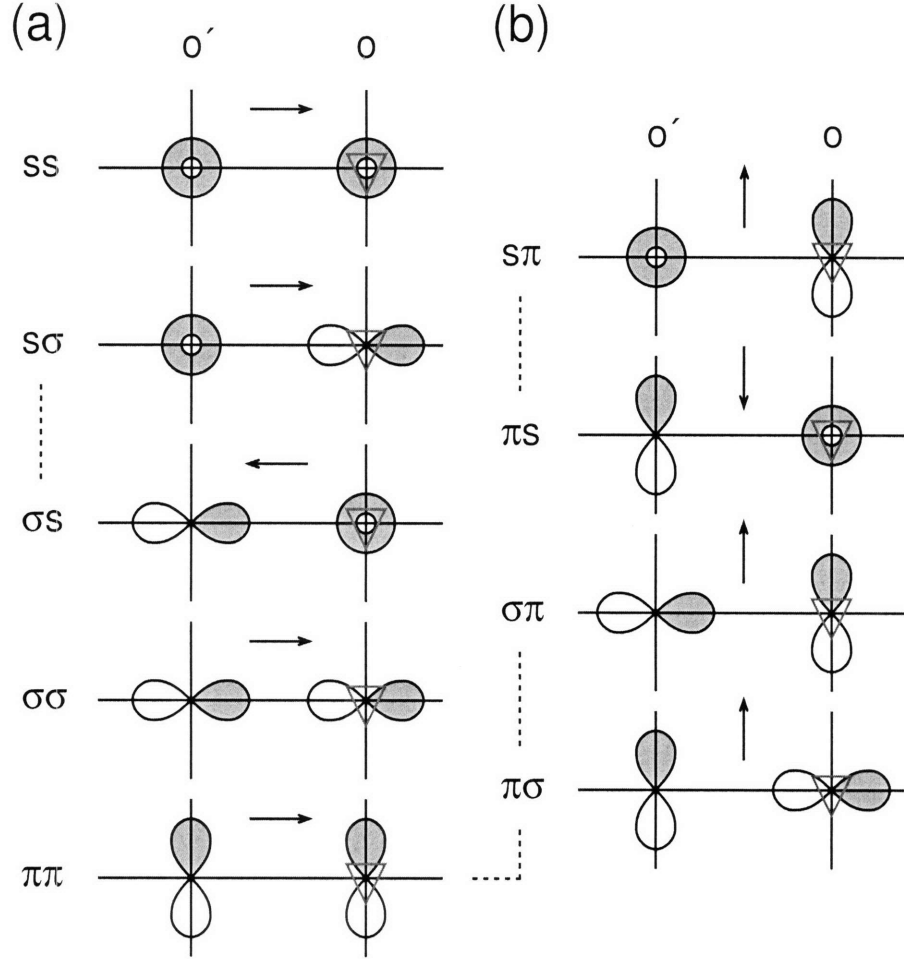


Figure 5-1: The molecular orbital configurations $o'o = ss, s\sigma, \sigma s, \sigma\sigma, \pi\pi, s\pi, \pi s, \sigma\pi, \pi\sigma$ for the atomic dipole transition matrix elements $d_{o'o}(R)$ similar to those shown in Fig. 3-3. The red ∇ indicates the gradient operator applied to the orbital o . The directions of $\mathbf{d}_{o'o}(\mathbf{R})$ are shown by arrows (a) parallel and (b) perpendicular to the interatomic vector $\mathbf{R} = \mathbf{R}_{us} - \mathbf{R}_{u's'}$. The dashed lines connect the configurations with the same $d_{o'o}(R)$. The Chebyshev polynomial expansions of $d_{o'o}(R)$ are given in Table 5.1. The calculated $d_{o'o}(R)$ dependencies are shown in Fig. 5-2.

sition matrix elements $d_{o'o}(R)$ are calculated using the pseudoatomic wavefunctions constructed within the ETB framework [122]. The calculated $d_{o'o}(R)$ functions are expanded in modified Chebyshev polynomials given by Eqs. (3.25) and (3.26). The expansion coefficients are listed in Table 5.1. The resulting $d_{o'o}(R)$ dependencies are shown in Fig. 5-2.

In the flat graphene sheet, the atomic dipole transition matrix elements involving σ and π molecular orbitals are decoupled and optical transitions in the visible range

Table 5.1: Coefficients C_n of the Chebyshev polynomial expansion according to Eqs. (3.25) and (3.26) for the atomic dipole transition matrix elements $d_{o'o}(R) = S(R)$ (in units of $10^{-2}/a_0$; $a_0 = 0.052917721$ nm is the Bohr radius) parallel and perpendicular to the interatomic vector $\mathbf{R} = \mathbf{R}_{us} - \mathbf{R}_{u's'}$. Boundaries of R are at $R_1 = 1.0$ and $R_2 = 7.0$ (in units of a_0). The molecular orbital configurations $o'o = ss, s\sigma, \sigma\sigma, \pi\pi, s\pi$ are shown in Fig. 5-1. The calculated $d_{o'o}(R)$ dependencies are shown in Fig. 5-2.

	d_{ss}	$d_{s\sigma}$	$d_{\sigma\sigma}$	$d_{\pi\pi}$
C_0	+1.3797923	-0.0769120	+1.6576666	+1.5877754
C_1	-0.8956832	-0.3301910	-1.8694800	-1.2203346
C_2	+0.0918082	+0.8076040	+1.7363412	+0.5019868
C_3	+0.2328328	-0.6441390	-0.8721264	-0.0136130
C_4	-0.1330832	+0.1950013	+0.0659965	-0.1143494
C_5	-0.0048863	+0.0533430	+0.1959986	+0.0732224
C_6	+0.0396586	-0.0759693	-0.1321612	-0.0230110
C_7	-0.0220959	+0.0330036	+0.0390193	+0.0025198
C_8	+0.0051811	-0.0062375	-0.0018662	+0.0011261
C_9	+0.0006500	-0.0008425	-0.0030800	-0.0006576

	$d_{s\pi}$
C_0	+1.1943359
C_1	-0.9434491
C_2	+0.4370124
C_3	-0.0649433
C_4	-0.0596295
C_5	+0.0495847
C_6	-0.0184022
C_7	+0.0028778
C_8	+0.0007665
C_9	-0.0006909

are governed by $d_{\pi\pi}(R)$ shown in the bottom trace of Fig. 5-2 (a). One can see in Fig. 5-2 (a) that $d_{\pi\pi}(R)$ almost vanishes at the second neighbor $R = a$, suggesting that the optical transitions in the graphene sheet occur primarily between the $2p$ orbitals on adjacent carbon atoms. To satisfy the energy conservation, the optical transitions take place for the electronic states along the contours of constant $E^c - E^v$ around the K and K' points in the first Brillouin zone of the graphene sheet. We replicate these contours calculated within the ETB framework from Fig. 3-23 (b) in Fig. 5-3 (a), where the transition energies are represented by spectral colors. The contour of

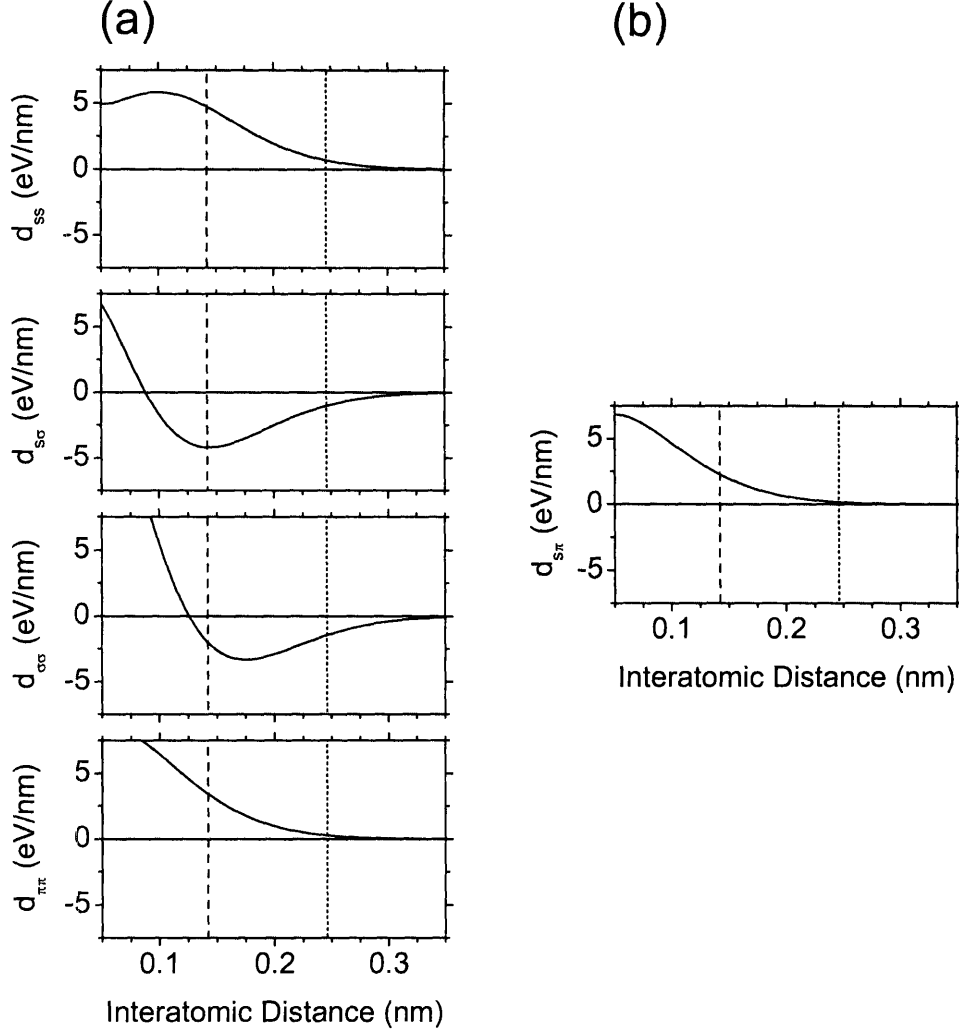


Figure 5-2: The atomic dipole transition matrix elements $d_{oo}(R)$ which are (a) parallel and (b) perpendicular to the interatomic vector $\mathbf{R} = \mathbf{R}_{us} - \mathbf{R}_{u's'}$, calculated by the Chebyshev polynomial expansions given in Table 5.1. The molecular orbital configurations $o'o = ss, s\sigma, \sigma\sigma, \pi\pi, s\pi$ are shown in Fig. 5-1. The dashed and dotted vertical lines indicate the first- and second-neighbor interatomic distances, $a_{CC} = 0.142$ nm and $a = \sqrt{3}a_{CC} = 0.246$ nm, respectively.

$E^c - E^v = 2.41$ eV corresponding to the wavelength of 514.5 nm from the Ar ion laser is shown by the black curve, and the position of the electron wavevector \mathbf{k} along the contour is parameterized by the polar angle ϕ . The optical dipole transition matrix element for the light absorption process $M_a^{c\lambda v}(\mathbf{k}, \mathbf{0}, \mathbf{k})$ is calculated from Eqs. (5.5) and (5.7) to (5.9) with the radiant flux density $I = 1$ mW/ μm^2 and for linear light polarization aligned with the armchair and zigzag directions in the graphene sheet,

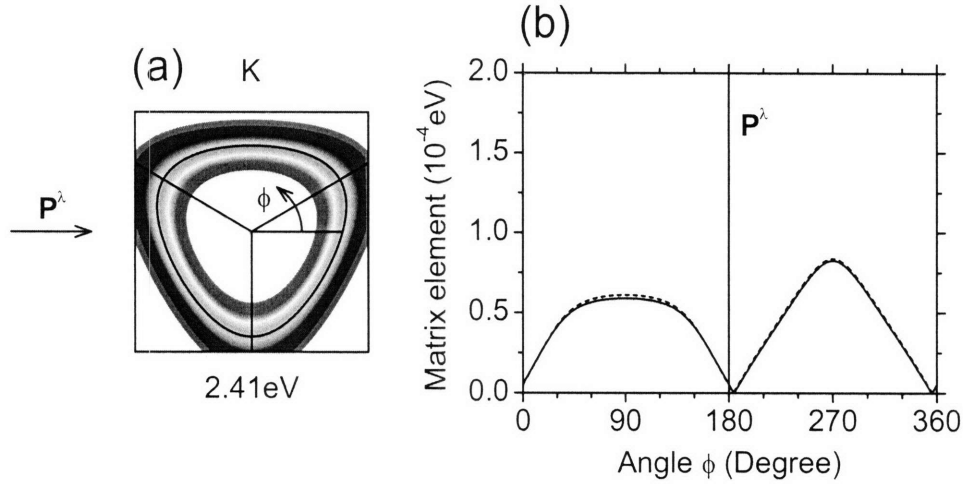


Figure 5-3: (a) The contours of constant transition energy $E^c - E^v$ around the K point in the first Brillouin zone of a graphene sheet within the ETB model as in Fig. 3-23 shown by colors in the visible range. The black lines show the KM directions. The polar angle ϕ parameterizes the position \mathbf{k} along the contour of $E^c - E^v = 2.41$ eV shown by the black curve. (b) The absolute value of the optical dipole transition matrix element for the light absorption process $|M_a^{c\lambda v}(\mathbf{k}, \mathbf{0}, \mathbf{k})|$ in the ETB model including nearest-neighbor and long-range interactions as a function of ϕ shown by the dashed and solid curves, respectively. The radiant flux density $I = 1 \text{ mW}/\mu\text{m}^2$. The linear light polarization vector in the armchair direction $\mathbf{P}^\lambda = \hat{\mathbf{x}}$ is shown by the arrow in (a) and by the vertical lines at angles $\phi = 0^\circ$ and 180° in (b).

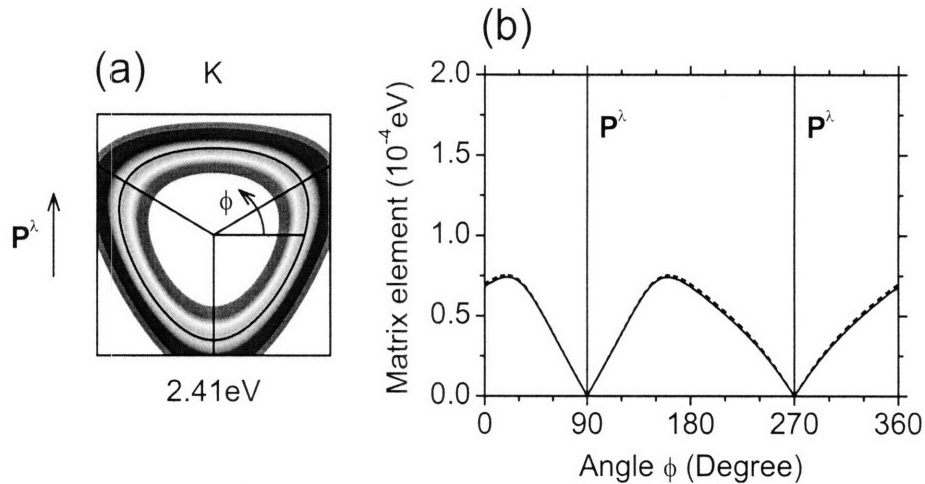


Figure 5-4: (a) The contours of constant transition energy and (b) the optical dipole transition matrix element identical to those shown in Fig. 5-3, except for the linear light polarization vector aligned with the zigzag direction $\mathbf{P}^\lambda = \hat{\mathbf{y}}$, as shown by the arrow in (a) and by the vertical lines at angles $\phi = 90^\circ$ and 270° in (b).

$\mathbf{P}^\lambda = \hat{\mathbf{x}}$ and $\mathbf{P}^\lambda = \hat{\mathbf{y}}$. Its absolute value as a function of ϕ is shown in Figs. 5-3 (b) and 5-4 (b) by the solid curves for the two linear light polarizations. For comparison, the same absolute value calculated in the nearest-neighbor approximation, $d_{\pi\pi}(R) = 0$ for $R > a_{CC}$, is shown by the dashed curves. The solid and dashed curves in Figs. 5-3 (b) and 5-4 (b) lie very close to each other, consistent with the small value of $d_{\pi\pi}(a)$ in Fig. 5-2 (a). Both the solid and dashed curves in Figs. 5-3 (b) and 5-4 (b) indicate that the optical transition rate is not homogeneous along the contours of constant $E^c - E^v$. Namely, the nodes appear in the optical transition rate in the direction of the linear light polarization in the reciprocal space of the graphene sheet [48, 133].

5.1.1 Dipole selection rules

Within the zone-folding technique, the optical dipole transition matrix elements in SWNTs are obtained by substituting the 1D angular μ and linear k momenta for the 2D momentum \mathbf{k} in Eqs. (5.5) and (5.7) to (5.9), according to Eq. (2.14). The curvature of the SWNT sidewall is taken into account by aligning the atomic orbitals $\phi_o(\mathbf{r} - \mathbf{R}_{us})$ along the tangential and normal directions, by analogy with Eq. (4.17). The atomic dipole transition vector takes the form:

$$\mathbf{d}_{o'o}(\mathbf{R}_{us} - \mathbf{R}_{u's'}) = \int \phi_{o'}^*(R^z(\phi_{u's'})(\mathbf{r} - \mathbf{R}_{u's'})) \nabla \phi_o(R^z(\phi_{us})(\mathbf{r} - \mathbf{R}_{us})) d\mathbf{r} \quad (5.10)$$

instead of Eq. (5.9), where the rotation matrix $R^z(\phi_{us})$ is given by Eq. (3.31). Then $\mathbf{d}_{o'o}(\mathbf{R}_{us} - \mathbf{R}_{u's'})$ is decomposed according to Fig. 5-1 and calculated using Table 5.1, as in the flat graphene sheet. Contrary to the flat graphene sheet, the atomic dipole transition matrix elements involving σ molecular orbitals are admixed to the optical transitions between the π energy bands. These matrix elements have a long-range nature according to Fig. 5-2, as opposed to $d_{\pi\pi}(R)$ vanishing at $R = a$.

While the energy conservation in SWNTs coincides with the one in the graphene sheet and is expressed by the delta function $\delta(E^b(\mu_f, k_f) \mp \hbar\omega - E^b(\mu_i, k_i))$ for the light absorption and emission processes, the dipole selection rules for SWNTs may differ from the momentum conservation in the graphene sheet depending on the light

propagation direction $\boldsymbol{\kappa}$ and polarization vector \mathbf{P}^λ with respect to the SWNT axis, thereafter aligned with the z -axis. Three distinct cases can be identified as schematically shown in the upper traces of Fig. 5-5:

(a) For light propagating perpendicular and linearly polarized parallel to the SWNT axis ($\boldsymbol{\kappa} \parallel \hat{\mathbf{x}}$ or $\boldsymbol{\kappa} \parallel \hat{\mathbf{y}}$ and $\mathbf{P}^\lambda = \hat{\mathbf{z}}$), the dipole selection rules read as follows, $\mu_f = \mu_i$ and $k_f = k_i$, obtained upon substituting Eq. (2.14) into the momentum conservation for the graphene sheet, $\mathbf{k}_f = \mathbf{k}_i$ [2, 48, 133, 140], or alternatively, derived from symmetry arguments [12, 14]. Considering that the direction from the K point to the critical wavevector \mathbf{k}_i in the reciprocal space of the graphene sheet is roughly perpendicular to the SWNT axis and taking into account the angular dependence of $|M^{b'\lambda b}(\mathbf{k}, \mathbf{0}, \mathbf{k})|$ shown in Figs. 5-3 (b) and 5-4 (b), the value of $|M^{b'\lambda b}(\mathbf{k}, \mathbf{0}, \mathbf{k})|$ nearly reaches its maximum at the E_{ii} Van Hove singularity (VHS) in the joint density of states (JDOS).

(b) For light propagating perpendicular and linearly polarized perpendicular to the SWNT axis ($\boldsymbol{\kappa} \parallel \hat{\mathbf{x}}$ and $\mathbf{P}^\lambda = \hat{\mathbf{y}}$ or $\boldsymbol{\kappa} \parallel \hat{\mathbf{y}}$ and $\mathbf{P}^\lambda = \hat{\mathbf{x}}$), the angular momentum is not conserved, $\mu_f = \mu_i \pm 1$, as obtained by direct calculations using Eqs. (5.5), (5.7), (5.8), and (5.10) [2, 48, 133, 140], and independently identified by group theory analysis [12, 14], while the linear momentum is still conserved, $k_f = k_i$. Accordingly, the $E_{\mu, \mu \pm 1}$ VHS in the JDOS for perpendicularly polarized light is roughly halfway between the $E_{\mu\mu}$ and $E_{\mu \pm 1, \mu \pm 1}$ VHSs in the JDOS for parallel polarized light because of a small asymmetry between the valence and conduction bands¹ [46, 133]. The value of $|M^{b'\lambda b}(\mathbf{k}, \mathbf{0}, \mathbf{k})|$ goes close to zero at the $E_{\mu, \mu \pm 1}$ VHS in the JDOS.

(c) For linearly polarized light propagating parallel to the SWNT axis ($\boldsymbol{\kappa} \parallel \hat{\mathbf{z}}$ and $\mathbf{P}^\lambda = \hat{\mathbf{x}}$ or $\mathbf{P}^\lambda = \hat{\mathbf{y}}$), the dipole selection rules and the magnitude of $|M^{b'\lambda b}(\mathbf{k}, \mathbf{0}, \mathbf{k})|$ are identical to those in case (b). For left and right circularly polarized light propagating parallel to the SWNT axis ($\boldsymbol{\kappa} \parallel \hat{\mathbf{z}}$ and $\mathbf{P}^\lambda = \frac{1}{\sqrt{2}}(\hat{\mathbf{x}} \pm i\hat{\mathbf{y}})$, respectively), the dipole selection rules for the angular momentum are constrained as follows: $\mu_f = \mu_i + 1$ for absorption of left (right) circularly polarized light by ZR/AL- (ZL/AR-) handed

¹The $E_{\mu, \mu \pm 1}$ VHS is labeled by μ rather than by i since $\mu \pm 1$ does not necessarily correspond to $i \pm 1$ for a pair of corresponding μ and i .

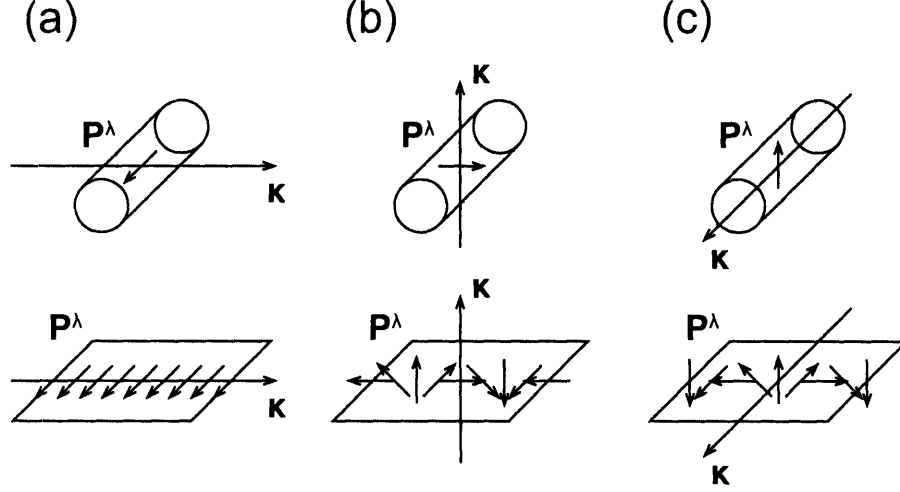


Figure 5-5: The light propagation direction κ and polarization vector \mathbf{P}^λ with respect to the SWNT (upper traces) and the unrolled flat graphene sheet (bottom traces). Cases (a), (b), and (c) are described in Section 5.1.1. In cases (b) and (c), the light gains momentum $\kappa = K_1 = 2/d_t$ due to the curvature of the SWNT sidewall.

SWNT, $\mu_f = \mu_i - 1$ for absorption of left (right) circularly polarized light by ZL/AR- (ZR/AL-) handed SWNT, and *vice versa* for light emission [133, 138]. Still, $k_f = k_i$ and $|M^{b'\lambda b}(\mathbf{k}, \mathbf{0}, \mathbf{k})|$ is close to zero as in case (b).

The angular momentum nonconservation in cases (b) and (c) is understood by considering the interaction of light with the unrolled SWNT, as shown in Fig. 5-5. When the SWNT is unrolled into the flat graphene sheet, the light polarized parallel to the SWNT axis is transformed to the light polarized parallel to the graphene sheet, according to Fig. 5-5 (a). The dipole selection rules are then obtained from the momentum conservation in the flat graphene sheet using Eq. (2.14). Perpendicular polarization, on the other hand, becomes transformed into the in-plane and out-of-plane polarization components in the unrolled graphene sheet, modulated in the circumferential direction with the period $C_h = \pi d_t$, as shown in Figs. 5-5 (b) and (c). The out-of-plane polarization component can be neglected because of the much stronger in-plane interaction in the graphene sheet. The in-plane polarization component thus gains a phase factor $\cos(\mathbf{K}_1 \cdot \mathbf{r})$, where $\mathbf{K}_1 = 2\pi C_h / C_h^2$ is the separation between the adjacent cutting lines, similar to trace $\mu = \pm 1$ in Fig. 2-6 (a). By expanding $\cos(\mathbf{K}_1 \cdot \mathbf{r})$ into a sum of $\exp(i\mathbf{K}_1 \cdot \mathbf{r})$ and $\exp(-i\mathbf{K}_1 \cdot \mathbf{r})$, we obtain two

plane waves with wavevectors \mathbf{K}_1 and $-\mathbf{K}_1$ polarized parallel to the graphene sheet. This results in the non-vertical optical transitions between the adjacent cutting lines in the reciprocal space of the graphene sheet, changing the angular momentum by one according to Eq. (2.14). In this way, the angular momentum nonconservation is associated with the wavevector of magnitude $K_1 = 2/d_t$ being much larger than the optical wavevector $\kappa = 2\pi/\lambda$, since the SWNT diameter $d_t \approx 1$ nm is much smaller than the optical wavelength $\lambda \approx 1$ μ m. Hence, an optical photon in the unrolled graphene sheet can be considered as an x-ray photon with respect to its spatial distribution, yet its frequency stays in the visible range. Such a “pseudo x-ray” photon is a source of breaking the angular momentum conservation in the case of perpendicular polarization [133, 140].

The small value of $|M^{b\lambda b}(\mathbf{k}, \mathbf{0}, \mathbf{k})|$ in cases (b) and (c) indicates that an interaction of the SWNT with the light polarized perpendicular to the SWNT axis is considerably suppressed by the depolarization effect, implying that the SWNT acts as a dipole antenna [2, 39, 66]. The depolarization effect complicates the observation of the non-vertical optical transitions, since the parallel polarization component dominates the optical response of the SWNT sample, unless the SWNTs are well aligned [46, 133]. The various types of alignment can be achieved by growing SWNTs under an electric field applied *in situ* [33, 102], by growing SWNTs along atomic steps on a sapphire substrate [53], by growing vertically aligned SWNT films [100, 175], by placing SWNTs inside a strong magnetic field [174], by mechanically stretching SWNT-polymer composites [60], and by some other techniques. The degree of alignment can be monitored using the perpendicular polarization geometry.

Equipped with the dipole selection rules and the depolarization effect, we can now calculate the optical dipole transition matrix elements for the parallel polarization geometry in SWNTs using Eqs. (5.5), (5.7), (5.9), and (5.10). The matrix elements for the E_{ii} transitions form the family patterns with a strong dependence on the SWNT chiral angle [59], similar to those observed in the ETB Kataura plot in Section 3.6. However, for a quantitative evaluation of the intensities of the optical transitions in SWNTs, many-body interactions must be taken into account, accord-

ing to Section 3.7. The optical dipole transition matrix elements between the excitonic wavefunctions calculated within the ETB framework are almost independent on the SWNT chiral angle [59], in a good agreement with the results of first-principles calculations [156]. For the perpendicular polarization geometry, the $E_{\mu, \mu \pm 1}$ VHSs in the JDOS are considerably blueshifted from their single-particle values and suppressed in intensity by the many-body interactions, as predicted theoretically using the effective-mass approximation [163]. The blueshift of the $E_{\mu, \mu \pm 1}$ excitonic transitions is detected experimentally in the photoluminescence excitation-emission spectra of SDS-encapsulated alcohol CVD SWNTs in D₂O [96].

5.2 Electron-phonon interaction

The interaction between electrons and the high-symmetry Γ and K (K') point phonon modes in the graphene sheet and SWNTs was assessed in Section 4.6 by the supercell method within the framework of the STB model. Away from the high-symmetry Γ and K (K') points, the linear response method was applied in Section 4.6. At a general wavevector \mathbf{q} , the phonon mode ν involves vibrations of atoms about their equilibrium positions \mathbf{R}_{us} . The atomic displacement vectors $\mathbf{r}_{us}^\nu(\mathbf{q}, t)$ are given by:

$$\begin{aligned} \mathbf{r}_{us}^\nu(\mathbf{q}, t) = \sqrt{\frac{\hbar}{2UM\omega^\nu(\mathbf{q})}} & \left(\sqrt{n^\nu(\mathbf{q})} \exp(+i\mathbf{q}\mathbf{R}_{us} - i\omega^\nu(\mathbf{q})t) \mathbf{e}_s^\nu(\mathbf{q}) \right. \\ & \left. + \sqrt{n^\nu(\mathbf{q}) + 1} \exp(-i\mathbf{q}\mathbf{R}_{us} + i\omega^\nu(\mathbf{q})t) \mathbf{e}_s^{\nu*}(\mathbf{q}) \right), \end{aligned} \quad (5.11)$$

similar to Eq. (4.2) but with the amplitude $\rho^\nu(\mathbf{q})$ expressed in the second quantization formalism. Here, \hbar is Planck's constant, U is the number of two-atom unit cells in the graphene sheet, M is the mass of a carbon atom, $\omega^\nu(\mathbf{q})$ is the phonon frequency, $n^\nu(\mathbf{q})$ is the phonon occupation number, and $\mathbf{e}_s^\nu(\mathbf{q})$ is the normal mode displacement.

The atomic vibrations described by Eq. (5.11) perturb the effective periodic potential $V(\mathbf{r})$ given by Eq. (3.6). In the rigid ion approximation, the effective spherically-symmetric potential $U(\mathbf{r} - \mathbf{R}_{u''s''})$ in Eq. (3.6) is moving along with the atom $\mathbf{R}_{u''s''}$ unperturbed in the field of the other atoms. The variation of the effective periodic

potential $V(\mathbf{r})$ in Eq. (3.6) is then expressed by the deformation potential:

$$\delta V^\nu(\mathbf{q}, \mathbf{r}, t) = - \sum_{u''s''} \nabla U(\mathbf{r} - \mathbf{R}_{u''s''}) \cdot \mathbf{r}_{u''s''}^\nu(\mathbf{q}, t). \quad (5.12)$$

Within first-order time-dependent perturbation theory, the electron-phonon scattering matrix element between the initial i and final f electronic states in the graphene sheet is given by [45, 57]:

$$M^{b'\nu b}(\mathbf{k}_f, \mathbf{q}, \mathbf{k}_i) = \langle \Psi^{b'}(\mathbf{k}_f, \mathbf{r}, t) | \delta V^\nu(\mathbf{q}, \mathbf{r}, t) | \Psi^b(\mathbf{k}_i, \mathbf{r}, t) \rangle, \quad (5.13)$$

where $\Psi^b(\mathbf{k}, \mathbf{r}, t)$ is the one-electron wavefunction of Eq. (3.2). Note that Eq. (5.13) does not take into account the rigid movement of the atomic orbitals along with the atoms. The movement of the atomic orbitals gives rise to the second term in the Hellmann-Feynman force of Eq. (3.28), and a similar term is expected to appear in Eq. (5.13). Incorporation of this term will be the subject of future work.

The electron-phonon scattering rate is determined by Fermi's Golden Rule:

$$W^{b'\nu b}(\mathbf{k}_f, \mathbf{q}, \mathbf{k}_i) = \frac{1}{\hbar^2 t_\nu} \left| \int_0^{t_\nu} dt M^{b'\nu b}(\mathbf{k}_f, \mathbf{q}, \mathbf{k}_i) \right|^2, \quad (5.14)$$

where t_ν is the electron-phonon interaction time. Integration over time t in Eq. (5.14) yields the delta function $\delta(E^{b'}(\mathbf{k}_f) \mp \hbar\omega^\nu(\mathbf{q}) - E^b(\mathbf{k}_i))$ that expresses the energy conservation. We thus conclude that the two terms in Eq. (5.1) describe the anti-Stokes (phonon absorption) and Stokes (phonon emission) processes, respectively. For both anti-Stokes and Stokes processes, the photoexcited electrons and holes away from the Fermi level are scattered within the same π valence or π^* conduction band, $b' = b = v$ or $b' = b = c$. The induced and spontaneous Stokes processes are represented by the terms $n^\nu(\mathbf{q})$ and 1 under the square root in Eq. (5.1), respectively. In thermal equilibrium, the phonon occupation number $n^\nu(\mathbf{q})$ is given by the Bose-Einstein distribution:

$$n^\nu(\mathbf{q}) = \frac{1}{\exp\left(\frac{\hbar\omega^\nu(\mathbf{q})}{k_B T}\right) - 1}, \quad (5.15)$$

where $k_B = 0.086173$ meV/K is the Boltzmann constant and T is the temperature. For the in-plane optical phonon modes around the Γ and K points that dominate the scattering of photoexcited electrons, $n^\nu(\mathbf{q}) \ll 1$ at room temperature $T = 300$ K, and the induced Stokes process is neglected in comparison to the spontaneous Stokes process.

The electron-phonon matrix elements, $M_a^{b\nu b}(\mathbf{k}_f, \mathbf{q}, \mathbf{k}_i)$ and $M_e^{b\nu b}(\mathbf{k}_f, \mathbf{q}, \mathbf{k}_i)$, for the anti-Stokes and spontaneous Stokes processes, respectively, are obtained upon substituting Eqs. (3.2), (5.11), and (5.12) into Eq. (5.13):

$$\begin{cases} M_a^{b\nu b}(\mathbf{k}_f, \mathbf{q}, \mathbf{k}_i) = -\sqrt{\frac{\hbar n^\nu(\mathbf{q})}{2UM\omega^\nu(\mathbf{q})}} D^{b\nu b}(\mathbf{k}_f, \mathbf{q}, \mathbf{k}_i), \\ M_e^{b\nu b}(\mathbf{k}_f, \mathbf{q}, \mathbf{k}_i) = -\sqrt{\frac{\hbar}{2UM\omega^\nu(\mathbf{q})}} D^{b\nu b*}(\mathbf{k}_i, \mathbf{q}, \mathbf{k}_f), \end{cases} \quad (5.16)$$

where $D^{b\nu b}(\mathbf{k}_f, \mathbf{q}, \mathbf{k}_i)$ is the deformation potential matrix element:

$$\begin{aligned} D^{b\nu b}(\mathbf{k}_f, \mathbf{q}, \mathbf{k}_i) &= \left\langle \Psi^b(\mathbf{k}_f, \mathbf{r}, 0) \left| \sum_{u''s''} \exp(i\mathbf{q}\mathbf{R}_{u''s''}) \right. \right. \\ &\quad \left. \left. \times \nabla U(\mathbf{r} - \mathbf{R}_{u''s''}) \cdot \mathbf{e}_{s''}^\nu(\mathbf{q}) \right| \Psi^b(\mathbf{k}_i, \mathbf{r}, 0) \right\rangle. \end{aligned} \quad (5.17)$$

Upon substituting the one-electron wavefunctions $\Psi^b(\mathbf{k}, \mathbf{r}, 0)$ from Eq. (3.2) into Eq. (5.17), we express the deformation potential matrix element in the following form:

$$D^{b\nu b}(\mathbf{k}_f, \mathbf{q}, \mathbf{k}_i) = \sum_{s'o'} \sum_{so} C_{s'o'}^{b*}(\mathbf{k}_f) D_{s'o'so}^\nu(\mathbf{k}_f, \mathbf{q}, \mathbf{k}_i) C_{so}^b(\mathbf{k}_i), \quad (5.18)$$

where $D_{s'o'so}^\nu(\mathbf{k}_f, \mathbf{q}, \mathbf{k}_i)$ is the deformation potential matrix:

$$\begin{aligned} D_{s'o'so}^\nu(\mathbf{k}_f, \mathbf{q}, \mathbf{k}_i) &= \frac{1}{U} \sum_{u''}^U \sum_{s''}^2 \sum_{u'}^U \sum_u^U \exp(-i\mathbf{k}_f\mathbf{R}_{u's'} + i\mathbf{q}\mathbf{R}_{u''s''} + i\mathbf{k}_i\mathbf{R}_{us}) \\ &\quad \times \int \phi_{o'}^*(\mathbf{r} - \mathbf{R}_{u's'}) \nabla U(\mathbf{r} - \mathbf{R}_{u''s''}) \cdot \mathbf{e}_{s''}^\nu(\mathbf{q}) \phi_o(\mathbf{r} - \mathbf{R}_{us}) d\mathbf{r}. \end{aligned} \quad (5.19)$$

The summation over the unit cell index u' in Eq. (5.19) yields the momentum conservation, $(-\mathbf{k}_f \pm \mathbf{q} + \mathbf{k}_i) = \mathbf{0}$, for the anti-Stokes and spontaneous Stokes processes,

respectively. Following the same approximation as for the Hamiltonian matrix of Eq. (3.4), we neglect the three-center integrals in Eq. (5.19) [144]. Then Eq. (5.19) splits into three terms for which $u''s'' = us$, $u''s'' = u's'$, and $u's' = us$:

$$\begin{aligned}
D_{s'o'so}^\nu(\mathbf{k}_f, \mathbf{q}, \mathbf{k}_i) = & \sum_u^U \left(\exp(i\mathbf{k}_f(\mathbf{R}_{us} - \mathbf{R}_{u's'})) \boldsymbol{\alpha}_{o'o}(\mathbf{R}_{us} - \mathbf{R}_{u's'}) \cdot \mathbf{e}_s^\nu(\mathbf{q}) \right. \\
& + \exp(i\mathbf{k}_i(\mathbf{R}_{us} - \mathbf{R}_{u's'})) \boldsymbol{\beta}_{o'o}(\mathbf{R}_{us} - \mathbf{R}_{u's'}) \cdot \mathbf{e}_{s'}^\nu(\mathbf{q}) \\
& \left. + \exp(i\mathbf{q}(\mathbf{R}_{us} - \mathbf{R}_{u's'})) \boldsymbol{\lambda}_{o'o}(\mathbf{R}_{us} - \mathbf{R}_{u's'}) \cdot \mathbf{e}_s^\nu(\mathbf{q}) \right), \tag{5.20}
\end{aligned}$$

where index u' labels the unit cell under consideration, and the atomic deformation potential vectors $\boldsymbol{\alpha}_{o'o}(\mathbf{R})$, $\boldsymbol{\beta}_{o'o}(\mathbf{R})$, and $\boldsymbol{\lambda}_{o'o}(\mathbf{R})$ are defined as follows [57]:

$$\begin{cases} \boldsymbol{\alpha}_{o'o}(\mathbf{R}) = \int \phi_{o'}^*(\mathbf{r}) \nabla U(\mathbf{r} - \mathbf{R}) \phi_o(\mathbf{r} - \mathbf{R}) d\mathbf{r}, \\ \boldsymbol{\beta}_{o'o}(\mathbf{R}) = \int \phi_{o'}^*(\mathbf{r}) \nabla U(\mathbf{r}) \phi_o(\mathbf{r} - \mathbf{R}) d\mathbf{r}, \\ \boldsymbol{\lambda}_{o'o}(\mathbf{R}) = \int \phi_{o'}^*(\mathbf{r}) \nabla U(\mathbf{r} - \mathbf{R}) \phi_o(\mathbf{r}) d\mathbf{r}, \end{cases} \tag{5.21}$$

where $\phi_o(\mathbf{r})$ is the atomic orbital, and $\mathbf{R} = \mathbf{R}_{us} - \mathbf{R}_{u's'}$ connects the two interacting atoms. Analogous to Section 4.6, we refer to $\boldsymbol{\alpha}_{o'o}(\mathbf{R})$ and $\boldsymbol{\beta}_{o'o}(\mathbf{R})$ as the off-site atomic deformation potential vectors, while $\boldsymbol{\lambda}_{o'o}(\mathbf{R})$ is called the on-site atomic deformation potential vector, indicating the electron scattering between two different atomic sites or within the same atomic site, respectively [135]. The normal mode displacements $\mathbf{e}_s^\nu(\mathbf{q})$ and $\mathbf{e}_{s'}^\nu(\mathbf{q})$ that enter Eq. (5.20) are calculated using the AFC model with the ETB force constants listed in Table 4.8.

While the $o = 2s$ atomic orbitals are spherically symmetric, the $o = 2p$ atomic orbitals can be projected into the σ and π molecular orbitals along and perpendicular to \mathbf{R} , as shown in Fig. 3-2. The atomic deformation potential vectors $\boldsymbol{\alpha}_{o'o}(\mathbf{R})$, $\boldsymbol{\beta}_{o'o}(\mathbf{R})$, and $\boldsymbol{\lambda}_{o'o}(\mathbf{R})$ of Eq. (5.21) are then decomposed into the nine components for the different configurations of molecular orbitals. These configurations are shown in Figs. 5-6, 5-7, and 5-8, respectively, along with the effective spherically-symmetric potential $U(\mathbf{r} - \mathbf{R}_{u''s''})$ whose gradient enters into Eq. (5.21). Symmetry arguments lead to the following relations between the off-site atomic deformation potential vectors

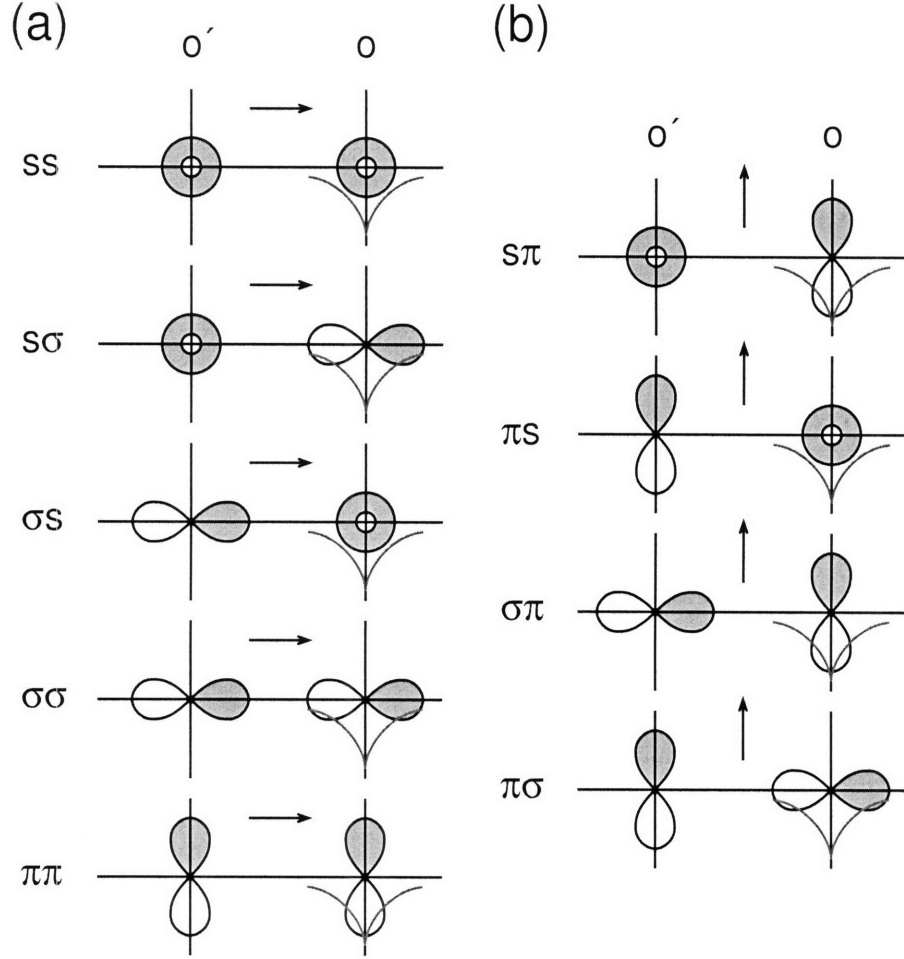


Figure 5-6: The molecular orbital configurations $o'o = ss, s\sigma, \sigma s, \sigma\sigma, \pi\pi, s\pi, \pi s, \sigma\pi, \pi\sigma$ for the off-site atomic deformation potential matrix elements $\alpha_{o'o}(R)$ similar to those shown in Figs. 3-3 and 5-1. The red curve represents the atomic potential whose gradient enters $\alpha_{o'o}(R)$. The directions of $\alpha_{o'o}(\mathbf{R})$ are shown by arrows (a) parallel and (b) perpendicular to the interatomic vector $\mathbf{R} = \mathbf{R}_{us} - \mathbf{R}_{u's'}$. The Chebyshev polynomial expansions of $\alpha_{o'o}(R)$ are given in Table 5.2. The calculated $\alpha_{o'o}(R)$ dependencies are shown in Fig. 5-9.

$\alpha_{o'o}$ and $\beta_{o'o}$:

$$\begin{cases} \beta_{ss}(\mathbf{R}) = -\alpha_{ss}(\mathbf{R}), & \beta_{s\sigma}(\mathbf{R}) = +\alpha_{\sigma s}(\mathbf{R}), & \beta_{s\pi}(\mathbf{R}) = +\alpha_{\pi s}(\mathbf{R}), \\ \beta_{\sigma s}(\mathbf{R}) = +\alpha_{s\sigma}(\mathbf{R}), & \beta_{\sigma\sigma}(\mathbf{R}) = -\alpha_{\sigma\sigma}(\mathbf{R}), & \beta_{\sigma\pi}(\mathbf{R}) = -\alpha_{\pi\sigma}(\mathbf{R}), \\ \beta_{\pi s}(\mathbf{R}) = +\alpha_{s\pi}(\mathbf{R}), & \beta_{\pi\sigma}(\mathbf{R}) = -\alpha_{\sigma\pi}(\mathbf{R}), & \beta_{\pi\pi}(\mathbf{R}) = -\alpha_{\pi\pi}(\mathbf{R}). \end{cases} \quad (5.22)$$

It is therefore sufficient to determine the $\alpha_{o'o}(\mathbf{R})$ and $\lambda_{o'o}(\mathbf{R})$ vectors [57].

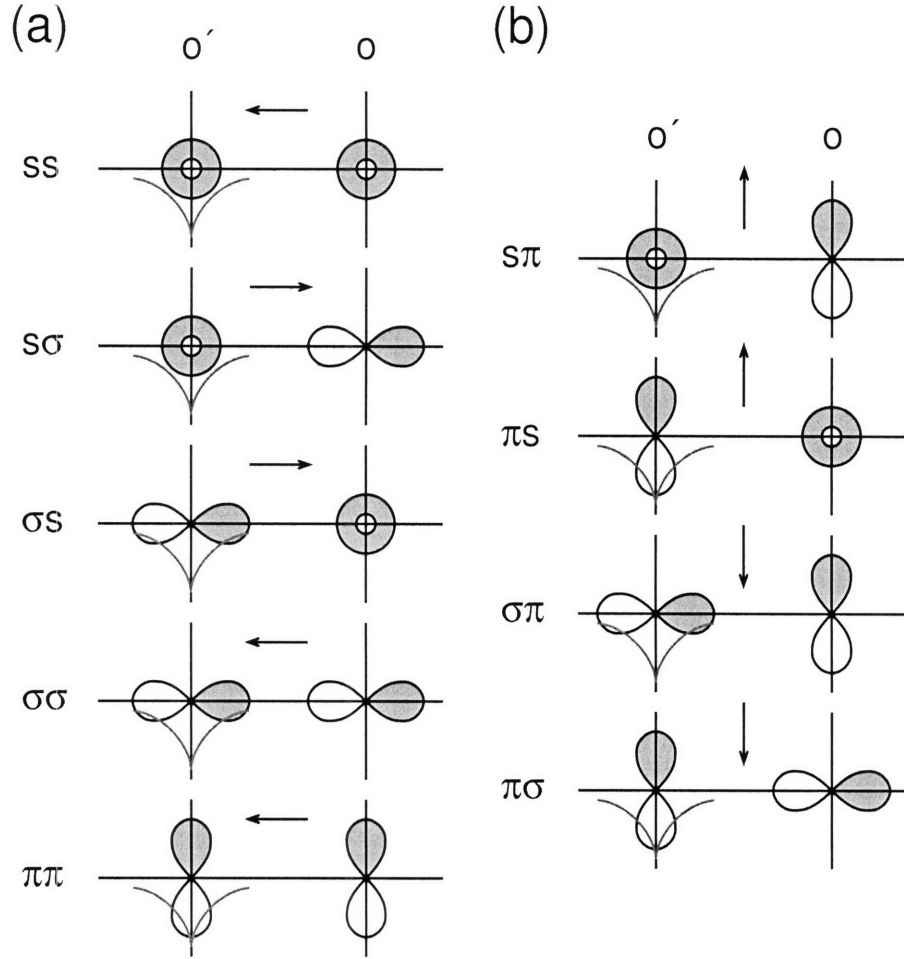


Figure 5-7: The molecular orbital configurations $o'o = ss, s\sigma, \sigma s, \sigma\sigma, \pi\pi, s\pi, \pi s, \sigma\pi, \pi\sigma$ for the off-site atomic deformation potential matrix elements $\beta_{o'o}(R)$ similar to those shown in Figs. 3-3, 5-1, and 5-6. The red curve represents the atomic potential whose gradient enters $\beta_{o'o}(R)$. The directions of $\beta_{o'o}(\mathbf{R})$ are shown by arrows (a) parallel and (b) perpendicular to the interatomic vector $\mathbf{R} = \mathbf{R}_{us} - \mathbf{R}_{u's'}$. The values of $\beta_{o'o}(R)$ are determined by the values of $\alpha_{o'o}(R)$ according to Eq. (5.22).

The directions of $\alpha_{o'o}(\mathbf{R})$ and $\lambda_{o'o}(\mathbf{R})$ can be either parallel or perpendicular to \mathbf{R} , as shown by arrows in Figs. 5-6 and 5-8, according to the symmetry of the spherical harmonic $Y_{21}(\theta, \phi)$. Along these directions, the magnitudes $\alpha_{o'o} = |\alpha_{o'o}|$ and $\lambda_{o'o} = |\lambda_{o'o}|$ only depend on the interatomic distances $R = |\mathbf{R}|$. The configurations of the molecular orbitals that have the same $\lambda_{o'o}(R)$ are connected by dashed lines in Fig. 5-8. For the nine inequivalent configurations $o'o = ss, s\sigma, \sigma s, \sigma\sigma, \pi\pi, s\pi, \pi s, \sigma\pi, \pi\sigma$ in Fig. 5-6 and the six inequivalent configurations $o'o = ss, s\sigma, \sigma\sigma, \pi\pi, s\pi, \sigma\pi$ in Fig. 5-

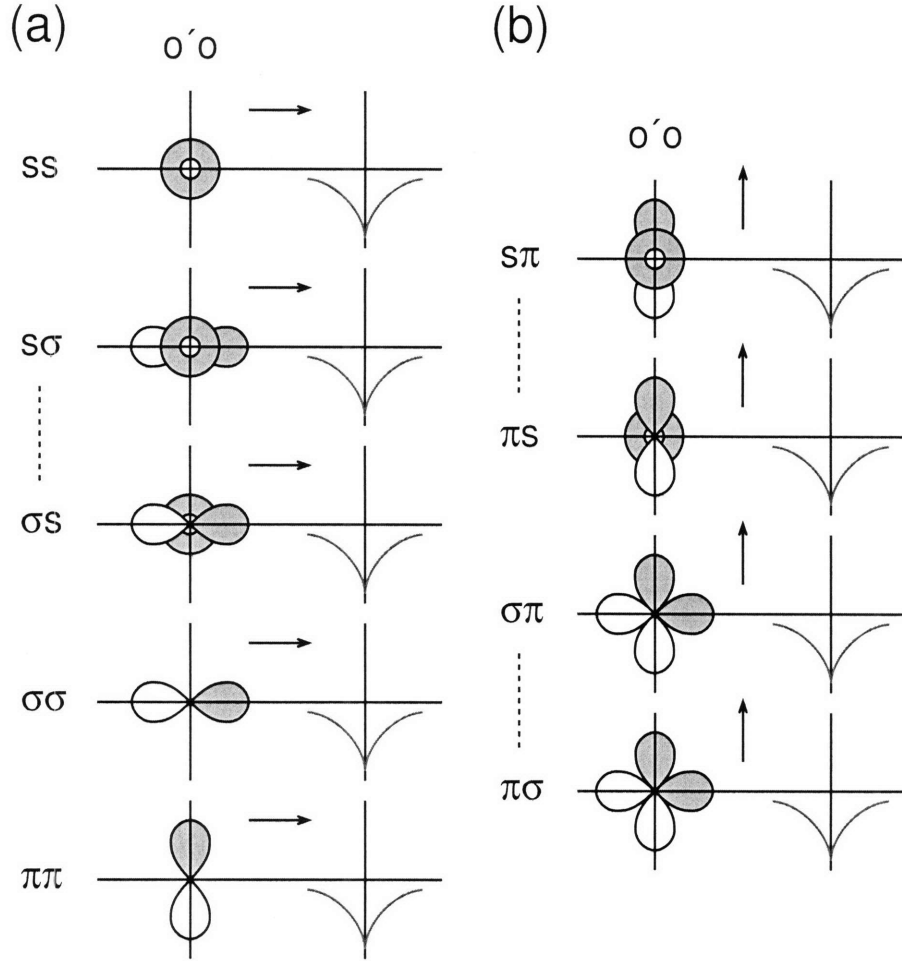


Figure 5-8: The molecular orbital configurations $o'o = ss, s\sigma, \sigma s, \sigma\sigma, \pi\pi, s\pi, \pi s, \sigma\pi, \pi\sigma$ for the on-site atomic deformation potential matrix elements $\lambda_{o'o}(R)$ similar to those shown in Figs. 3-3, 5-1, 5-6, and 5-7. The red curve represents the atomic potential whose gradient enters $\lambda_{o'o}(R)$. The directions of $\lambda_{o'o}(\mathbf{R})$ are shown by arrows (a) parallel and (b) perpendicular to the interatomic vector $\mathbf{R} = \mathbf{R}_{us} - \mathbf{R}_{u's'}$. The dashed lines connect the equivalent configurations with the same $\lambda_{o'o}(R)$. The Chebyshev polynomial expansions of $\lambda_{o'o}(R)$ are given in Table 5.3. The calculated $\lambda_{o'o}(R)$ dependencies are shown in Fig. 5-10.

8, the atomic deformation potential matrix elements $\alpha_{o'o}(R)$ and $\lambda_{o'o}(R)$ are calculated using the pseudoatomic wavefunctions and the Kohn-Sham potential of a neutral pseudoatom constructed within the ETB framework [122]. The calculated $\alpha_{o'o}(R)$ and $\lambda_{o'o}(R)$ functions are expanded in modified Chebyshev polynomials given by Eqs. (3.25) and (3.26). The expansion coefficients are listed in Tables 5.2 and 5.3. The resulting $\alpha_{o'o}(R)$ and $\lambda_{o'o}(R)$ dependencies are shown in Figs. 5-9 and 5-10.

Table 5.2: Coefficients C_n of the Chebyshev polynomial expansion according to Eqs. (3.25) and (3.26) for the off-site atomic deformation potential matrix elements $\alpha_{o'o}(R) = S(R)$ (in units of $10^{-3}E_h/a_0$; $E_h = 27.21138$ eV is the Hartree energy; $a_0 = 0.052917721$ nm is the Bohr radius) parallel and perpendicular to the inter-atomic vector $\mathbf{R} = \mathbf{R}_{us} - \mathbf{R}_{u's'}$. Boundaries of R are at $R_1 = 1.0$ and $R_2 = 7.0$ (in units of a_0). The molecular orbital configurations $o'o = ss, s\sigma, \sigma s, \sigma\sigma, \pi\pi, s\pi, \pi s, \sigma\pi, \pi\sigma$ are shown in Fig. 5-6. The calculated $\alpha_{o'o}(R)$ dependencies are shown in Fig. 5-9.

	α_{ss}	$\alpha_{s\sigma}$	$\alpha_{\sigma s}$	$\alpha_{\sigma\sigma}$	$\alpha_{\pi\pi}$
C_0	-0.3635210	+2.1097169	-0.2789600	+3.1539574	-0.4334657
C_1	+0.2606741	-1.7553088	+0.1457182	-2.6009458	+0.3727524
C_2	-0.0547213	+0.9753109	+0.1019037	+1.4066316	-0.2348758
C_3	-0.0823304	-0.2875030	-0.2270835	-0.3953886	+0.1037152
C_4	+0.0986310	-0.0503021	+0.1882425	-0.0660246	-0.0265339
C_5	-0.0540925	+0.1125453	-0.0929704	+0.1333231	-0.0017626
C_6	+0.0138564	-0.0715774	+0.0269190	-0.0745124	+0.0058298
C_7	+0.0040047	+0.0288868	-0.0011577	+0.0249039	-0.0035711
C_8	-0.0058742	-0.0078778	-0.0030690	-0.0050061	+0.0014483
C_9	+0.0040747	+0.0011106	+0.0022411	+0.0002651	-0.0005261

	$\alpha_{s\pi}$	$\alpha_{\pi s}$	$\alpha_{\sigma\pi}$	$\alpha_{\pi\sigma}$
C_0	+2.0170524	+0.5117628	+2.9238227	-0.4332595
C_1	-1.7408714	-0.4439417	-2.4874925	+0.3725599
C_2	+1.1027912	+0.2872697	+1.5009569	-0.2347203
C_3	-0.4768517	-0.1329031	-0.5801167	+0.1036100
C_4	+0.0984163	+0.0369983	+0.0730035	-0.0264748
C_5	+0.0376300	+0.0013507	+0.0737419	-0.0017902
C_6	-0.0481280	-0.0083581	-0.0620821	+0.0058407
C_7	+0.0270518	+0.0057948	+0.0268863	-0.0035749
C_8	-0.0103584	-0.0026121	-0.0075600	+0.0014496
C_9	+0.0031477	+0.0010337	+0.0015057	-0.0005265

In the flat graphene sheet, the atomic deformation potential matrix elements involving σ and π molecular orbitals are decoupled and electron-phonon scattering involving electronic states near the Fermi level is governed by $\alpha_{\pi\pi}(R)$ and $\lambda_{\pi\pi}(R)$ shown in the bottom traces of Figs. 5-9 (a) and 5-10 (a). One can see in Figs. 5-9 (a) and 5-10 (a) that $\alpha_{\pi\pi}(R)$ and $\lambda_{\pi\pi}(R)$ almost vanish at the second neighbor $R = a$, suggesting that the phonon-assisted electron transitions in the graphene sheet occur primarily between the $2p$ orbitals on adjacent carbon atoms. To satisfy the energy conservation,

Table 5.3: Coefficients C_n of the Chebyshev polynomial expansion according to Eqs. (3.25) and (3.26) for the on-site atomic deformation potential matrix elements $\lambda_{o'o}(R) = S(R)$ (in units of $10^{-3}E_h/a_0$; $E_h = 27.21138$ eV is the Hartree energy; $a_0 = 0.052917721$ nm is the Bohr radius) parallel and perpendicular to the inter-atomic vector $\mathbf{R} = \mathbf{R}_{us} - \mathbf{R}_{u's'}$. Boundaries of R are at $R_1 = 1.0$ and $R_2 = 7.0$ (in units of a_0). The molecular orbital configurations $o'o = ss, s\sigma, \sigma\sigma, \pi\pi, s\pi, \sigma\pi$ are shown in Fig. 5-8. The calculated $\lambda_{o'o}(R)$ dependencies are shown in Fig. 5-10.

	λ_{ss}	$\lambda_{s\sigma}$	$\lambda_{\sigma\sigma}$	$\lambda_{\pi\pi}$
C_0	-0.9906740	-0.7849724	-1.6517170	-0.8190939
C_1	+0.7766919	+0.5992836	+1.3174189	+0.6645416
C_2	-0.3713484	-0.2456202	-0.6639543	-0.3781723
C_3	+0.0671177	-0.0336741	+0.1424873	+0.1683272
C_4	+0.0744466	+0.1590298	+0.1104668	-0.0576039
C_5	-0.1002167	-0.1593283	-0.1561639	+0.0093309
C_6	+0.0725572	+0.1047476	+0.1086829	+0.0049105
C_7	-0.0367535	-0.0507720	-0.0515711	-0.0052864
C_8	+0.0131416	+0.0179875	+0.0168903	+0.0026743
C_9	-0.0021051	-0.0037290	-0.0025965	-0.0010938

	$\lambda_{s\pi}$	$\lambda_{\sigma\pi}$
C_0	+0.7343579	+0.7428290
C_1	-0.6526167	-0.6662996
C_2	+0.4669766	+0.4870691
C_3	-0.2760352	-0.2929132
C_4	+0.1344400	+0.1429532
C_5	-0.0506701	-0.0531581
C_6	+0.0118058	+0.0120052
C_7	+0.0017003	+0.0017170
C_8	-0.0034039	-0.0032757
C_9	+0.0025751	+0.0023110

the phonon-assisted transitions take place between the electronic states along the two contours of constant $E^c - E^v$ separated by twice the phonon energy. These contours can be wrapped either around the same K (K') point or around different K and K' (K' and K) points, which we refer to as the intra-valley and inter-valley scattering, respectively [132]. For the inter-valley scattering, the incident and scattered contours calculated within the ETB framework are shown in Fig. 5-11 (a), where the square boxes are identical to that shown in Fig. 3-23 (a) and the transition energies are rep-

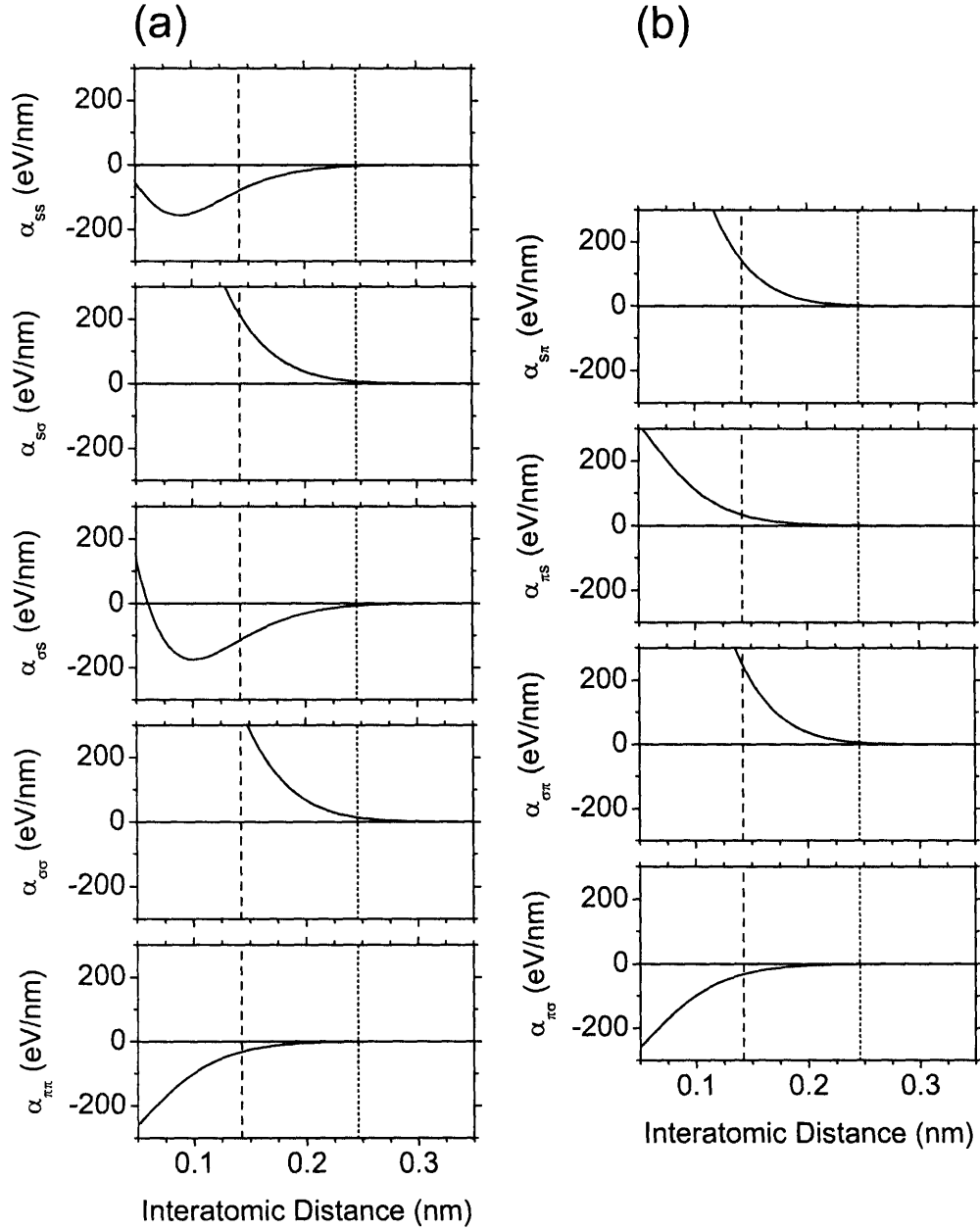


Figure 5-9: The off-site atomic deformation potential matrix elements $\alpha_{o'o}(R)$ which are (a) parallel and (b) perpendicular to the interatomic vector $\mathbf{R} = \mathbf{R}_{us} - \mathbf{R}_{u's'}$ calculated by the Chebyshev polynomial expansions given in Table 5.2. The molecular orbital configurations $o'o = ss, s\sigma, \sigma s, \sigma\sigma, \pi\pi, s\pi, \pi s, \sigma\pi, \pi\sigma$ are shown in Fig. 5-6. The dashed and dotted vertical lines indicate the first- and second-neighbor interatomic distances, $a_{CC} = 0.142$ nm and $a = \sqrt{3}a_{CC} = 0.246$ nm, respectively.

resented by spectral colors similar to Fig. 5-3 (a). The contours of $E^c - E^v = 2.41$ eV corresponding to the Ar ion laser wavelength of 514.5 nm and $E^c - E^v = 2.09$ eV

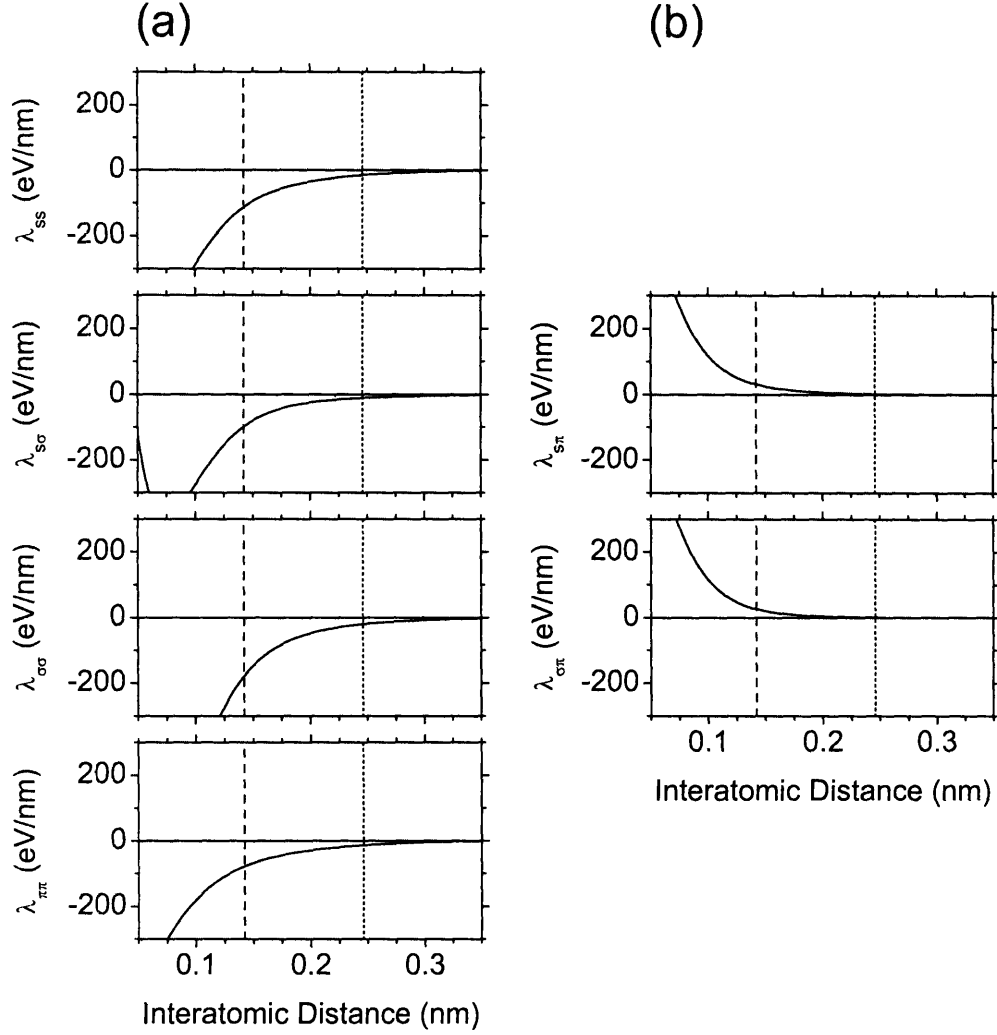


Figure 5-10: The on-site atomic deformation potential matrix elements $\lambda_{o'o}(R)$ which are (a) parallel and (b) perpendicular to the interatomic vector $\mathbf{R} = \mathbf{R}_{us} - \mathbf{R}_{u's'}$ calculated by the Chebyshev polynomial expansions given in Table 5.3. The molecular orbital configurations $o'o = ss, s\sigma, \sigma\sigma, \pi\pi, s\pi, \sigma\pi$ are shown in Fig. 5-8. The dashed and dotted vertical lines indicate the first- and second-neighbor interatomic distances, $a_{CC} = 0.142$ nm and $a = \sqrt{3}a_{CC} = 0.246$ nm, respectively.

downshifted by twice the frequency of the A'_1 K point phonon mode, $\omega \approx 1300$ cm^{-1} , are shown in Fig. 5-11 (a) by the black curves. The positions of the initial \mathbf{k}_i and final \mathbf{k}_f electron wavevectors are shown by the solid dot along the $K\Gamma$ direction and parameterized by the polar angle ϕ , respectively. The electron-phonon scattering matrix element for the phonon emission process $M_e^{bvb}(\mathbf{k}_f, \mathbf{q}, \mathbf{k}_i)$ using the momentum conservation $\mathbf{q} = \mathbf{k}_i - \mathbf{k}_f$ is calculated from Eqs. (5.16), (5.18), (5.20), and (5.21) with the

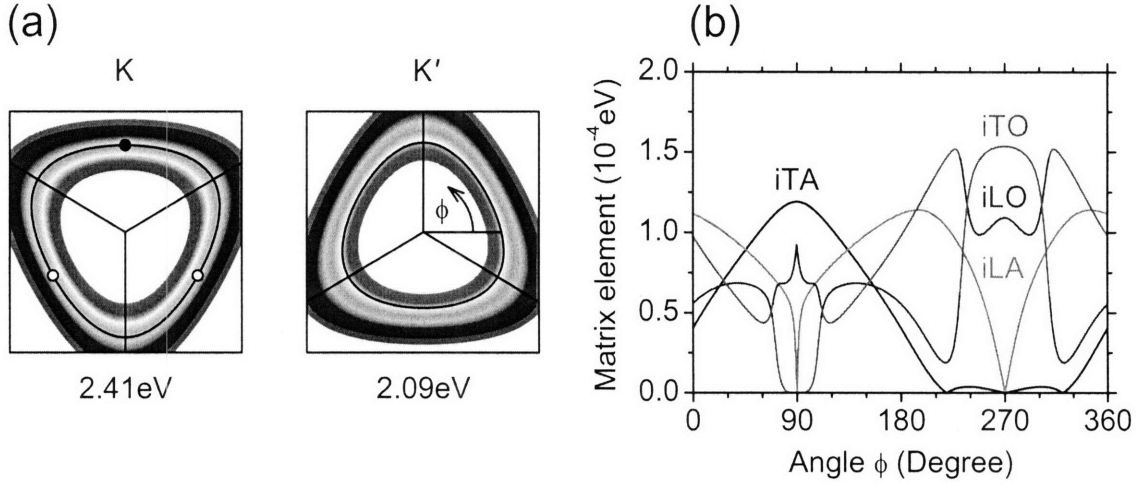


Figure 5-11: (a) The contours of constant transition energy $E^c - E^v$ around the K and K' points in the first Brillouin zone of a graphene sheet within the ETB model as in Fig. 3-23 shown by colors in the visible range. The black curves correspond to the contours of $E^c - E^v = 2.41$ eV and $E^c - E^v = 2.09$ eV and the black lines show the KM directions. The wavevector \mathbf{k}_i is shown by the solid dot along the K Γ direction and the wavevector \mathbf{k}_f is parameterized by the polar angle ϕ , respectively. (b) The absolute value of the electron-phonon scattering matrix element for the Stokes process $|M_e^{c\nu c}(\mathbf{k}_f, \mathbf{q}, \mathbf{k}_i) - M_e^{v\nu v}(\mathbf{k}_f, \mathbf{q}, \mathbf{k}_i)|$ assuming $\mathbf{q} = \mathbf{k}_i - \mathbf{k}_f$ in the ETB model as a function of ϕ shown by the green, black, blue, and red curves for the phonon modes $\nu = iTA, iLA, iLO, iTO$, respectively. The number of unit cells $U = 1$.

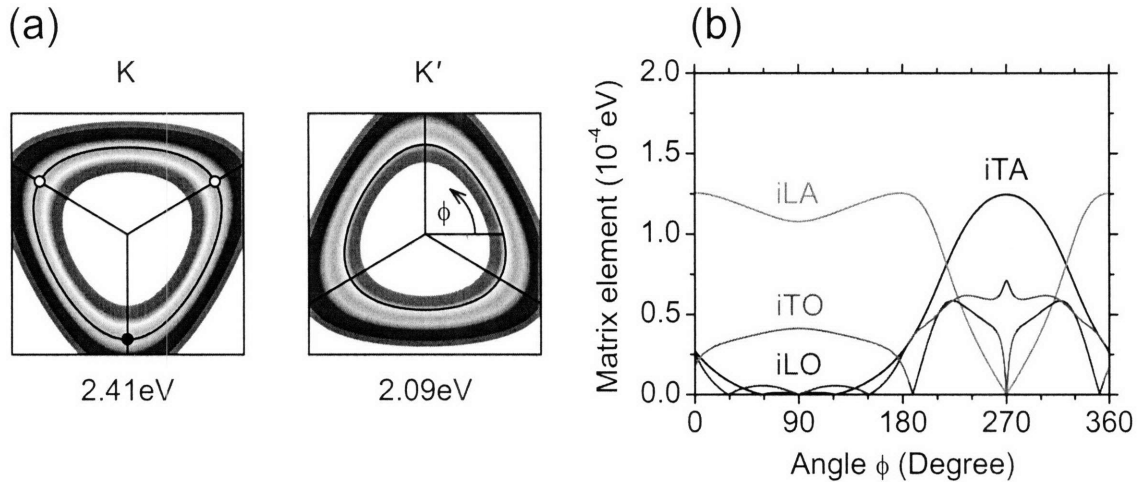


Figure 5-12: (a) The contours of constant transition energy around the K and K' points in the first Brillouin zone and (b) the electron-phonon scattering matrix element identical to those shown in Fig. 5-11, except for the position of the initial electron wavevector \mathbf{k}_i shown by the solid dot along the KM direction in (a).

number of unit cells $U = 1$. The absolute value $|M_e^{c\nu c}(\mathbf{k}_f, \mathbf{q}, \mathbf{k}_i) + M_e^{\nu\nu\nu}(\mathbf{k}_i, -\mathbf{q}, \mathbf{k}_f)|$ reflecting interference between electron-phonon and hole-phonon scattering is shown in Fig. 5-11 (b) as a function of ϕ , where four curves of different colors correspond to the in-plane phonon modes, $\nu = \text{iTA, iLA, iLO, iT0}$. For comparison, the same absolute value calculated for the position of the initial electron wavevector \mathbf{k}_i along the KM direction is shown in Fig. 5-12 (b). Both Figs. 5-11 (b) and 5-12 (b) indicate that the electron-phonon scattering rate is not homogeneous along the contours of constant $E^c - E^\nu$. Namely, nodes appear in the electron-phonon scattering rate in different directions in the reciprocal space of the graphene sheet [45, 57].

5.2.1 Vibrational selection rules

Within the zone-folding technique, the electron-phonon scattering matrix elements in SWNTs are obtained by substituting (μ, k) and (η, q) for \mathbf{k} and \mathbf{q} in Eqs. (5.16), (5.18), (5.20), and (5.21), according to Eqs. (2.14) and (4.16). The curvature of the SWNT sidewall is taken into account by aligning the atomic orbitals $\phi_o(\mathbf{r} - \mathbf{R}_{us})$ along the tangential and normal directions, by analogy with Eq. (5.10). The atomic deformation potential vectors take the form:

$$\left\{ \begin{array}{l} \alpha_{o'o}(\mathbf{R}_{us} - \mathbf{R}_{u's'}) \\ \quad = \int \phi_{o'}^*(R^z(\phi_{u's'})(\mathbf{r} - \mathbf{R}_{u's'})) \nabla U(R^z(\phi_{us})(\mathbf{r} - \mathbf{R}_{us})) \phi_o(R^z(\phi_{us})(\mathbf{r} - \mathbf{R}_{us})) d\mathbf{r}, \\ \beta_{o'o}(\mathbf{R}_{us} - \mathbf{R}_{u's'}) \\ \quad = \int \phi_{o'}^*(R^z(\phi_{u's'})(\mathbf{r} - \mathbf{R}_{u's'})) \nabla U(R^z(\phi_{u's'})(\mathbf{r} - \mathbf{R}_{u's'})) \phi_o(R^z(\phi_{us})(\mathbf{r} - \mathbf{R}_{us})) d\mathbf{r}, \\ \lambda_{o'o}(\mathbf{R}_{us} - \mathbf{R}_{u's'}) \\ \quad = \int \phi_{o'}^*(R^z(\phi_{u's'})(\mathbf{r} - \mathbf{R}_{u's'})) \nabla U(R^z(\phi_{us})(\mathbf{r} - \mathbf{R}_{us})) \phi_o(R^z(\phi_{u's'})(\mathbf{r} - \mathbf{R}_{u's'})) d\mathbf{r}, \end{array} \right. \quad (5.23)$$

instead of Eq. (5.21), where the rotation matrix $R^z(\phi_{us})$ is given by Eq. (3.31). Then $\alpha_{o'o}(\mathbf{R}_{us} - \mathbf{R}_{u's'})$, $\beta_{o'o}(\mathbf{R}_{us} - \mathbf{R}_{u's'})$, and $\lambda_{o'o}(\mathbf{R}_{us} - \mathbf{R}_{u's'})$ are decomposed according to Figs. 5-6 to 5-8 and are calculated using Tables 5.2 and 5.3 and Eq. (5.22), as is done in the flat graphene sheet as discussed above. Contrary to the flat graphene sheet,

the atomic deformation potential matrix elements involving σ molecular orbitals are admixed through electron-phonon scattering between the π energy bands. These matrix elements almost vanish at the second neighbor $R = a$ according to Figs. 5-9 and 5-10, similar to the matrix elements involving π molecular orbitals.

The energy conservation and vibrational selection rules for the electron-phonon scattering in SWNTs are obtained by substituting the 1D angular η and linear q momenta for the 2D momentum \mathbf{q} in the energy and momentum conservation relations for the electron-phonon scattering in the graphene sheet according to Eq. (4.16). The energy conservation is given by $\delta(E^b(\mu_f, k_f) \mp \hbar\omega^\nu(\eta, q) - E^b(\mu_i, k_i))$ for the anti-Stokes (phonon absorption) and Stokes (phonon emission) processes in SWNTs, respectively. The vibrational selection rules read as $\mu_f \mp \eta - \mu_i = 0$ and $k_f \mp q - k_i = 0$ for the anti-Stokes and Stokes processes, respectively [45, 57, 140]. Alternatively, the vibrational selection rules can be derived using group theory [12]. The vibrational selection rules for SWNTs thus coincide with the momentum conservation for the electron-phonon scattering in the graphene sheet, contrary to the dipole selection rules for SWNTs, which may differ from the momentum conservation for the electron-phonon scattering in the graphene sheet depending on the light propagation and polarization directions with respect to the SWNT axis, as shown in Section 5.1.1.

The electron-phonon scattering matrix elements for electronic transitions within the same critical angular μ_i^b and linear k_i^b momenta by the $\nu = \text{RBM}, G^T, G^L$ phonon modes at the Γ point $(\eta, q) = (0, 0)$ calculated using Eqs. (5.16), (5.18), (5.20), and (5.23) form the strong family patterns with a SWNT chiral angle dependence [59], similar to those observed in the ETB Kataura plot in Section 3.6. However, for a quantitative analysis of the optical processes in SWNTs that are dominated by excitonic transitions according to Section 3.7, the phonon-assisted scattering matrix elements between the excitonic wavefunctions must be evaluated. The *exciton-phonon* scattering matrix elements calculated within the ETB framework do not differ much from the *electron-phonon* scattering matrix elements [59], in a good agreement with the results of first-principles calculations [85].

5.3 Resonance Raman scattering

The Raman effect is a phenomenon of inelastic light scattering by molecular vibrations in individual molecules or by phonon modes in solids. The frequencies of the phonon modes in solids are much smaller than the frequency of a photon in the visible range. Hence, the direct interaction of the electromagnetic field with the phonon modes gives rise to the non-resonant Raman scattering, which is contaminated by other light absorption and emission processes. However, the light can couple to the phonon modes indirectly through the electronic subsystem, resulting in the resonance Raman scattering (RRS) process. In the RRS process, the excitation energy of the incident laser beam coincides with a particular electronic transition in the graphene sheet. The phonon modes coupled to the photoexcited electrons and holes exhibit an enhanced Raman scattering intensity. The RRS process is further increased when the incident laser beam is tuned to an exciton transition associated with one of the VHSs in SWNTs.

The differential cross-section for the RRS process in the graphene sheet is given by the following expression [87]:

$$\frac{d\sigma_{ea}^{\lambda'\lambda}(E_e, E_a)}{d\Omega_e} = \frac{\kappa^2 V^2 E_e E_a}{4\pi^2 \hbar^4 c^4} \left| K_{ea}^{\lambda'\lambda}(E_e, E_a) \right|^2, \quad (5.24)$$

where E_a and E_e are the energies of the incident and scattered photons of polarizations λ and λ' , respectively, Ω_e is the solid angle for collecting the scattered light, κ is the dielectric constant, V is the quantization volume for the electromagnetic field, \hbar is Planck's constant, c is the speed of light in vacuum, and $K_{ea}^{\lambda'\lambda}(E_e, E_a)$ is an appropriate high-order matrix element of interaction between the electromagnetic field and the graphene sheet. The energy conservation is expressed in the form $E_e = E_a - \hbar\omega$ where ω is the Raman shift that consists of a difference or sum of one or more frequencies of absorbed or emitted phonon modes in the graphene sheet for the anti-Stokes and Stokes RRS process for which $\omega < 0$ and $\omega > 0$, respectively. The differential cross-section of Eq. (5.24) is often referred to as the resonance Raman spectral profile $I(\omega)$ or the resonance Raman excitation profile $I(E_a)$.

5.3.1 First-order RRS process in graphene

For the first-order Stokes resonance Raman scattering in the graphene sheet, the matrix element $K_{ea}^{\lambda\lambda}(E_e, E_a)$ in Eq. (5.24) is derived in the third-order time-dependent perturbation theory [87]:

$$K_{ea}^{\lambda\lambda}(E_e, E_a) = \sum_{\nu}^6 \frac{2A}{\sqrt{3} W a^2} \sum_w^W \frac{M_e^{v\lambda c}(\mathbf{k}_w, \mathbf{0}, \mathbf{k}_w) \left(M_e^{c\nu c}(\mathbf{k}_w, \mathbf{0}, \mathbf{k}_w) + M_e^{\nu\nu\nu}(\mathbf{k}_w, \mathbf{0}, \mathbf{k}_w) \right) M_a^{c\lambda\nu}(\mathbf{k}_w, \mathbf{0}, \mathbf{k}_w)}{\left(E_a - E^c(\mathbf{k}_w) + E^v(\mathbf{k}_w) - \hbar\omega^{\nu}(\mathbf{0}) - i\gamma_e \right) \left(E_a - E^c(\mathbf{k}_w) + E^v(\mathbf{k}_w) - i\gamma_e \right)}, \quad (5.25)$$

where the transition matrix elements $M_a^{v\lambda c}(\mathbf{k}_w, \mathbf{0}, \mathbf{k}_w)$ and $M_e^{c\lambda\nu}(\mathbf{k}_w, \mathbf{0}, \mathbf{k}_w)$ from Section 5.1 describe light absorption and emission processes, the transition matrix elements $M_e^{c\nu c}(\mathbf{k}_w, \mathbf{0}, \mathbf{k}_w)$ and $M_e^{\nu\nu\nu}(\mathbf{k}_w, \mathbf{0}, \mathbf{k}_w)$ from Section 5.2 correspond to the phonon emission by an electron and a hole, $E^b(\mathbf{k}_w)$ is the electron energy, $\omega^{\nu}(\mathbf{0})$ is the frequency of the emitted phonon mode, W is the number of the sampling \mathbf{q}_w points in the first Brillouin zone, A is the area of the graphene sheet exposed to light, and γ_e is a broadening factor associated with the finite lifetime τ_e of the intermediate electronic states according to the uncertainty principle, $\gamma_e\tau_e = \frac{1}{2}\hbar$.

The momentum conservation implicit in Eq. (5.25) involves both photons and phonons at the Γ point, $\boldsymbol{\kappa} = \mathbf{0}$ and $\mathbf{q} = \mathbf{0}$, within the dipole approximation introduced in Section 5.1. However, not all of the Γ point phonon modes for the graphene sheet are Raman-active. The Raman-active modes transform as the components of the polarizability tensor. The representation of the second-rank symmetric tensor is decomposed into the sum of irreducible representations $\Gamma_{ten.} = 2A_{1g} + E_{1g} + E_{2g}$ in the point group D_{6h} , according to Table 4.1. By comparing $\Gamma_{ten.}$ with the representation for the molecular vibrations $\Gamma_{m.v.} = A_{2u} + B_{2g} + E_{1u} + E_{2g}$ from Section 4.1, we conclude that the only Raman-active modes in the graphene sheet are the iLO and iTO components of the doubly degenerate E_{2g} phonon at the Γ point, whose normal mode displacements are shown in Figs. 4-2 (d) and (e) [34].

According to the energy conservation accompanying Eq. (5.25), the Raman shift is given by the frequency of the E_{2g} phonon mode, $\omega = \omega^{E_{2g}}(\mathbf{0}) = 1582 \text{ cm}^{-1}$. Hence,

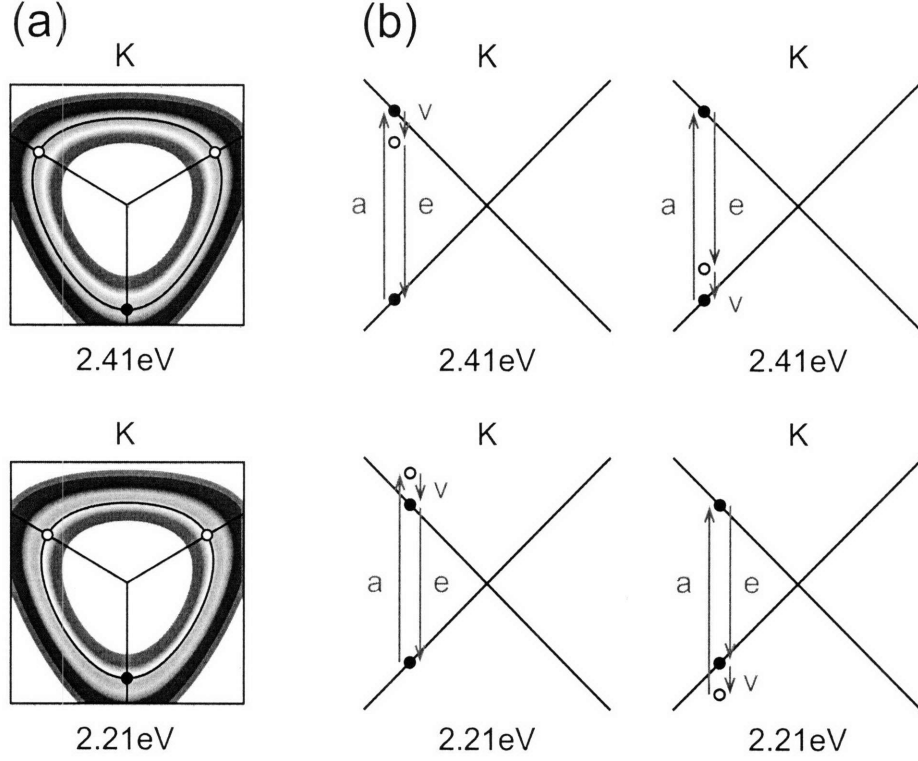


Figure 5-13: The first-order Stokes resonance Raman scattering in the graphene sheet. (a) The contours of constant transition energy around the K point identical to those shown in Fig. 5-11. (b) The schematic of the electronic band structure taken along a vertical cut of (a). Black lines show the valence and conduction bands around the K point. Solid and open dots represent the resonant and virtual electronic states, respectively. Red arrows marked by “a”, “e”, and “v” indicate light absorption, light emission, and phonon emission processes, respectively. The upper and lower traces show the resonance with the incident and scattered light. The left and right traces correspond to electron-phonon and hole-phonon scattering described by terms $M_e^{cvc}(\mathbf{k}_w, \mathbf{0}, \mathbf{k}_w)$ and $M_e^{v\bar{v}v}(\mathbf{k}_w, \mathbf{0}, \mathbf{k}_w)$ in the parentheses in the numerator of Eq. (5.25).

either of the two factors in the denominator of Eq. (5.25) exhibits a resonant enhancement for the electron wavevector \mathbf{k}_w on the contours of constant transition energy resonant with the incident and scattered light, $E^c(\mathbf{k}_w) - E^v(\mathbf{k}_w) = E_a$ and $E^c(\mathbf{k}_w) - E^v(\mathbf{k}_w) = E_e$, while the other factor is non-resonant and represents a virtual electronic state. On the other hand, the electronic states \mathbf{k}_w away from these contours give only a small contribution to the first-order Stokes RRS process in the graphene sheet. For illustration purposes, the contours resonant with $E_a = 2.41$ eV and $E_e = E_a - \hbar\omega^{E_{2g}}(\mathbf{0}) = 2.21$ eV calculated within the ETB framework are shown

in the upper and lower traces of Fig. 5-13 (a). The scattering processes involving electronic states on these contours are depicted in Fig. 5-13 (b), where left and right traces correspond to electron-phonon and hole-phonon scattering represented by two terms in the parentheses in the numerator of Eq. (5.25).

The resonance Raman spectral profile $I(\omega)$ is described by a single Dirac delta function $A\delta(\omega - \omega^{E_{2g}}(\mathbf{0}))$ of the spectral area A , even though many different \mathbf{k}_w states on the contours of constant transition energy contribute to the third-order matrix element $K_{ea}^{\lambda\lambda}(E_e, E_a)$ of Eq. (5.25). Within the Green's function formalism, the anharmonic phonon-phonon scattering introduces the Lorentzian lineshape [72]:

$$I(\omega) = \frac{A}{\pi} \frac{\frac{1}{2} \gamma_p}{\left(\omega - \omega^{E_{2g}}(\mathbf{0})\right)^2 + \frac{1}{4} \gamma_p^2}, \quad (5.26)$$

where γ_p is a broadening factor associated with the finite lifetime τ_p of the phonon modes according to the uncertainty principle, $\gamma_p \tau_p = \frac{1}{2} \hbar$. The first-order Stokes resonance Raman spectral profile of the graphene sheet thus consists of a single Lorentzian peak known as the G -band centered at a frequency of $\omega^{E_{2g}}(\mathbf{0}) = 1582 \text{ cm}^{-1}$ [43, 44].

5.3.2 Second-order RRS process in graphene

For the second-order Stokes-Stokes resonance Raman scattering in the graphene sheet, the matrix element $K_{ea}^{\lambda\lambda}(E_e, E_a)$ in Eq. (5.24) is derived in the fourth-order time-dependent perturbation theory, similar to Eq. (5.25) [87, 161]:

$$K_{ea}^{\lambda\lambda}(E_e, E_a) = \sum_{\nu'}^6 \sum_{\nu}^6 \left(\frac{2A}{\sqrt{3} W a^2} \right)^2 \sum_{w'}^W \sum_w^W \left(\frac{N^{vc}}{D^{vc}} + \frac{N^{cv}}{D^{cv}} \right), \quad (5.27)$$

where subscripts vc and cv indicate a sequence of electron-phonon and hole-phonon scattering events, and numerators N^{vc} and N^{cv} are given by:

$$\begin{cases} N^{vc} = M_e^{v\lambda'c}(\mathbf{k}_{w'}, \mathbf{0}, \mathbf{k}_{w'}) M_e^{v\nu'v}(\mathbf{k}_w, -\mathbf{q}, \mathbf{k}_{w'}) M_e^{c\nu'c}(\mathbf{k}_{w'}, \mathbf{q}, \mathbf{k}_w) M_a^{c\lambda v}(\mathbf{k}_w, \mathbf{0}, \mathbf{k}_w), \\ N^{cv} = M_e^{v\lambda'c}(\mathbf{k}_{w'}, \mathbf{0}, \mathbf{k}_{w'}) M_e^{c\nu'c}(\mathbf{k}_{w'}, \mathbf{q}, \mathbf{k}_w) M_e^{v\nu'v}(\mathbf{k}_w, -\mathbf{q}, \mathbf{k}_{w'}) M_a^{c\lambda v}(\mathbf{k}_w, \mathbf{0}, \mathbf{k}_w), \end{cases} \quad (5.28)$$

and denominators D^{vc} and D^{cv} are written as:

$$\left\{ \begin{array}{l} D^{vc} = \left(E_a - E^c(\mathbf{k}_{w'}) + E^v(\mathbf{k}_{w'}) - \hbar\omega^\nu(\mathbf{q}) - \hbar\omega^{\nu'}(-\mathbf{q}) - i\gamma_e \right) \\ \quad \times \left(E_a - E^c(\mathbf{k}_w) + E^v(\mathbf{k}_w) - \hbar\omega^\nu(\mathbf{q}) - i\gamma_e \right) \\ \quad \times \left(E_a - E^c(\mathbf{k}_w) + E^v(\mathbf{k}_w) - i\gamma_e \right), \\ D^{cv} = \left(E_a - E^c(\mathbf{k}_w) + E^v(\mathbf{k}_w) - \hbar\omega^\nu(-\mathbf{q}) - \hbar\omega^{\nu'}(\mathbf{q}) - i\gamma_e \right) \\ \quad \times \left(E_a - E^c(\mathbf{k}_{w'}) + E^v(\mathbf{k}_{w'}) - \hbar\omega^\nu(-\mathbf{q}) - i\gamma_e \right) \\ \quad \times \left(E_a - E^c(\mathbf{k}_{w'}) + E^v(\mathbf{k}_{w'}) - i\gamma_e \right), \end{array} \right. \quad (5.29)$$

and $\mathbf{q} = \mathbf{k}_w - \mathbf{k}_{w'}$ according to the electron-phonon momentum conservation.

The second-order RRS process involves two phonons with opposite momenta \mathbf{q} and $-\mathbf{q}$ as described by Eqs. (5.28) and (5.29). Hence, the total momentum conservation does not require \mathbf{q} to be zero, in contrast to the first-order RRS process discussed in Section 5.3.1. All phonon modes are thus in principle Raman active in the second-order RRS process, because the direct product of an irreducible representation with itself always contains the totally symmetric irreducible representation A_1 also present in the representation of the second-rank symmetric tensor $\Gamma_{ten.}$ given in Section 5.3.1. However, only a small fraction of these phonon modes is coupled to resonantly photoexcited electrons and holes.

The resonant incident and scattered electron wavevectors \mathbf{k}_w and $\mathbf{k}_{w'}$ in Eqs. (5.28) and (5.29) lie on the contours of constant transition energies $E^c(\mathbf{k}_w) - E^v(\mathbf{k}_w) = E_a$ and $E^c(\mathbf{k}_{w'}) - E^v(\mathbf{k}_{w'}) = E_e$. The contours are separated in energy by the Raman frequency shift $\omega = \omega^\nu(\mathbf{q}) + \omega^{\nu'}(-\mathbf{q})$ or $\omega = \omega^\nu(-\mathbf{q}) + \omega^{\nu'}(\mathbf{q})$ for the two terms in Eq. (5.27), according to the energy conservation. The contours are wrapped either around the same K (K') point or around different K and K' (K' and K) points in the first Brillouin zone of the graphene sheet. The two cases are referred to in Section 5.2 as the intra-valley and inter-valley scattering [132]. The intra-valley and inter-valley scattering involve phonon wavevectors \mathbf{q} and $-\mathbf{q}$ near the Γ point and near the K and K' points, respectively, according to the momentum conservation.

Let us consider the inter-valley scattering of the 514.5 nm laser line by two identical phonon modes $\nu' = \nu = i\text{TO}$. Figure 5-14 (a) shows the resonant incident and

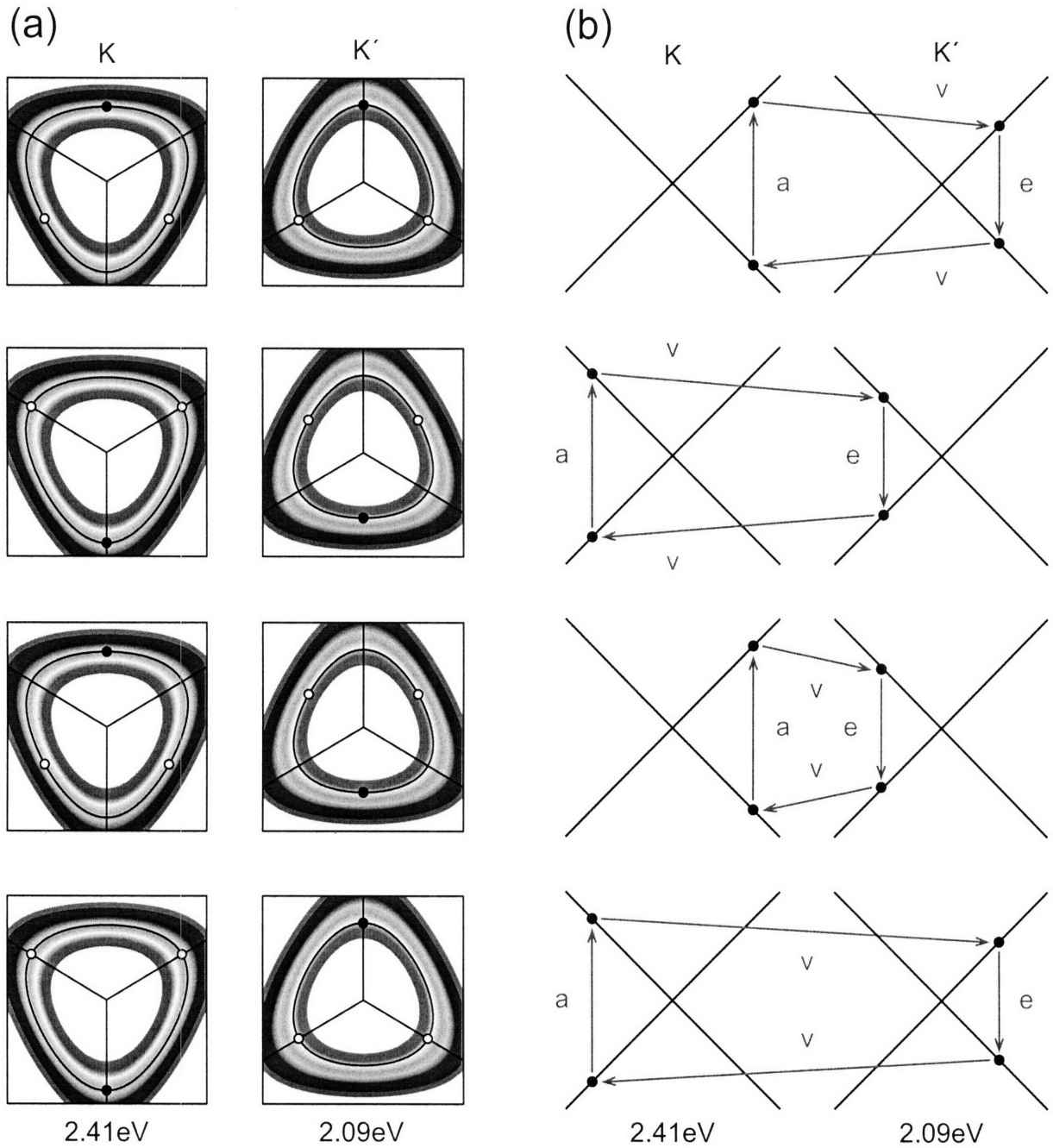


Figure 5-14: The second-order Stokes resonance Raman scattering in the graphene sheet. (a) The contours of constant transition energy around the K and K' points identical to those shown in Fig. 5-11. The schematic of the electronic band structure taken along a vertical cut of (a). Black lines show the valence and conduction bands around the K and K' points. Red arrows marked by “a”, “e”, and “ ν ” indicate light absorption, light emission, and phonon emission processes, respectively. The four traces correspond to different positions of the resonant electronic states shown by solid black dots.

scattered contours $E_a = 2.41$ eV and $E_e = 2.09$ eV replicated from Fig. 5-11 (a). The second-order scattering processes are illustrated in Fig. 5-14 (b), similar to Fig. 5-13 (b) for the first-order scattering processes. The four traces of Fig. 5-13 correspond to the resonant incident and scattered electron wavevectors \mathbf{k}_w and $\mathbf{k}_{w'}$ on the contours around the K and K' points along the high-symmetry directions $K\Gamma$, KM , $K'M$, and $K'\Gamma$. In contrast to the first-order scattering processes that involve virtual electronic states represented by open dots in Fig. 5-13 (b), all intermediate electronic states for the second-order scattering processes shown by solid dots in Fig. 5-14 (b) are resonant, given two identical phonon modes $\nu' = \nu$ and neglecting the asymmetry between the valence and conduction bands. This implies that all three factors in the denominators D^{vc} and D^{cv} given by Eq. (5.29) are resonant. Note that there are other possible second-order scattering channels involving two electron-phonon and two hole-phonon scattering events. These scattering channels would be expressed by terms N^{cc}/D^{cc} and N^{vv}/D^{vv} contributing in Eq. (5.27). However, these terms involve at least one virtual electronic state and therefore negligible compared to terms N^{vc}/D^{vc} and N^{cv}/D^{cv} illustrated in Fig. 5-14 (b).

The resonant incident and scattered electronic states with wavevectors \mathbf{k}_w and $\mathbf{k}_{w'}$ shown in Fig. 5-14 (a) are coupled to each other by phonon modes with wavevectors $\mathbf{q} = \mathbf{k}_w - \mathbf{k}_{w'}$ according to the momentum conservation. Upon subtracting the contours around the K and K' points in the left and right panels of Fig. 5-14 (a), we obtain the manifold of phonon wavevectors \mathbf{q} around the K' point represented by the black curves in Fig. 5-15 (a) [19]. For scaling purposes, the blue box in Fig. 5-15 (a) outlines the area of linear dimensions $K\Gamma/3 = 4\pi/(9a)$ around the K' point in the first Brillouin zone of the graphene sheet similar to Fig. 3-14. The density of phonon states in this manifold is shown in Fig. 5-15 (b) as a function of $q_{K'}$, where $\mathbf{q}_{K'} = \mathbf{q} - \mathbf{K}'$ is the phonon wavevector measured from the central K' point. The phonon wavevectors \mathbf{q} represented by the four vertical red lines in Fig. 5-15 (b), from left to right, or the four red circles in Fig. 5-15 (a), from the inner to the outer, couple together the electronic wavevectors \mathbf{k}_w and $\mathbf{k}_{w'}$ along the high-symmetry directions $K\Gamma$, KM , $K'M$, and $K'\Gamma$ indicated by solid dots in the four traces of Fig. 5-14 (a),

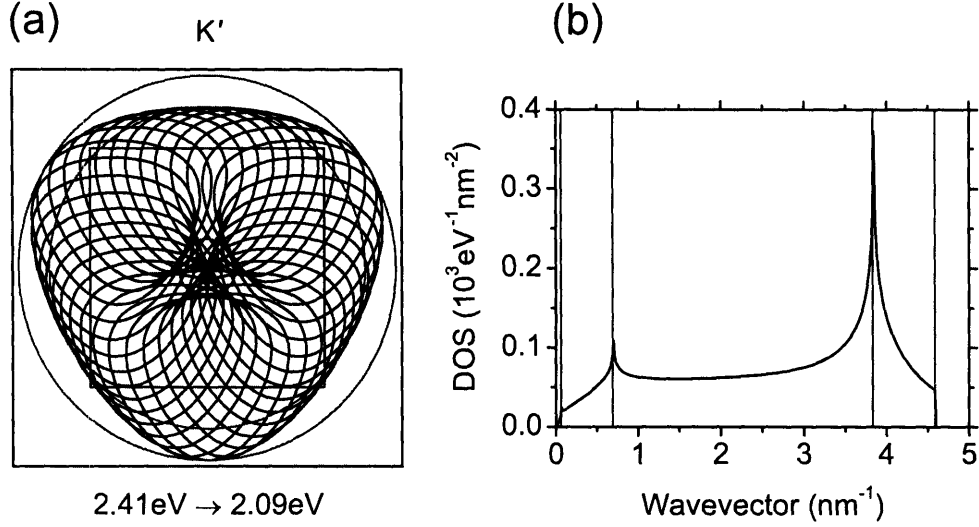


Figure 5-15: (a) The phonon states \mathbf{q} around the K' point that connect the electronic states \mathbf{k}_i and \mathbf{k}_f on the contours around the K and K' points shown in Fig. 5-14 according to the momentum conservation $\mathbf{q} = \mathbf{k}_i - \mathbf{k}_f$. The blue box outlines the area of linear dimensions $K\Gamma/3 = 4\pi/(9a)$ around the K' point in the first Brillouin zone of the graphene sheet similar to Fig. 3-14. The four red circles, from the inner to the outer, correspond to the electronic states in the four traces of Fig. 5-14, from the top to the bottom. (b) The density of phonon states in (a) as a function of the phonon wavevector $\mathbf{q}_{K'} = \mathbf{q} - \mathbf{K}'$ measured from the K' point. The four vertical red lines, from left to right, correspond to the four red circles in (a), from the inner to the outer.

second and third traces of Fig. 5-14 (a) for which either $\mathbf{k}_{w'}$ or both \mathbf{k}_w and $\mathbf{k}_{w'}$ appear at flat portions of the contours give rise to the smaller and larger peaks in the phonon DOS in Fig. 5-15 (b). We refer to these peaks by the phonon wavevectors at which they appear, $q_{K'} \approx 0$ and $q_{K'} \approx k_K + k_{K'}$, where $\mathbf{k}_K = \mathbf{k}_w - \mathbf{K}$ and $\mathbf{k}_{K'} = \mathbf{k}_{w'} - \mathbf{K}'$ are the phonon wavevectors measured from the K and K' points. In a similar fashion, the smaller $q_\Gamma \approx 0$ and larger $q_\Gamma \approx 2k_\Gamma$ peaks appear in the phonon DOS around the Γ point for the intra-valley scattering. While the larger $q \approx 2k$ peaks give rise to the second-order features in the resonance Raman spectrum of the graphene sheet [19], the smaller $q \approx 0$ peaks are suppressed by the negative interference at the Γ , K , and K' points, as shown by analytical integration of Eq. (5.27) [91].

Different phonon modes $\nu', \nu = iTA, iLA, iLO, iTO$ may have different contributions to the second-order resonance Raman spectrum of the graphene sheet because

of the inhomogeneity of the electron-phonon scattering along the contours of constant transition energy illustrated in Figs. 5-11 (b) and 5-12 (b). For the intra-valley scattering process, the light polarized along the armchair direction $\mathbf{P}^\lambda = \hat{\mathbf{x}}$ excites the electronic states with wavevectors near the K point along the $K\Gamma$ and KM directions corresponding to angles $\phi = 90^\circ$ and $\phi = 270^\circ$ in Fig. 5-3 (b). These electronic states are scattered to the vicinity of the K' point in the $K'\Gamma$ and $K'M$ directions, respectively, as shown in the two bottom traces of Fig. 5-14. The scattering processes are mediated by the phonon modes with wavevectors $q_{K'} \approx 2k_K$ whose densities of states are marked by the two rightmost vertical red lines in Fig. 5-15 (b), respectively. The coupling of these phonon modes to the aforementioned electronic states is governed by the matrix elements from Figs. 5-11 (b) and 5-12 (b) at angles $\phi = 270^\circ$ and $\phi = 90^\circ$, respectively. These matrix elements reach their maximum values for the iTO and iLO phonon modes with wavevectors $q_{K'} \approx 2k_K$ along the $K'M$ direction and for the iLA and iTO phonon modes with wavevectors $q_{K'} \approx 2k_K$ along the $K'\Gamma$ direction, respectively, according to Figs. 5-11 (b) and 5-12 (b). Upon increasing the excitation energy E_a , the phonon wavevector $q_{K'} \approx 2k_K$ deviates further away from the K' point, according to the electronic dispersion relations of Eq. (3.14). This deviation is illustrated in Fig. 5-16 (a) which shows the density of phonon states for $E_a = 1.5$, 2.0, and 2.5 eV similar to Fig. 5-15 (b) for $E_a = 2.41$ eV. The peak frequencies of the second-order Raman bands thus show dispersive behavior with changing excitation energy E_a [88, 132, 134, 161].

The inter-valley second-order Stokes-Stokes resonance Raman spectral profile $I(\omega)$ is calculated by numerical integration of Eq. (5.27) on a polar grid with steps in the radial and angular directions $\Delta k_r = 1/(300a)$ and $\Delta k_\phi = 2^\circ$ centered at the K and K' points using the ETB electronic dispersion relations from Section 3.6, the AFC phonon dispersion relations with the ETB force constants from Section 4.3.2, the ETB optical dipole transition matrix element from Section 5.1 with $\mathbf{P}^\lambda = \hat{\mathbf{x}}$, the ETB electron-phonon scattering matrix element from Section 5.2, the broadening factors $\gamma_e = 10$ meV and $\gamma_p = 1$ cm⁻¹ in Eqs. (5.29) and (5.26), and the excitation energies $E_a = 1.5$, 2.0, and 2.5 eV. Note that the Bloch amplitudes $C_{so}^b(\mathbf{k}_w)$ and the normal

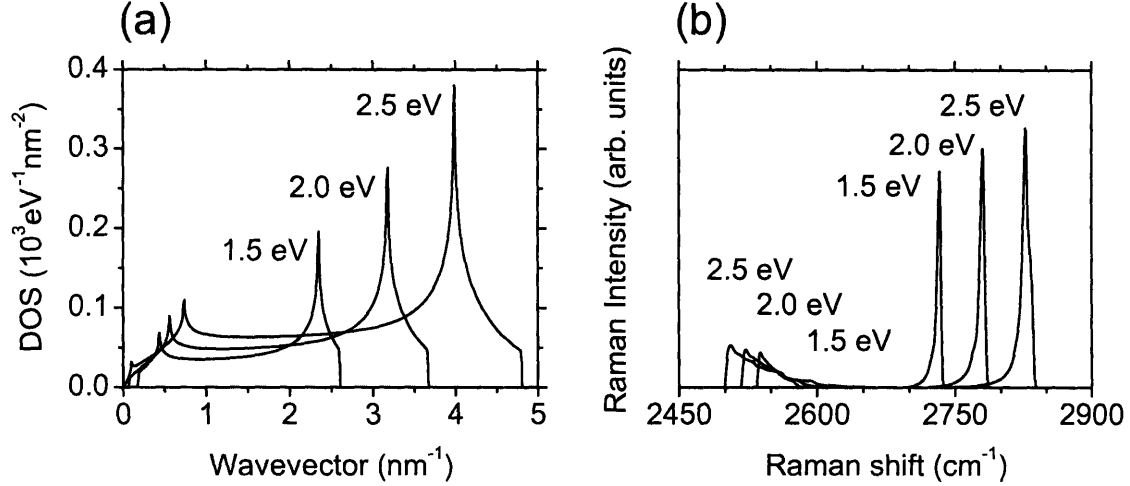


Figure 5-16: (a) The density of phonon states as a function of the phonon wavevector $\mathbf{q}_{\mathbf{K}'} = \mathbf{q} - \mathbf{K}'$ measured from the \mathbf{K}' point at the excitation energy $E_a = 1.5, 2.0,$ and 2.5 eV , similar to the one from Fig. 5-15. (b) The inter-valley second-order Stokes-Stokes resonance Raman spectral profile $I(\omega)$ obtained by numerical integration of Eq. (5.27). The Raman features at 2530 cm^{-1} and 2780 cm^{-1} are known as the G'^- and G' bands, respectively. The frequency dispersions of the Raman shifts ω with E_a are fitted to $\omega^{G'^-} = 2590 \text{ cm}^{-1} - 33E_a \text{ cm}^{-1}/\text{eV}$ and $\omega^{G'} = 2590 \text{ cm}^{-1} + 93E_a \text{ cm}^{-1}/\text{eV}$.

mode displacements $\mathbf{e}_s^{\nu}(\mathbf{q})$ that enter the transition matrix elements have arbitrary phase factors as obtained by diagonalizing the Hamiltonian and dynamical matrices. The interference of the intermediate electronic states contributing to Eq. (5.27) is taken into account by adjusting the phase factors of $C_{so}^b(\mathbf{k}_w)$ and $\mathbf{e}_s^{\nu}(\mathbf{q})$ in accordance with the symmetry requirements. The calculated spectral profiles $I(\omega)$ for $E_a = 1.5, 2.0,$ and 2.5 eV are shown in Fig. 5-16 (b) where the two spectral features near 2500 cm^{-1} and 2700 cm^{-1} are known as the G'^- and G' bands. The G'^- band comes from the combination of the iLA and iTO phonon modes along the $\text{K}\Gamma$ direction, thus clarifying earlier tentative assignments [91, 145, 159], and the G' band comes from the two iTO phonon modes along the KM direction, in accordance with the above discussion. The G' band is associated with the larger peak in the phonon DOS in Fig. 5-15 (b), and the G'^- band with the right shoulder of this peak marked by the rightmost red line in Fig. 5-15 (b), resulting in the relatively low intensity of the G'^- band compared to the G' band. The frequency dispersions of the G'^- and G' bands with E_a in Fig. 5-16 (b) are fitted to $\omega^{G'^-} = 2590 \text{ cm}^{-1} - 33E_a \text{ cm}^{-1}/\text{eV}$ and

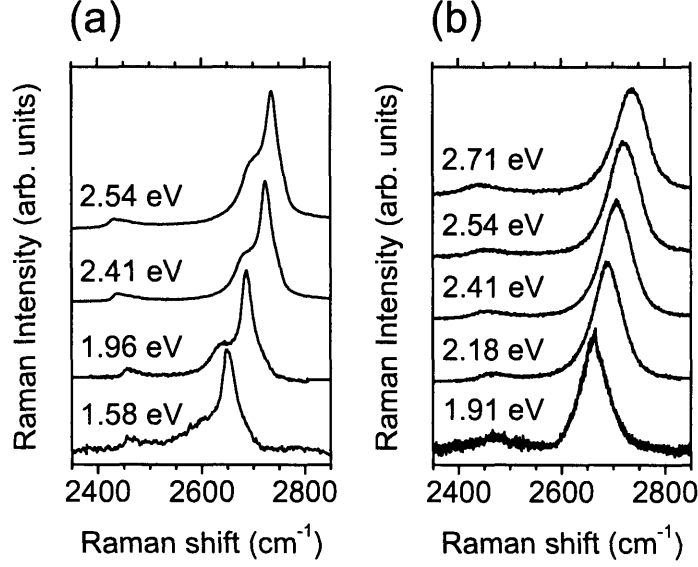


Figure 5-17: The resonance Raman spectral profile measured from (a) highly-oriented pyrolytic graphite (HOPG) and (b) polyparaphenylene (PPP) at different excitation energies E_a . The Raman features around 2450 cm^{-1} and 2700 cm^{-1} are known as the G'^{-} and G' bands, respectively. The frequency dispersions of the Raman shifts ω with E_a for these bands are fitted to the form $\omega^{G'^{-}} = 2510 \text{ cm}^{-1} - 30E_a \text{ cm}^{-1}/\text{eV}$ and $\omega^{G'} = 2510 \text{ cm}^{-1} + 90E_a \text{ cm}^{-1}/\text{eV}$ [31].

$\omega^{G'} = 2590 \text{ cm}^{-1} + 93E_a \text{ cm}^{-1}/\text{eV}$. The other combinations of the phonon modes also contribute to $I(\omega)$. The combination of the two iLA phonon modes appears at much lower ω , the two iLO and the iLO with iT0 phonon modes contribute to the linewidth of the G' -band according to the phonon dispersion relations in Fig. 4-14 (b), whereas the contribution from the other phonon modes is negligible. The linewidth of the larger peak in the phonon DOS in Fig. 5-15 (b) also contributes to the broadening of the G'^{-} and G' bands along with the natural linewidth γ_p of Eq. (5.26). The second-order Raman features thus have non-Lorentzian profiles.

For comparison, we show in Fig. 5-17 the experimental resonance Raman spectral profile $I(\omega)$ measured from highly-oriented pyrolytic graphite (HOPG) and from polyparaphenylene (PPP) at several different excitation energies E_a [31]. The experimental frequency dispersions of the G'^{-} and G' bands with E_a are fitted to the form $\omega^{G'^{-}} = 2510 \text{ cm}^{-1} - 30E_a \text{ cm}^{-1}/\text{eV}$ and $\omega^{G'} = 2510 \text{ cm}^{-1} + 90E_a \text{ cm}^{-1}/\text{eV}$. While the experimental dispersion slope shows good agreement with the results of numerical cal-

calculations shown in Fig. 5-16 (b), the absolute value of the experimental Raman shift is redshifted by 80 cm^{-1} from the theoretical prediction. This redshift can be attributed to the quasiparticle self-energy correction similar to Eq. (3.35) for SWNTs [70] which is not included in the calculation of $I(\omega)$ in Fig. 5-16 (b).

In a similar fashion, the intra-valley second-order Stokes-Stokes resonance Raman scattering can be analyzed. It involves the iLO and iTO phonon modes around the Γ point that give rise to the Raman band around 3200 cm^{-1} [158]. Furthermore, the defect-induced second-order processes take place involving inelastic electron scattering by a phonon and elastic electron scattering by a defect. The inter-valley defect-induced second-order process gives rise to the D band Raman feature associated with the iTO phonon mode at a half frequency of the G' band [88, 132, 134, 158, 161]. On the other hand, the Raman features associated with the intra-valley defect-induced second-order process appear at the same frequency as the first-order G band [89, 90] and therefore can only be observed in highly defective graphitic materials [150, 158]. The matrix element of inelastic electron-defect scattering can be derived from the electron-phonon scattering matrix element using the frozen phonon approach for a given defect type [68]. Alternatively, the type and concentration of defects can be deduced by analyzing the experimental defect-induced second-order resonance Raman spectral profile [18, 20].

5.3.3 The RRS process in nanotubes

The differential cross-sections for the first- and second-order resonance Raman scattering (RRS) processes in SWNTs are obtained from Eqs. (5.24), (5.25), and (5.27) to (5.29) in the single-particle approximation upon substituting Eqs. (2.14) and (4.16) for the 2D electronic \mathbf{k} and phonon \mathbf{q} momenta, replacing $E^b(\mathbf{k})$ and $\omega^\nu(\mathbf{q})$ with the electronic $E^b(\mu, k)$ and phonon $\omega^\nu(\eta, q)$ dispersion relations for SWNTs from Chapters 3 and 4, and calculating the electron-photon and electron-phonon matrix elements from Sections 5.1 and 5.2 for optimized SWNT geometries [55, 120]. The many-body effects are taken into account by adding the quasiparticle self-energies and exciton binding energies, and by including the exciton-photon and exciton-phonon matrix

elements in the above calculation scheme. In what follows, we briefly review the calculations of the resonance Raman spectral $I(\omega)$ and excitation $I(E_a)$ profiles in the single-particle approximation [17, 55, 120], and we discuss significant effects of the many-body interactions on $I(\omega)$ and $I(E_a)$.

For the first-order RRS process, the curvature of the SWNT sidewall gives rise to the RBM mode and splits the double degenerate G -band of the graphene sheet into the G^T and G^L modes or equivalently, into the G^- and G^+ modes, as discussed in Sections 4.4 and 4.5 [67]. The RBM, G^- , and G^+ modes have Lorentzian spectral profiles of Eq. (5.26) except for the G^- mode in metallic SWNTs that softens in frequency and exhibits the Breit-Wigner-Fano (BWF) lineshape:

$$I(\omega) = \frac{A}{\pi} \frac{\frac{1}{2} \gamma_p}{\left(\omega - \omega^{G^-}(0, 0)\right)^2 + \frac{1}{4} \gamma_p^2} \left(1 + \frac{2 \left(\omega - \omega^{G^-}(0, 0)\right)}{q \gamma_p}\right)^2, \quad (5.30)$$

where $1/q$ is the peak asymmetry parameter. The origin of the BWF lineshape, originally attributed to plasmon-phonon coupling [16, 54, 116], was more recently interpreted in terms of the Kohn anomaly arising from electron-phonon coupling in metallic SWNTs, as explained in Section 4.6.

The first-order RRS process in chiral (achiral) SWNTs excites 14 (6) Raman-active phonon modes, including the aforementioned RBM, G^- , and G^+ modes [3, 12]. The RBM, G^- , and G^+ modes, associated with the mode index $\nu = \text{oTA}, \text{iTO}, \text{iLO}$ and the angular $\eta = 0$ and linear $q = 0$ momenta, belong to the irreducible representation A_1 (A_{1g}) of point group D_N (D_{2nh}) for chiral (achiral) SWNTs [3, 12]. The 14 (6) Raman-active modes also include the modes with index $\nu = \text{iTO}, \text{iLO}$ and the angular $\eta = \pm 1, \pm 2$ and linear $q = 0$ momenta that belong to the irreducible representations E_1 and E_2 (E_{1g} and E_{2g}) [3, 12]. The mechanism for the Raman activity of the E_1 and E_2 (E_{1g} and E_{2g}) modes is understood from the dipole selection rules and the vibrational selection rules discussed in Sections 5.1.1 and 5.2.1 [64, 140]. Let us consider transitions between electronic states labeled by the band energies $E^b(\mu, k)$. For light polarized parallel or perpendicular to the SWNT axis, the angular momentum μ

is conserved or changed by ± 1 , according to Section 5.1.1. The A_1 , E_1 , and E_2 (A_{1g} , E_{1g} , and E_{2g}) phonon modes, on the other hand, conserve μ and change it by ± 1 and ± 2 , according to Section 5.2.1. The first-order RRS processes are then classified into five categories for electron-phonon scattering:

$$\begin{aligned}
E^v(\mu, k) &\xrightarrow{\parallel} E^c(\mu, k) \xrightarrow{A_1} E^c(\mu, k) \xrightarrow{\parallel} E^v(\mu, k), \\
E^v(\mu, k) &\xrightarrow{\perp} E^c(\mu \pm 1, k) \xrightarrow{A_1} E^c(\mu \pm 1, k) \xrightarrow{\perp} E^v(\mu, k), \\
E^v(\mu, k) &\xrightarrow{\parallel} E^c(\mu, k) \xrightarrow{E_1} E^c(\mu \pm 1, k) \xrightarrow{\perp} E^v(\mu, k), \\
E^v(\mu, k) &\xrightarrow{\perp} E^c(\mu \pm 1, k) \xrightarrow{E_1} E^c(\mu, k) \xrightarrow{\parallel} E^v(\mu, k), \\
E^v(\mu, k) &\xrightarrow{\perp} E^c(\mu \pm 1, k) \xrightarrow{E_2} E^c(\mu \mp 1, k) \xrightarrow{\perp} E^v(\mu, k),
\end{aligned} \tag{5.31}$$

and five analogous categories for hole-phonon scattering, where \parallel and \perp stand for light polarized parallel and perpendicular to the SWNT axis. Equation (5.31) implies that the A_1 , E_1 , and E_2 (A_{1g} , E_{1g} , and E_{2g}) phonon modes have a different dependence on the relative polarizations of the incident and scattered light with respect to the SWNT axis. Indeed, polarization Raman studies of individual semiconducting SWNTs reveal six Lorentzian peaks in the G -band frequency range [64].

The second-order RRS process in SWNTs is similar to that in the graphene sheet in the sense that all phonon modes become Raman-active but only the most intense second-order features are observed experimentally including those overlapping with the first-order G -band [89, 90, 150], the second-order D - and G' -bands [152, 154], and the intermediate frequency modes (IFMs) [40, 41]. What differs, however, is the excitation profile $I(E_a)$ for both first- and second-order RRS processes in SWNTs compared to $I(E_a)$ in the graphene sheet. The excitation profile $I(E_a)$ is determined by the joint density of electronic states (JDOS) and thus $I(E_a)$ of the graphene sheet has a monotonic dependence on E_a while $I(E_a)$ of SWNTs has a resonant dependence on E_a . The excitation profile $I(E_a)$ exhibits resonances at each Van Hove singularity (VHS) in the JDOS for parallel or perpendicular polarization of light with respect to the SWNT axis, E_{ii} or $E_{\mu, \mu \pm 1}$, for both incident and scattered light, E_a and $E_e = E_a - \hbar\omega$. In particular, different processes in Eq. (5.31) appear at distinct resonances in $I(E_a)$. The resonant magnitude of $I(E_a)$ is sufficiently

high to allow observation of the RRS signal from individual SWNTs disposed on a Si/SiO₂ substrate, implying that the Raman bands of the SWNT and those of Si have comparable intensities, even though the ratio of the number of C atoms to the number of Si atoms contributing to the RRS process is on the order of 10⁻⁶ [65]. Comparing the magnitudes of the resonances in $I(E_a)$ with the experimental RRS excitation-emission density map as the one shown in Fig. 3-17 yields the relative distribution of (n, m) SWNTs in the sample [55, 120]. In general, the resonances in $I(E_a)$ may have different widths or shapes depending on the relative values of the electron finite lifetime broadening factor γ_e , the Raman shift $\hbar\omega$, and the energy difference $E_{i+1, i+1} - E_{ii}$ between adjacent VHSs [17, 55]. For the G -band in armchair-like metallic SWNTs $E_{ii}^{\text{MH}} - E_{ii}^{\text{ML}} < \hbar\omega$ and the higher energy resonance $E_a = E_{ii}^{\text{MH}}$ in $I(E_a)$ is suppressed by the negative interference with the lower energy resonance $E_a = E_{ii}^{\text{ML}}$ [17, 55]. The higher energy resonance $E_a = E_{11}^{\text{MH}}$ in $I(E_a)$ is thus absent in the experimental Kataura plot of Fig. 3-17 and has been observed only for a few selected M SWNTs [149].

Previous calculations of the resonance Raman spectral $I(\omega)$ and excitation $I(E_a)$ profiles in SWNTs have been performed in the single-particle approximation neglecting many-body effects [17, 55, 120]. Meanwhile, many-body interactions significantly affect the electronic transition energies and the optical dipole transition and electron-phonon scattering matrix elements, as shown in Sections 3.7, 5.1, and 5.2, respectively. For light polarized parallel to the SWNT axis, the lowest energy bright excitonic states are blueshifted by about 200—300 meV from the single-particle transition energies E_{ii} , according to Section 3.7. For light polarized perpendicular to the SWNT axis, the excitonic states are much further blueshifted and are significantly less suppressed by the depolarization effect than the single-particle $E_{\mu, \mu\pm 1}$ values. The optical dipole transition matrix elements between the excitonic wavefunctions show a quantitatively different dependence on the SWNT chiral angle than the matrix elements between the single-particle wavefunctions [59]. The exciton-phonon scattering matrix elements, on the other hand, have values close to the electron-phonon scattering matrix elements [59]. The $I(\omega)$ and $I(E_a)$ profiles calculated in the excitonic picture are thus

expected to show quantitative differences from the previously reported single-particle profiles [17, 55, 120]. Such calculations will be the subject of future work.

5.4 Band gap photoluminescence

The resonance Raman process in graphene sheets and in SWNTs is a light scattering phenomenon involving virtual intermediate states, as described in Section 5.3. The scattered photon is thus coherent with the incident photon. On the other hand, the band gap photoluminescence in semiconducting SWNTs is related to a light absorption process. The photoexcited charge carriers relax through real intermediate states to the band edge, scattered between themselves or with phonons. The carriers then recombine radiatively at the band edge by interband spontaneous emission. The emitted photon is therefore incoherent with the incident photon, contrary to the resonance Raman scattering. Accordingly, the two processes differ substantially in time scale. The resonance Raman scattering involves a virtual state whose lifetime does not exceed a few tens of femtoseconds, according to Heisenberg's Uncertainty Principle. For the band gap photoluminescence, the relaxation to the band edge requires time on the order of picoseconds, while the radiative interband recombination takes about a nanosecond.

The band gap photoluminescence in semiconducting SWNTs is experimentally observed in the frequency domain [8, 95] or in the time domain [76, 77, 166] from SWNT samples dispersed in a surfactant solution and excited with the light of a lamp or a pulsed laser. The frequency domain studies are commonly summarized in the form of an excitation-emission density map such as the one shown in Fig. 3-16 of Section 3.6. The bright spots in the excitation-emission density map correspond to the excitonic transitions E_{ii} and to the phonon-assisted sidebands [26, 52, 81, 118] in different (n, m) SWNTs, though the exact mechanism of the sideband formation is still questionable [25, 96, 114]. Time-resolved studies reveal multiple fast and slow relaxation processes on the time scale from hundreds of femtoseconds to tens of picoseconds associated with nonradiative exciton-exciton and exciton-phonon scattering pathways

in semiconducting SWNTs whose precise assignment is not certain [25, 49, 51, 84]. Because of the fast nonradiative relaxation channels and the dark excitonic states, the band gap photoluminescence has a quantum efficiency less than 10^{-3} [62].

The band gap photoluminescence intensities and relaxation lifetimes in semiconducting SWNTs have been calculated in the single-particle approximation [56, 108]. The relaxation lifetime is obtained as an inverse of the electron-phonon relaxation rate given by the products of the electron-phonon scattering rates defined by Eq. (5.14) for different electron relaxation channels [56]. The calculated lifetimes show qualitative agreement with time-resolved measurements, though a more detailed theoretical analysis of competitive electron relaxation pathways may improve the results of calculations [56]. The photoluminescence intensity is given by the product of the optical absorption rate of Eq. (5.3), the aforementioned electron-phonon relaxation rate, and the optical emission rate of Eq. (5.3) [108]. The calculations indicate that the smaller diameter armchair-like S1 SWNTs have higher photoluminescence intensities, implying that the experimental PL excitation-emission density map does not reflect the relative distribution of (n, m) SWNTs in the sample [108]. The latter distribution is given by the ratio of the measured to calculated photoluminescence intensities, limited by the experimental resolution and more importantly by the accuracy of the calculation of the electron-phonon relaxation rate [108].

Previous calculations of the band gap photoluminescence intensities and relaxation lifetimes in semiconducting SWNTs are performed in the single-particle approximation ignoring many-body interactions [56, 108]. Meanwhile, many-body interactions have a considerable effect on the optical dipole transition and electron-phonon scattering matrix elements, as discussed in Section 5.3.3 with respect to resonance Raman scattering calculations in SWNTs. Furthermore, the electron-phonon relaxation rate depends crucially on the selection of competitive electron relaxation pathways that complicates the numerical calculation. Given the exciton-photon and exciton-phonon transition matrix elements [59], the band gap photoluminescence intensities and relaxation lifetimes in semiconducting SWNTs can now be calculated in the excitonic picture. Such calculations will be the subject of future work.

5.5 Concluding remarks and future directions

We report calculations of the electron-photon and electron-phonon transition matrix elements in the graphene sheet and SWNTs within the ETB framework introduced in Chapter 3. Using the transition matrix elements, we calculate the resonance Raman spectra of the graphene sheet in the framework of the free electron model. The results of our calculations show good agreement with the resonance Raman spectral profiles measured from different graphitic materials at various excitation energies, clarifying the origin of the G'^- feature, which was not clear from the previous theoretical and experimental studies. Such an assignment is imperative for the purpose of sample characterization by resonance Raman spectroscopy, as well as for a better understanding of the electronic relaxation processes in the graphene sheet and SWNTs.

We review recent calculations of the resonance Raman scattering and band gap photoluminescence in SWNTs performed in the single-particle approximation. The optical and relaxation properties in SWNTs, however, are governed by excitonic effects, and the free electron model fails to quantitatively reproduce the relative intensities of the spectral features observed in experiments. The exciton-photon and exciton-phonon transition matrix elements are calculated upon substituting the excitonic wavefunctions obtained within the ETB framework into Eqs. (5.1) and (5.13) [59]. Future calculations of the resonance Raman scattering and band gap photoluminescence involving the exciton-photon and exciton-phonon transition matrix elements are expected to provide better agreement with the results of experimental observations. Also, the electron-defect and exciton-defect elastic scattering matrix elements can be calculated for different types of structural defects using the frozen phonon approach [68]. This will allow quantitative characterization of structural defects in the graphene sheet and SWNTs using resonance Raman spectroscopy. Finally, the phonon-phonon scattering matrix elements need to be calculated for evaluation of the thermal conductivity in the graphene sheet and in SWNTs, as discussed in Section 4.6.2.

Chapter 6

Conclusions

This thesis reviews recent advances made in optical studies of single-wall carbon nanotubes (SWNTs). Various optical techniques such as absorption spectroscopy, infrared spectroscopy, resonance Raman spectroscopy, and band gap photoluminescence provide a quick, accurate, contactless, non-destructive probe for electronic and vibrational properties of SWNTs under ambient conditions. Optical spectra of large diameter SWNTs prepared by conventional synthesis techniques such as arc discharge and laser ablation are well understood using the zone-folded electron and phonon dispersion relations of the graphene sheet, neglecting the curvature of the SWNT sidewall. However, recent progress with novel synthesis techniques such as high pressure CO decomposition (HiPCO) and chemical vapor deposition (CVD) revealed drastic changes in the optical spectra of small diameter SWNTs. This thesis exploits the connection of these changes with the curvature of the SWNT sidewall.

The excitation-emission density maps obtained by resonance Raman spectroscopy and band gap photoluminescence show bright spots corresponding to the E_{ii} energies of different electronic transitions in individual (n, m) SWNTs. The E_{ii} transition energies corresponding to small diameter SWNTs of constant $2n + m$ form family patterns in the excitation-emission density maps. The family patterns cannot be explained within the zone-folding approximation and are tentatively attributed to the effects of curvature of the SWNT sidewall. In this thesis, we develop the extended tight-binding (ETB) model that takes into account the long-range atomic interactions

and the rehybridization of the σ and π molecular orbitals, which are irrelevant in the flat graphene sheet but play an increasingly important role as the SWNT diameter decreases. We optimize geometrical structures of different (n, m) SWNTs and calculate the E_{ii} transition energies within the framework of the ETB model. The calculated E_{ii} values accurately reproduce the family patterns in the excitation-emission density maps, except for the overall blueshift of the experimental families. The family patterns are thus attributed primarily to the geometrical structure relaxation caused by the curvature of the SWNT sidewall. The overall blueshift of the experimental family patterns from the ETB values is associated with the many-body interactions including the band gap renormalization and the excitonic binding of the photoexcited charge carriers.

Since the ETB model has been proven to accurately describe the electronic transitions in small diameter SWNTs, we employ it to study the vibrational properties and the transition matrix elements relevant to optical spectroscopy of SWNTs. The force constants for the graphene sheet and SWNTs are calculated within the ETB framework, and the resulting phonon dispersion relations show good agreement with the phonon frequencies measured by spectroscopic techniques. In particular, the ETB calculations closely fit the linear Kohn anomalies in the graphene sheet observed experimentally and obtained from first-principles calculations, though the ETB calculations fail to describe the much sharper Kohn anomalies in metallic SWNTs due to the intrinsic limitations of the force constant approach. We therefore implement the supercell method and the linear response method for direct calculation of the dynamical matrix without involving the force constant approximation. Such calculated phonon dispersion relations accurately reproduce the logarithmic Kohn anomalies predicted by the first-principles calculations for truly metallic armchair SWNTs and accurately reproduce the linear Kohn anomalies observed experimentally from the mini band gap semiconducting chiral and zigzag SWNTs. This once again proves the strong merit of the ETB model for SWNT studies in spite of its relative simplicity.

The resonant energies and the frequency shifts observed by spectroscopic techniques from SWNT samples are well fitted by the results of the ETB calculations.

However, studies of the spectroscopic intensities within perturbation theory requires knowledge of the transition matrix elements. The optical dipole transition and electron-phonon scattering matrix elements are calculated for the graphene sheet and for SWNTs within the ETB framework. The resonance Raman scattering from the graphene sheet is then calculated in the single-particle approximation with the help of these matrix elements. The calculated resonance Raman spectra show quantitative agreement with experimental measurements from different graphitic samples. Our calculations thus clarify the origin of the previously unassigned G'^- feature. On the other hand, photoluminescence and resonance Raman intensities for SWNTs calculated within the ETB framework in the single-particle approximation only show qualitative agreement with experimental results. This implies the importance of many-body effects in SWNTs which, because of their 1D nature, enhance the Coulomb interaction.

There have been several major breakthroughs over the last few years in the field of optical spectroscopy of SWNTs, including the ones described in this thesis. The ETB model has proven to accurately describe the electronic, vibrational, and structural properties of smaller diameter SWNTs. The more we learn, however, the more unanswered questions appear in the field. Below we suggest a few possible directions for future research, such as revision of the geometrical structure optimization procedures for chiral SWNTs, investigation of many-body corrections and quasiparticle and excitonic effects, calculation of photoluminescence and resonance Raman intensities within the excitonic picture, quantitative analysis of specific structural defects in SWNT samples, and anharmonic effects responsible for the thermal conductivity in the graphene sheet and SWNTs.

The optimization of geometrical structures in this thesis has been performed maintaining the translational symmetry of SWNTs. Meanwhile, chiral SWNTs do not exhibit the C_2 rotation axes nor the σ_h mirror planes and therefore can break the translational symmetry. The geometrical structures of chiral SWNTs thus should be optimized over the torsional angle associated with the helical symmetry of chiral SWNTs. Such an optimization will be the subject of future work, and it will provide

more insight into the structural properties of chiral SWNTs and the single-particle E_{ii} transition energies. Many-body corrections to the single-particle E_{ii} transition energies also have to be studied more systematically, including their dependence on temperature, doping, mechanical strain, hydrostatic pressure, and the dielectric properties of the SWNT environment, from both experimental and theoretical points of view.

Upon constructing the excitonic wavefunctions within the framework of the ETB model, the exciton-photon and exciton-phonon transition matrix elements are assembled from the electron-photon and electron-phonon transition matrix elements. Photoluminescence and resonance Raman intensities should then be calculated using the excitonic transition matrix elements. Such calculations are expected to give a quantitative agreement with experimental spectra. For quantitative studies of the structural defects in SWNT samples, the electron-defect and exciton-defect elastic scattering matrix elements must be calculated. Within the frozen phonon approximation, a structural defect is represented as a linear superposition of phonon modes and the elastic scattering matrix elements are obtained upon summing the electron-phonon and exciton-phonon matrix elements with appropriate weights. This approach has an important potential application of identifying the structural defects in the graphene sheet and in SWNTs by their spectroscopic signatures. Finally, the phonon-phonon scattering matrix elements must be calculated similarly to the aforementioned electron-photon and electron-phonon transition matrix elements. The anharmonic effects and thermal conductivity in the graphene sheet and in SWNTs can then be studied in a more systematic way. Our preliminary analysis indicates that the highest-frequency phonon mode at the K point associated with the Kohn anomaly exhibits a strong anharmonic behavior and therefore plays an important role in determining the thermal conductivity of the graphene sheet and in SWNTs.

Bibliography

- [1] H. Ajiki and T. Ando. Electronic states of carbon nanotubes. *J. Phys. Soc. Jpn.*, 62:1255, 1993.
- [2] H. Ajiki and T. Ando. Aharonov-bohm effect in carbon nanotubes. *Physica B*, 201:349, 1994.
- [3] O. E. Alon. From spatial symmetry to vibrational spectroscopy of single-walled nanotubes. *J. Phys. Cond. Mat.*, 15:S2489, 2003.
- [4] T. Ando. Excitons in carbon nanotubes. *J. Phys. Soc. Jpn.*, 66:1066, 1997.
- [5] P. T. Araujo, S. K. Doorn, S. Maruyama, H. Chacham, M. A. Pimenta, and A. Jorio. Anomalous scaling and a new ratio problem in the optics of carbon nanotubes. (*unpublished*).
- [6] G. B. Arfken and H. J. Weber. *Mathematical methods for physicists*. Academic Press, 1995.
- [7] M. S. Arnold, S. Lan, S. C. Cruz, J. E. Sharping, S. I. Stupp, P. Kumar, and M. C. Hersam. Optical absorption and transient photobleaching in solutions of surfactant encapsulated and dna wrapped single-walled carbon nanotubes. In M. Razeghi and G. J. Brown, editors, *Quantum sensing and nanophotonic devices*, number 5359 in Proc. of SPIE, page 376, Bellingham, WA, 2004. SPIE, SPIE Press.

- [8] S. M. Bachilo, M. S. Strano, C. Kittrell, R. H. Hauge, R. E. Smalley, and R. B. Weisman. Structure-assigned optical spectra of single-walled carbon nanotubes. *Science*, 298:2361, 2002.
- [9] R. Barnett, E. Demler, and E. Kaxiras. Electron-phonon interaction in ultrasmall-radius carbon nanotubes. *Phys. Rev. B*, 71:035429, 2005.
- [10] S. Baroni, S. de Gironcoli, A. Dal Corso, and P. Giannozzi. Phonons and related crystal properties from density-functional perturbation theory. *Rev. Mod. Phys.*, 73:515, 2001.
- [11] E. B. Barros, R. B. Capaz, A. Jorio, G. G. Samsonidze, A. G. Souza Filho, S. Ismail-Beigi, C. D. Spataru, S. G. Louie, G. Dresselhaus, and M. S. Dresselhaus. Selection rules for one- and two-photon absorption by excitons in carbon nanotubes. *Phys. Rev. B*, 73:241406, 2006.
- [12] E. B. Barros, A. Jorio, G. G. Samsonidze, R. B. Capaz, A. G. Souza Filho, J. Mendez Filho, G. Dresselhaus, and M. S. Dresselhaus. Review on the symmetry-related properties of carbon nanotubes. *Physics Reports*, 431:261, 2006.
- [13] K.-P. Bohnen, R. Heid, H. J. Liu, and C. T. Chan. Lattice dynamics and electron-phonon interaction in (3, 3) carbon nanotubes. *Phys. Rev. Lett.*, 93:245501, 2004.
- [14] I. Božović, N. Božović, and M. Damnjanović. Optical dichroism in nanotubes. *Phys. Rev. B*, 62:6971, 2000.
- [15] M. J. Bronikowski, P. A. Willis, D. T. Colbert, K. A. Smith, and R. E. Smalley. Gas-phase production of carbon single-walled nanotubes from carbon monoxide via the hipco process: A parametric study. *J. Vacuum Sci. Technol. A*, 19:1800, 2001.

- [16] S. D. M. Brown, A. Jorio, P. Corio, M. S. Dresselhaus, G. Dresselhaus, R. Saito, and K. Kneipp. Origin of the breit-wigner-fano lineshape of the tangential g -band feature of metallic carbon nanotubes. *Phys. Rev. B*, 63:155414, 2001.
- [17] G. Bussi, J. Menendez, J. Ren, M. Canonico, and E. Molinari. Quantum interferences in the raman cross section for the radial breathing mode in metallic carbon nanotubes. *Phys. Rev. B*, 71:041404, 2005.
- [18] L. G. Cançado, M. A. Pimenta, B. R. A. Neves, M. S. S. Dantas, and A. Jorio. Influence of the atomic structure on the raman spectra of graphite edges. *Phys. Rev. Lett.*, 93:247401, 2004.
- [19] L. G. Cançado, M. A. Pimenta, R. Saito, A. Jorio, L. O. Ladeira, A. Grüneis, A. G. Souza Filho, G. Dresselhaus, and M. S. Dresselhaus. Stokes and anti-stokes double resonance raman scattering in two-dimensional graphite. *Phys. Rev. B*, 66:035415, 2002.
- [20] L. G. Cançado, K. Takai, T. Enoki, M. Endo, Y. A. Kim, H. Mizusaki, A. Jorio, L. N. Coelho, R. Magalhães-Paniago, and M. A. Pimenta. General equation for the determination of the crystallite size l_a of nanographite by raman spectroscopy. *Appl. Phys. Lett.*, 88:163106, 2006.
- [21] R. B. Capaz, C. D. Spataru, S. Ismail-Beigi, and S. G. Louie. Diameter and chirality dependence of exciton properties in carbon nanotubes. *arXiv:cond-mat/0606474*.
- [22] R. B. Capaz, C. D. Spataru, P. Tangney, M. L. Cohen, and S. G. Louie. Hydrostatic pressure effects on the structural and electronic properties of carbon nanotubes. *Phys. Stat. Sol. B*, 214:3352, 2004.
- [23] R. B. Capaz, C. D. Spataru, P. Tangney, M. L. Cohen, and S. G. Louie. Temperature dependence of the band gap of semiconducting carbon nanotubes. *Phys. Rev. Lett.*, 94:036801, 2005.

- [24] E. Chang, G. Bussi, A. Ruini, and E. Molinari. Excitons in carbon nanotubes: an ab initio symmetry-based approach. *Physical Review Letters*, 92:196401, 2004.
- [25] S. G. Chou, M. F. DeCamp, J. Jiang, G. G. Samsonidze, E. B. Barros, F. Plentz, A. Jorio, M. Zheng, G. B. Onoa, E. D. Semke, A. Tokmakoff, R. Saito, G. Dresselhaus, and M. S. Dresselhaus. Phonon-assisted exciton relaxation dynamics for a (6, 5)-enriched dna-wrapped single-walled carbon nanotube sample. *Phys. Rev. B*, 72:195415, 2005.
- [26] S. G. Chou, F. Plentz, J. Jiang, R. Saito, D. Nezich, H. B. Ribeiro, A. Jorio, M. A. Pimenta, G. G. Samsonidze, A. P. Santos, M. Zheng, G. B. Onoa, E. D. Semke, G. Dresselhaus, and M. S. Dresselhaus. Phonon-assisted excitonic recombination channels observed in dna-wrapped carbon nanotubes using photoluminescence spectroscopy. *Phys. Rev. Lett.*, 94:127402, 2005.
- [27] D. Connétable, G.-M. Rignanese, J.-C. Charlier, and X. Blase. Room temperature peierls distortion in small diameter nanotubes. *Phys. Rev. Lett.*, 94:015503, 2005.
- [28] P. Corio, P. S. Santos, V. W. Brar, G. G. Samsonidze, S. G. Chou, and M. S. Dresselhaus. Potential dependent surface raman spectroscopy of single-wall carbon nanotube films on platinum electrodes. *Chem. Phys. Lett.*, 370:675, 2003.
- [29] S. B. Cronin, A. K. Swan, M. S. Ünlü, B. B. Goldberg, M. S. Dresselhaus, and M. Tinkham. Resonant raman spectroscopy on individual metallic and semiconducting single-wall carbon nanotubes under uniaxial strain. *Phys. Rev. B*, 72:035425, 2005.
- [30] S. B. Cronin, Y. Yin, A. Walsh, Rodrigo B. Capaz, A. Stolyarov, P. Tangney, Marvin L. Cohen, Steven G. Louie, A. K. Swan, M. S. Ünlü, B. B. Goldberg, and M. Tinkham. Temperature dependence of the optical transition energies of

- carbon nanotubes: the role of electron-phonon coupling and thermal expansion. *Phys. Rev. Lett.*, 96:127403, 2006.
- [31] L. G. Cançado D. Mafra, A. Jorio, and M. A. Pimenta. (*unpublished*).
- [32] M. Damnjanović, T. Vuković, and I. Milošević. Modified group projectors: tight-binding method. *J. Phys. A: Math. Gen.*, 33:6561, 2000.
- [33] S. Dittmer, J. Svensson, and E. E. B. Campbell. Electric field aligned growth of single-walled carbon nanotubes. *Curr. Appl. Phys.*, 4:595, 2004.
- [34] M. S. Dresselhaus, G. Dresselhaus, and A. Jorio. *Group theory: application to the physics of condensed matter*. Springer, 2006.
- [35] M. S. Dresselhaus, G. Dresselhaus, R. Saito, and A. Jorio. Exciton photophysics of carbon nanotubes. In (*unpublished*).
- [36] M. S. Dresselhaus, G. Dresselhaus, R. Saito, and A. Jorio. Raman spectroscopy of carbon nanotubes. *Phys. Rep.*, 409:47, 2005.
- [37] O. Dubay and G. Kresse. Accurate density functional calculations for the phonon dispersion relations of graphite layer and carbon nanotubes. *Phys. Rev. B*, 67:035401, 2003.
- [38] O. Dubay, G. Kresse, and H. Kuzmany. Accurate density functional calculations for the phonon dispersion relations of graphite layer and carbon nanotubes. *Phys. Rev. Lett.*, 88:235506, 2002.
- [39] G. S. Duesberg, I. Loa, M. Burghard, K. Syassen, and S. Roth. Polarized raman spectroscopy on isolated single-wall carbon nanotubes. *Phys. Rev. Lett.*, 85:5436, 2000.
- [40] C. Fantini, A. Jorio, M. Souza, L. O. Ladeira, A. G. Souza Filho, R. Saito, G. G. Samsonidze, G. Dresselhaus, M. S. Dresselhaus, and M. A. Pimenta. One-dimensional character of combination modes in the resonance raman scattering of carbon nanotubes. *Phys. Rev. Lett.*, 93:087401, 2004.

- [41] C. Fantini, A. Jorio, M. Souza, R. Saito, G. G. Samsonidze, M. S. Dresselhaus, and M. A. Pimenta. Steplike dispersion of the intermediate-frequency raman modes in semiconducting and metallic carbon nanotubes. *Phys. Rev. B*, 72:085446, 2005.
- [42] C. Fantini, A. Jorio, M. Souza, M. S. Strano, M. S. Dresselhaus, and M. A. Pimenta. Optical transition energies for carbon nanotubes from resonant raman spectroscopy: environment and temperature effects. *Phys. Rev. Lett.*, 93:147406, 2004.
- [43] A. C. Ferrari, J. C. Meyer, V. Scardaci, C. Casiraghi, M. Lazzeri, F. Mauri, S. Piscanec, D. Jiang, K. S. Novoselov, S. Roth, and A. K. Geim. The raman fingerprint of graphene. *arXiv:cond-mat/0606284*.
- [44] D. Graf, F. Molitor, K. Ensslin, C. Stampfer, A. Jungen, C. Hierold, and L. Wirtz. Spatially resolved raman spectroscopy of single- and few-layer graphene. *arXiv:cond-mat/0607562*.
- [45] A. Grüneis. *Resonance Raman spectroscopy of single-wall carbon nanotubes*. PhD dissertation, Tohoku University, Department of Physics, September 2004.
- [46] A. Grüneis, R. Saito, J. Jiang, G. G. Samsonidze, M. A. Pimenta, A. Jorio, A. G. Souza Filho, G. Dresselhaus, and M. S. Dresselhaus. Resonant raman spectra of carbon nanotube bundles observed by perpendicularly polarized light. *Chem. Phys. Lett.*, 387:301, 2004.
- [47] A. Grüneis, R. Saito, T. Kimura, L. G. Cançado, M. A. Pimenta, A. Jorio, A. G. Souza Filho, G. Dresselhaus, and M. S. Dresselhaus. Determination of two-dimensional phonon dispersion relation of graphite by raman spectroscopy. *Phys. Rev. B*, 65:155405, 2002.
- [48] A. Grüneis, R. Saito, G. G. Samsonidze, T. Kimura, M. A. Pimenta, A. Jorio, A. G. Souza Filho, G. Dresselhaus, and M. S. Dresselhaus. Inhomogeneous

- optical absorption around the k point in graphite and carbon nanotubes. *Phys. Rev. B*, 67:165402, 2003.
- [49] A. Hagen, M. Steiner, M. B. Raschke, C. Lienau, T. Hertel, H. Qian, A. J. Meixner, and A. Hartschuh. Exponential decay lifetimes of excitons in individual single-walled carbon nanotubes. *Phys. Rev. Lett.*, 95:197401, 2005.
- [50] N. Hamada, S. Sawada, and A. Oshiyama. New one-dimensional conductors: graphitic microtubules. *Phys. Rev. Lett.*, 68:1579, 1992.
- [51] T. Hertel, Z. Zhu, J. Crochet, C. McPheeters, H. Ulbricht, and D. Resasco. Exciton dynamics probed in carbon nanotube suspensions with narrow diameter distribution. *Phys. Stat. Sol. B*, 243:3186, 2006.
- [52] H. Htoon, M. J. O’Connell, S. K. Doorn, and V. I. Klimov. Single carbon nanotubes probed by photoluminescence excitation spectroscopy: the role of phonon-assisted transitions. *Phys. Rev. Lett.*, 94:127403, 2005.
- [53] A. Ismach, D. Kantorovich, and E. Joselevich. Carbon nanotube graphoepitaxy: highly oriented growth by faceted nanosteps. *J. Am. Chem. Soc.*, 127:11554, 2005.
- [54] C. Jiang, K. Kempa, J. Zhao, U. Schlecht, U. Kolb, T. Basché, M. Burghard, and A. Mews. Strong enhancement of the breit-wigner-fano raman line in carbon nanotube bundles caused by plasmon band formation. *Phys. Rev. B*, 66:161404, 2002.
- [55] J. Jiang, R. Saito, A. Grüneis, S. G. Chou, G. G. Samsonidze, A. Jorio, G. Dresselhaus, and M. S. Dresselhaus. Intensity of the resonance raman excitation spectra of single-wall carbon nanotubes. *Phys. Rev. B*, 71:205420, 2005.
- [56] J. Jiang, R. Saito, A. Grüneis, S. G. Chou, G. G. Samsonidze, A. Jorio, G. Dresselhaus, and M. S. Dresselhaus. Photoexcited electron relaxation processes in single-wall carbon nanotubes. *Phys. Rev. B*, 71:045417, 2005.

- [57] J. Jiang, R. Saito, G. G. Samsonidze, S. G. Chou, A. Jorio, G. Dresselhaus, and M. S. Dresselhaus. Electron-phonon matrix elements in single-wall carbon nanotubes. *Phys. Rev. B*, 72:235408, 2005.
- [58] J. Jiang, R. Saito, G. G. Samsonidze, A. Jorio, S. G. Chou, G. Dresselhaus, and M. S. Dresselhaus. Chirality dependence of the exciton effects in single-wall carbon nanotubes. (*unpublished*).
- [59] J. Jiang, R. Saito, K. Sato, J. S. Park, G. G. Samsonidze, A. Jorio, G. Dresselhaus, and M. S. Dresselhaus. Exciton-photon and exciton-phonon matrix elements and resonance raman intensities of single-wall carbon nanotubes. (*unpublished*).
- [60] L. Jin, C. Bower, and O. Zhou. Alignment of carbon nanotubes in a polymer matrix by mechanical stretching. *Appl. Phys. Lett.*, 73:1197, 1998.
- [61] R. A. Jishi, L. Venkataraman, M. S. Dresselhaus, and G. Dresselhaus. Phonon modes in carbon nanotubules. *Chem. Phys. Lett.*, 209:77, 1993.
- [62] M. Jones, C. Engtrakul, W. K. Metzger, R. J. Ellingson, A. J. Nozik, M. J. Heben, and G. Rumbles. Analysis of photoluminescence from solubilized single-walled carbon nanotubes. *Phys. Rev. B*, 71:115426, 2005.
- [63] A. Jorio, C. Fantini, M. A. Pimenta, R. B. Capaz, G. G. Samsonidze, G. Dresselhaus, M. S. Dresselhaus, J. Jiang, N. Kobayashi, A. Grüneis, and R. Saito. Resonance raman spectroscopy (n, m) dependent effects in small diameter single-walled carbon nanotubes. *Phys. Rev. B*, 71:075401, 2005.
- [64] A. Jorio, M. A. Pimenta, A. G. Souza Filho, G. G. Samsonidze, A. K. Swan, M. S. Ünlü, B. B. Goldberg, R. Saito, G. Dresselhaus, and M. S. Dresselhaus. Resonance raman spectra of carbon nanotubes by cross-polarized light. *Phys. Rev. Lett.*, 90:107403, 2003.
- [65] A. Jorio, R. Saito, J. H. Hafner, C. M. Lieber, M. Hunter, T. McClure, G. Dresselhaus, and M. S. Dresselhaus. Structural (n, m) determination of isolated

- single-wall carbon nanotubes by resonant raman scattering. *Phys. Rev. Lett.*, 86:1118, 2001.
- [66] A. Jorio, A. G. Souza Filho, V. W. Brar, A. K. Swan, M. S. Ünlü, B. B. Goldberg, A. Righi, J. H. Hafner, C. M. Lieber, R. Saito, G. Dresselhaus, and M. S. Dresselhaus. Polarized resonant raman study of isolated single-wall carbon nanotubes: symmetry selection rules, dipolar and multipolar antenna effects. *Phys. Rev. B*, 65:121402, 2002.
- [67] A. Jorio, A. G. Souza Filho, G. Dresselhaus, M. S. Dresselhaus, A. K. Swan, M. S. Ünlü, B. B. Goldberg, M. A. Pimenta, J. H. Hafner, C. M. Lieber, and R. Saito. *g*-band resonant raman study of 62 isolated single-wall carbon nanotubes. *Phys. Rev. B*, 65:155412, 2002.
- [68] Y. Oyama J. Jiang L. G. Cançado M. A. Pimenta A. Jorio G. G. Samsonidze G. Dresselhaus K. Sato, R. Saito and M. S. Dresselhaus. D-band raman intensity of graphitic materials as a function of laser energy and crystallite size. *Chem. Phys. Lett.*, 427:117, 2006.
- [69] C. L. Kane. Materials science: erasing electron mass. *Nature*, 438:168, 2005.
- [70] C. L. Kane and E. J. Mele. Electron interactions and scaling relations for optical excitations in carbon nanotubes. *Phys. Rev. Lett.*, 93:197402, 2004.
- [71] H. Kataura, Y. Kumazawa, Y. Maniwa, I. Umez, S. Suzuki, Y. Ohtsuka, and Y. Achiba. Optical properties of single-wall carbon nanotubes. *Synth. Metals*, 103:2555, 1999.
- [72] A. Kawabata. Green function theory of raman scattering. *J. Phys. Soc. Jpn.*, 30:68, 1971.
- [73] Y. Kawashima and G. Katagiri. Fundamentals, overtones, and combinations in the raman spectrum of graphite. *Phys. Rev. B*, 52:10053, 1995.

- [74] Y. Kawashima and G. Katagiri. Observation of the out-of-plane mode in the raman scattering from the graphite edge plane. *Phys. Rev. B*, 59:62, 1999.
- [75] A. Kleiner and S. Eggert. Band gaps of primary metallic carbon nanotubes. *Phys. Rev. B*, 63:073408, 2001.
- [76] J. Kono, G.N. Ostojic, S. Zaric, M.S. Strano, V.C. Moore, J. Shaver, R.H. Hauge, and R.E. Smalley. Ultra-fast optical spectroscopy of micelle-suspended single-walled carbon nanotubes. *Appl. Phys. A*, 78:1093, 2004.
- [77] O. J. Korovyanko, C.-X. Sheng, Z. V. Vardeny, A. B. Dalton, and R. H. Baughman. Ultrafast spectroscopy of excitons in single-walled carbon nanotubes. *Phys. Rev. Lett.*, 92:017403, 2004.
- [78] G. Kresse, J. Furthmüller, and J. Hafner. Ab initio force constant approach to phonon dispersion relations of diamond and graphite. *Europhys. Lett.*, 32:729, 1995.
- [79] J. Kürti, V. Zólyomi, A. Grüneis, and H. Kuzmany. (*private communication*).
- [80] J. Kürti, V. Zólyomi, M. Kertesz, and G. Sun. The geometry and the radial breathing mode of carbon nanotubes: beyond the ideal behaviour. *New J. of Phys.*, 5:125, 2003.
- [81] J. Lefebvre, P. Finnie, and Y. Homma. Temperature-dependent photoluminescence from single-walled carbon nanotubes. *Phys. Rev. B*, 70:045419, 2004.
- [82] Z. M. Li, V. N. Popov, and Z. K. Tang. A symmetry-adapted force-constant lattice-dynamical model for single-walled carbon nanotubes. *Sol. Stat. Comm.*, 130:657, 2004.
- [83] H. Liang and M. Upmanyu. Axial-strain-induced torsion in single-walled carbon nanotubes. *Phys. Rev. Lett.*, 96:165501, 2006.

- [84] Y.-Z. Ma, L. Valkunas, S. L. Dexheimer, S. M. Bachilo, and G. R. Fleming. Femtosecond spectroscopy of optical excitations in single-walled carbon nanotubes: evidence for exciton-exciton annihilation. *Phys. Rev. Lett.*, 94:157402, 2005.
- [85] M. Machon, S. Reich, H. Telg, J. Maultzsch, P. Ordejon, and C. Thomsen. Strength of radial breathing mode in single-walled carbon nanotubes. *Phys. Rev. B*, 71:035416, 2005.
- [86] C. Mapelli, C. Castiglioni, G. Zerbi, and K. Müllen. Common force field for graphite and polycyclic aromatic hydrocarbons. *Phys. Rev. B*, 60:12710, 1999.
- [87] R. M. Martin and L. M. Falicov. *Light Scattering in Solids I: Introductory Concepts*, edited by M. Cardona, volume 8 of *Topics in Applied Physics*, chapter 3, page 79. Springer-Verlag, Berlin, Heidelberg, New York, second edition, 1983.
- [88] M. J. Matthews, M. A. Pimenta, G. Dresselhaus, M. S. Dresselhaus, and M. Endo. Origin of dispersive effects of the raman d band in carbon materials. *Phys. Rev. B*, 59:R6585, 1999.
- [89] J. Maultzsch, S. Reich, U. Schlecht, and C. Thomsen. High-energy phonon branches of an individual metallic carbon nanotube. *Phys. Rev. Lett.*, 91:087402, 2003.
- [90] J. Maultzsch, S. Reich, and C. Thomsen. Raman scattering in carbon nanotubes revisited. *Phys. Rev. B*, 65:233402, 2002.
- [91] J. Maultzsch, S. Reich, and C. Thomsen. Double-resonant raman scattering in graphite: interference effects, selection rules, and phonon dispersion. *Phys. Rev. B*, 70:155403, 2004.
- [92] J. Maultzsch, S. Reich, C. Thomsen, H. Requardt, and P. Ordejon. Phonon dispersion in graphite. *Phys. Rev. Lett.*, 92:075501, 2004.

- [93] M. Menon, E. Richter, and K. Subbaswamy. Structural and vibrational properties of fullerenes and nanotubes in a nonorthogonal tight-binding scheme. *J. Chem. Phys.*, 5875:1996, 104.
- [94] J. Milnor. *Morse Theory*. Princeton University Press, 1963.
- [95] Y. Miyauchi, S. Chiashi, Y. Murakami, Y. Hayashida, and S. Maruyama. Fluorescence spectroscopy of single-walled carbon nanotubes synthesized from alcohol. *Chem. Phys. Lett.*, 387:198, 2004.
- [96] Y. Miyauchi, M. Oba, and S. Maruyama. Cross-polarized optical absorption of single-walled nanotubes probed by polarized photoluminescence excitation spectroscopy. (*unpublished*).
- [97] H. J. Monkhorst and J. D. Pack. Special points for brillouin-zone integrations. *Phys. Rev. B*, 13:5188, 1976.
- [98] V. C. Moore, M. S. Strano, E. H. Haroz, R. H. Hauge, and R. E. Smalley. Individually suspended single-walled carbon nanotubes in various surfactants. *Nano Lett.*, 3:1379, 2003.
- [99] N. Mounet and N. Marzari. First-principles determination of the structural, vibrational and thermodynamic properties of diamond, graphite, and derivatives. *Phys. Rev. B*, 71:205214, 2005.
- [100] Y. Murakami, S. Chiashi, E. Einarsson, and S. Maruyama. Polarization dependence of resonant raman scattering from vertically aligned single-walled carbon nanotube films. *Phys. Rev. B*, 71:085403, 2005.
- [101] R. Nicklow, N. Wakabayashi, and H. G. Smith. Lattice dynamics of pyrolytic graphite. *Phys. Rev. B*, 5:4951, 1972.
- [102] A. Nojeh, A. Ural, R. F. Pease, and H. Dai. Electric-field-directed growth of carbon nanotubes in two dimensions. *J. Vac. Sci. Technol. B*, 22:3421, 2004.

- [103] K. S. Novoselov, E. McCann, S. V. Morozov, V. I. Fal'ko, M. I. Katsnelson, U. Zeitler, D. Jiang, F. Schedin, and A. K. Geim. Unconventional quantum hall effect and berry's phase of 2π in bilayer graphene. *Nature Physics*, 2:177, 2006.
- [104] M. J. O'Connell, S. M. Bachilo, X. B. Huffman, V. C. Moore, M. S. Strano, E. H. Haroz, K. L. Rialon, P. J. Boul, W. H. Noon, C. Kittrell, J. Ma, R. H. Hauge, R. B. Weisman, and R. E. Smalley. Band gap fluorescence from individual single-walled carbon nanotubes. *Science*, 297:593, 2002.
- [105] Y. Ohno, S. Iwasaki, Y. Murakami, S. Kishimoto, S. Maruyama, and T. Mizutani. Chirality-dependent environmental effects in photoluminescence of single-walled carbon nanotubes. *Phys. Rev. B*, 73:235427, 2006.
- [106] C. Oshima, T. Aizawa, R. Souda, and Y. Ishizawa. Surface phonon dispersion curves of graphite (0001) over the entire energy region. *Solid State Commun.*, 65:1601, 1988.
- [107] M. Ouyang, J.-L. Huang, C. L. Cheung, and C. M. Lieber. Energy gaps in metallic single-walled carbon nanotubes. *Science*, 292:702, 2001.
- [108] Y. Oyama, R. Saito, K. Sato, J. Jiang, G. G. Samsonidze, A. Grüneis, Y. Miyauchi, S. Maruyama, A. Jorio, G. Dresselhaus, and M. S. Dresselhaus. Photoluminescence intensity of single-wall carbon nanotubes. *Carbon*, 44:873, 2006.
- [109] G. S. Painter and D. E. Ellis. Electronic band structure and optical properties of graphite from a variational approach. *Phys. Rev. B*, 1:4747, 1970.
- [110] D. A. Papaconstantopoulos, M. J. Mehl, S. C. Erwin, and M. R. Pederson. Tight-binding hamiltonians for carbon and silicon. In P. E. A. Turchi, A. Gonis, and L. Columbo, editors, *Tight-binding approach to computational materials science*, number 491 in Mater. Res. Soc. Symp. Proc., page 221, Warrendale, PA, 1998. MRS, MRS Press.

- [111] P. Pavone, R. Bauer, K. Karch, O. Schütt, S. Vent, W. Windl, D. Strauch, S. Baroni, and S. Gironcoli. Ab initio phonon calculations in solids. *Phys. B: Cond. Mat.*, 219-220:439, 1996.
- [112] T. G. Pedersen. Variational approach to excitons in carbon nanotubes. *Phys. Rev. B*, 67:073401, 2003.
- [113] V. Perebeinos, J. Tersoff, and Ph. Avouris. Scaling of excitons in carbon nanotubes. *Phys. Rev. Lett.*, 92:257402, 2004.
- [114] V. Perebeinos, J. Tersoff, and Ph. Avouris. Effect of exciton-phonon coupling in the calculated optical absorption of carbon nanotubes. *Phys. Rev. Lett.*, 94:027402, 2005.
- [115] R. Pfeiffer, F. Simon, H. Kuzmany, and V. N. Popov. Fine structure of the radial breathing mode of double-wall carbon nanotubes. *Phys. Rev. B*, 72:161404, 2005.
- [116] M. A. Pimenta, A. Marucci, S. Empedocles, M. Bawendi, E. B. Hanlon, A. M. Rao, P. C. Eklund, R. E. Smalley, G. Dresselhaus, and M. S. Dresselhaus. Raman modes of metallic carbon nanotubes. *Phys. Rev. B*, 58:R16016, 1998.
- [117] S. Piscanec, M. Lazzeri, F. Mauri, A. C. Ferrari, and J. Robertson. Kohn anomalies and electron-phonon interactions in graphite. *Phys. Rev. Lett.*, 93:185503, 2004.
- [118] F. Plentz, H. B. Ribeiro, A. Jorio, M. S. Strano, and M. A. Pimenta. Direct experimental evidence of exciton-phonon bound states in carbon nanotubes. *Phys. Rev. Lett.*, 95:247401, 2005.
- [119] V. N. Popov. Curvature effects on the structural, electronic and optical properties of isolated single-walled carbon nanotubes within a symmetry-adapted non-orthogonal tight-binding model. *New J. Phys.*, 6:17, 2004.

- [120] V. N. Popov, L. Henrard, and P. Lambin. Electron-phonon and electron-photon interactions and resonant raman scattering from the radial-breathing mode of single-walled carbon nanotubes. *Phys. Rev. B*, 72:035436, 2005.
- [121] V. N. Popov and P. Lambin. Radius and chirality dependence of the radial breathing mode and the g -band phonon modes of single-walled carbon nanotubes. *Phys. Rev. B*, 73:085407, 2006.
- [122] D. Porezag, Th. Frauenheim, Th. Köhler, G. Seifert, and R. Kaschner. Construction of tight-binding-like potentials on the basis of density-functional theory: application to carbon. *Phys. Rev. B*, 51:12947, 1995.
- [123] P. M. Rafailov, J. Maultzsch, C. Thomsen, and H. Kataura. Electrochemical switching of the peierls-like transition in metallic single-walled carbon nanotubes. *Phys. Rev. B*, 72:045411, 2005.
- [124] P. M. Rafailov, M. Stoll, and C. Thomsen. Strain determination in electrochemically doped single-walled carbon nanotubes via raman spectroscopy. *J. Phys. Chem. B*, 108:19241, 2004.
- [125] A. M. Rao, E. Richter, S. Bandow, B. Chase, P. C. Eklund, K. W. Williams, S. Fang, K. R. Subbaswamy, M. Menon, A. Thess, R. E. Smalley, G. Dresselhaus, and M. S. Dresselhaus. Diameter-selective raman scattering from vibrational modes in carbon nanotubes. *Science*, 275:187, 1997.
- [126] S. Reich, J. Maultzsch, C. Thomsen, and P. Ordejón. Tight-binding description of graphene. *Phys. Rev. B*, 66:035412, 2002.
- [127] S. Reich, C. Thomsen, and J. Maultzsch. *Carbon nanotubes: basic concepts and physical properties*. Wiley, 2004.
- [128] S. Reich, C. Thomsen, and P. Ordejón. Phonon eigenvectors of chiral nanotubes. *Phys. Rev. B*, 64:195416, 2001.

- [129] R. Saito, G. Dresselhaus, and M. S. Dresselhaus. *Physical properties of carbon nanotubes*. Imperial College Press, 1998.
- [130] R. Saito, G. Dresselhaus, and M. S. Dresselhaus. Trigonal warping effect of carbon nanotubes. *Phys. Rev. B*, 61:2981, 2000.
- [131] R. Saito, M. Fujita, G. Dresselhaus, and M. S. Dresselhaus. Electronic structure of chiral graphene tubules. *Appl. Phys. Lett.*, 60:2204, 1992.
- [132] R. Saito, A. Grüneis, G. G. Samsonidze, V. W. Brar, G. Dresselhaus, M. S. Dresselhaus, A. Jorio, L. G. Cançado, C. Fantini, M. A. Pimenta, and A. G. Souza Filho. Double resonance raman spectroscopy of single-wall carbon nanotubes. *New J. Phys.*, 5:157, 2003.
- [133] R. Saito, A. Grüneis, G. G. Samsonidze, G. Dresselhaus, M. S. Dresselhaus, A. Jorio, L. G. Cançado, M. A. Pimenta, and A. G. Souza Filho. Optical absorption of graphite and single-wall carbon nanotubes. *Appl. Phys. A*, 78:1099, 2004.
- [134] R. Saito, A. Jorio, A. G. Souza Filho, G. Dresselhaus, M. S. Dresselhaus, and M. A. Pimenta. Probing phonon dispersion relations of graphite by double resonance raman scattering. *Phys. Rev. Lett.*, 88:027401, 2002.
- [135] R. Saito and H. Kamimura. Vibronic states of polyacetylene, $(\text{CH})_x$. *J. Phys. Soc. Jpn.*, 52:407, 1983.
- [136] R. Saito, K. Sato, Y. Oyama, J. Jiang, G. G. Samsonidze, G. Dresselhaus, and M. S. Dresselhaus. Cutting lines near the fermi energy of single-wall carbon nanotubes. *Phys. Rev. B*, 72:153413, 2005.
- [137] G. G. Samsonidze, E. B. Barros, R. Saito, J. Jiang, G. Dresselhaus, and M. S. Dresselhaus. Electron-phonon coupling mechanism in two-dimensional graphite and single-wall carbon nanotubes. (*unpublished*).

- [138] G. G. Samsonidze, A. Grüneis, R. Saito, A. Jorio, A. G. Souza Filho, G. Dresselhaus, and M. S. Dresselhaus. Interband optical transitions in left- and right-handed single-wall carbon nanotubes. *Phys. Rev. B*, 69:205402, 2004.
- [139] G. G. Samsonidze, R. Saito, J. Jiang, A. Grüneis, N. Kobayashi, A. Jorio, S. G. Chou, G. Dresselhaus, and M. S. Dresselhaus. Corrections to the optical transition energies in single-wall carbon nanotubes of smaller diameters. In D. L. Carroll, B. Weisman, S. Roth, and A. Rubio, editors, *Functional carbon nanotubes*, number 858E in Mater. Res. Soc. Symp. Proc., page HH7.2, Warrendale, PA, 2005. MRS, MRS Press.
- [140] G. G. Samsonidze, R. Saito, A. Jorio, M. A. Pimenta, A. G. Souza Filho, A. Grüneis, G. Dresselhaus, and M. S. Dresselhaus. The concept of cutting lines in carbon nanotube science. *J. Nanosci. Nanotech.*, 3:431, 2003.
- [141] G. G. Samsonidze, R. Saito, A. Jorio, A. G. Souza Filho, A. Grüneis, M. A. Pimenta, G. Dresselhaus, and M. S. Dresselhaus. Anisotropy in the phonon dispersion relations of graphite and carbon nanotubes measured by raman spectroscopy. In D. L. Carroll, B. Weisman, S. Roth, and A. Rubio, editors, *Quantum confined semiconductor nanostructures*, number 737 in Mater. Res. Soc. Symp. Proc., page F8.10, Warrendale, PA, 2003. MRS, MRS Press.
- [142] G. G. Samsonidze, R. Saito, A. Jorio, A. G. Souza Filho, A. Grüneis, M. A. Pimenta, G. Dresselhaus, and M. S. Dresselhaus. Phonon trigonal warping effect in graphite and carbon nanotubes. *Phys. Rev. Lett.*, 90:027403, 2003.
- [143] G. G. Samsonidze, R. Saito, N. Kobayashi, A. Grüneis, J. Jiang, A. Jorio, S. G. Chou, G. Dresselhaus, and M. S. Dresselhaus. Family behavior of the optical transition energies in single-wall carbon nanotubes of smaller diameters. *Appl. Phys. Lett.*, 85:5703, 2004.
- [144] G. Seifert and H. Eschrig. Lcao- α calculations of transition metal clusters. *Phys. Stat. Sol. B*, 127:573, 1985.

- [145] T. Shimada, T. Sugai, C. Fantini, M. Souza, L. G. Cançado, A. Jorio, M. A. Pimenta, R. Saito, A. Grüneis, G. Dresselhaus, M. S. Dresselhaus, Y. Ohnog, T. Mizutani, and H. Shinohara. Origin of the 2450 cm^{-1} raman bands in hopg, single-wall and double-wall carbon nanotubes. *Carbon*, 43:1049, 2005.
- [146] S. Siebentritt, R. Pues, K. H. Rieder, and A. M. Shikin. Surface phonon dispersion in graphite and in a lanthanum graphite intercalation compound. *Phys. Rev. B*, 55:7927, 1997.
- [147] J. C. Slater and G. F. Koster. Simplified lcao method for the periodic potential problem. *Phys. Rev.*, 94:1498, 1954.
- [148] H. Son, Y. Hori, S. G. Chou, D. Nezich, G. G. Samsonidze, G. Dresselhaus, M. S. Dresselhaus, and E. B. Barros. Environment effects on the raman spectra of individual single-wall carbon nanotubes: suspended and grown on polycrystalline silicon. *Appl. Phys. Lett.*, 85:4744, 2004.
- [149] H. Son, A. Reina Cecco, G. G. Samsonidze, R. Saito, A. Jorio, J. Kong, and M. S. Dresselhaus. Raman characterization of electronic transition energies of metallic single-wall carbon nanotubes. (*unpublished*).
- [150] M. Souza, A. Jorio, C. Fantini, B. R. A. Neves, M. A. Pimenta, R. Saito, A. Ismach, E. Joselevich, V. W. Brar, G. G. Samsonidze, G. Dresselhaus, and M. S. Dresselhaus. Single- and double-resonance raman g-band processes in carbon nanotubes. *Phys. Rev. B*, 69:241403, 2004.
- [151] A. G. Souza Filho, M. Endo, H. Muramatsu, T. Hayashi, Y. A. Kim, E. B. Barros, N. Akuzawa, G. G. Samsonidze, R. Saito, and M. S. Dresselhaus. Resonance raman scattering studies in br_2 -adsorbed double-wall carbon nanotubes. *Phys. Rev. B*, 73:235413, 2006.
- [152] A. G. Souza Filho, A. Jorio, A. K. Swan, M. S. Ünlü, B. B. Goldberg, R. Saito, J. H. Hafner, C. M. Lieber, M. A. Pimenta, G. Dresselhaus, and M. S. Dres-

- selhaus. Anomalous two-peak g' -band raman effect in one isolated single-wall carbon nanotube. *Phys. Rev. B*, 65:085417, 2002.
- [153] A. G. Souza Filho, N. Kobayashi, J. Jiang, A. Grüneis, R. Saito, S. B. Cronin, J. Mendes Filho, G. G. Samsonidze, G. Dresselhaus, and M. S. Dresselhaus. Strain-induced interference effects on the resonance raman cross section of carbon nanotubes. *Phys. Rev. Lett.*, 95:217403, 2005.
- [154] A. G. Souza Filho, A. Jorio and G. G. Samsonidze, G. Dresselhaus, M. S. Dresselhaus, A. K. Swan, M. S. Ünlü, B. B. Goldberg, R. Saito, J. H. Hafner, C. M. Lieber, and M. A. Pimenta. Probing the electronic trigonal warping effect in individual single-wall carbon nanotubes using phonon spectra. *Chem. Phys. Lett.*, 354:62, 2002.
- [155] C. D. Spataru, S. Ismail-Beigi, L. X. Benedict, and S. G. Louie. Excitonic effects and optical spectra of single-walled carbon nanotubes. *Phys. Rev. Lett.*, 92:077402, 2004.
- [156] C. D. Spataru, S. Ismail-Beigi, R. B. Capaz, and S. G. Louie. Theory and ab initio calculation of radiative lifetime of excitons in semiconducting carbon nanotubes. *Phys. Rev. Lett.*, 95:247402, 2005.
- [157] B. Stojetz, C. Miko, L. Forró, and C. Strunk. Effect of band structure on quantum interference in multiwall carbon nanotubes. *Phys. Rev. Lett.*, 94:186802, 2005.
- [158] P. Tan, S. Dimovski, and Y. Gogotsi. Raman scattering of non-planar graphite: arched edges, polyhedral crystals, whiskers and cones. *Phil. Trans. R. Soc. Lond. A*, 362:2289, 2004.
- [159] P. H. Tan, C. Y. Hu, J. Dong, W. C. Shen, and B. F. Zhang. Polarization properties, high-order raman spectra, and frequency asymmetry between stokes and anti-stokes scattering of raman modes in a graphite whisker. *Phys. Rev. B*, 64:214301, 2001.

- [160] P. H. Tan, Y. Tang, Y. M. Deng, F. Li, Y. L. Wei, and H. M. Cheng. Resonantly enhanced raman scattering and high-order raman spectra of single-walled carbon nanotubes. *Appl. Phys. Lett.*, 75:1524, 1999.
- [161] C. Thomsen and S. Reich. Double resonant raman scattering in graphite. *Phys. Rev. Lett.*, 85:5214, 2000.
- [162] M. Tommasini, E. Di Donato, C. Castiglioni, and G. Zerbi. Relaxing the graphite lattice along critical directions: the effect of the electronphonon coupling on the π electron band structure. *Chem. Phys. Lett.*, 414:166, 2005.
- [163] S. Uryu and T. Ando. Exciton absorption of perpendicularly polarized light in carbon nanotubes. *Phys. Rev. B*, 74:155411, 2006.
- [164] F. Villalpando-Paez, H. Son, G. G. Samsonidze, S. G. Chou, Y.A. Kim, H. Muramatsu, T. Hayashi, J. Kong, H. Terrones, G. Dresselhaus, M. Endo, M. Terrones, and M. S. Dresselhaus. Raman spectroscopy of boron-doped double-wall carbon nanotubes. (*unpublished*).
- [165] P. R. Wallace. The band theory of graphite. *Phys. Rev.*, 71:622, 1947.
- [166] F. Wang, G. Dukovic, L. E. Brus, and T. F. Heinz. Time-resolved fluorescence of carbon nanotubes and its implication for radiative lifetimes. *Phys. Rev. Lett.*, 92:177401, 2004.
- [167] N. Wang, Z. K. Tang, G. D. Li, and J. S. Chen. Single-walled 4 Å carbon nanotube arrays. *Nature*, 408:50, 2000.
- [168] R. B. Weisman and S. M. Bachilo. Dependence of optical transition energies on structure for single-walled carbon nanotubes in aqueous suspension: an empirical katura plot. *Nano Lett.*, 3:1235, 2003.
- [169] J. W. G. Wildöer, L. C. Venema, A. G. Rinzler, R. E. Smalley, and C. Dekker. Electronic structure of carbon nanotubes investigated by scanning tunneling spectroscopy. *Nature*, 391:59, 1998.

- [170] L. Wirtz and A. Rubio. The phonon dispersion of graphite revisited. *Sol. Stat. Comm.*, 131:141, 2004.
- [171] L. Yang and J. Han. Electronic structure of deformed carbon nanotubes. *Phys. Rev. Lett.*, 85:154, 2000.
- [172] L. H. Ye, B. G. Liu, D. S. Wang, and R. Han. Ab initio phonon dispersions of single-wall carbon nanotubes. *Phys. Rev. B*, 69:235409, 2004.
- [173] Y. Yin, S. Cronin, A. Walsh, A. Stolyarov, M. Tinkham, A. Vamivakas, W. Bacsa, M. S. Ünlü, B. B. Goldberg, and A. K. Swan. Intrinsic optical transition energies in carbon nanotubes. *arXiv:cond-mat/0505004*.
- [174] S. Zaric, G. N. Ostojic, J. Kono, J. Shaver, V. C. Moore, M. S. Strano, R. H. Hauge, R. E. Smalley, and X. Wei. Optical signatures of the aharonov-bohm phase in single-walled carbon nanotubes. *Science*, 304:1129, 2004.
- [175] G. Zhang, D. Mann, L. Zhang, A. Javey, Y. Li, E. Yenilmez, Q. Wang, J. P. McVittie, Y. Nishi, J. Gibbons, and H. Dai. Ultra-high-yield growth of vertical single-walled carbon nanotubes: hidden roles of hydrogen and oxygen. *PNAS*, 102:16141, 2005.
- [176] Y. Zhang, Y.-W. Tan, H. L. Stormer, and P. Kim. Experimental observation of the quantum hall effect and berry's phase in graphene. *Nature*, 438:201, 2005.
- [177] H. Zhao and S. Mazumdar. Electron-electron interaction effects on the optical excitations of semiconducting single-walled carbon nanotubes. *Phys. Rev. Lett.*, 93:157402, 2004.